



Boston Scientific

Optimising Laser Lithotripsy

Bingyuan Yang

bingyuan.yang@nds.ox.ac.uk

Wadham College

October 2024

Supervisors:

Prof. Ben Turney	University of Oxford
Prof. Robin Cleveland	University of Oxford
Dr. Aditi Ray	Boston Scientific

Table of Contents

Publications, prizes and presentations arising from this work 9

1. Introduction 11

Laser physics 13

Basic principles 13

Stimulated emission versus spontaneous emission 13

Population inversion 15

The 3-level laser 15

Anatomy of a laser system 16

Laser media 17

The history of lasers in stone surgery 18

Ureteroscopy and early endoscopic stone treatment 18

Endoscopic lithotripters 19

Laser-tissue interactions 20

Early in vitro laser development 24

Optical fibres 25

Q-switched Nd:YAG lasers 26

Pulsed dye lasers 27

Clinical use: laser induced shockwave lithotripsy 28

Early laser mechanisms: plasma and photoacoustic effect 29

Selecting the best lithotripter 30

Second generation solid-state lasers 31

Mechanism of the Ho:YAG laser 32

A paradigm shift in lasers 34

Adapting the photoacoustic laser: FREDDY 35

Ho:YAG laser development: ablation efficacy, retropulsion and particle size 36

The Moses effect 37

Pulse-modulated Ho:YAG lasers 37

Erbium-based lasers 38

Thulium-based lasers 38

Fibre lasers 39

The modern thulium fibre laser 40

Systems involved in laser lithotripsy 41

Human factors 42

Ureteroscope technology 43

Endoscopic display 44

Irrigation system 45

Experimental lasers 46

P120 46

Soltive 47

Prototype 47

2. Laser pulse measurement 49

Methods 49

Results 50

Laser pulse profiles 50

Pulse width measurements 54

Pulse widths – P120 56

Pulse widths – Soltive 57

Pulse widths – prototype 58

3. Ablation rate 59

Introduction 59

BegoStone as a stone phantom 59

Measuring ablation rate using BegoStone phantoms 61

Ablation rate apparatus 62

Ablation rate in contact 64

Scan speed 65

Methods 66

Results - unsoaked stones 69

Results - pre-soaked stones 75

Discussion 78

Alternative ablation rate calculation using volume measurement 82

Ablation rate at a distance 84

Methods 84

Results – unsoaked stones 86

Results – pre-soaked stones 89

Discussion 92

Conclusions 100

4. Retropulsion 103

Introduction 103

Pendulum experiments 107

Methods 107

Results 110

Discussion – pendulum experiments 115

Linear experiments 117

Methods 117

Results 120

Discussion 129

Analysis of trajectory and variability 131

Results with NRSS 136

Conclusions 140

5. Particle size 144

Introduction 144

Objectives 149

Particle size distribution of canine stones 150

Methods 150

Results 152

Discussion 157

Washout of stone particles 159

Quartz-based stone dust model 160
Quartz dust sedimentation experiments 162
Microscopy of quartz and stone dust particles 167
Kidney washout experiment 170
Washout introduction and objectives 170
Methods 171
Results 175
Discussion 184
Conclusions 185
6. Integrated model 187
Introduction 187
Methods 187
Results 190
Discussion 198
Conclusions 201
7. Conclusions 202
Ablation rate 202
Retropulsion 205
Particle size 208
The current state of urological lasers 212
The future of lasers in stone surgery 215
Appendix 1: BegoStone preparation 219

BegoStone mixture 219

Flat BegoStone preparation 219

Cylindrical BegoStone preparation 221

Appendix 2: Software used for stone ablation volume analysis 223

Perl script for analysing ablation trenches 223

Appendix 3: High-speed photography of laser-induced vapour bubbles 230

Appendix 4: High-speed photography of stone motion 232

Geometric considerations in calculating motion 232

Parallax error 232

Movement out of plane 235

Experimental constraints for linear retropulsion 243

Pendulum stone trajectory 244

Image tracking algorithm and limitations 246

Python image tracking script 249

References 254

Thanks to my supervisors at the University of Oxford and Boston Scientific for their support and guidance

Thanks to my family for their patience and understanding

Thanks to Boston Scientific for sponsoring this project

Publications, prizes and presentations arising from this work

Publications:

- Yang B, Ray A, Zhang JJ, Peng S, O'Brien M, Turney B. Stone ablation efficacy: a comparison of a thulium fibre laser and two pulse-modulated holmium:YAG lasers. Urolithiasis. 2023 Jan 12;51(1):31
- Yang B, Ray A, Zhang J, Turney B. How Effective Is Ureteroscopic Irrigation at Evacuating Stone Dust?. JU Open Plus. 2024 May 2(5):e00036

Manuscripts pending submission:

- The role of acceleration in stone retropulsion of Ho:YAG and thulium fibre lasers
- Variability in stone retropulsion trajectory of Ho:YAG and thulium fibre lasers
- Quartz sand is a viable phantom for human stone dust

Prizes:

- SPIE Photonics West 2023, Best Student Paper Award – Analysis of stone trajectory during laser lithotripsy: an in vitro study
- SPIE Photonics West 2024, Best Paper Award – Does stone composition impact particle size distribution following laser ablation?
- American Urological Association Annual Meeting 2024, Award-Winning Video – How effective is ureteroscopic irrigation at evacuating stone dust?

Presentations:

- European Association of Urology Annual Congress 2021 (virtual) – In vitro evaluation of a prototype Holmium laser with pulse modulation
- American Urological Association Annual Meeting 2021 (virtual) – Stone ablation efficiency of a new prototype Holmium:YAG pulse-modulated laser at working distances of up to 3mm

- World Conference of Endourology and Urotechnology 2021 (virtual) – Stone ablation efficiency of a new prototype pulse-modulated laser and a 120W Holmium-YAG laser
- World Conference of Endourology and Urotechnology 2021 (virtual) – The effect of peak power and pulse modulation on lithotripsy particle size
- World Conference of Endourology and Urotechnology 2021 (virtual) – Stone ablation efficiency of a new prototype pulse-modulated laser at working distances of up to 3mm
- SPIE Photonics West 2023 – Analysis of stone trajectory during laser lithotripsy: an in vitro study
- World Conference of Endourology and Urotechnology 2023 (converted to virtual) – Particle size distribution of urinary stones after Ho:YAG laser ablation
- World Conference of Endourology and Urotechnology 2023 (converted to virtual) – Which stone fragments are left behind after ureteroscopy? An in vitro model
- American Urological Association Annual Meeting 2024 – How effective is ureteroscopic irrigation at evacuating stone dust?

Posters:

- European Association of Urology Annual Congress 2024 - Washing out stone dust: does ureteroscopic irrigation work?

1. Introduction

"Almost every new technique initially evokes a euphoric reaction among surgeons and patients. This period is often followed by indifference and rejection when long-term effects and limitations become obvious."

- Markolf Niemz, *Laser-Tissue Interactions (Fourth Edition)*

No generative artificial intelligence, large language model or equivalent technology has been used in the writing of this thesis.

Urinary stone disease is a major and growing medical field, with significant impact on patients' quality of life and health. It can lead to renal colic, where stones in the kidney migrate into the ureter and cause severe pain, often requiring diagnosis and treatment in a hospital emergency department. It commonly affects younger patients under 44 [1] and so has a significant cost in terms of lost productivity in addition to the cost of treatment. It has been estimated that the cost of stone disease in the USA alone was $2.07 billion in 2000 (without adjusting for inflation), increasing by 35% by 2007 as a result of a combination of prevalence and population changes [2].

Once diagnosed, urinary stones can be managed by either a conservative or interventional strategy. Many smaller stones in the ureter can be treated conservatively by allowing the stone to pass spontaneously [3]. Some stones in the kidney can also be managed conservatively, with a risk that they might migrate and trigger an episode of acute renal colic. However, other stones may be unsuitable for conservative management, or the patient might prefer active treatment. This usually takes the form of shockwave lithotripsy (SWL), ureteroscopy/ureterorenoscopy (URS) or percutaneous lithotripsy (PCNL) [4].

SWL is a non-surgical procedure where ultrasonic shockwaves are transmitted through the patient's skin targeted at the stone in order to break it into smaller fragments that can then be passed

spontaneously. It has historically been a safe, effective and popular treatment modality but is not suitable for all stones or patients. In particular, stones that cannot be visualised by fluoroscopy or ultrasound cannot be treated by SWL.

URS is a minimally invasive surgical procedure where an endoscope is introduced to the urinary tract via the urethra, and a laser is used to break up the stone under direct vision. It is usually done under either a general or spinal anaesthetic. In recent years this has increasingly become the treatment modality of choice, and in the UK it has recently overtaken SWL as the largest volume stone procedure [5]. It is the most relevant setting for laser lithotripsy, and this is the context for the work in this thesis.

PCNL is a minimally invasive surgical procedure where an endoscope is introduced to the urinary tract via a nephrostomy (a tract through the skin overlying the kidney). It is usually done under a general anaesthetic. While it is still minimally invasive, it is significantly more complex surgery than URS and comes with more serious risks [6] and is therefore generally reserved for cases that are unsuitable for URS. A variety of lithotripsy modalities are available for PCNL, including laser, ultrasonic and mechanical lithotripters. Due to the significantly different clinical environment, the use of lasers in PCNL will not be a focus of this thesis.

In addition to the above scenarios, it is also possible for patients to develop stones in the bladder. These bladder stones are usually associated with pathological bladder outlet obstruction, as a stone that is able to migrate through the ureter usually has no problem passing through the (usually) much larger urethra. These stones may also require surgical treatment in the form of cystolithotomy. As with PCNL, this is a significantly different clinical environment to URS and will not be a focus of this thesis.

Finally, there are some soft tissue applications of lasers in urology in tumour ablation and prostate enucleation. These procedures involve radically different laser-tissue interactions to lithotripsy and will not be considered further.

To begin with, the history of urological laser lithotripsy will be reviewed to provide the context for modern stone surgery. The following chapters will then consider specific elements of laser lithotripsy for improvement in turn, and finally bring the findings together with a projection for future development.

Laser physics

Basic principles

The word “laser” originated as an acronym for the concept of “Light Amplification by Stimulated Emission of Radiation”. Today it is often used to refer to a system for producing light using this concept. The theoretical basis was established by Einstein in 1917 [7] using the concept of applying energy to a laser medium material to cause stimulated emission of discrete quanta of coherent light. A laser medium (such as holmium:YAG) consists of atoms or molecules that can exist in more than one energy state, and where decay from a higher energy state to a lower energy state involves emission of radiation. This is sometimes also referred to as the gain medium, as it is the medium by which the amplification (or gain) occurs.

The laser medium is “pumped” with externally applied energy such as light energy, in order to excite atoms into a high energy state. When a majority of atoms are in a high energy state, this is known as population inversion. This results in net emission of photons with a specific wavelength (determined by the laser medium), which are then amplified by the process of stimulated emission of the excited medium atoms to produce coherent light. These processes will be discussed in detail below.

Stimulated emission versus spontaneous emission

Spontaneous emission is the process where excited atoms decay spontaneously by a stochastic process. This is where individual events occur in a random and unpredictable fashion, but the rate of decay events over a large number of atoms and known period of time is predictable. These decay events emit energy in the form of a photon with frequency determined by the energy difference

between ground and excited states. However, these photons are emitted stochastically so there is no fixed phase relationship between each photon. In physics terms, the emission is incoherent.

Stimulated emission is the process where an excited atom may be stimulated by a photon into decaying to the ground state and emitting another photon in the process. This additional photon has the same wavelength and phase as the original photon. In other words, the emission is coherent.

There is a third process which is important to consider, which is absorption. A ground state atom may absorb a photon without any emission, and without going into a high energy state. This process thereby reduces the amount of photons being emitted by the system, and must be overcome in order to produce net emission of photons.

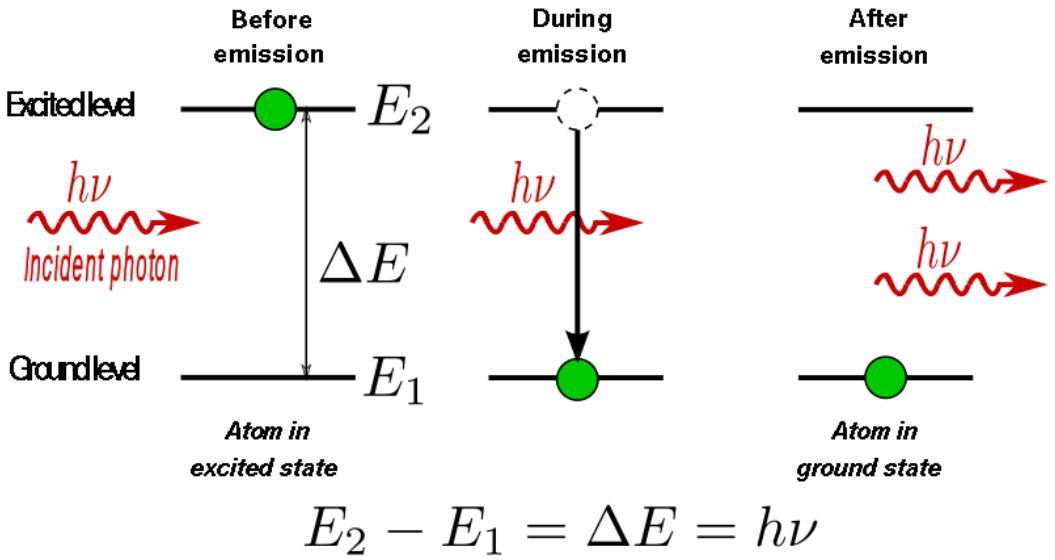


Figure 1. Energy states during stimulated emission. Reproduced from [8].

Einstein showed that the probability of a photon causing emission in an excited atom is the same as the probability of a photon being absorbed by a ground state atom. Consider the situation when photons produced by spontaneous emission are fed back into the system.

If there are more atoms in the ground state than the excited state, there will be net absorption of photons, eventually all photons will be re-absorbed and there will be no net emission.

If there are equal numbers of atoms in the excited and ground states, then the rate of atoms being absorbed by ground state atoms is equal to the rate of stimulated emission. The rate of emission is

therefore equal to the rate of spontaneous emission. This is referred to as being optically transparent.

If there are more atoms in the excited state than the ground state, there are more photons generated by stimulated emission than absorbed by ground state atoms. This therefore causes a positive feedback loop resulting in net emission of coherent light i.e. laser operation.

Population inversion

The concept of having more atoms in the excited state than the ground state is known as population inversion. This is necessary to achieve the light amplification that is integral to laser operation.

Unfortunately the second law of thermodynamics means that applying more pumping energy results in a corresponding increase in the rate of decay of excited atoms. The mathematical equations that govern the ratio of excited to ground state atoms show that this ratio cannot exceed 1:1 at equilibrium (and even this requires an infinite temperature). A 2-level laser model can therefore at best achieve optical transparency but can never achieve laser operation. Another approach is required.

The 3-level laser

The concept of a 3-level laser requires atoms with 3 energy levels instead of just 2. Emission occurs during decay from medium to low energy states. This produces 3 linked dynamic processes:

1. Low energy atoms are pumped into high energy atoms
2. High energy atoms decay spontaneously into medium energy atoms
3. Medium energy atoms decay via spontaneous and stimulated emission into low energy atoms

The medium is chosen so that the decay from medium to low energy is relatively slow compared to the decay from high to medium energy. Then the populations of the energy states will change as follows.

1. High energy atoms are generated rapidly by pumping of low energy atoms, and lost rapidly by decay into medium energy atoms.
    a. The population of high energy atoms will tend towards zero
2. Medium energy atoms are generated rapidly by decay of high energy atoms, and lost slowly by decay into low energy atoms.
    a. The population of medium energy atoms will increase up to a dynamic equilibrium
3. Low energy atoms are generated slowly by decay of medium energy atoms, and lost quickly by pumping into high energy atoms.
    a. The population of low energy atoms will decrease down to a dynamic equilibrium

By careful choice of medium and sufficiently rapid pumping, this 3-level system can maintain a larger population of medium energy atoms than low energy atoms, and thereby achieve population inversion. Since the medium energy atoms decay by stimulated and spontaneous emission, they can form a functioning laser. In practice, energy states are more complex than this simplified model but the concept illustrates how such a laser is feasible within the bounds of physics. There are also 4 (or more) level lasers based on similar principles.

Anatomy of a laser system

Figure 2 illustrates the key components of a laser system, including:

- A laser medium that performs the light amplification
- A pump source that provides energy to start laser operation

- An optical resonator that confines light within the laser medium

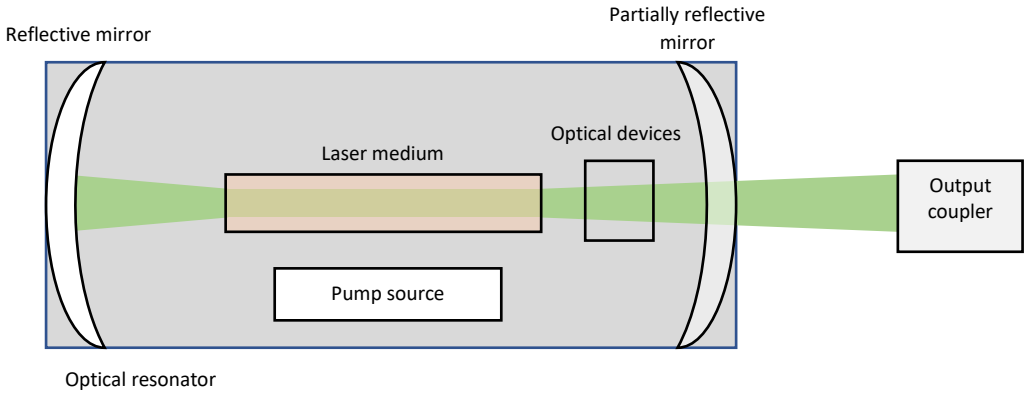


Figure 2. Schematic of a laser system.

Laser media

Laser media can be solid, liquid or gaseous. Liquid and gaseous media typically consist solely of the laser active compound. Solid media usually consist of an optically transparent substance (such as yttrium aluminium garnet crystals, or YAG) which is "doped" by adding a proportion of a laser active compound (such as holmium). The combined solid laser medium is referred to by combining both names (such as holmium:YAG or Ho:YAG), and such lasers are generally referred to as solid-state lasers.

Pump source

The pump source provides the initial energy to start the light amplification process. This is usually in the form of light energy, and can come from a flashlamp or even another laser. Other forms of pump energy such as electrical or heat energy are less common.

Optical resonator

The laser medium and resulting light are confined within an optical resonator, usually with two or more mirrors. Often this resonator is sealed to minimise attenuation of the light, and this is obviously essential for liquid or gaseous media. This is also referred to as the laser cavity.

One of the mirrors is usually partially reflective and allows a proportion of the light energy to escape in the form of the output laser beam.

Other components

In the most basic form, light is produced from the laser system as a simple conical beam. This can be used directly, or connected to an output coupler device to re-focus or transmit the beam. Silica optical fibres are often used to transmit this light using the principle of total internal refraction.

In some cases, optical devices can be placed in the resonator to modify the output light. The most commonly encountered are Q-switches, which are devices that modulate the light output from a continuous beam into short pulses.

The history of lasers in stone surgery

The development and evolution of urological lasers occurred in parallel with the development of the instruments required to introduce them into the upper urinary tract. An understanding of the history of ureteroscopes themselves, as well as the other intracorporeal lithotripters that were used before lasers, sheds some light onto the way in which lasers were adapted into these procedures and why early lasers were so different to the lasers used today.

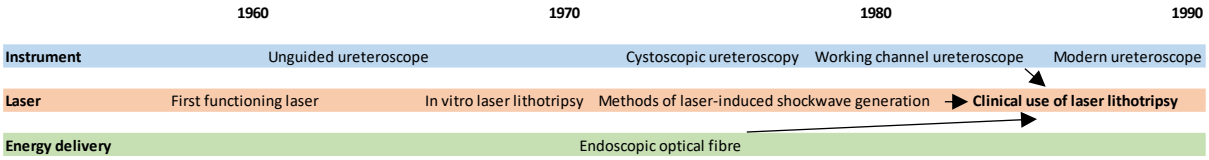


Figure 3. Historical timeline of ureteroscopy and laser development.

Ureteroscopy and early endoscopic stone treatment

The first dedicated ureteroscope was introduced in the early 1960s [9] as purely diagnostic instruments that lacked a working channel. It was a relatively primitive unguided flexible instrument that could do little more than confirm the presence of a ureteric calculus.

There were some reports in the 1970s of paediatric cystoscopes being used in the ureter [10, 11] as these had a working channel and irrigation, but they were limited by their size and length to the

distal ureter in suitable patients. Even then, the lack of suitable instruments meant that they were not regularly used for stone treatment at this point.

The start of the 1980s saw the introduction of instruments intended as dedicated rigid ureteroscopes [12]. Like the other endoscopes of the time, they used a rod lens to transmit light based on Harold Hopkins' design [13]. Early instruments had wider diameters than modern instruments (up to 14.5 French gauge) and were still limited to the distal ureter by their short length. These instruments had working channels, but the selection of treatment devices at the time was restricted to basket retrieval [14], helped by the dilatation of the ureter that was necessary to introduce these large scopes. Flexible ureteroscopes were initially non-steerable and were used where the ureter could not be navigated by these early rigid ureteroscopes, rather than for treatment of renal stones.

By the end of the 1980s, the diameter of rigid ureteroscopes had reduced to the 7.2-9.4 French gauge of modern instruments, and there was a wider selection of lengths up to 50cm that can access the entire ureter [15]. These smaller and more versatile instruments allowed the treatment of stones anywhere in the ureter.

Steerable flexible ureteroscopes were also developed [16]. The original rigid rod lens could not be used as it did not allow sufficient flexibility, and instead a fibre optic bundle was used. This was a tightly packed bundle of optical fibres where each individual fibre transmitted a small part of the image, leading to the characteristic honeycomb appearance when viewing the combined bundle. This flexible bundle allowed the scope to be actively deflected by cables and to access the entirety of the kidney.

Endoscopic lithotripters

In the 1950s, ultrasound and electrohydraulic lithotripters had begun to be used for urinary calculi. Ultrasonic lithotripters used ultrasonic waves delivered via a transducer to shatter stones, whilst

electrohydraulic devices use current passing between two electrodes to rapidly vaporise fluid and create a shockwave. Both these techniques relied primarily on kinetic energy to destroy stones.

Ultrasonic lithotripters transmitted high frequency vibrations into the stone to disintegrate it. This caused minimal damage to soft tissue as it would not resonate at those frequencies [17], although the probe would still heat up with prolonged use and so care was still required.

Electrohydraulic lithotripters produced much more extreme variations in pressure in the form of multiple high pressure shockwaves in the fluid medium, which would shatter the stone. A rapidly expanding vapour bubble was initially created, which then collapsed (causing a second shockwave) and could then "rebound" and collapse again (causing a third shockwave). Pressures of up to 25 MPa could be generated close to a stone, with the greatest pressure coming from the first bubble collapse [18].

With the development of ureteroscopes with working channels, successful attempts were made to use both these technologies in ureteroscopy [19, 20]. Ultrasound was generally considered safe and effective, and is still in use today. However, there were concerns regarding ureteric injury from electrohydraulic lithotripsy [21].

Pneumatic lithotripters were developed for intracorporeal use in the 1990s, most notably the Swiss Lithoclast [22]. This used compressed air to rapidly move a solid probe in a similar way to a pneumatic drill, creating shockwaves to break up the stone. These are still used today in both endoscopic and percutaneous procedures, with modern devices that can even be used with flexible ureteroscopes.

Laser-tissue interactions

Lasers interact with tissue through a variety of mechanisms. Urologists tend to categorise these as photothermal effects, photomechanical effects and photochemical effects [23]. There is significant overlap between the physical processes underlying these mechanisms, particularly photothermal

and photomechanical effects [24], and these will be discussed below. The focus of this section will be on interactions with urinary stones rather than soft tissue in general.

Photothermal effects are caused by a temperature increase from absorbing laser energy as heat energy. This includes all effects from direct photothermal laser-tissue interactions, i.e. absorption of laser energy by the stone. The direct effects on stone include phase changes (melting or plasma formation) and the breaking of chemical bonds. Effects associated with thermal decomposition of the stone in this way can be considered purely photothermal in nature. Thermal expansion of the stone can also trigger secondary mechanical effects. Although these resulting photomechanical effects are a result of photothermal interactions, they are generally referred to as photomechanical effects in literature [23, 25].

Photomechanical effects are caused by changes in the shape of a material from absorbing laser energy, the most basic being thermal expansion. Rapid expansion can generate pressure transients within the stone which can lead to fracturing or cracking of the stone. The nature of these pressure transients depends on the duration of the laser pulse. Extremely short pulses can result in stress confinement, where the laser induces stress waves more quickly than they can propagate through the stone, resulting in very high pressures. This is illustrated in Figure 4. There are also indirect effects from heating of the water within stone matrix, which can itself expand and cause mechanical stress on the stone from within (analogous to the vaporisation of soft tissue). Again, this is generally referred to as a photomechanical effect, despite being caused by a photothermal interaction. These indirect effects may not follow the guidelines shown in Figure 4. The related concept of thermal confinement refers to situations where the laser introduces thermal energy more quickly than it can be distributed through or radiated from the material. When thermal confinement is achieved (by a high power density laser), energy is added too quickly to achieve equilibrium and so extremely high temperatures can be achieved during laser emission.

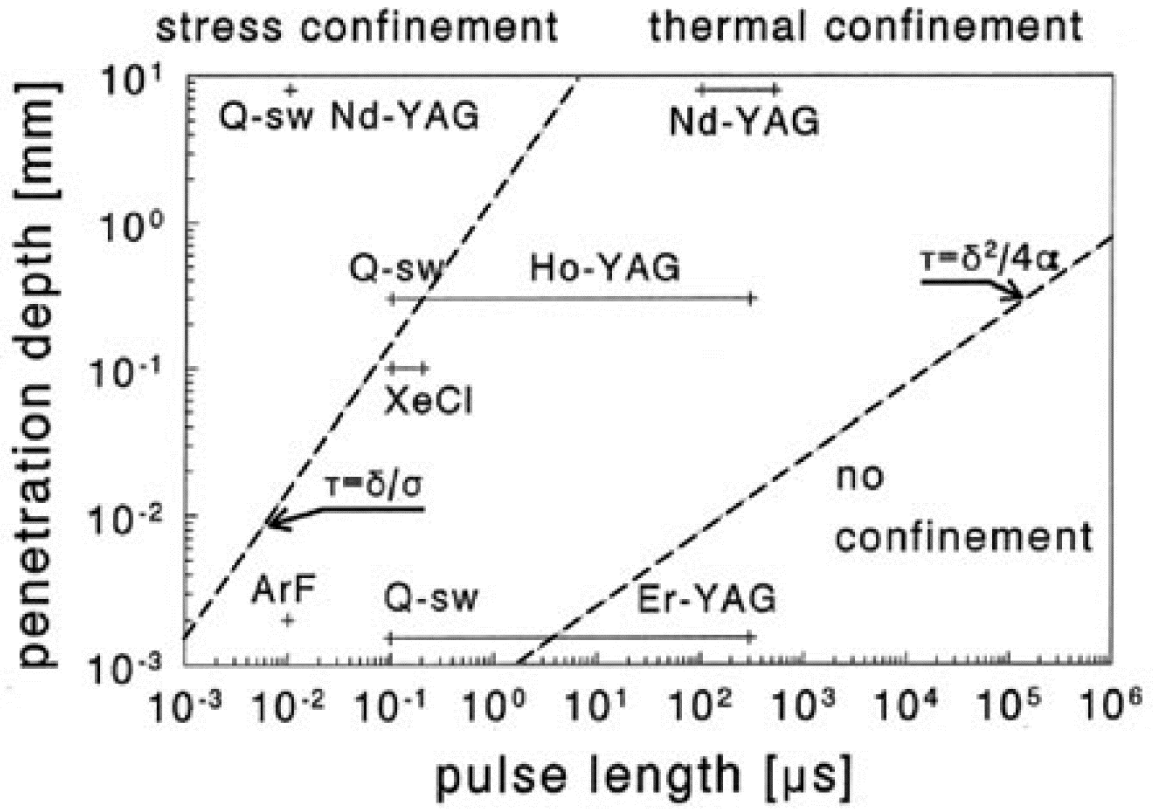


Figure 4. Pressure transient confinement from different laser types. Reproduced with permission from [25].

Very rapid thermal expansion or plasma formation of the surrounding medium can lead to large pressure gradients in the form of shockwaves, which can then act on the stone. This is referred to as a photoacoustic effect, and is not a result of direct interaction between light and stone. It therefore does not follow the same principles that guide direct interactions.

Photochemical effects refer to chemical changes that are mediated directly from light energy absorption and not thermal or mechanical effects: an example would be the effect of sunlight on chlorophyll, or the effect of ultraviolet light on certain molecular bonds. These effects are not thought to be significant in the context of urological stones. Laser ablation of stone can result in chemical decomposition [26], but this is accompanied by large, rapid temperature changes which have been shown to be the likely primary mechanism of their action. Laser ablation will therefore be considered as thermal decomposition rather than chemical.

Plasma-induced ablation is a separate mechanism that is not included here as it is not a significant factor in modern urological lasers, but will be discussed later in the appropriate historical contexts.

Photoablation is not discussed here as it is only relevant for ultraviolet laser emission, which has no current or historical use in stone disease [27].

Figure 5 summarises the range of laser-tissue interactions, where greyed-out interactions are thought to be insignificant in the context of urological stones. For consistency, the following terminology will be used.

- "Photothermal effect" refers to the consequences of phase changes, thermal decomposition and thermal expansion of the stone and any fluid held within the stone. They result from direct interaction between light and the stone.
- "Photoacoustic effect" refers to the consequences of pressure gradients outside the stone as a result of interactions between light and the surrounding medium.

Photothermal effects tend to dominate for laser pulse durations of about 1 μs or longer [27], and this is relevant to evolution of urological lasers over time.

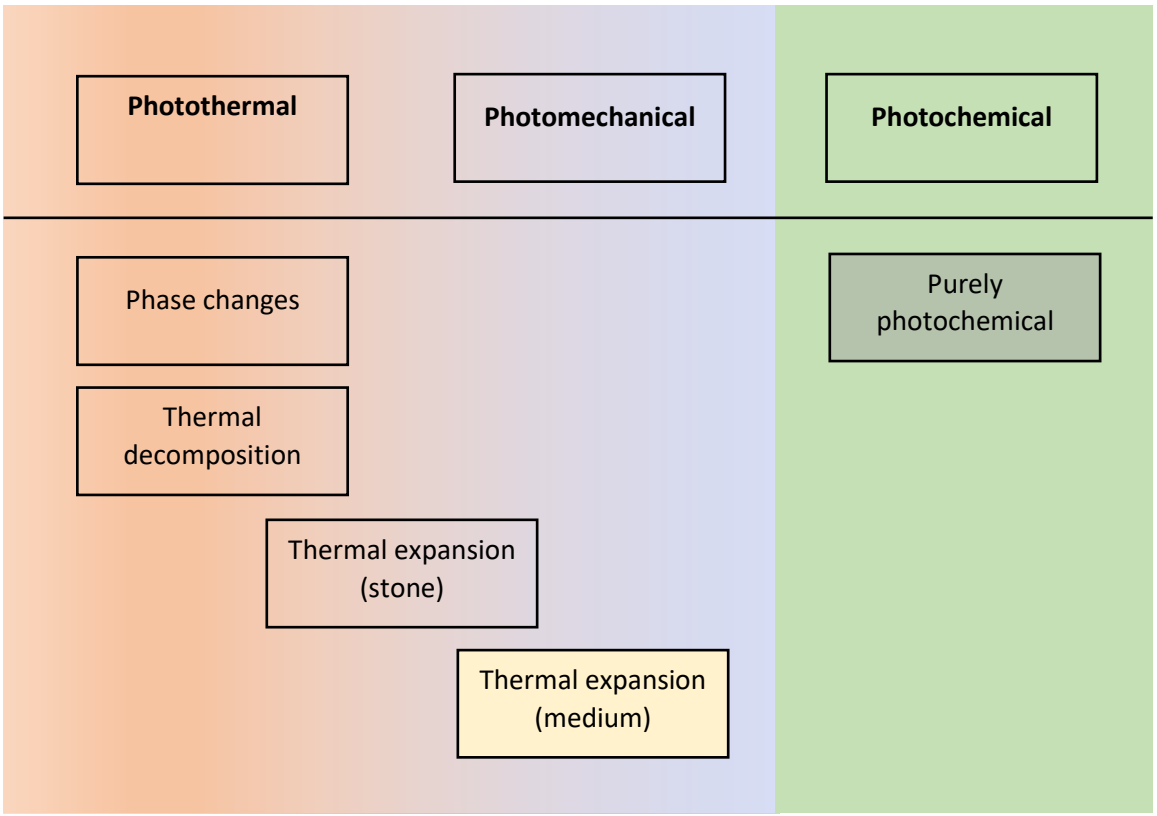


Figure 5: Laser-tissue interactions. Grey boxes are not thought to be significant for stones. Thermal expansion of the medium is a result of laser-medium interactions, not direct laser-stone interaction.

Early in vitro laser development

The first functioning laser was built in 1960 [28] using ruby (red corundum). Towards the end of the decade, it was found that laser energy could effectively fragment urinary calculi ex vivo [29]. The laser in question was a ruby laser with a wavelength of 694nm, and it was noted that the fragmentation could be enhanced by dyeing the stone blue or black, and immersing it in fluid.

At this stage, this work was largely theoretical since the phenomenal amounts of energy delivered (50 to 300 J per pulse) were clearly not feasible inside a patient, not to mention the difficulty in transmitting this energy into the patient safely and effectively. Nevertheless, this laid the groundwork for work to come on the relationship between laser wavelength and absorption, as well as the physical processes behind laser stone ablation.

Early research suggested that this first laser functioned by producing a photoacoustic effect in the form of shockwaves in the fluid, which then broke up the stone. This mechanism was already

established as a successful one in the context of electrohydraulic lithotripsy, and so much of the research in the 1970s on applying lasers to stone surgery was focused on maximising this photoacoustic effect. Many of these efforts used an intermediate material to act effectively as a transducer converting the laser energy into shockwaves [30, 31].

By 1978, Fair was able to produce shockwaves with pressures of up to 10 kbar (100 MPa) using 2J pulses from ruby and Nd-glass lasers firing onto a thin aluminium film [31], capable of fragmenting urinary stones in vitro. This early approach of using the laser beam primarily as a shockwave generator provided a way to mitigate the thermal component of the laser energy, which was seen at the time as a completely undesirable side effect that could cause soft tissue injury.

Attempts were made to apply continuous wave lasers such as carbon dioxide lasers or continuous wave Nd:YAG lasers. These were able to burn or melt stones in vitro [32] but it was clear that these used a primarily photothermal effect to heat the stone to extreme temperatures, and this was considered not feasible in clinical settings. Initial focus therefore remained on pulsed lasers.

Optical fibres

In order to be used clinically, there needed to be a means of safely and efficiently transmitting the laser beam to the target area. Laser energy is usually transmitted via long, thin optical fibres by the principle of total internal reflection. To minimise energy absorption by the fibre and avoid potentially dangerous heating effects, they must be optically transparent to the wavelength of laser energy being transmitted. Silica based fibres such as quartz are commonly used as they were transparent to a wide range of wavelengths.

Optical fibres for the purpose of medical lasers had further limitations in that they needed to be able to transmit laser beams with powers that could be in the megawatt range, through a fibre with a very narrow cross-section. It was therefore important to consider the power density of lasers,

defined as shown below as the power per unit area. This is equivalent to the irradiance, and is measured in W/cm^2.

$$\text{Power density} = \frac{\text{Power}}{\text{Cross} - \text{sectional area}}$$

Very high power densities could result in damage or destruction of laser fibres, so in general higher power lasers required larger calibre optical fibres [33]. In turn, thicker fibres were stiffer and required larger instruments. Even so, there are practical limitations to the power that could be safely transmitted by any given optical fibre depending on the optical transparency of the fibre material to the wavelength of light being carried. This limits the maximum power that can be transmitted, particularly through smaller calibre fibres.

In the early 1970s, a method was developed for successfully transmitting laser energy into a patient via an endoscope [34]. A 150 µm quartz optical fibre was used to transmit a 6W argon laser beam and successfully ablate liver tissue. This removed the need for bulky and complex mirror arrangements for direct transmission of laser energy, although it would be some years before instrument-capable ureteroscopes were in widespread use.

Q-switched Nd:YAG lasers

In the early 1980s, it was found that shortening the pulse durations (from the order of microseconds to the order of nanoseconds) would increase the pressure of shockwaves generated [35].

Nd:YAG lasers were used as a base as they were found rapidly fragment all types of urinary stone in air, despite the fact that their wavelength of 1064 nm was poorly absorbed by the stone. Q-switching is a process by which the output of a laser can be modulated into pulses. It can be thought of as effectively “charging up” the laser during the inactive period where the laser medium continues to be pumped with energy, but there is no emission. This achieves a higher degree of population inversion than could be achieved with continuous emission. The result is that when the

energy is emitted during the short firing period, much higher peak powers can be achieved than with continuous firing.

The Q-switched Nd:YAG laser could produce a pulse duration of 15 ns, resulting in extremely high peak powers (about 67 MW with a 1J pulse). This caused difficulties with transmission of the power through optical fibres, and it would be several years before the quality of fibres was sufficient to transmit this reliably.

Pulsed dye lasers

Dye lasers use organic dyes as the laser medium, as opposed to solid media such as ruby or gaseous media such as carbon dioxide. The advantage of dye lasers is that the wavelength they produce can be tuned within a relatively large range. This was particularly useful for research purposes as altering the wavelength changes the absorption by different materials.

Still in the early 1980s, the established wisdom in urological lasers was that the primary mode of stone destruction would be photoacoustic (i.e. via the creation of high pressure shockwaves) and efforts centred around maximising the shockwave while minimising the unwanted thermal side effects [36]. Watson had already established that shorter pulses generated higher pressures with the Nd:YAG laser, and turned next to pulsed dye lasers in search of a better absorbed wavelength.

Experiments with a range of wavelengths and pulse durations led to a 504 nm wavelength (produced by coumarin green dye) and 1 µs pulse duration being found to have good absorption by stone alongside low tissue absorption [37]. Although this pulse duration was orders of magnitude longer than the 8-15 ns pulses used in the Nd:YAG lasers, it was transmitted more reliably by the optical fibres of the time. The recommended pulse energies trialled in animal models were around 50 mJ, corresponding to a peak power of 50 kW – much lower than that produced by the Nd:YAG laser.

Clinical use: laser induced shockwave lithotripsy

By the late 1980s, all the technological components for ureteroscopic laser lithotripsy were approaching maturity. Dedicated ureteroscopes with working and irrigation channels had been developed, both Q-switched Nd:YAG and pulsed dye lasers had been proven to be effective and safe in animal models, and sufficiently high quality optical fibres could transmit that laser energy reliably through the scope.

A Q-switched Nd:YAG laser was successfully used clinically by 1987 with an 8 ns pulse duration, 50Hz frequency and 35 mJ pulse energy (in patients) [38]. It is interesting to note that this would have produced a peak power during emission of approximately 4.375 MW (i.e. over 4 million Watts) but with an average power of just 1.75 W once gaps between pulses are taken into account. This technique was described most aptly as "Laser induced shockwave lithotripsy" (LISL). The huge power density that this laser produced required relatively large fibres of 600 µm or greater diameter, and the fibre tip had to be protected during the procedure by either a focusing device (allowing non-contact operation) or an optomechanical coupler [39]. This significantly limited the range of stones that could be treated by this laser.

A pulsed dye laser with a 504 nm wavelength was also successfully used clinically from the same year [40] using a 1 µs pulse duration and 5Hz frequency. Again it is interesting to note that commonly used pulse energies were around 60 mJ [41] which would have produced a peak power of approximate 60 kW, despite an average power of just 0.3 W. This is illustrative of the design philosophy behind these early clinical lasers, which aimed to create large shockwaves through very high peak powers while keeping average power low to minimise any thermal effect. The energy density of the pulse dye laser was much lower than the Nd:YAG laser, allowing for slimmer and more flexible 200 µm optical fibres that could operate even with damage to the fibre tip, allowing for direct fibre-to-stone contact. These were sufficiently thin to fit into the flexible ureteroscopes that were being developed around this time.

Early laser mechanisms: plasma and photoacoustic effect

With the successful clinical use of lasers for lithotripsy, more attention was turned to the mechanism by which they caused stone destruction.

The very high power density of Q-switched Nd:YAG lasers was capable of generating ionised plasma [42], which expanded and contracted at extremely high speeds. It was thought that the acoustic shockwaves created by the plasma were the primary mechanism of stone destruction. This plasma is visualised as a characteristic bright spark at the surface of the stone pointing towards the laser source, accompanied by an acoustic report.

Analysis of pulsed dye lasers [43] (and the subsequent alexandrite lasers [44]) demonstrated that they too were also capable of producing plasma. The Q-switched Nd:YAG laser generated this plasma from the water or saline fluid medium (independent of stone absorption), while the lower power densities of the pulsed dye laser used the target stone to generate plasma and was therefore dependent on stone absorption of the laser energy.

Parallel research on the use of Nd:YAG lasers on gallstones had suggested that these lasers were more effective when the stone was immersed in a fluid medium of water or saline [45], and it was shown that the magnitude of shockwaves was increased by immersion [46]. This was thought to be a result of the plasma being confined by water, amplifying the shockwaves in a similar way to the aluminium film and other devices developed in the 1970s for ruby lasers [31].

Measurements of shockwave pressures from laser emission showed that nanosecond pulsed Q-switched Nd:YAG lasers generated the highest pressures during laser emission whereas microsecond pulsed dye lasers generated the highest pressures during bubble collapse [47]. Pulsed dye lasers could generate pressures of 53.2 – 58.5 MPa on bubble collapse when a stone is present, depending on the laser and settings used [47, 48]. In comparison, contemporary electrohydraulic lithotripters could generate pressures of 25 – 30 MPa and early Ho:YAG lasers could generate pressures of 0.18 – 0.36 MPa [47, 48].

It was known that ionised plasma could itself have an ablative effect on stone independent of thermal or mechanical effects, in a phenomenon known as plasma-induced ablation. Teng characterised this in 1987 as “microscopic particles vaporized as blow-off material” which would then initiate the plasma cloud that was seen with these lasers and create the shockwaves. This phenomenon would have excellent applications in other fields such as ophthalmology thanks to the precision with which it could ablate optically transparent tissue at the µm scale [49]. However, the effect that it had on urological stone ablation was probably negligible compared to the plasma mediated photoacoustic effect.

Selecting the best lithotripter

In the 1990s, laser lithotripsy was established in clinical use along with suitable rigid and flexible ureteroscopes.

The Nd:YAG laser’s large calibre fibres and bulky coupling devices limited its manoeuvrability. Special methods of polishing and treating the fibre tip could turn it into a self-focusing device that did not require a coupler, but this required the operator to keep the fibre out of contact with the stone at all times and any damage would render the fibre inoperable [39]. Clinical use had shown poor results on hard stones such as calcium oxalate monohydrate [15, 36, 50], the common stone type in humans.

The pulsed dye laser’s disadvantages were the complexity, cost and inconvenience involved in exchange and maintenance of the toxic dyes used in the laser medium [27]. It also did not work well on cystine stones [50] and produced a mix of small and larger particles [15]. However, the flexibility of the 200 µm fibre that could be used in direct contact with stones allowed it to tackle a wider range of stones and fit flexible instruments, and it was the more popular laser in this period.

Other intracorporeal lithotripters were still in widespread use, with electrohydraulic and ultrasonic devices still popular choices as well as the Swiss Lithoclast pneumatic lithotripter that was developed in this period [22].

It should also be noted that ultrasound and piezoelectric mediated extracorporeal shockwave lithotripsy (ESWL) techniques had been well established as safe and effective methods of treating many ureteric stones [51] whereas intracorporeal laser lithotripsy carried significant risks of ureteric perforation and stricture. Perforation rates of 7% had been reported [52] even with lasers that were considered incapable of injuring the mucosa, and this was considered an inevitable risk of instrumentation rather than a consequence of laser devices.

In these early days of laser lithotripsy, the act of pushing a proximal stone retrogradely into the renal pelvis in order to perform ESWL was considered a viable or even preferential way to treat these stones [51] whereas later on this would become an unwelcome consequence of unsuccessful ureteroscopic efforts.

Second generation solid-state lasers

At the end of the 1980s and early 1990s, attempts were made to develop a new type of laser to combine the strengths of the Nd:YAG and pulsed dye lasers without inheriting their weaknesses.

The Q-switched alexandrite laser was one result of these efforts [53]. This was a solid-state laser like the Nd:YAG laser, avoiding the difficulties associated with dye media. It produced a 750 nm wavelength beam with a pulse width of 150-800 ns and pulse energies of 30-80 mJ. Part of the technological advancement was an intentionally elongated pulse width to reduce the power density (permitting smaller calibre optical fibres) while remaining short enough to meet the threshold for plasma ignition.

With a power density similar to pulsed dye lasers, the alexandrite laser was capable of operating with 200-300 µm quartz fibres without the need for any coupling device. Initial clinical reports with

pulse energies of 80 mJ and frequencies of 10 Hz [50] would correspond with a peak power of 100-533 kW and an average power of 0.8 W, similar to other LISL lasers.

The alexandrite laser was shown to be effective in clinical use, although like existing lasers it suffered from poor effectiveness on certain stones such as pale struvite and urate [54]. At a glance it seemed like a technological step forward over existing lasers, but another laser developed in this time was probably the reason it did not gain much traction.

The long-pulsed Ho:YAG laser was another result of the search for a next generation solid-state laser. This produced light with wavelengths between 2075-2135 nm [55] but typically around 2120 nm [56]. Pulses were relatively wide and could range from 100-1000 µs. These had been under investigation for use on other tissue such as cardiac valves and gastrointestinal polyps [57], but had also shown to effectively ablate bone [58]. This laser had much lower power densities than previous lasers, allowing its use with slim optical fibres that were more flexible and could fit in smaller instruments.

Ex vivo trials on human urinary stones and ureters showed effective fragmentation of urate and struvite stones with a pulse energy of 0.5J and frequency of 5 Hz. Unlike the Nd:YAG laser, it was capable of producing incidental ureteric damage even without direct contact with the ureteric wall, with the degree of damage increased with pulse energy and frequency [59]. The degree of damage was limited to the submucosa at settings of 0.5J and 5Hz, and the risk was considered manageable with careful use.

Initial clinical trials using a 400µm fibre suggested that the Ho:YAG laser was capable of destroying the hard cystine and calcium oxalate stones that previous lasers had struggled with [60, 61], as well as being a versatile tool for ablating urological soft tissue tumours [62]. It was also noted to produce fine particles without much physical movement of the stone [60], both considered desirable traits.

Mechanism of the Ho:YAG laser

The Ho:YAG laser was remarkably different to previous lasers used for lithotripsy. The longer, near infrared wavelength of 2120 nm was known to be well absorbed by water from its soft tissue applications [57], and the typical 250-350 μs pulses were orders of magnitude wider than the nanosecond pulses of the Nd:YAG laser or the microsecond pulses of the pulsed dye and alexandrite lasers. The result was much lower peak powers in the range of 2-6 kW in initial experiments, with correspondingly lower power densities that were below levels usually required for the plasma formation associated with previous lasers.

The effect of the longer pulse duration of Ho:YAG lasers was examined in detail by the use of Q-switching to modulate the pulse duration independently of other laser parameters [63]. It was shown that when Q-switched to a 500 ns pulse duration, Ho:YAG lasers could produce spherical bubbles with an initial pressure wave in the same manner as LISL lasers. However, when the pulse duration was increased to 100 μs or greater (without Q-switching), there was no detectable initial stress wave and an asymmetrical, “pear shaped” bubble. The bubble collapse still created pressure gradients of 66 bars (660 KPa) but these decreased dramatically for pulse widths of 460 μs to 9 bars (90 KPa) and were undetectable for pulse widths of 1100 μs. These pressures were substantially lower than the pressures generated by bubble collapse of the pulsed dye laser (on the order of 5 MPa) and suggested an alternative mechanism.

A multifaceted investigation into the mechanism of Ho:YAG lasers was able to convincingly demonstrate a primarily photothermal mechanism and refute any significant photoacoustic effect [64].

- Pressure measurements made with and without a stone present showed that although pressure gradients from bubble formation and collapse could be measured when fired in water alone, no pressure gradients above 2 bars (20 kPa) could be detected when the laser was fired on a stone in the normal position.

- High speed photography of the firing process also demonstrated stone fragment ejection immediately after laser emission but prior to bubble collapse.
- High speed imaging in a completely darkened environment demonstrated an incandescent glow on the stone at the site of irradiation, implying a significant localised temperature increase.
- Analysis of irradiated stones showed thermal products in the fragments and fluid medium that were not present in the parent stone, e.g. calcium carbonate in fragments from calcium oxalate monohydrate stones, and free sulphur in fragments from cystine stones. This implied sufficient thermal absorption and temperature increase for thermochemical reactions to occur.

A paradigm shift in lasers

The Ho:YAG laser heralded a paradigm shift in the design and goals of lasers in lithotripsy. The evolution is summarised in the table below.

	Nd:YAG laser	**Pulsed dye laser**	**Ho:YAG laser**
Primary mechanism	Photoacoustic	Photoacoustic	Photothermal
Typical peak power	4375 kW	60 kW	4 kW
Typical average power	< 2 W	< 1 W	2.5 – 60 W
Thermal effect	Minimal	Minimal	High, essential
Stone energy absorption	Irrelevant	Variable	High, essential
Stone type	Important	Important	Unimportant
Effect on soft tissue	Negligible	Superficial	Significant
Kinetic energy	High	High	Low
Particle size	Small	Small and large	Smallest [65]
Bubble/laser beam interaction	None	None	Emission continues during bubble formation

Table 1. Evolution of properties of lasers used for lithotripsy.

Before this, lithotripsy lasers were designed to deliver small amounts of energy in extremely short bursts in order to create shockwaves and minimise heat. Inability to damage soft tissue was seen as an advantageous safety feature. After the Ho:YAG laser became popular, the goal switched to delivering high amounts of energy in (often intentionally) longer bursts in order to create a thermal

effect and minimise shockwaves, and the ability to ablate soft tissue became a versatile tool with applications in tumour ablation. This philosophy remains the case for modern lasers today.

Adapting the photoacoustic laser: FREDDY

While the Ho:YAG laser was becoming established as the laser of choice for intracorporeal lithotripsy, a new type of Nd:YAG laser was being developed at the end of the 1990s and early 2000s. The frequency-doubled, double-pulse Nd:YAG laser (known as the FREDDY) was a Q-switched flashlamp pumped solid-state laser [66]. This was based on earlier design philosophies with small amounts of energy (insufficient to cause any significant heating effect) delivered in relatively short, Q-switched pulses in order to generate a photoacoustic effect involving plasma formation. However, it featured two key innovations in the form of a long resonator fibre, and a second crystal that induced resonant frequencies.

The resonator fibre was a long, 25-30m optical fibre between the primary Nd:YAG laser medium and the fully reflective end mirror. This technique effectively extended the length of the resonator chamber and consequently allowed for much longer Q-switched pulses [67], up to 1.4µs [66] compared to the nanosecond pulses of prior Q-switched lasers.

The second crystal used was a potassium-trihydrogenphosphate (KTP) crystal that converted about 20% of the laser output into frequency doubled (i.e. half wavelength) green light. This produced a "double pulse" of synchronous pulses at 1064nm and 532nm which were intended to work synergistically.

The FREDDY laser did not gain significant traction in clinical use, and signalled the end of the era of photoacoustic lasers. As with prior Nd:YAG and pulsed dye lasers, its effectiveness was stone composition dependent [68, 69] and its lack of effect on tissue was seen as a disadvantage as much as it was a benefit [69]. Nevertheless, the principles behind the resonator fibres and multiple synergistic pulses would pave the way for the next developments in laser lithotripsy.

Ho:YAG laser development: ablation efficacy, retropulsion and particle size

The Ho:YAG laser did not have any obvious deficiencies compared to its predecessors. Instead, development turned towards refining characteristics that were considered clinically important, particularly ablation efficacy, retropulsion and particle size. These will be briefly described here and discussed in detail in the corresponding chapters.

Ablation efficacy is the rate at which a laser destroys stones, and is tied to operating time. Higher ablation rates results in shorter operations, which are in turn associated with fewer complications [70, 71]. Despite this, higher ablation efficacy in vitro does not always translate into shorter lasing times in clinical trials [72] and outside of a handful of double-blinded RCTs, the scope for bias and confounding variables is high. Early efforts to improve this included the development of high power Ho:YAG lasers (>30W) using multiple laser cavities whose outputs are combined into a single output beam [56].

Retropulsion is the concept of stones being physically pushed away from the laser fibre during laser operation. The term originates from historical times when photoacoustic lasers in the ureter could push the stone up the ureter against the flow of urine. In the modern era where lasers are used to treat stones in the kidney and bladder in addition to the ureter, the ureter remains the most relevant and most commonly investigated setting. Due to the technical difficulties in objectively measuring movement in vivo, clinical trials usually measure retropulsion by subjective ratings such as Likert scales [73].

Particle size refers to the size of the dust and stone fragments produced by laser stone destruction, and two related outcomes. The first is the size of the largest particles once stone destruction is complete, which is related to the idea that small residual stone fragments at the end of treatment are often considered clinically insignificant [74]. The second is the distribution of the size of these particles, which is important for the behaviour of those particles in liquid suspension as smaller

particles up to 250µm in diameter are thought to wash out of the urinary tract more readily [75], while smaller particles that do not wash out carry a smaller risk of requiring further treatment [76].

The Moses effect

Like pulsed dye lasers, Ho:YAG lasers depend on delivering energy directly to the stone rather than the surrounding fluid medium (as in the case of Nd:YAG lasers). The 2120nm wavelength of Ho:YAG has an absorption coefficient several orders of magnitude higher than the 504 nm wavelength of the pulsed dye laser [77], which rapidly attenuates the beam, reducing the amount of effective energy reaching the stone. In the process, the water is rapidly heated and expands into a bubble [78]. It had been hypothesized that these vapour bubbles could reduce laser attenuation through a fluid medium [79] and this was referred to as a "Moses effect" in the way that "the waters were divided".

This idea was developed into a technology called MOSES technology in 2017 (Lumenis, Israel) where two Ho:YAG pulses are delivered in rapid succession (100-200µs apart). The first pulse would form a vapour bubble and the second would fire through the bubble before it collapsed [80]. Early results suggested that this could improve ablation efficacy and reduce retropulsion [81] though a recent meta-analysis suggest that clinical outcomes, lasing times and total energy delivery are similar to conventional Ho:YAG lasers [72]. Similar technology exists as Virtual Basket and Bubble Blast [82] (Quanta System SpA, Italy) though published outcomes to date are scarce.

Pulse-modulated Ho:YAG lasers

MOSES technology is an example of pulse-modulation applied to Ho:YAG lasers. This refers to the modification of a laser's output; in the case of MOSES technology, the output is briefly turned off to produce two very closely spaced laser pulses.

Other Ho:YAG pulse-modulation technologies modify the power and duration of a single laser pulse, usually by producing a longer pulse duration. This is based on evidence in vitro that delivering the same energy with a longer pulse can reduce retropulsion [83]. Examples include Vapor Tunnel [82]

(Quanta System SpA, Italy), Advanced Mode [84] (Dornier MedTech GmbH, Germany) and Stabilization Mode [85] (Olympus Corporation, Japan). All of these examples claim to reduce retropulsion though published clinical outcomes are again scarce.

It remains to be seen what the effect of these and future pulse-modulated Ho:YAG technologies will be.

Erbium-based lasers

While improvements were being made to Ho:YAG lasers, other types of lasers with different wavelengths were also being investigated. The two most promising were based on erbium and thulium, which had the shared trait of high water absorption.

Erbium-based lasers generally used Er:YAG to produce light with wavelengths of around 2940 nm, much longer than Ho:YAG. These lasers were already well established in dentistry for ablation of tooth enamel [86] and so had proven efficacy on hard, mineralised tissue. The characteristic wavelength of erbium corresponded with a local maximum of water absorption in that region of the light spectrum, with a water absorption coefficient more than two orders of magnitude greater than that of Ho:YAG [77].

In vitro, the Er:YAG laser showed promise in lithotripsy compared to Ho:YAG [87] but was limited by the fact that it could not be transmitted by current standard glass-based optical fibres, but required specialised sapphire optical fibres. As a result, there has been no further investigation into Er:YAG applications in urology [88].

Thulium-based lasers

Like the Er:YAG laser, the thulium:YAG laser was already in use in other medical specialties in the 2010s, mostly for its effective ablation of soft tissue. This is notably similar to the way that Ho:YAG lasers were introduced to lithotripsy.

Tm:YAG produced wavelengths in the range of 1870-2160 nm, overlapping with the commonly used Ho:YAG wavelengths but generally slightly shorter. These shorter wavelengths resulted in far higher water absorption, though not nearly as high as Er:YAG. In one comparison of commercially available lasers, the 2013 nm wavelength Tm:YAG laser had 84% higher water absorption than the 2080 nm wavelength Ho:YAG laser [89]. This would seem to be a disadvantage for Tm:YAG considering that the water absorption of Ho:YAG already caused problems with energy loss that needed to be mitigated with pulse modulation technologies.

Although a handful of studies have been published investigating long pulse Tm:YAG, it did not gain any substantial traction in lithotripsy in the lab nor in clinical practice when it was first evaluated in the 2010s. Instead another development of laser technology took things in a different direction.

Fibre lasers

Most solid-state lasers up to this point in the 2000s used an optically transparent crystal rod (such as YAG) which was then doped by adding small amounts the laser-active agent (such as holmium). Lasers like the FREDDY demonstrated potential advantages of using optical fibres within the laser resonator, and interest grew in another type of solid-state laser called fibre lasers.

Fibre lasers do not use a traditional crystal as the laser medium. Instead they used an optical fibre doped with the laser-active agent. While the concept was proven in the 1960s, the milliwatt powers they generated meant that applications were initially limited.

Fibre lasers have some design advantages over previous “bulk lasers” because the optical fibre acts as an immediate waveguide and channels the light along the lengths of the fibre. This simplifies the design of the resonator into reflecting the light within the fibre, instead of the precise positioning and alignment of mirrors required for bulk lasers. The main disadvantages related to the limited powers that they could generate due to various physical phenomena. Some of the key differences are summarised in Table 2.

	Bulk laser	Fibre laser
Gain medium	Doped crystal rod	Doped silica fibre
Resonator length extension	Difficult with precise mirrors	Easy with loops of fibre
Resonator chamber design	Precise mirror alignment/position	Fibre end mirrors
Pump method	Versatile, often flashlamp	Fibre-coupled diode only
Thermal properties of medium	High volume – difficult to cool, leading to lens effect	High surface area – easier to cool
Power losses through medium	High (>10000 dB/km)	Low (<10 dB/km)
Gain of laser	Low	High

Table 2. Comparison of fibre lasers vs bulk lasers.

The optical transparency of fibre lasers was extremely high, resulting in very low power losses through the medium compared to crystal rods. However, unlike bulk lasers, where the laser medium rod could be pumped by a flashlamp that delivered high amounts of input power, fibre lasers require the pump to be optically coupled to the fibre so the energy can enter the system. This restricted pumps to diodes that were originally limited to a few Watts of input power [90]. Thus, despite the high gains that fibre lasers could produce, their output powers were initially far lower than bulk lasers. Early thulium-based fibre lasers produced maximum powers around the 100-110W range [91, 92], compared to contemporary Ho:YAG lasers that produced powers in the kW range [93].

Improvements in the design of the laser media fibres and the diodes used to pump them in the 2000s led to higher power fibre lasers [90]. Meanwhile early trials on thulium-based fibre lasers suggested potential applications in lithotripsy.

The modern thulium fibre laser

Thulium fibre lasers (TFLs) entered clinical use for lithotripsy towards the end of the 2010s. These used Tm3+ doped glass fibres as the active laser medium and had a wavelength around 1940 nm [94]. This slightly shorter wavelength than previous Tm:YAG lasers corresponds with a much higher water absorption (a local peak at 22C) [95]. More recently, improved methods of pumping these lasers by “superpulsing” the input diode lasers has resulted in output peak powers of up to 500W [96].

Pre-clinical trials have suggested promising potential for TFLs in lithotripsy [56] though results from initial clinical trials have focused on safety rather than effectiveness, and comparative data are still lacking [97-101]. In particular, there has been poor understanding of optimal settings for TFL. In early series, most have reported using high frequency settings (e.g. an average of 0.2J and 175Hz = 35W for ureteric stones in a large North American series [99]) with fewer reports of higher pulse energies (e.g. 1J and 15Hz = 15W in a Romanian series [100]). There is in vitro evidence that higher average powers are associated with increased risk of thermal injury [102, 103] and experienced urologists have recently advocated for maintaining lower average powers below 25W [104]. Although there was early speculation on the wavelength of TFL having a role in these thermal injuries, the underlying physics would imply that the heating effect of Ho:YAG light should be essentially identical to TFL at the same power. No large series could be identified reporting similarly high average power Ho:YAG settings, and this likely stems from the high (and justified) level of caution regarding potential thermal and tissue injury from Ho:YAG introduction into clinical use.

At this time, long term clinical outcomes and robust randomised controlled data regarding TFL are still awaited.

Systems involved in laser lithotripsy

In addition to the laser system, and a means to deliver laser energy safely to the stone, there are many other elements involved in performing laser lithotripsy. These will broadly be divided into human factors and technological elements. A schematic of the intraoperative setup for ureteroscopic laser lithotripsy is shown below in Figure 6.

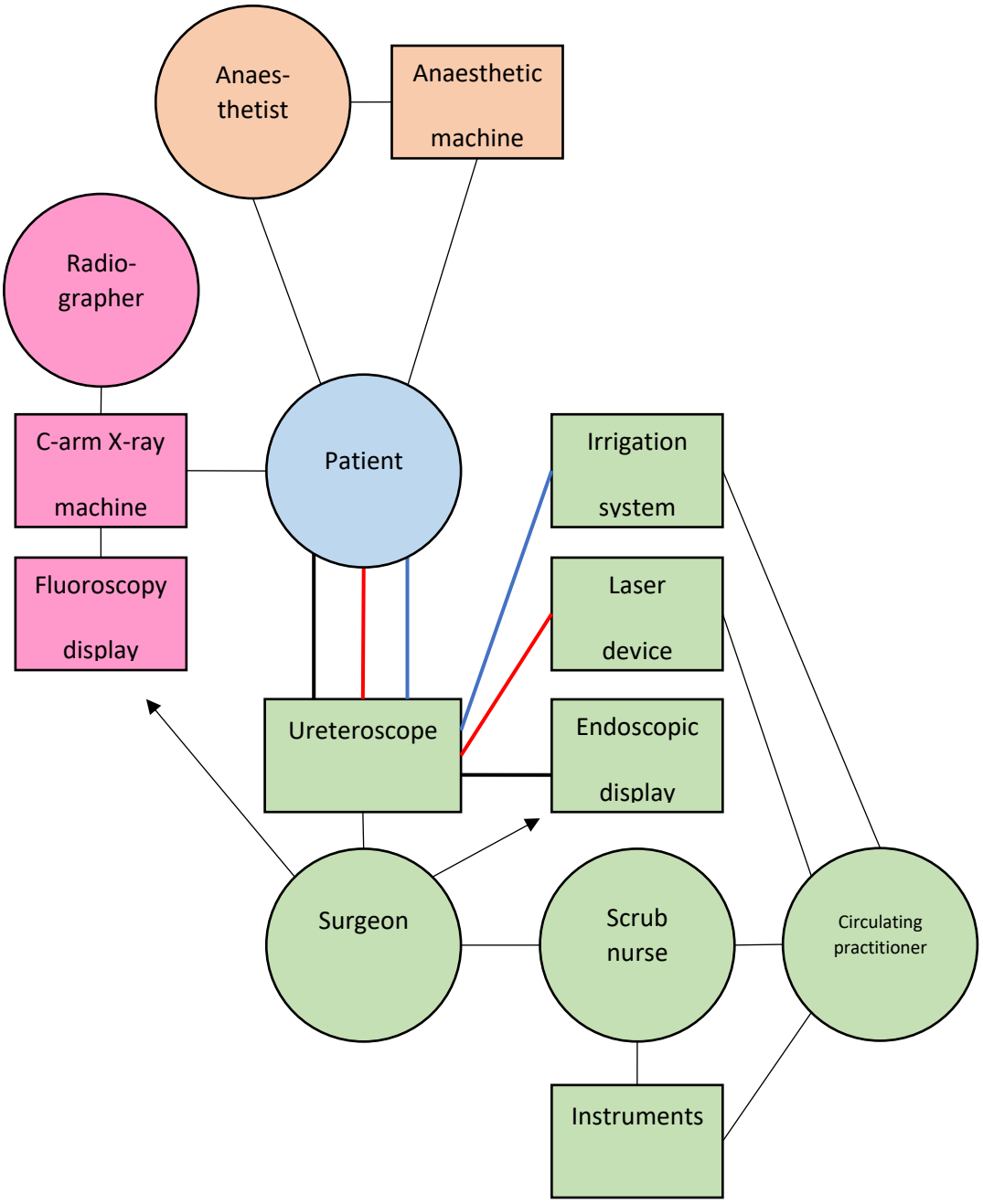


Figure 6. Schematic of intraoperative components required for ureteroscopic laser lithotripsy. Human factors are shown in circles and technological elements in rectangles. Direct interactions are indicated with lines, and visual interactions are indicated with arrows.

Human factors

The majority of human factors are either broadly applicable to all types of surgery, or are governed by specifically designed training programmes. These are far too broad to cover here. However, it is worth noting the roles of clinician skills and knowledge.

Ureterorenoscopy is a highly skill dependent surgical procedure, and the experience of the surgeon is correlated to higher success rates and lower complication rates [105]. It is therefore important to consider training and learning curves when evaluating changes in the field, especially when new and/or disruptive technologies are involved.

Ureteroscope technology

For the 20 years from their introduction in the 1980s until the mid-2000s, endoscopes remained largely analogue devices that used lenses or optical fibres to transmit images. The image could then either be viewed directly by the clinician placing their eye against the viewport, or on an external display by coupling a camera head to the viewport.

As digital imaging technology improved and scaled down, it eventually became small and accessible enough to place in the tip of an endoscope and the first digital ureteroscopes were released in 2006 [106].

Introduction of digital ureteroscopes

Digital ureteroscopes captured the image using a device in the tip of the scope (either a charge-coupled device, CCD, or complementary metal oxide semiconductor, CMOS). This was translated into a digital signal, and could then be transmitted as a digital electronic signal through the length of the scope and into a suitable display using a wire. This mean that the main length of the endoscope could be thinner, more flexible and robust than analogue designs that needed to accommodate a bundle of optical fibres, but at the cost of placing a larger and bulkier electronic component in the tip of the scope. As a result, early digital flexible ureteroscopes were larger calibre than analogue equivalents. They also lacked a viewport for the clinician to directly view the image, or any camera coupling mechanism by which the clinician could rotate the image.

The combination of the larger size, greater cost and different failure modes meant that uptake of these early digital ureteroscopes was limited. The lack of a camera that the clinician could rotate also lead to unfamiliarity and potential disorientation [106].

Single use digital ureteroscopes

Attempts were made at single use ureteroscopes from 2011, with a device called the Polyscope combining a disposable flexible catheter with a reusable fibre optic bundle. While this provided some cost savings by retaining the relatively expensive fibre optic components, it had practical drawbacks in the form of reduced deflection [107] and was not widely adopted.

As digital imaging matured, the point eventually came when it became economical to produce an entirely disposable, single use digital ureteroscope. The first such model was released in 2016 as the LithoVue, with a tip diameter of 7.7 Fr and outer diameter of 9.5 Fr that were comparable to reusable scopes of the time.

Modern single use digital ureteroscopes have been demonstrated as having equivalent or better optical, deflection and flow characteristics compared to reusable ureteroscopes in vitro [108] and comparable clinical outcomes [109, 110]. In contemporary settings, the choice of scope largely comes down to clinician preference and economic factors.

Endoscopic display

Modern endoscopes generally output their images to an external display rather than requiring the clinician to view the image directly via a viewport on the instrument. Modern displays are capable of outputting at either a “4K” resolution (3840 x 2160 pixels) or a “Full HD” resolution (1920 x 1080 pixels). In contrast, flexible ureteroscopes are able to resolve a maximum of 110 lines across the field of view [111]. In other words, the ureteroscope becomes unable to optically resolve detail long before the display limits the resolution. As the display is not the rate limiting factor, display

technology has largely mirrored commercially available displays and higher display resolution is unlikely to materially improve image quality.

Irrigation system

Ureteroscopy is usually performed with continuous irrigation through the working channel, usually with 0.9% sodium chloride solution. This improves visibility by washing away debris, and in the context of laser lithotripsy is particularly important in removing stone fragments/dust and carrying away heat from the laser.

The system usually consists of a bag of saline solution connected to the working channel of the ureteroscope with a method of pressurisation. This pressurisation is required to overcome the high resistance of the long, narrow working channel. Poiseuille's law for laminar flow in a tube is stated below.

$$Q = \frac{(P_2 - P_1)\pi r^4}{8\eta l}$$

Modern flexible ureteroscopes usually use a 3.6 Fr (French gauge; equivalent to 1.2mm diameter) working channel, which carries both the irrigation and any instruments such as laser fibres into the patient [112]. The relatively small diameter of this channel means that flow rates are similarly limited. Typical irrigation rates in vitro for most flexible ureteroscopes are 35-40 ml/min with an empty working channel, and halved to about 15-20 ml/min with a 200µm laser fibre [111]. In a clinical scenario where the flow is further impeded by positive pressure in the kidney, flow drops further to about 30 ml/min with an empty working channel and 15 ml/min with a 200µm laser fibre.

Some manufacturers have produced or are producing instruments with larger working channel diameters such as 4.8 or 5.1 Fr. Data on the effect of these instruments are limited, though in vitro experiments suggest that irrigation rate can be increased by about 5 ml/min in all scenarios with a 4.8 Fr working channel [111].

Experimental lasers

Three lasers were used for this experimental work. These were selected to represent the two most commonly used laser types for urological stone surgery today, i.e. Ho:YAG pulsed lasers and thulium fibre lasers. They are the Pulse 120h (Boston Scientific, Marlborough, USA), the Soltive SuperPulsed Laser System (Olympus, Tokyo, Japan) and a prototype Ho:YAG research laser (Boston Scientific, Marlborough, USA).

P120

The Pulse 120h ("P120") is an example of a Ho:YAG solid state bulk laser. It supports 200µm, 365µm and 550µm class laser fibres, with the 200µm class fibre being the most suited to the narrow working channels of flexible ureteroscopes. It can output pulses of 0.2-6J with a sustained output average power of up to 120W [113], though when a 200µm class fibre is in use this is limited to 0.2-2J with a sustained output average power of up to 60W. The maximum pulse frequency is 80Hz.

The P120 has 3 firing modes: standard mode, Moses Contact (MC) and Moses Distance (MD). Standard mode produces a pulsed output which appears to be in a free-running mode, without any further pulse modulation. The duration of the standard pulse can be further adjusted to be "short", "medium" or "long", but remain on the order of hundreds of microseconds in each case. MC mode splits each pulse into two closely spaced sub-pulses of similar energy, with the goal of the second sub-pulse coinciding with the vapour bubble formation from the first sub-pulse and thereby reducing energy loss from water absorption. MD mode also splits each pulse in two closely spaced sub-pulses but these are asymmetrical and advertised as being more suitable when the fibre is further away from the target stone.

Soltive

The Soltive SuperPulsed Laser System ("Soltive") is an example of a thulium solid state fibre laser. It supports 200µm, 365µm and 550µm class laser fibres. It can output pulses of 0.025-6J with a sustained output average power of up to 60W. The maximum pulse frequency is 2400Hz.

The Soltive has a single firing mode, which produces a pulsed output which appears to be in a free-running mode without any pulse modulation. The duration of the standard pulse can be adjusted to "short", "medium" or "long". As with the P120, this produces a corresponding change in the pulse peak energy, though the impact is more pronounced in the Soltive.

Prototype

The prototype research laser ("prototype") is a Ho:YAG solid state bulk laser. It supports 200µm and 365µm class laser fibres and can output pulses of 0.2-3.5J with a sustained output average power of up to 70W. The maximum pulse frequency is 80Hz.

The prototype has 3 firing modes: standard mode, dusting mode and fragmentation mode. As with the P120, standard mode produced a pulsed output which appears to be in a free-running mode, with further "short" and "long" pulse options. Dusting mode splits each pulse into 20-32 closely spaced sub-pulses of approximately equal energy. Fragmentation mode splits each pulse into 7 closely spaced sub-pulses, again of approximately equal energy.

For example, selecting 1J 20Hz in fragmentation mode will produce "pulses" that are actually pulse trains consisting of 7 sub-pulses at 143mJ each, delivered over approximately 1.2ms. These pulse trains occur at a frequency of 20Hz. Figure 7 illustrates how the P120 and prototype pulse modulation modes look in practice.

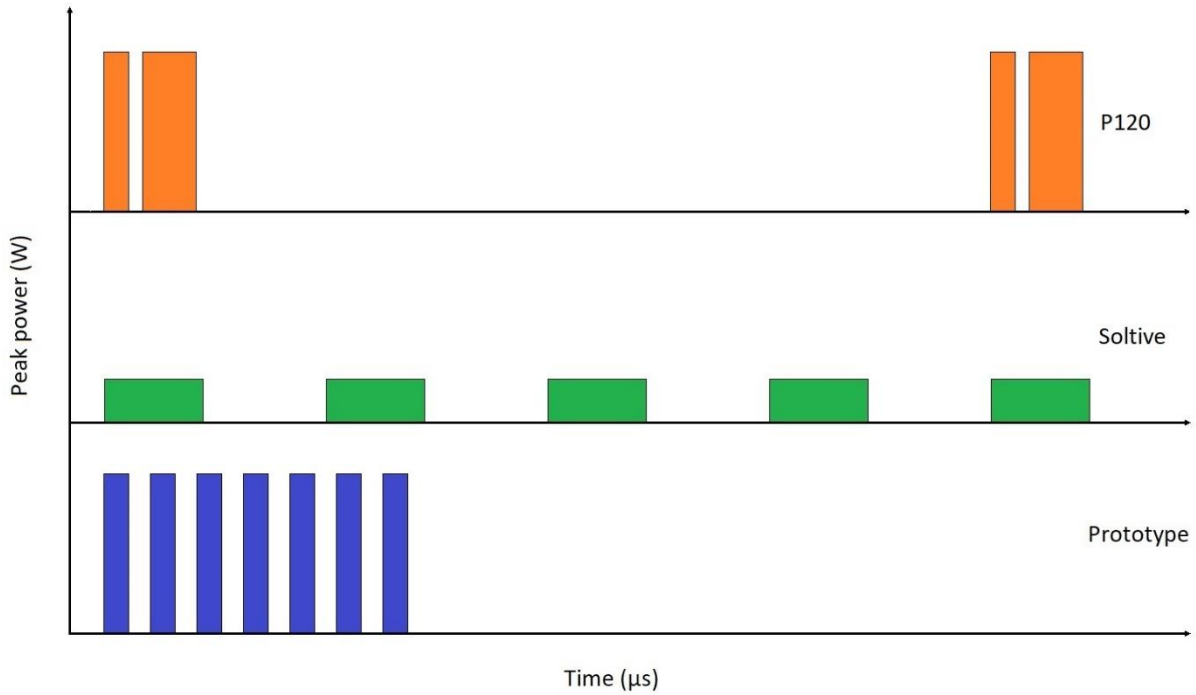


Figure 7. Illustration of pulse modulation firing modes. P120 is showing Moses Distance mode with 2 asymmetric sub-pulses, and prototype is showing fragmentation mode with 7 sub-pulses. Soltive is in standard mode. Not to scale.

Prior to experimentation, the baseline laser pulse characteristics of all 3 lasers were measured using a photodetector. The process and results are detailed in the following chapter.

2. Laser pulse measurement

The laser output of the P120, Soltive and prototype lasers were measured using a photodetector across all available firing modes and a range of pulse energy settings. From this, the pulse widths can be calculated as well as the nature of any pulse modulation.

Methods

Pulses were measured using a photodetector (PDA10T, Thorlabs, NJ, USA) and oscilloscope (DSOX4024A, Keysight Technologies, CA, USA). The equipment was set up as shown in Figure 8. The laser fibre was aimed at a matt white target surface and the photodetector positioned to capture reflected laser energy. A single fibre was used for all readings, and inspected prior to and after each reading to ensure both the fibre and cladding material remained undamaged with a uniform aiming beam. A 1500nm long pass filter (FEL1500, Thorlabs, NJ, USA) was used to filter out light from the visible spectrum while allowing the output light from the laser to be detected. The expected output wavelength was 2120nm for the Ho:YAG lasers and 1940nm for the TFL.

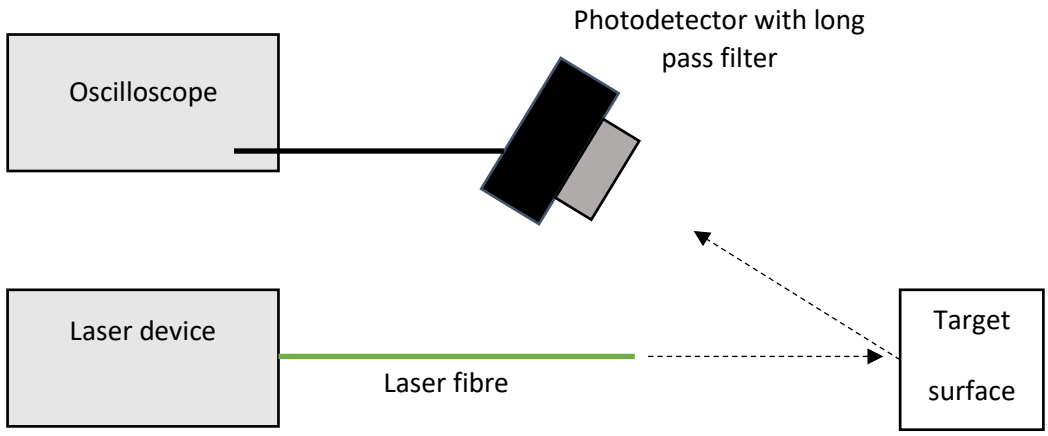


Figure 8. Pulse measurement experimental setup.

The photodetector bandwidth was set to 1MHz, and the photodetector position was adjusted for each laser setting to ensure that the sensor was not saturated by increasing the distance between the photodetector and the target surface as required. The laser was fired continuously at each

setting, and the resulting signal was captured in run/stop mode using an edge trigger. In this mode, the oscilloscope identifies the start of a signal wave when it detects an “edge” in the waveform, indicated by a sudden change in the magnitude of the signal. An average of 30 consecutive pulses was recorded using the oscilloscope’s built-in averaging function. This process was then repeated with the photodetector bandwidth set to 50kHz, to produce a second set of lower resolution data with less noise.

Pulse width was calculated using a full width, half maximum technique. The 50kHz bandwidth data set was used for this calculation, to ensure the pulse width was not disproportionately influenced by large transient spikes in intensity. For P120 pulse modulated firing modes (MC and MD), the width of each of the 2 subpulses was calculated separately. For prototype laser pulse modulated firing modes (dusting and fragmentation), all subpulses are the same width.

Results

Laser pulse profiles

Qualitative examples of pulse measurements for each laser and firing mode are shown below. The y-axis is in arbitrary units (photodetector voltage). The x-axis scale is kept consistent for settings within each laser, but varies between different lasers.

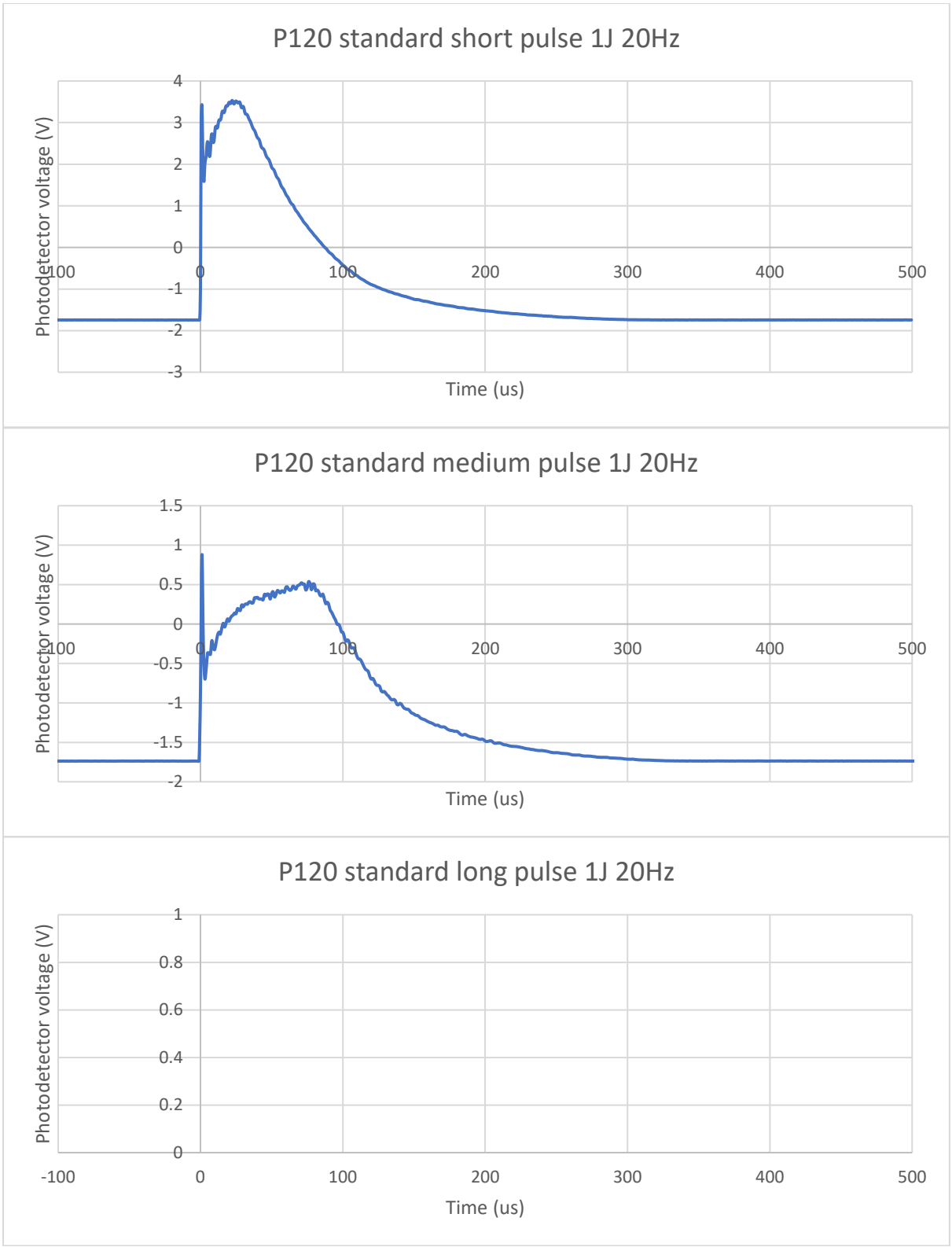


Figure 9. P120 standard pulse, 1J 20Hz in short, medium and long pulse modes.

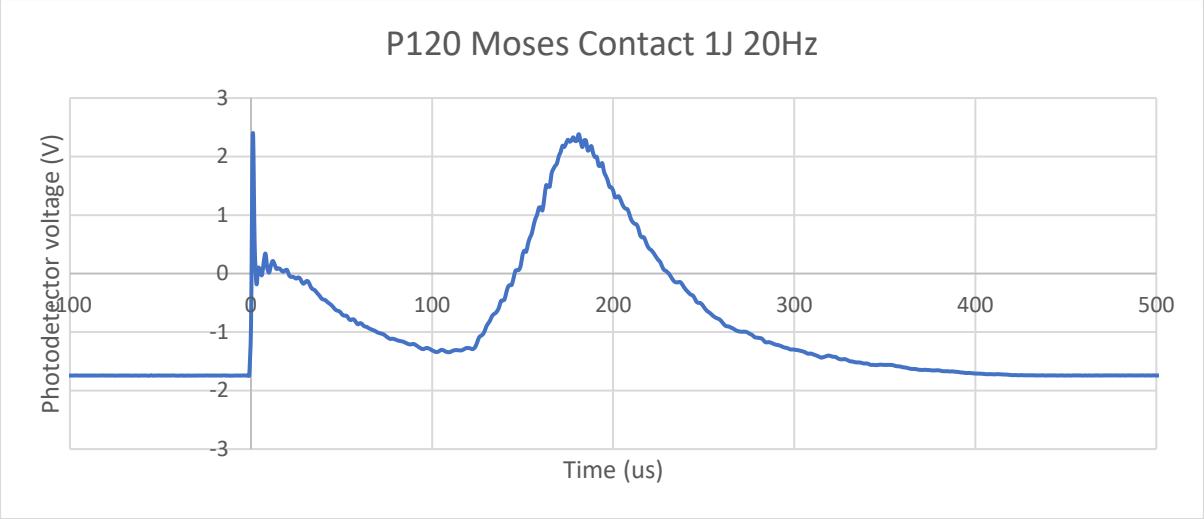


Figure 10. P120 Moses contact mode, 1J 20Hz.

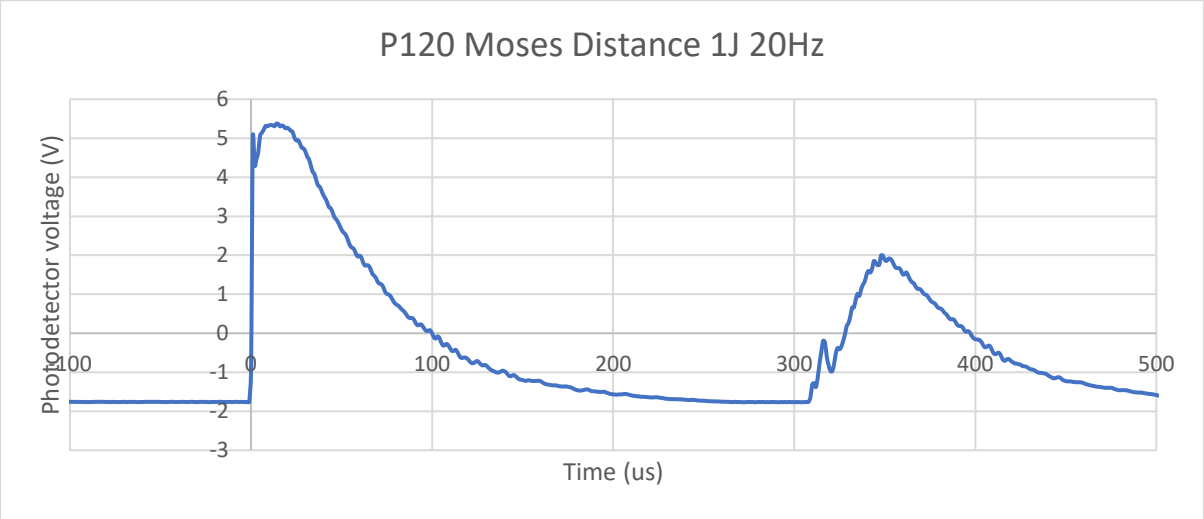


Figure 11. P120 Moses Distance mode, 1J 20Hz.

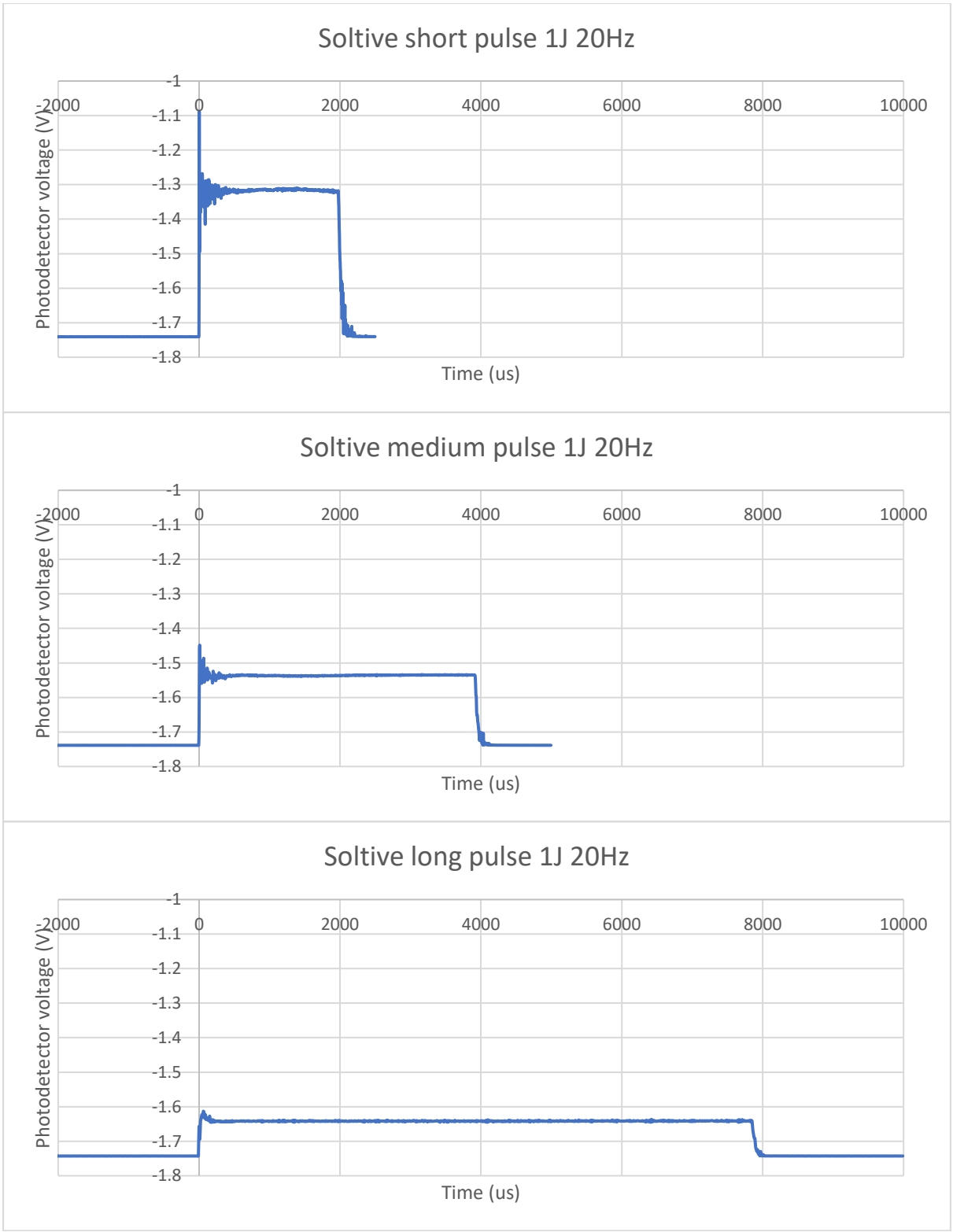


Figure 12. Soltive standard pulse, 1J 20Hz in short, medium and long pulse modes.

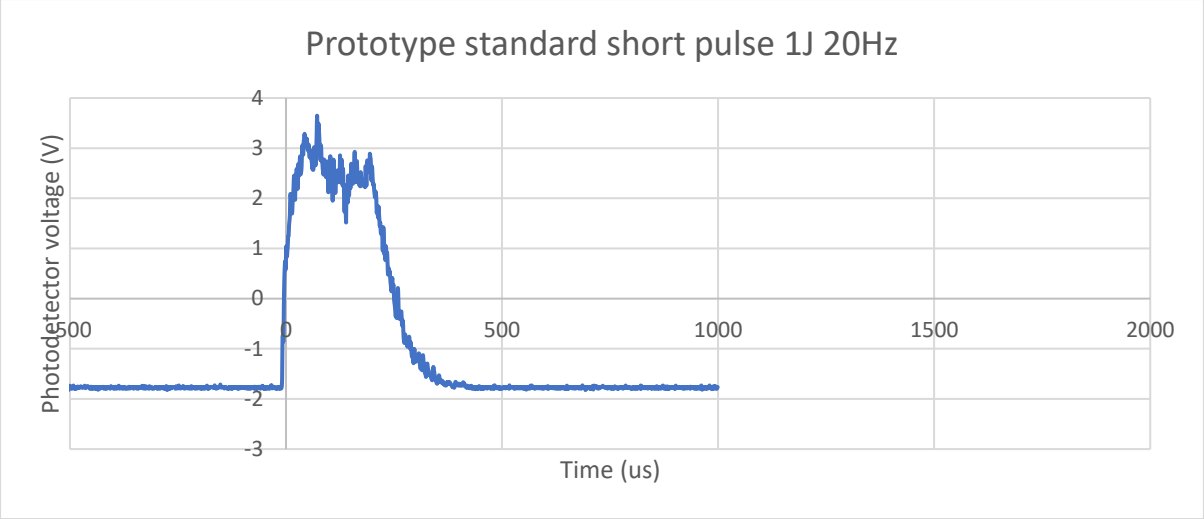


Figure 13. Prototype standard short pulse, 1J 20Hz.

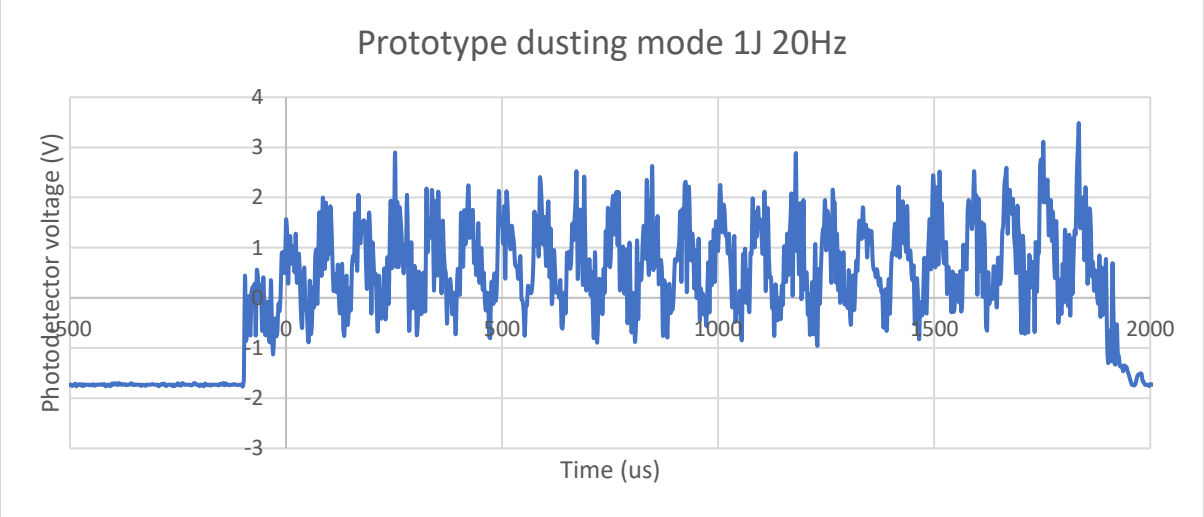


Figure 14. Prototype dusting mode, 1J 20Hz.

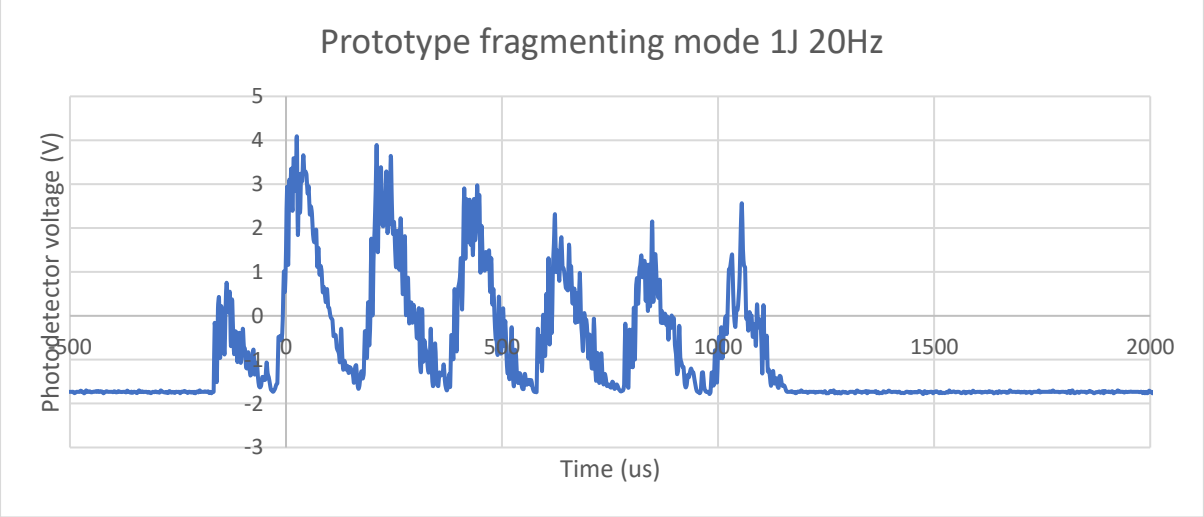


Figure 15. Prototype fragmenting mode, 1J 20Hz.

Pulse width measurements

Pulse width calculations for each laser (full width, half maximum) were performed on the oscilloscope output as follows using a template created in Microsoft Excel.

1. The baseline voltage is taken as the reading immediately prior to the oscilloscope detecting activity at time 0.
2. The maximum voltage is taken as the highest voltage reading during recording. Some pulse recordings feature a brief transient initial voltage spike lasting <1µs (and therefore delivering negligible amounts of energy). In these cases, the maximum voltage outside of this spike is taken instead, to avoid the spike from disproportionately skewing the results.
3. The pulse amplitude is calculated as the difference between maximum and baseline voltage, and halved to produce the half-maximum.
4. The pulse voltage threshold is calculated by adding the half-maximum to the baseline voltage.
5. The duration of pulse activity is determined by counting the readings after time 0 with a voltage above the calculated voltage threshold.

The pulse widths for all lasers in standard mode are shown in Table 3 below. Pulse modulated modes are not included as they are not comparable between lasers, and are difficult to calculate accurately using the above FWHM technique.

Standard mode	**P120 (µs)**			**Soltive (µs)**			**Prototype (µs)**	
Pulse energy (J)	**Short**	**Medium**	**Long**	**Short**	**Medium**	**Long**	**Short**	**Long**
0.2	46	58.5	101.5	385	638	1517.25	67.5	72.5
0.4	64.5	118	208.5					
0.5	64	56.5	110	975	1955	3840	127.5	192.5
0.6	59	68.5	131					
0.8	55.5	91.5	173.5					
1	66.5	117	219	1997.5	3935	7850	221	397.5
1.2	82	142	265					
1.4	96.5	169	310					
1.5	97	183	334					
1.6	104.5	196	356					
1.8	120	223	400					
2	134	247	448	3890	8030	15875	224	410
4				7910	16100	31700		

Table 3. Pulse widths in standard mode.

The combined pulse width results are shown in Figure 16. As the pulse widths for Soltive are so much larger than for the Ho:YAG lasers, the pulse width is plotted on the y-axis with a logarithmic scale.

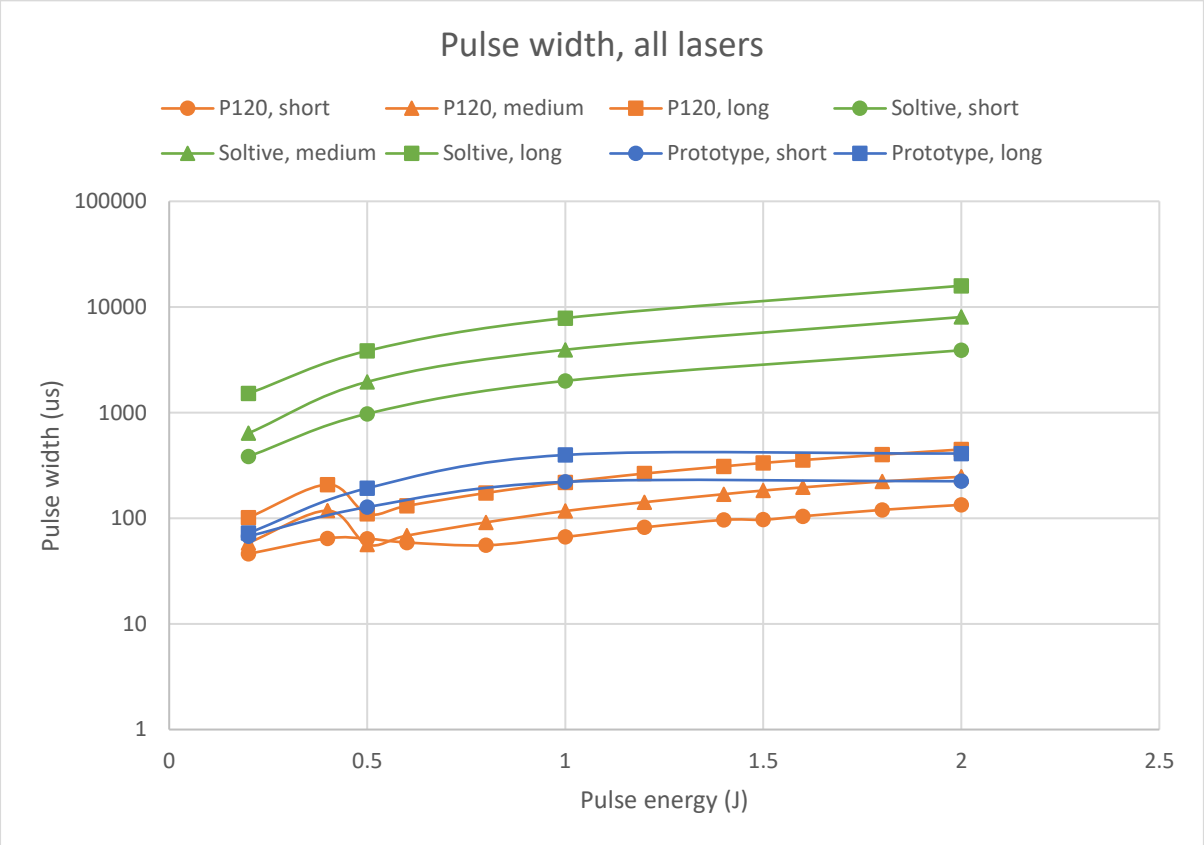


Figure 16. Pulse width in standard mode, demonstrating Soltive pulse width relative to Ho:YAG lasers. To improve clarity, the y-axis (pulse width) is plotted on a logarithmic scale.

Pulse widths – P120

P120 standard pulses have the characteristic "shark fin" appearance described in the literature [114]. They are often accompanied by a brief, transient initial spike for a single reading (i.e. no more than 0.5µs), which has also been commonly reported. As this is able to pass the 1500nm long pass filter, it is not simply leakage from the laser's flashlamp, but it was not possible to confirm the exact wavelength. This may reflect the nature of the pumping energy, which is delivered in a brief, large burst.

The pulse widths of P120 standard mode have a clear linear relationship with pulse energy at higher pulse energies. At 0.5J and above, the medium and long pulses have R^2 of 0.999 and 1.000

respectively on linear regression. The short pulse only develops a clear linear relationship at 0.8J and above, with an R^2 of 0.994. This is likely to represent the laser achieving its maximum peak power output at these thresholds, and calibrating the amount of energy delivered in each pulse by adjusting the pulse width alone.

Below these thresholds are some initially unexpected results. Medium and long pulses are approximately double the width at 0.4J than at 0.5J, which means there should be a corresponding increase in peak power going from 0.4J to 0.5J. The threshold for short pulse occurs somewhere between 0.4J and 0.6J but it is unclear where exactly it lies.

It is known that the P120 contains 4 separate laser resonator chambers that produce the laser output. The behaviour of medium and long pulses going from 0.4J to 0.5J may represent a change in the number of resonator chambers used to produce the output. There may be a similar effect for short pulse, though the small differences in pulse width make it difficult to pinpoint the exact threshold where this occurs.

The implication for clinicians is that increasing pulse energy from 0.4J to 0.5J may produce unexpected changes in pulse width (and therefore peak power) that are not proportional to the change in power. This may then alter retropulsion or fragmentation characteristics in an unexpected way.

Pulse widths – Soltive

Soltive standard pulses have a square wave appearance. Like P120, pulses are sometimes also accompanied by a brief, transient initial spike. This appearance is strongly suggestive of a continuous wave laser operating at a steady state output, which is in keeping with the technological precursor to clinical TFLs being electrically modulated continuous wave lasers [115]. This means that during laser emission, the pump energy source delivers constant pumping energy and the laser operates as a continuous wave laser, with the pulses being generated by turning the pump energy on and off.

The pulse widths of Soltive have a clear linear relationship with pulse energy at all settings tested, with R^2 of 1.000 on linear regression for short, medium and long settings. There is also a very clear relationship between these three modes, with long having double the pulse width of medium, which in turn has double the width of short.

The consistent amplitude of the square Soltive pulses makes it straightforward to calculate the peak power. Short pulse has a peak power of 500-520W, medium pulse has a peak power of 248-260W and long pulse has a peak power of 126-132W. Based on the 500W peak power commonly reported in similar devices, it is likely that the true values are 500W (short), 250W (medium) and 125W (long).

It is noteworthy that Soltive pulses are approximately 30-36 times as long as the equivalent P120 standard pulses at the same pulse energy. This implies that the peak power of equivalent P120 standard pulses will be far higher than Soltive pulses, in a similar ratio. Even Soltive short pulse are approximately 10 times the length of P120 standard long pulses. These two lasers can therefore be expected to behave differently as a result.

Pulse widths – prototype

Prototype standard pulses have a similar “shark fin” appearance to P120 pulses. They are sometimes accompanied by brief, transient initial spikes although this was captured less frequently than it was for P120.

The pulse widths of the prototype standard mode have a linear relationship with pulse energy at lower pulse energies up to 1J, with an R^2 of 1.000 for both short and long pulse. The pulse width then remains constant up to 2J. This is likely to represent the laser maintaining a certain peak power at pulse energies up to 1J, and then calibrating the pulse energy above 1J by increasing peak power without changing pulse width. This is the opposite to what is observed in P120, and so it is possible that standard mode may perform quite differently between these two lasers even at identical settings.

3. Ablation rate

Introduction

Historically, one of the important parameters in laser lithotripsy has been the ablation rate [92]. This represents how rapidly the laser can destroy stone, and is usually defined as follows.

$$Ablation\ rate = \frac{\Delta\ dry\ stone\ mass}{time}$$

The reason for its importance is that a laser that can more rapidly ablate stone should result in shorter operations, improving operating theatre efficiency and potentially a reduced rate of complications [70, 71]. With that said, there are many conflating variables that could account for the relationship between a prolonged operation duration and complication rate, such as patient/stone complexity, experience of the surgeon/centre and presence of a pre-operative stent. Despite the convincing correlation between operating time and complication rate, it is far from clear that reducing operating time in an otherwise straightforward case would result in any further reduction in complication rate. Nevertheless, this serves as an effective motivation for lasers with higher ablation rates.

Ablation rate in vivo is highly variable as the surgeon is often limited by other factors such as ability to manoeuvre the scope and fibre into position, patient anatomy, surgeon experience, visibility, respiratory movement, duty cycle and stone retropulsion (amongst other things). It is also difficult to measure ablation rate of urinary stones in a reproducible way in vitro, as urinary stones are extremely variable in size, shape, density, chemical composition and structure. Therefore, appropriate stone phantoms are usually used instead for reproducible in vitro results.

BegoStone as a stone phantom

BegoStone (BEGO GmbH & Co. KG, Bremen, Germany) is a gypsum-based ($Ca_2SO_4 \cdot 2H_2O$) dental plaster which has been demonstrated to have similar physical mechanical and acoustic properties to

many urinary stones [116]. It is made up by mixing a powder with water at specific ratios, producing a viscous fluid that hardens over approximately 30 minutes and dries completely in about 2 hours. This means that it can be poured into moulds to create consistent flat surfaces that lend themselves well to reproducible bench experiments.

The key physical properties of BegoStone are shown below in Table 4, using data from [116]. The impedance values are the resistance to propagation of waves through the stone in the direction indicated. Poisson's ratio indicates the extent to which a compressive force results in expansile strain in a perpendicular direction. Young's modulus represents stiffness in response to a compressive or tensile force. Bulk modulus represents resistance to compressive force, and shear modulus represents resistance to shear forces.

Stone	Density (kg/m^3)	Longitudinal impedance (mg/m^2s)	Transverse impedance (mg/m^2s)	Poisson's ratio	Young's modulus (GPa)	Bulk modulus (GPa)	Shear modulus (GPa)
BegoStone 15:3	**1995 ± 18**	**8.30**	**4.63**	**0.27**	**27.4**	**20.2**	**10.7**
COM	2038 ± 34	9.24	4.35	0.33	24.5	9.2	24.3
Calcium phosphate	2157 ± 16	8.48	3.93	0.36	19.5	7.2	23.8
Uric acid	1546 ± 12	5.37	2.26	0.39	9.2	3.3	14.2
Struvite	1587 ± 68	4.44	2.59	0.24	10.5	4.2	6.8

Table 4. Physical properties of common urinary stone types and BegoStone in a 15:3 mix of powder to water by mass. COM: calcium oxalate monohydrate.

BegoStone made up with a 15:3 ratio of powder to water results in a stone phantom with similar density and acoustic properties to hard stones like calcium oxalate monohydrate (COM), which are the major component of about 80% of human stones [117, 118]. It should be kept in mind that BegoStone has a higher resistance to compressive forces than COM, but is weaker when exposed to shear forces. As the majority of force exerted on stone by lasers are likely to be compressive in nature, this may make BegoStone phantoms less likely to shatter (fragment) than human stones.

While these most relevant physical properties have been analysed and compared, it is not known if there are other properties that may impact on ablation rate, or how those properties might compare to urinary stones. For example, dry BegoStone is porous and these pores fill with water when soaked, but it is not known how this porosity compares to urinary stones. It is known that BegoStone

is an imperfect phantom for actual stone and specific differences or limitations will be discussed as they arise.

Measuring ablation rate using BegoStone phantoms

Published ablation rate experiments are usually designed to deliver continuous laser light perpendicularly into a stone phantom at known settings. The laser fibre is constantly moved across the stone surface to minimise the amount of time that the laser is firing into an already-ablated cavity in the stone. Once ablation is completed, the quantity of stone ablated must be calculated. This can be done either by mass (i.e. weighing the stone before and after) or by volume (using volumetric scans such as computed tomography or scanning electron microscopy [119, 120]).

A variety of published ablation rate studies were reviewed to inform the methods chosen for these ablation rate studies [89, 92, 119, 121]. Based on these, it was decided to move the laser fibre in straight lines using a motorised arm as shown in Figure 17 below. This would allow the fibre speed to be easily kept constant, and produce ablation trenches with long straight components that would be well suited to volumetric scanning. The alternative method of rotating the stone would have required complex adjustments in rotation speed to maintain a constant relative speed between fibre and stone, and the resulting spiral shaped trench would have required a more complex volume calculation.

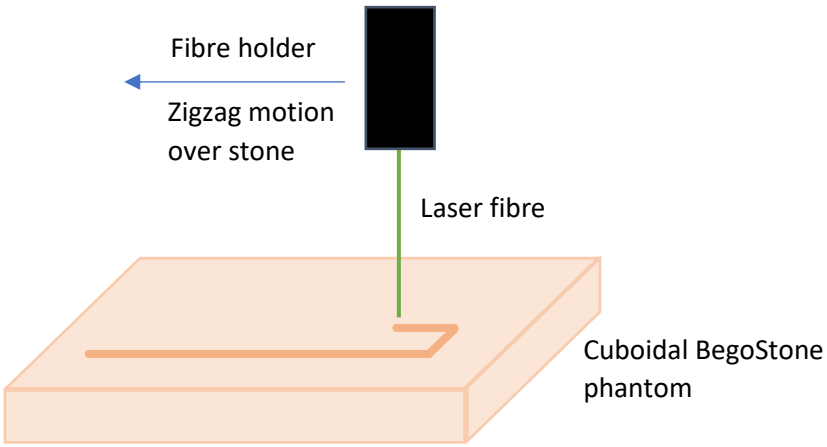


Figure 17. Schematic for ablation rate experimental setup.

Two sets of experiments were designed. The first set simulates attempting to keep the laser fibre in contact with the stone. Maintaining actual continuous contact is not practical as the fibre will drag on the stone surface resulting in uneven motion and fibre damage, so this is instead modelled as "pseudocontact" with the fibre as close to the stone as is practical. The second set involved maintaining a longer, fixed distance between fibre and stone, to represent performance when contact cannot be maintained. Throughout this chapter, the phrase "working distance" (WD) will refer to the distance maintained between the laser fibre and the stone phantom.

Ablation rate apparatus

A bespoke ablation rate station was commissioned from a mechanical engineering company (Faztech USA, IN, USA). A schematic for the design is shown below in Figure 18.

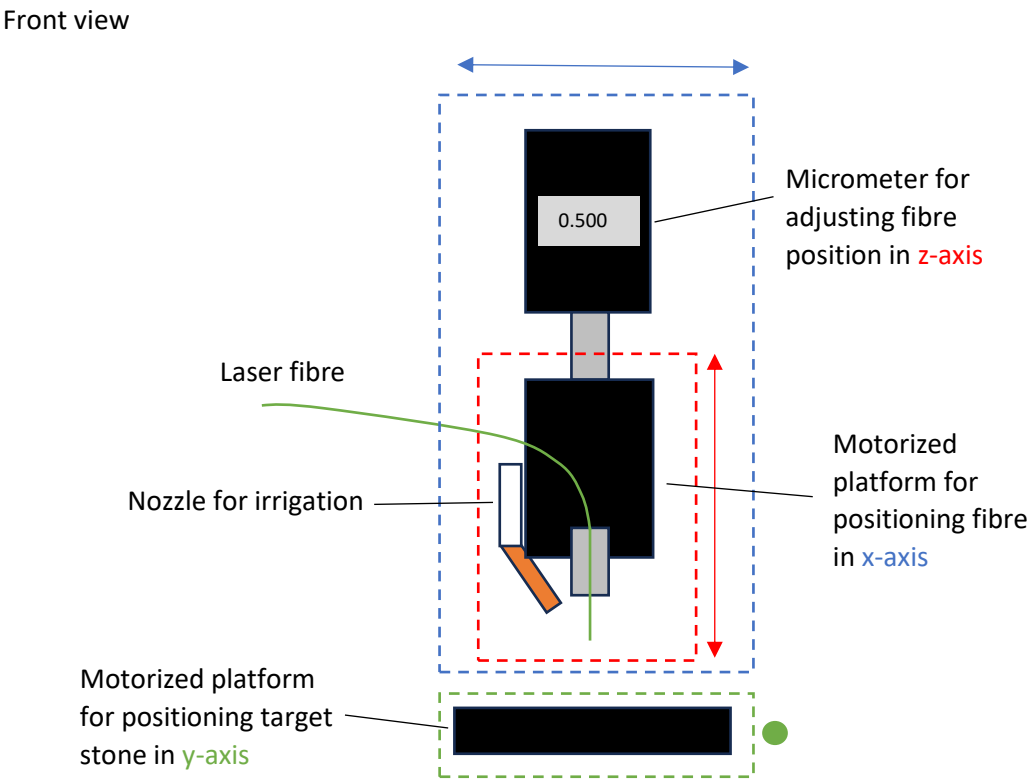


Figure 18. Schematic of bespoke ablation rate station, allowing positioning of the fibre in 3 axes.

The laser fibre is held on a movable platform, where the vertical height (and hence working distance) can be adjusted on a per-experiment basis using a high precision micrometer. This movement is shown by the red arrow. The stone is held fixed in a stone holder on the bottom movable platform. The fibre is then moved relative to the stone by two stepper motors, allowing for independent movement in the x- and y-axes (i.e. on the horizontal plane, shown by the blue and green arrows). A nozzle attached to the fibre holder platform allows constant fluid irrigation during experiments to keep the stone submerged, maintain cooling and wash away stone dust.

The actual ablation rate station used is shown in Figure 19.



Figure 19. Bespoke ablation rate station, with empty stone holder fixed to the bottom motorised platform.

Ablation rate in contact

In theory, optimal laser ablation will occur when the laser fibre is in direct contact with the stone with no intervening water. This would completely eliminate energy losses from water absorption. However, initial experiments showed that even with robust quality control, stone phantoms still have a degree of unevenness and imperfections on their surfaces that could result in the laser fibre getting caught on the stone surface as it moved.

A series of one-off experiments was performed to determine if maintaining true contact between the fibre and stone was feasible, and if not, how close they could be maintained. The starting working distances were 0mm, 0.1mm, 0.3mm, 0.5mm and 0.7mm.

Working distances of 0mm and 0.1mm resulted in the fibre getting caught against the stone in almost all experiments. This often resulted in the laser "digging" deep holes where it was caught, further compounding the problem, until it eventually moved rapidly and unpredictably and skipped over large areas of stone. Working distances of 0.3mm reduced the rate at which these events occurred but did not eliminate them, but they were not observed at all at working distances of 0.5mm and 0.7mm. Therefore, a 0.5mm working distance was set as "pseudocontact" for the purpose of contact experiments.

Scan speed

There is no single "gold standard" approach to selecting the speed at which the fibre is moved relative to the stone. Indeed, some studies such as [89] moved the fibre in a spiral pattern where, despite the authors' best efforts, the spacing between laser craters (and therefore the scan speed) can clearly be seen to change at different points during a single experiment.

Furthermore, there is a large range of reported scan speeds being used in similar experiments. Petzold quotes scan speeds of 500mm/min to 1500mm/min using a TFL (although it is unclear which part of the rotating disc this speed refers to) [89]. These correspond to 8.3mm/s to 25mm/s. Others such as Terry do not report scan speed as a variable but instead maintain a constant number of pulses per mm [119], with 10 pulses/mm to create trenches using a Ho:YAG laser. They report data on 0.4J and 1J pulses, so the equivalent scan speeds to deliver 20W of average power would be 2mm/s for 1J and 5mm/s for 0.4J.

Preliminary experiments were done using the ablation rate station with P120 and prototype lasers at 0.5mm/s, 1mm/s, 1.5mm/s, 2mm/s, 2.5mm/s and 3mm scan speeds. The scan speed that produced

the highest ablation rate was selected for each laser setting. Scan speed at longer working distances was maintained at 1mm/s at all settings.

Preliminary experiments on scan speeds for the Soltive showed that scan speeds of 1-2mm/s were insufficient to produce satisfactory ablation trenches. Given the variable but very high scan speeds reported for BegoStone ablation with TFLs, the scan speed in pseudocontact was calibrated for each Soltive laser setting by adjusting the scan speed upwards from 1mm/s, 2mm/s, 3mm/s, 5mm/s, 8mm/s, 10mm/s to 12mm/s, until a satisfactory ablation trench with seen without evidence of charring/burning. At longer working distances, a scan speed of 1mm/s was sufficient to produce satisfactory ablation trenches at all settings under test.

Methods

Flat 30mm x 20mm x 4mm BegoStone phantoms were prepared as described in Appendix 1: BegoStone preparation, using a 15:3 ratio of BegoStone powder to deionised water. Once dry, each phantom was weighed on an Entris II balance (Sartorius Lab Instruments GmbH, Goettingen, Germany). The first set of experiments was done with unsoaked stones that were left dry until experimentation, and the second set was done with pre-soaked stones that were immersed in water for 24 hours prior to experimentation.

The ablation rate station was configured to ablate in a zig-zag pattern consisting of 20mm lines in the x-axis alternating with 2.5mm lines in the y-axis, as shown in Figure 20. The total distance moved by the fibre was 110mm. The working distance was set to 0.5mm in all cases. This was set by initially positioning the fibre tip in contact with the stone, and then moving the fibre platform vertically in the z-axis by 0.500mm using the integrated micrometer.



Figure 20. Ablation pattern for ablation rate experiments. Total distance moved was 110mm. This phantom was a discarded stone that was used for illustration purposes, and does not form part of the data set presented.

During ablation, the phantoms were constantly irrigated with normal saline directed towards the tip of the laser fibre. This was driven by gravity with a maximum of 50cm of H_2O, and further reduced by manually reducing the aperture of the tubing using the integrated roller to deliver the minimal flow necessary to wash away dust. Typical flow rates were 50-100 ml/min. For comparison, typical irrigation rates during ureteroscopy range from about 10-50 ml/min depending on a variety of factors including pressure, scope, presence of laser fibre, and use of access sheath.

Initial experiments with unsoaked stones used a wide range of laser settings to establish trends and identify settings for further experimentation. The laser settings and scan speeds used for soaked stones were derived based on these initial results, and are found in Table 6. The power levels of 20W, 40W and 60W were selected to provide a cross-section of settings across the entire power range available to these lasers using a 200µm-class fibre. The specific laser settings were selected to represent what local clinicians at Oxford University Hospitals would consider using at 20W and 40W.

60W was not a power level that was recommended for ureteroscopic stone surgery, so settings at this power were selected based on cystoscopic use for bladder stones. At the time of experimental design, there was no consensus for recommended TFL laser settings for dusting or fragmentation, and these settings were informed by advice from the manufacturer to favour higher frequencies than Ho:YAG lasers. The exact laser settings used are described in each subsection.

9 phantoms were ablated for each setting. After each phantom, the laser fibre was stripped and cleaved. This is a process to "renew" the tip of the fibre, as the process of ablating stone degrades it and results in loss of power. The fibre cladding was stripped 2cm from the end using a precision Micro-Strip stripper (Micro Electronics Inc, MA, USA) with a 0.014 diameter blade for P120 fibres and a 0.016 diameter blade for Soltive and prototype fibres. The end of the fibre was then cleaved using a ruby DualScribe optic scribe (THORLABS GmbH, Münchner, Germany). The renewed fibre was checked both by visual inspection of the integrated aiming beam pattern, and by power measurement using a fan cooled thermal laser Ophir power sensir (MKS Instruments, MA, USA). A minimum of 100 pulses was measured and average power within +/- 10% of the selected power setting was considered acceptable.

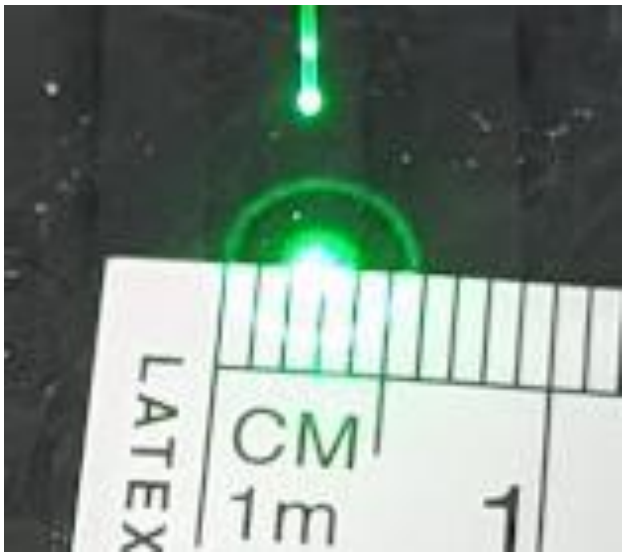


Figure 21. Satisfactory aiming beam pattern following cleaving of P120 laser fibre.

An example of a satisfactory aiming beam pattern after cleaving is shown in Figure 21. It consists of completely round concentric circles of even thickness. There are no artifacts or imperfections, and light is not seen bleeding out beyond the expected pattern. Experience gained during the course of experiments indicated that this aiming beam patter was a better indicator of fibre output than the laser power meter measurement, which could not always detect small imperfections.

After ablation, all phantoms were rinsed in water to remove residual dust and saline, then dried at room temperature for 24 hours and weighed again (preliminary experiments indicated that prolonged drying made no difference to weights at 48 hours and 7 days drying). The ablation rate was calculated by dividing the weight change by the ablation time. Post-hoc statistical analysis was performed by pairwise comparison between different lasers for matched settings, using a two-sample two-tailed t-test.

Results - unsoaked stones

The first set of ablation rate experiments were performed using unsoaked stones to determine suitable settings for further study as well as scaling with pulse energy, frequency and overall power. Data for the prototype laser in this set of experiments was provided by the Boston Scientific team in San Jose from equivalent experiments using the same methodology. Data for P120 and Soltive in this data set, as well as all other results, was obtained from experiments performed in Oxford. Figure 22 provides a high level summary of the results, with detailed discussion of individual lasers in the following section. The shape of the data point indicates the laser firing mode, with squares indicating dusting mode (prototype) or Moses contact (P120) and triangles indicating fragmentation mode (prototype) or Moses Distance (P120. Circles indicate standard short pulse, which was only used for the Soltive in this data set. The size of the marker corresponds to the pulse energy used. At the same power level, a larger marker indicates a higher pulse energy and therefore a corresponding lower frequency.

The pulse energies used range from 0.2-2J for P120 and 1-3.5J for the prototype. The single data point for Soltive used a 1J 40Hz standard short pulse, and the reason for the lack of Soltive data here will be discussed later.

Laser and firing mode	Pulse energy (J)	Frequency (Hz)	Power (W)	Speed (mm/s)
P120 Moses contact	0.2	50	10	1
P120 Moses contact	0.2	80	16	1
P120 Moses contact	0.3	80	24	1
P120 Moses contact	0.4	50	20	1
P120 Moses contact	0.5	80	40	1
P120 Moses contact	0.6	50	30	1
P120 Moses contact	0.6	60	36	1
P120 Moses contact	0.6	80	48	2
P120 Moses contact	0.8	50	40	1
P120 Moses contact	1	10	10	1
P120 Moses contact	1	15	15	1
P120 Moses contact	1	20	20	1
P120 Moses contact	1	40	40	1
P120 Moses contact	1	50	50	2
P120 Moses contact	1	60	60	2
P120 Moses contact	1.2	30	36	1
P120 Moses contact	2	10	20	1
P120 Moses contact	2	15	30	1
P120 Moses contact	2	20	40	1
P120 Moses contact	2	30	60	2
P120 Moses distance	0.3	80	24	1
P120 Moses distance	0.4	50	20	1
P120 Moses distance	0.5	80	40	1
P120 Moses distance	1	40	40	1
P120 Moses distance	1	50	50	2
P120 Moses distance	1	60	60	2
P120 Moses distance	2	15	30	1
P120 Moses distance	2	20	40	1
P120 Moses distance	2	30	60	2
Prototype Fragmenting	1	5	5	1
Prototype Fragmenting	1	10	10	1
Prototype Fragmenting	1	15	15	1
Prototype Fragmenting	1	20	20	1
Prototype Fragmenting	2	5	10	1
Prototype Fragmenting	2	10	20	1
Prototype Fragmenting	2	15	30	1
Prototype Fragmenting	2	20	40	2
Prototype Fragmenting	3	5	15	1
Prototype Fragmenting	3	10	30	2
Prototype Fragmenting	3	15	45	2.5
Prototype Fragmenting	3	20	60	3
Prototype Fragmenting	3.5	5	17.5	1.5
Prototype Fragmenting	3.5	10	35	2
Prototype Fragmenting	3.5	15	52.5	3
Prototype Dusting	1	5	5	1
Prototype Dusting	1	10	10	1
Prototype Dusting	1	15	15	1
Prototype Dusting	1	20	20	1.5
Prototype Dusting	2	5	10	1
Prototype Dusting	2	10	20	1
Prototype Dusting	2	15	30	1
Prototype Dusting	2	20	40	2.25
Prototype Dusting	3	5	15	1
Prototype Dusting	3	10	30	1
Prototype Dusting	3	15	45	1.5
Prototype Dusting	3	20	60	1.5
Prototype Dusting	3.5	5	17.5	1
Prototype Dusting	3.5	10	35	1
Prototype Dusting	3.5	15	52.5	2.5
Soltive standard short pulse	1	40	40	1

Table 5. Laser settings used for pseudocontact ablation rate experiments with unsoaked stones, and corresponding scan speeds.

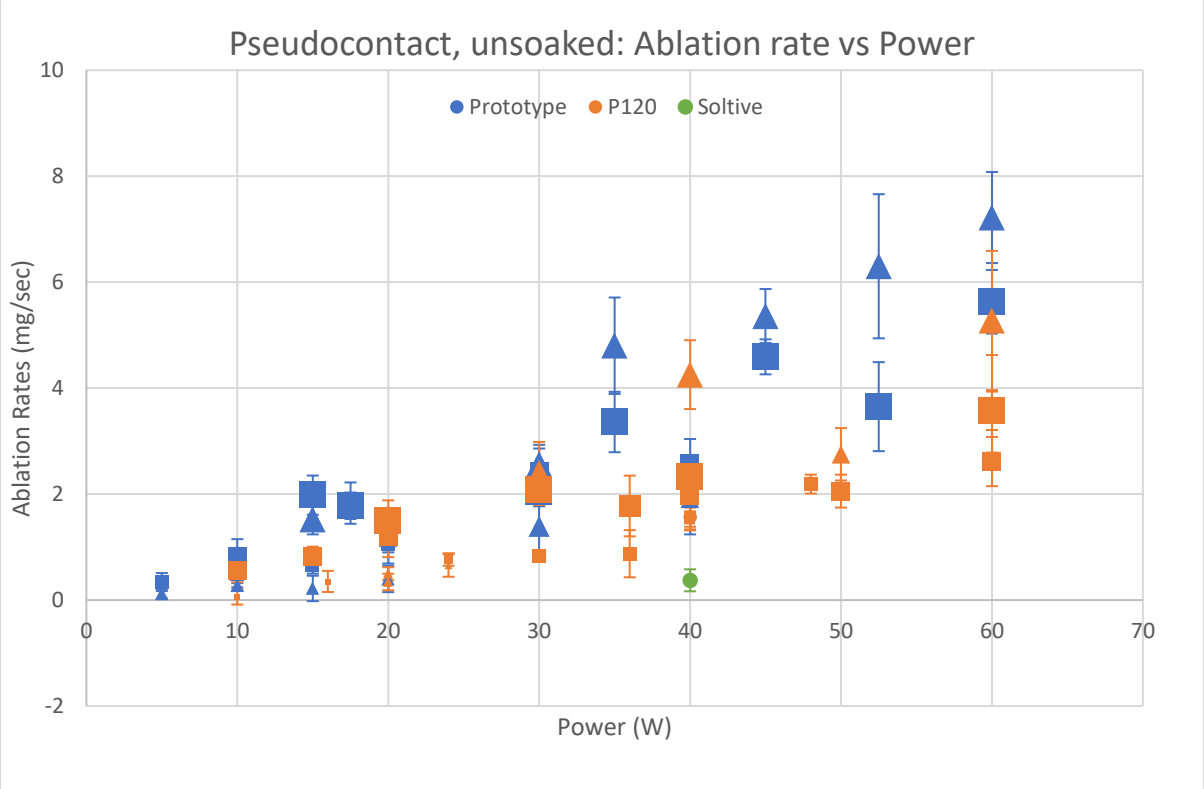


Figure 22. Ablation rate in pseudocontact using unsoaked stones. Squares indicate dusting mode (prototype) or Moses contact (P120). Triangles indicate fragmentation mode (prototype) or Moses distance (P120). Circles indicate standard short pulse. Error bars indicate one standard deviation. Data for the prototype laser provided by Boston Scientific.

The combined data suggests a positive correlation between average power and ablation rate for both P120 and Soltive, but with a lot of variation between individual settings at the same power level. To gain further insight, the results of individual lasers will be examined in detail. P120 results are presented in Figure 23 below.

The P120 results in Figure 23 are grouped by pulse energy and firing mode (MC vs MD). Square points/solid trendlines indicate MC while triangular points/dashed trendlines indicate MD. Orange borders indicate 2J pulse energy, blue borders indicate 1J pulse energy, green borders indicate 0.6J pulse energy and grey borders indicate 0.2J pulse energy. Some data points have been excluded from this graph to improve clarity (pulse energies of 0.3J, 0.4J, 0.5J, 0.8J and 1.2J) as they consisted of a single data point each.

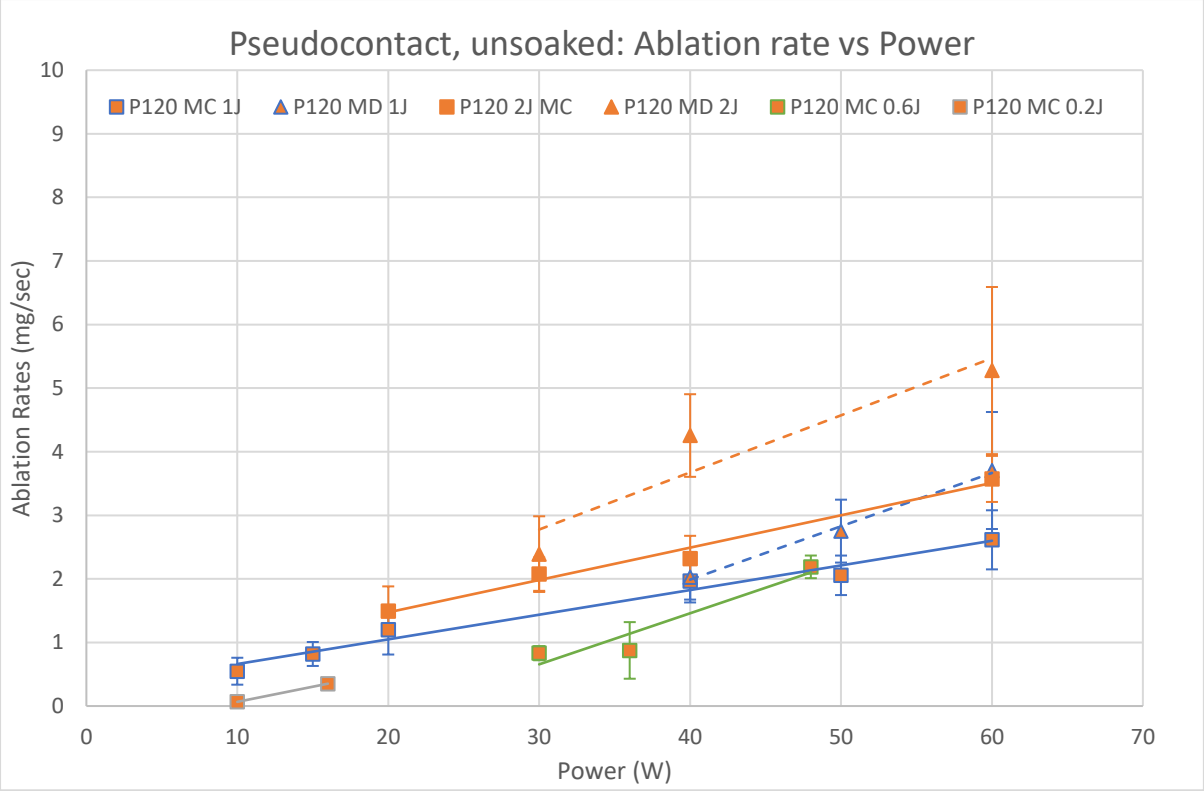


Figure 23. Ablation rate in pseudocontact using unsoaked stones. P120 results only. Square points/solid trendlines indicate Moses contact. Triangular points/dashed trendlines indicate Moses distance. Data are grouped by pulse energy, indicated by the border colour of each point. Error bars indicate one standard deviation.

As expected, an increase in average power (achieved by increasing frequency) resulted in an increase in ablation rate in all pulse energy groups for P120. The relationship looks approximately linear although the number of data points is too small to draw definitive conclusions here. The MD settings (triangles/dashed lines) appear to produce higher ablation rates than the equivalent MC settings (squares/solid lines) although the differences are small and the error bars overlap with the one exception of 2J 20Hz (40W). Previously published data has suggested that MD can be expected to produce higher ablation rates at 1mm WD [122].

Comparing different pulse energies suggests that higher pulse energies produce higher ablation rates at the same average power. For example, if average power is fixed at 60W, the 2J 30Hz setting produces a higher ablation rate than 1J 60Hz in both MC and MD modes. This effect is seen across all pulse energies from 2J down to 0.2J, including 0.3 - 0.5J pulse energy settings. The one exception was one 0.6J setting (06J 80Hz MC). This one 48W setting produced a slightly higher ablation rate than a 1J 50Hz setting (50W) although the difference is small and does not achieve any statistical

significance. The overall trend suggests that a higher ablation rate will be achieved with P120 using a higher pulse energy at the same average power level.

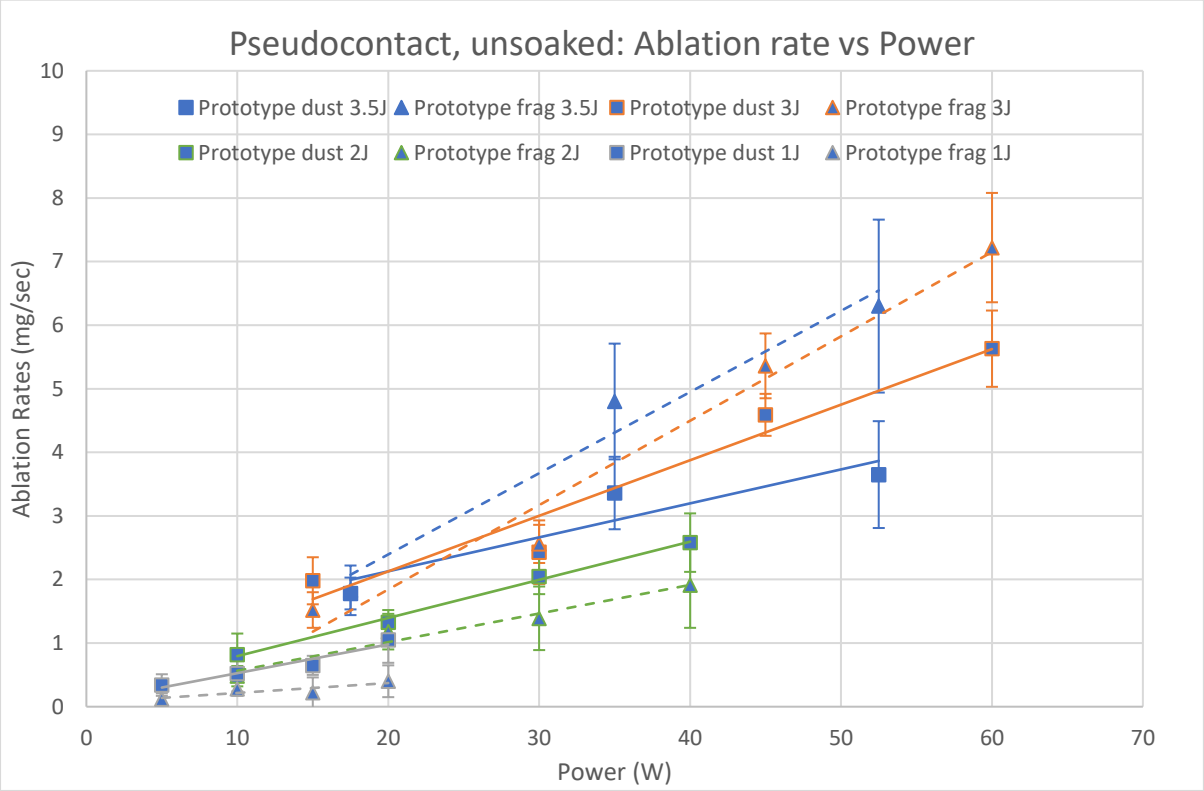


Figure 24. Ablation rate in pseudocontact using unsoaked stones. Prototype results only. Square points/solid trendlines indicate dusting mode. Triangular points/dashed trendlines indicate fragmentation mode. Data are grouped by pulse packet energy, indicated by the border colour of each point. Error bars indicate one standard deviation.

As with the P120 graph, the prototype results in Figure 24 are grouped by pulse packet energy and firing mode (dusting vs fragmentation). Square points/solid trendlines indicate dusting mode while triangular points/dashed trendlines indicate fragmentation mode. Blue borders indicate 3.5J pulse packet energy, orange borders indicate 3J pulse packet energy, green borders indicate 2J pulse packet energy and grey borders indicate 1J pulse packet energy.

As with P120, an increase in average power resulted in a roughly linear increase in ablation rate in all pulse energy groups. The dusting settings (triangles/dashed lines) appear to produce higher ablation rates than the equivalent fragmentation settings (squares/solid lines) at high pulse packet energies of 3.5J and 3J, but lower ablation rates at lower pulse packet energies of 1J.

Comparing different pulse energies suggests that up to 3J pulse packet energy, a higher pulse packet energy will produce a higher ablation rate. This is the case for both dusting and fragmentation mode. The effect of increasing pulse packet energy from 3J to 3.5J is less clear, with fragmentation mode showing a slight increase but dusting mode showing a slight decrease. This may represent an inflexion point or a data outlier. Since the benefit from 3.5J pulse packet energy is unclear and the power levels (17.5W, 35W and 52.5W) prevent like-for-like comparisons with the other lasers, 3J was selected as the upper limit for further testing.

Soltive data was problematic using unsoaked stones. Figure 25 shows some typical ablation trenches using a 1J 40Hz standard short pulse setting with a 1mm/s scan speed. On the left, P120 produced deep trenches of roughly constant depth, with even looking sides and bases. The colour and texture of the BegoStone looks consistent throughout. In contrast, the Soltive on the right produced trenches of very inconsistent depth. The sides are even but the bases are not, with some areas deeper than others. There were also some areas of red/grey discoloration that resembled charring (despite the experiment being performed immersed in saline with constant saline irrigation). This resulted in extremely low ablation rates compared to the other two lasers at the same settings.



Figure 25. Ablation trenches using 1J 40Hz standard short pulse. Left: P120. Right: Soltive.

Scan speed optimisation was then performed in the same way as the other lasers. Figure 26 shows example trenches from 0.05J 600Hz standard short pulse. The slowest scan speed supported by the platform (0.33 mm/s) did produce some clean looking trenches but these were interspersed with charred and burned looking areas. All other scan speeds simply resulted in a light discoloration of

the BegoStone under the laser fibre path, without any discernible trench or measurable weight change.

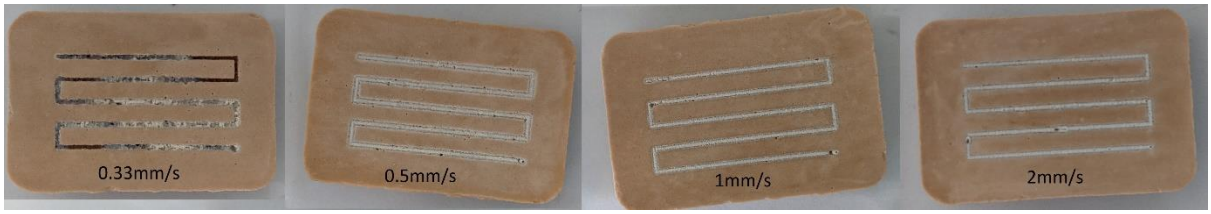


Figure 26. Soltive ablation trenches using 0.05J 600Hz at varying scan speeds.

A literature review was performed in light of these puzzling results, and it was found that other authors such as Taratkin et al [121] had also experienced and reported on inconsistent ablation and charring when ablating BegoStone with a TFL. They reported a dramatic increase in ablation rate from "hydrating" the phantoms, which they did by soaking them in water for 24 hours prior to ablation. It was also noted that high ablation rates were achieved by authors such as Petzold et al [89] using much higher quoted scan speeds of 8.3 mm/s up to 25 mm/s. Potential explanations for these observations will be discussed later.

Results - pre-soaked stones

The protocol for the second set of experiments was determined from the unsoaked stone results. The settings were selected with the aim of demonstrating "best case" ablation for each laser at the specific power level, so for P120 and the prototype, the settings prioritise pulse energy over frequency. For Soltive, there was no suitable data from unsoaked stones. Based on published literature and manufacturer advice, higher frequency settings were selected as this was thought to be optimal for TFL at the time.

Laser	**20W**		**40W**		**60W**	
P120 Moses contact	0.4J 50Hz	1 mm/s	1J 40Hz	1 mm/s	2J 30Hz	2 mm/s
P120 Moses distance	1J 20Hz	1 mm/s	1J 40Hz	1 mm/s	2J 30Hz	2 mm/s
Soltive dusting	0.2J 100Hz	1 mm/s	0.2J 200Hz	5 mm/s	0.2J 300Hz	12 mm/s
Soltive fragmentation	0.5J 40Hz	1 mm/s	0.5J 80Hz	2 mm/s	0.5J 120Hz	8 mm/s
Prototype dusting	1J 20Hz	1.5 mm/s	2J 20Hz	1.5 mm/s	3J 20Hz	1.5 mm/s
Prototype fragmentation	1J 20Hz	1 mm/s	2J 20Hz	2.5 mm/s	3J 20Hz	3 mm/s

Table 6. Laser settings used for pseudocontact ablation rate experiments with soaked stones, and corresponding scan speeds.

Ablation rate results using pre-soaked stones are shown in Figure 28. Example stone phantoms using a 20W setting are shown in Figure 27. With the soaked stones and optimised scan speeds, Soltive was able to produce even and consistent ablation trenches with no or minimal charring. Note that these use different scan speeds so the depth of the trenches cannot be directly compared. This difference in scan speed (and therefore total ablation time) is normalised by the ablation rate calculation.

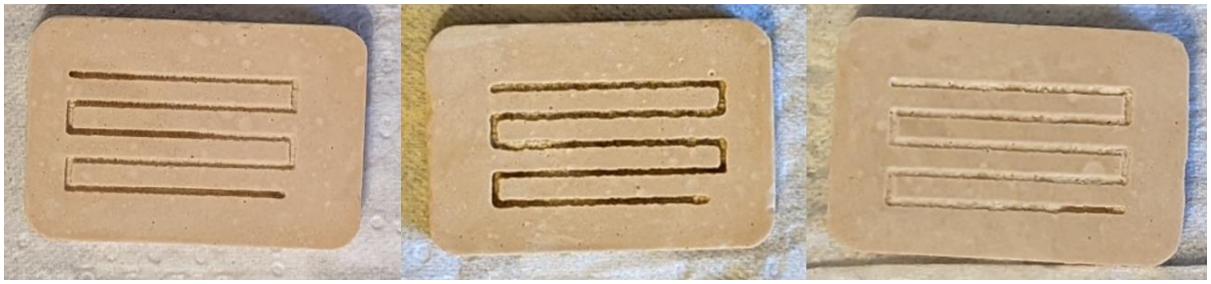


Figure 27. Example ablation trenches on pre-soaked BegoStone phantoms at 20W. From left to right: P120 (0.4J 50Hz Moses contact at 1 mm/s), prototype (1J 20Hz dusting mode at 1.5 mm/s), Soltive (0.2J 100Hz short pulse at 5 mm/s).

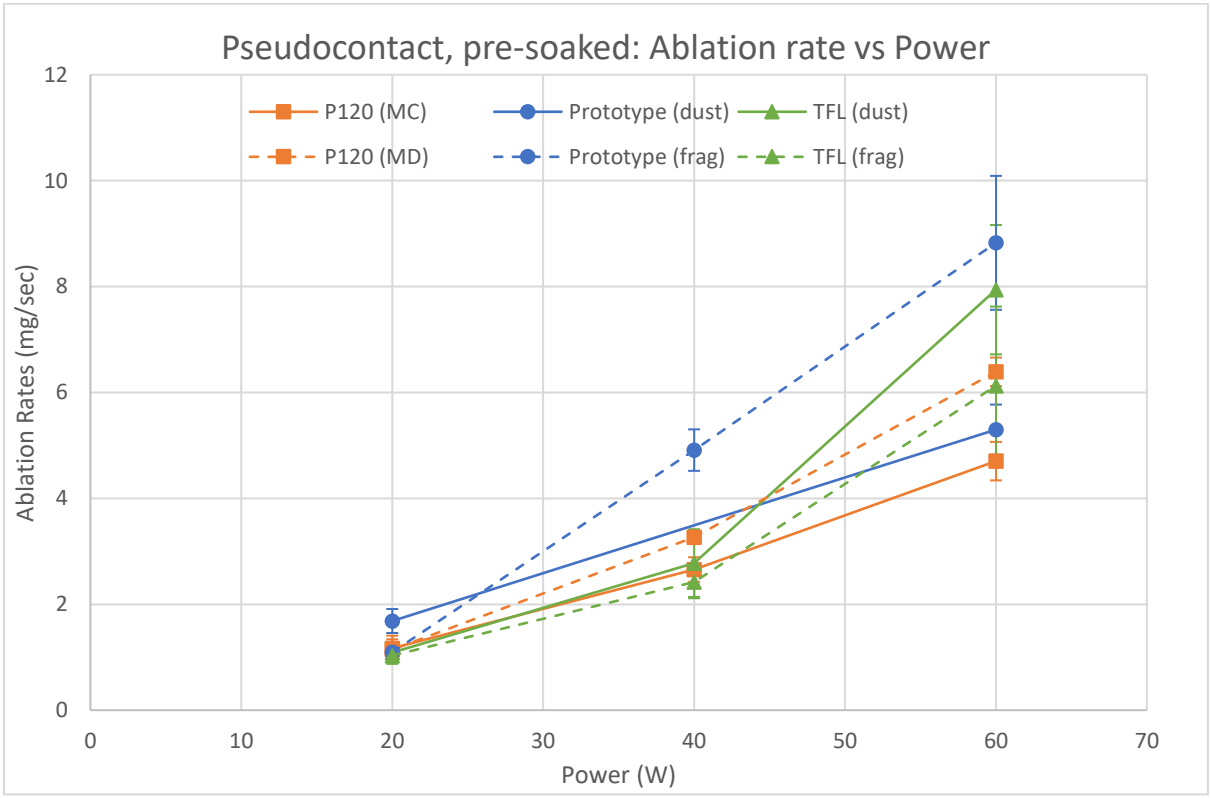


Figure 28. Ablation rate in pseudocontact using pre-soaked stones. Error bars indicate one standard deviation.

Laser and power	Ablation rate			Vs laser (p values)					
20W	Mean (mg/s)	S.D. (mg/s)	95% CI (mg/s)	RHL dust	RHL frag	TFL dust	TFL frag	Proto. dust	Proto. frag
P120 Moses contact	1.170	0.309	0.933 – 1.407	-	0.837	0.465	0.282	**0.002**	0.496
P120 Moses distance	1.142	0.255	0.946 – 1.338	0.837	-	0.564	0.328	**<0.001**	0.606
TFL dust (short pulse)	1.089	0.085	1.023 – 1.154	0.465	0.564	-	0.459	**<0.001**	0.921
TFL frag (short pulse)	1.032	0.206	0.874 – 1.190	0.282	0.328	0.459	-	**<0.001**	0.440
Prototype dust	1.684	0.295	1.457 – 1.910	**0.002**	**<0.001**	**<0.001**	**<0.001**	-	**<0.001**
Prototype frag	1.093	0.105	1.012 – 1.174	0.496	0.606	0.921	0.440	**<0.001**	-
40W									
P120 Moses contact	2.655	0.303	2.423 – 2.888	-	**<0.001**	0.685	0.178	-	**<0.001**
P120 Moses distance	3.268	0.117	3.177 – 3.358	**<0.001**	-	0.118	**<0.001**	-	**<0.001**
TFL dust (short pulse)	2.778	0.831	2.139 – 3.417	0.685	0.178	-	0.268	-	**<0.001**
TFL frag (short pulse)	2.420	0.398	2.114 – 2.726	0.178	**<0.001**	0.268	-	-	**<0.001**
Prototype dust	-	-		-	-	-	-	-	-
Prototype frag	4.912	0.509	4.520 – 5.303	**<0.001**	**<0.001**	**<0.001**	**<0.001**	-	-
60W									
P120 Moses contact	4.703	0.473	4.340 – 5.067	-	**<0.001**	**<0.001**	0.062	**0.036**	**<0.001**
P120 Moses distance	6.390	0.350	6.121 – 6.659	**<0.001**	-	**0.019**	0.699	**<0.001**	**0.002**
TFL dust (short pulse)	7.941	1.588	6.720 – 9.161	**<0.001**	**0.019**	-	**0.047**	**0.001**	0.241
TFL frag (short pulse)	6.127	1.945	4.632 – 7.622	0.062	0.699	**0.047**	-	0.251	**0.005**
Prototype dust	5.298	0.616	4.824 – 5.772	**0.036**	**<0.001**	**0.001**	0.251	-	**<0.001**
Prototype frag	8.826	1.645	7.604 – 10.132	**<0.001**	**0.002**	0.241	**0.005**	**<0.001**	-

Table 7. Ablation rate in pseudocontact, pre-soaked stones. Statistically significant differences ($p < 0.05$) are in bold, calculated by two-sided t-test.

All lasers demonstrated an approximately linear relationship between average power and ablation rate. Ablation rates were slightly higher for soaked stones compared to unsoaked stones for all Ho:YAG laser settings except for prototype dusting mode 3J 20Hz. This increased ablation rate from using soaked stones is similar to that reported by Taratkin et al [121] although the magnitude of their reported difference is larger.

Statistical analysis is presented above in Table 7 with pairwise comparison between lasers and firing modes. Care should be taken when interpreting these results as the large number of comparisons may inflate the number of type I errors. In other words, there will be an increased number of false positives where spurious differences may be detected as a result of the number of comparisons.

With this in mind, at 20W the prototype laser in dusting mode produced a higher ablation rate than all other settings ($p < 0.002$ in all cases). The mean ablation rate for the prototype in dusting mode was 1.684 mg/s (95% CI 1.457-1.910), while other settings produced means from 1.032-1.170 mg/s. The nature of these differences and the p-values involved suggest that this reflects a true difference in underlying ablation rate. No other statistically significant differences were detected between other settings at this power.

At 40W, the prototype laser in fragmentation mode produced a higher ablation rate than all other settings ($p < 0.001$). The mean ablation rate for this setting was 4.912 mg/s (95% CI 4.520-5.303), while other settings produced means from 2.420-3.268 mg/s. Again, this is likely to represent a true difference rather than a type I error. Some other statistically significant differences in pairwise comparisons were noted but these were not consistent across all firing modes, so they should be considered inconclusive evidence of a true difference.

At 60W, the prototype laser in fragmentation mode produced a higher ablation rate than all other settings except for Soltive in dusting mode ($p < 0.005$) with a mean of 8.826 mg/s (95% CI 7.604-10.132). Similarly, Soltive in dusting mode produced a higher ablation rate than all other settings except for the prototype laser in fragmentation mode ($p < 0.047$) with a mean of 7.941 mg/s (95% CI 6.720-9.161). All other settings produced means from 4.703-6.390 mg/s. The differences between these two highlighted settings and others likely reflects a true difference. No significant differences were detected between these two settings. As before, some statistically significant differences in other settings were inconsistent and therefore not conclusive evidence of any other underlying differences.

Discussion

The pre-soaked stone results suggest that for the 3 lasers tested, BegoStone ablation rate is broadly similar when each laser is optimised individually. While there were some statistically significant differences at individual power levels, there was no single laser or firing mode that demonstrated global superiority at all powers. Bearing in mind the inflated possibility of type I errors from the large number of comparisons, the sensible conclusion is that this data does not demonstrate any clear superiority in ablation rate for any single laser firing mode.

Each laser and firing mode does demonstrate clear scaling with average power, and while the number of power levels is too small to perform meaningful linear regression, the scaling does appear to be approximately linear. This is in line with intuitive expectations. While the prototype and Soltive

settings are easily compared between power levels with a fixed pulse/pulse packet energy and only frequency changing, the P120 settings require additional interpretation as the pulse energy also differs. As previously mentioned, the reason for this was to limit the settings to ones that were clinically realistic. It was not thought to be plausible for a clinician who wished to remain at 20W average power (e.g. for a ureteric stone) to select a 2J 10Hz setting, whereas a clinician who wanted 60W of average power was likely operating on a bladder stone for which a 2J 30Hz setting seemed reasonable.

The optimised scan speeds for each laser are also interesting. The effect of optimising scan speed for the two Ho:YAG lasers was relatively small, with a <20% difference between the “best” and “worst” scan speeds for the highest power P120 2J 30Hz settings tested with 1-3 mm/s scan speeds. The differences for the prototype laser were generally similar in magnitude, but this scan speed data was provided by Boston Scientific (using unsoaked stones) and not independently repeated. In contrast, ablation rate for Soltive varied much more dramatically with scan speed. At 0.5J 120Hz, ablation rate ranged from 1.22 mg/s at a 1 mm/s scan speed, to 14.7 mg/s at an 8 mm/s scan speed. This is in keeping with the higher scan speeds used for TFLs by other authors, although it is not always clear how those scan speeds were determined. While such scan speeds may be “optimal” in this bench setting, in a clinical setting it seems implausible that an 8 mm/s scan speed could be safely maintained for any significant amount of time, as this would often mean traversing the diameter of a typical stone in a second or less. True measurements of scan speed could not be found in the literature. This therefore raises the question of what scan speeds would be realistic in clinical practice, and the impact that would have on ablation rate. Our limited data suggests that the relative impact on TFL would be greater than it would for Ho:YAG lasers, but further work should be done to investigate this in detail.

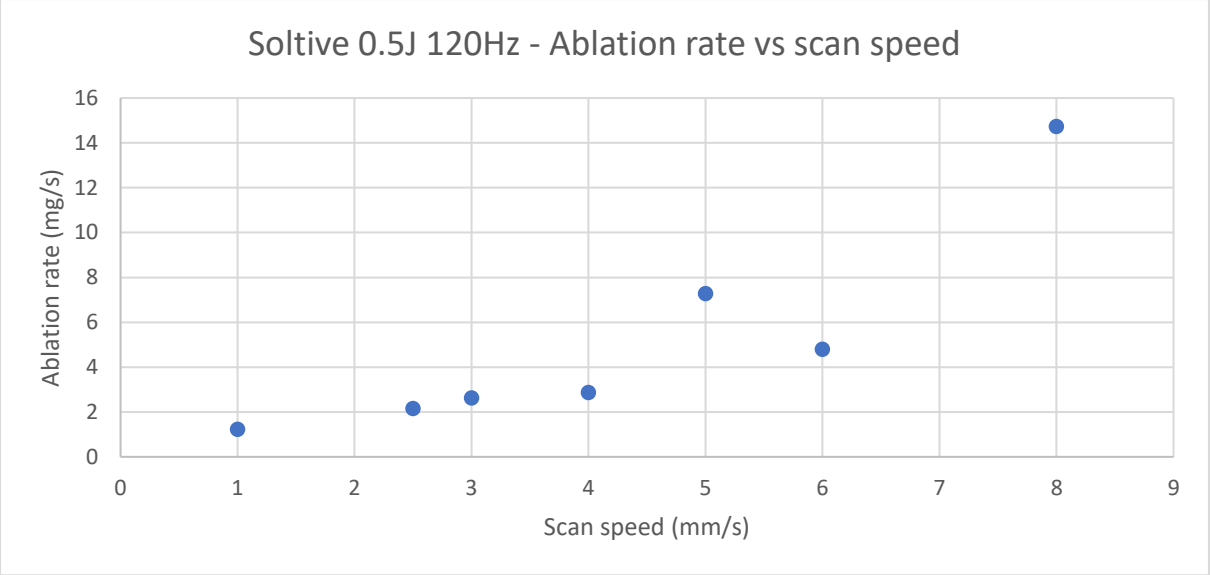


Figure 29. Effect of scan speed on Soltive ablation rate at 0.5J 120Hz standard short pulse.

As noted in the unsoaked stone results, initial Soltive results were plagued by puzzling incomplete looking ablation, with pale discoloured flat lines instead of trenches or trenches interrupted by irregular charred looking areas. This was mitigated (but not entirely eliminated) by pre-soaking the stone phantoms in water for 24 hours, and has also been reported by other authors using TFL on BegoStone such as Taratkin et al. These lasers are thought to ablation stone primarily through a photothermal mechanism, and this mechanism appears to be highly dependent on water content within the stone [121]. It is also known that state-of-the-art TFLs in 2023 have a much lower peak power than contemporary Ho:YAG lasers; typically TFLs have a maximum peak power of 500W compared to Ho:YAG lasers which can reach about 10kW. This means that the energy of a TFL pulse is delivered at a lower rate than the same energy Ho:YAG pulse, and over a much longer period of time.

The lower rate of TFL energy delivery may impact the nature of its interactions with stone. Modern Ho:YAG lasers are able to deliver energy sufficiently rapidly to achieve thermal confinement [25], where laser energy is deposited more rapidly than it can radiate or conduct through the target and therefore the temperature will continuously rise during laser irradiation. There is some evidence that TFL's much longer pulses are also able to achieve thermal confinement based on the radiant energy density [91], but the evidence remains scarce and the question has not been directly

addressed experimentally yet. If thermal confinement is not achievable with TFL then there will be a maximum achievable equilibrium temperature which will affect its interactions with stone. This is roughly analogous to diathermy, where a certain threshold must be met to achieve vaporisation instead of coagulation.

The appearances of TFL-ablated BegoStone are also interesting. BegoStone is based on gypsum which has a relatively low melting point of about 100-150 centigrade. When considering the TFL-ablated stones with no visible trenches and pale discoloured lines, it is possible that this is a result of the phantom melting and re-solidifying rather than breaking into fragments. A similar appearance was achieved by ablating dry stones in air, and this mirrors Taratkin's findings, providing further evidence in support of melting. Anecdotally there is also clinician experience of TFL appearing to char, burn or melt human stone both in Oxford and elsewhere [123], although there has been relatively little published data on this phenomenon. This is not usually seen with Ho:YAG lasers (or older historical lasers such as pulsed dye lasers) and so is presumably linked to the properties of TFL.

Next to consider is the sensitivity of TFL to scan speed. Even when stones are soaked in water for 24 hours, increasing the scan speed resulted in higher ablation rate and less instances of melted or charred appearances. In particular, at 0.5J 120Hz, a scan speed of 8 mm/s resulted in a greater mass change than a scan speed of 1 mm/s. In other words, delivering less energy per unit area of target stone actually resulted in greater ablation per unit area. A possible explanation for this unusual finding is that the long duration of TFL pulses may be significant, independent of the peak power. If the early part of a pulse is sufficient to vaporise all the water content within the target stone's penetration depth, further energy from the remainder of the pulse will irradiate an effectively dessicated stone and potentially even impair ablation, for example by melting the stone and preventing fragmentation. This may explain why ablation is improved by increasing the scan speed and reducing the time for which each unit area is irradiated. Future clinical experience will be

essential to determine if these TFL interactions are specific to BegoStone or if they are also applicable in clinical environments.

Alternative ablation rate calculation using volume measurement

The volume of ablated stone used for ablation rate calculations was based on mass changes. An alternative volume measurement based on volumetric scanning was also investigated. A small selection of ablated phantoms was scanned using a micro-CT scanner (usually used for scanning rodents and similar sized objects) with a 40µm resolution. 3 unsoaked stones from each of the following P120 settings were scanned: 0.2J 80Hz (Moses contact), P120 1J 40Hz (Moses distance) and 2J 15Hz (Moses distance).

The volumetric scans were initially processed using ImageJ software (National Institutes of Health/Laboratory for Optical and Computational Instrumentation at University of Wisconsin). The trenches were aligned in a single axis and one representative trench selected for analysis.

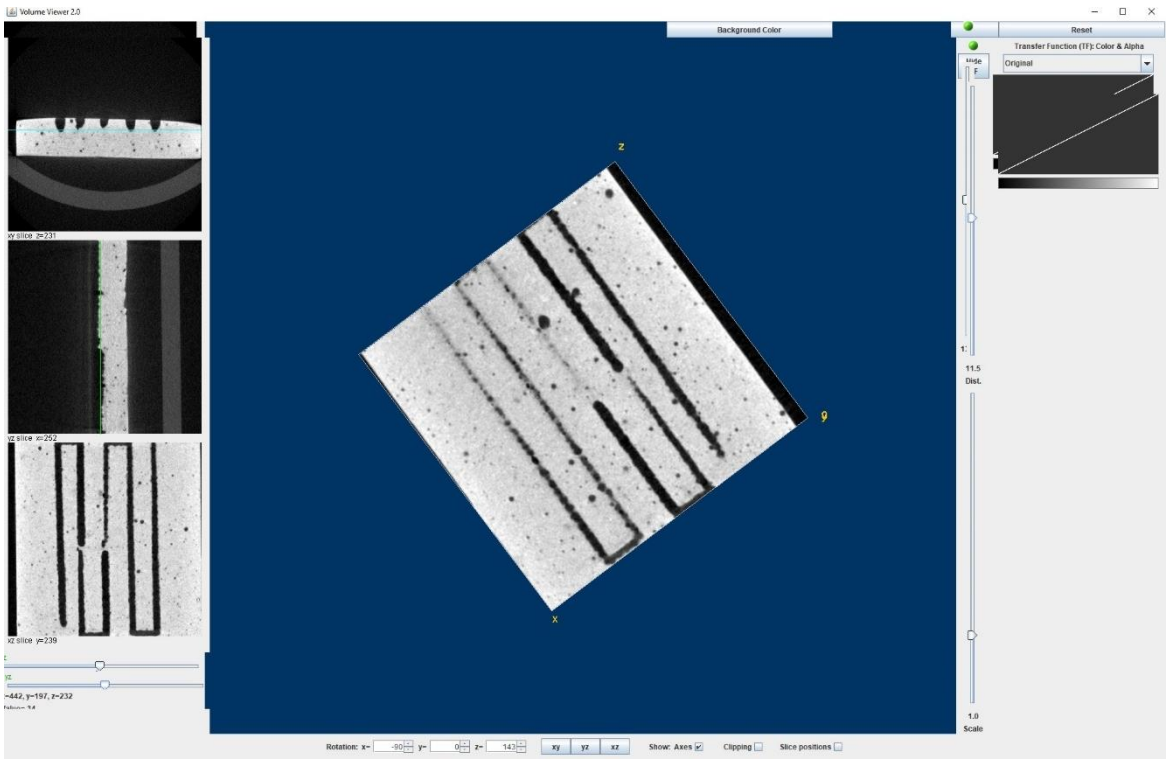


Figure 30. Volumetric scan of phantom ablated with P120 1J 40Hz, Moses Distance, as viewed in ImageJ.

The scan was rotated so the top surface around the selected ablation trench was horizontal and the top of the image stack was level with the top of the stone. Once properly aligned, the volumetric scan was split into a series of stacked 2D monochrome image slices to facilitate further analysis. Each ablation trench could then be reconstructed as the combination of a top-down profile and a side-on profile, as shown in Figure 31.

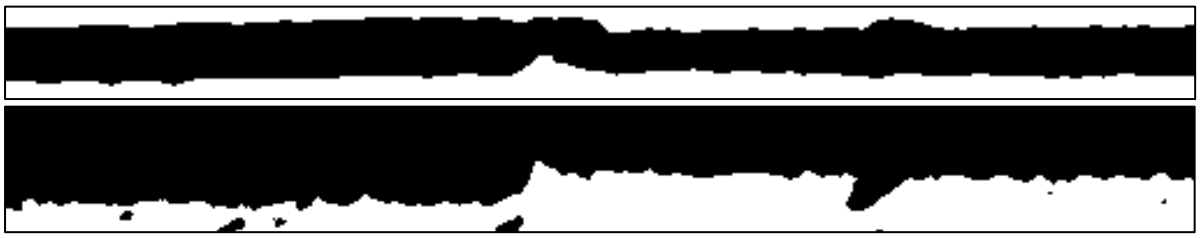
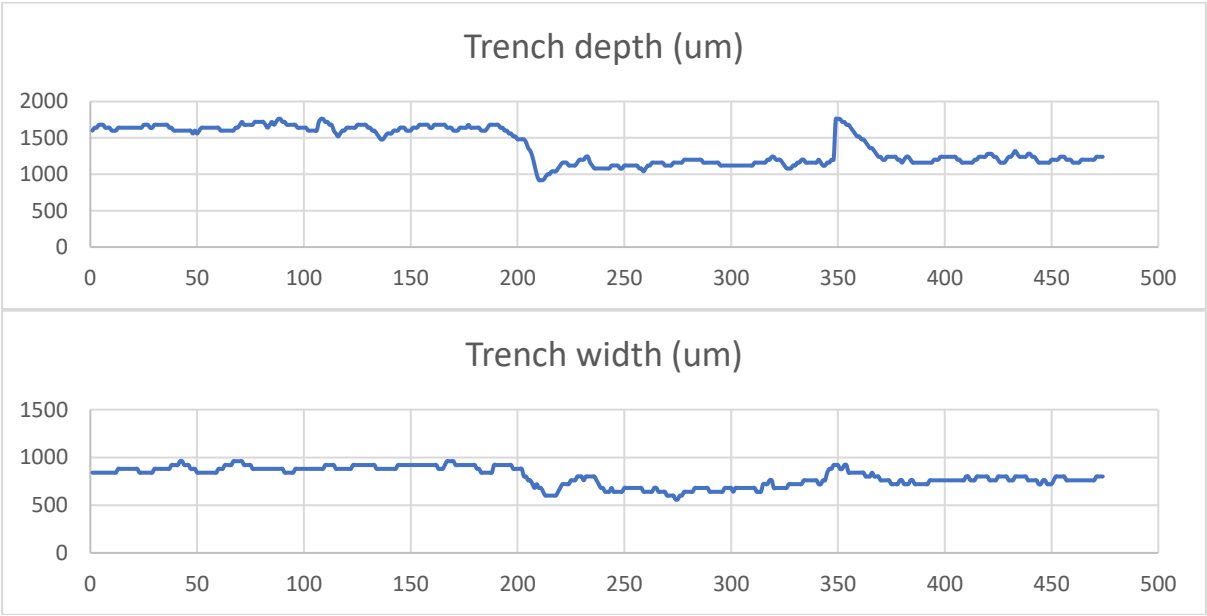


Figure 31. Ablation trench from P120 1J 40Hz, Moses Distance. White indicates stone and black indicates the ablated volume. Top: Top-down profile. Bottom: Side-on profile.

The height and width of the ablated volume at every point along the trench was calculated using software written for this purpose in Perl. The complete script is provided in Appendix 2: Software used for stone ablation volume analysis. The total ablated volume was then calculated by summing the cross-sectional area at each point along the trench, using the known micro-CT image resolution of 40µm per pixel. Figure 32 shows these measurements for the example trench above.



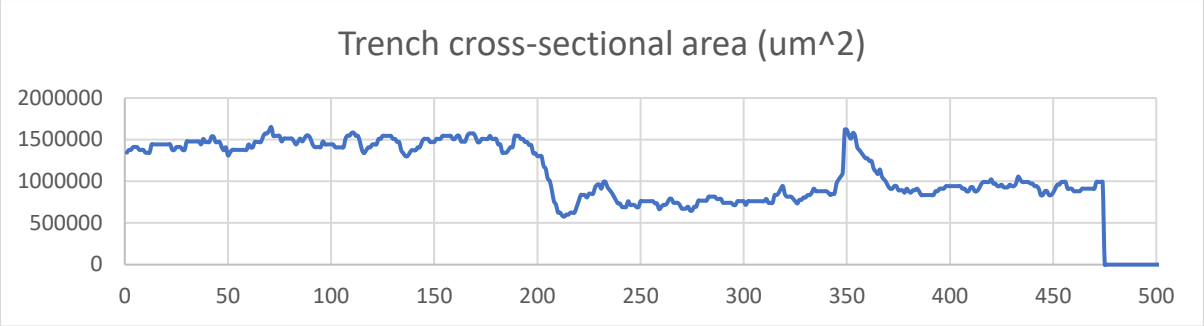


Figure 32. Ablation trench depth, width and cross-sectional area from P120 1J 40Hz, Moses Distance.

While it was interesting to observe the variation in trench depth and width during ablation, this method of volume calculation had some limitations. Without scanning the stones prior to ablation, the exact ablated volume could only be inferred from assuming the stone surface was flat. However, the scans showed that there were frequently small curvatures or other imperfections in the ablated surface which could impact the volume calculation. In addition, the sides of the ablation trenches were often not vertical which resulted in inaccuracies when combining them into a single top-down profile. Accurate calculation would therefore require scanning both before and after ablation, followed by a volumetric subtraction. With the amount of stone phantoms and limited access to the shared micro-CT scanner, it was unfortunately not feasible to use this as a large scale method for the approximately 1500 stone phantoms ablated in this section.

Ablation rate at a distance

Ablation rate when the fibre is at a longer distance to the stone is arguably even more important than ablation rate when the fibre is in contact with the stone. Although contact theoretically represents the best-case scenario for ablation, some clinical techniques such as pop-dusting involve intentionally firing when the fibre is not in contact with the stone. Additionally, even when the intention is to maintain contact, it has been shown that upwards of half of laser pulses could be delivered at a >0.5mm working distance [124].

Methods

The equipment and methodology for ablation at a distance was identical to that used for pseudocontact. The same 30mm x 20mm x 4mm BegoStone phantoms were used along with the

same ablation apparatus. The only difference was in calibrating the working distance between the fibre and stone. After placing the laser fibre initially in contact with the stone, the integrated micrometer was used to move the laser fibre to the desired working distance instead of the 0.5mm working distance used for pseudocontact.

As with pseudocontact, two sets of experiments were performed. The first set used unsoaked stones and was performed alongside the unsoaked pseudocontact experiments. The second set was performed after resolving the Soltive ablation issues described previously, and used pre-soaked stones with the benefit of information gained from the unsoaked data.

The working distances selected were 1mm, 2mm and 3mm, and combined with pseudocontact data which had a working distance of 0.5mm. This was based on water absorption data for Ho:YAG lasers and TFLs. Ho:YAG lasers producing light of wavelength 2120nm have a water absorption coefficient of approximately $3mm^{-1}$, while TFLs producing light of wavelength 1940nm have a water absorption coefficient of approximately $14mm^{-1}$ in water at 20 centigrade [56]. The amount of laser energy penetrating a depth of water can be calculated as follows, where $d_{working}$ is the working distance and c is the absorption coefficient.

$$Energy_{wd} = Pulse\ energy\ \times\ e^{-c \times d_{working}}$$

This calculation shows that for Ho:YAG, 95% of the initial pulse energy is absorbed by 1mm of water and for TFL, 95% of the initial energy is absorbed by 0.2mm of water. This is a vast over-simplification as it does not take into account any Moses effect from vaporisation of the water, effect on absorption coefficient of heating or other attenuation of the divergent output beam. However, it does suggest that the effect of water absorption on Ho:YAG lasers and TFLs differs by less than 1mm and so any difference greater than this is likely to result from other differences such as the extent of any Moses effect. Since the water penetration of both lasers was expected to drop off to near-zero within the space of <1mm, once the ablation trench was seen to visibly degrade, a

final working distance would be set at 0.5mm longer. It was expected that no ablation would occur beyond that final working distance.

For the initial unsoaked series, power levels of 20W and 40W were selected to represent the upper limit of what clinicians were expected to use for ureteric and renal stones. The laser settings used are shown in Table 8. These choices were informed by the unsoaked pseudocontact data, selecting clinically feasible settings that provided the highest ablation rate in pseudocontact. The scan speed was 1 mm/s throughout for all working distances >0.5mm.

Laser	**20W**	**40W**
P120 Moses Distance	0.4J 50Hz	1J 40Hz
P120 Moses Distance	1J 20Hz	
Soltive dusting		1J 40Hz
Prototype fragmentation	2J 10Hz	3J 15Hz
Prototype fragmentation	1J 20Hz	3.5J 10Hz

Table 8. Laser settings used for ablation at a distance experiments with unsoaked stones.

The prototype laser had technical issues with the originally planned 40W setting of 2J 20Hz, and so instead two similar power settings were used: 3J 15Hz at 45W and 3.5J 10Hz at 35W.

Results – unsoaked stones

Data for the prototype laser in this set of experiments was provided by the Boston Scientific team in San Jose from equivalent experiments using the same methodology. This and the pseudocontact prototype laser data using unsoaked stones are the only data sets provided by Boston Scientific; all other data was collected in Oxford.

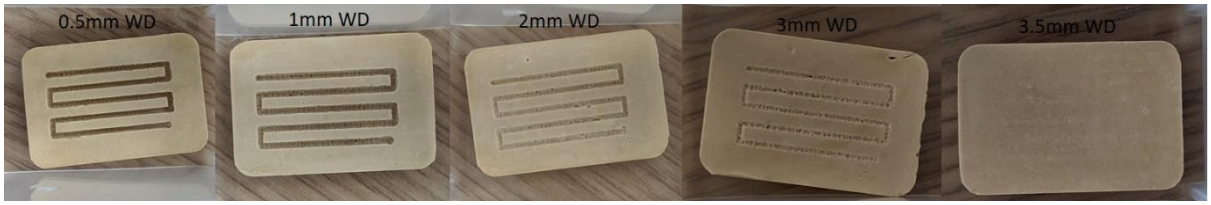


Figure 33. Example ablation trenches for P120, 1J 40Hz Moses Distance. Working distance from left to right: 0.5mm, 1mm, 2mm, 3mm and 3.5mm.

Figure 33 shows some example ablation trenches from the P120 40W setting of 1J 40Hz, Moses Distance. The trenches can be seen to get shallower as the working distance increases, with no

visible trench at all at 3.5mm working distance. The corresponding ablation rates are shown below in Figure 34.

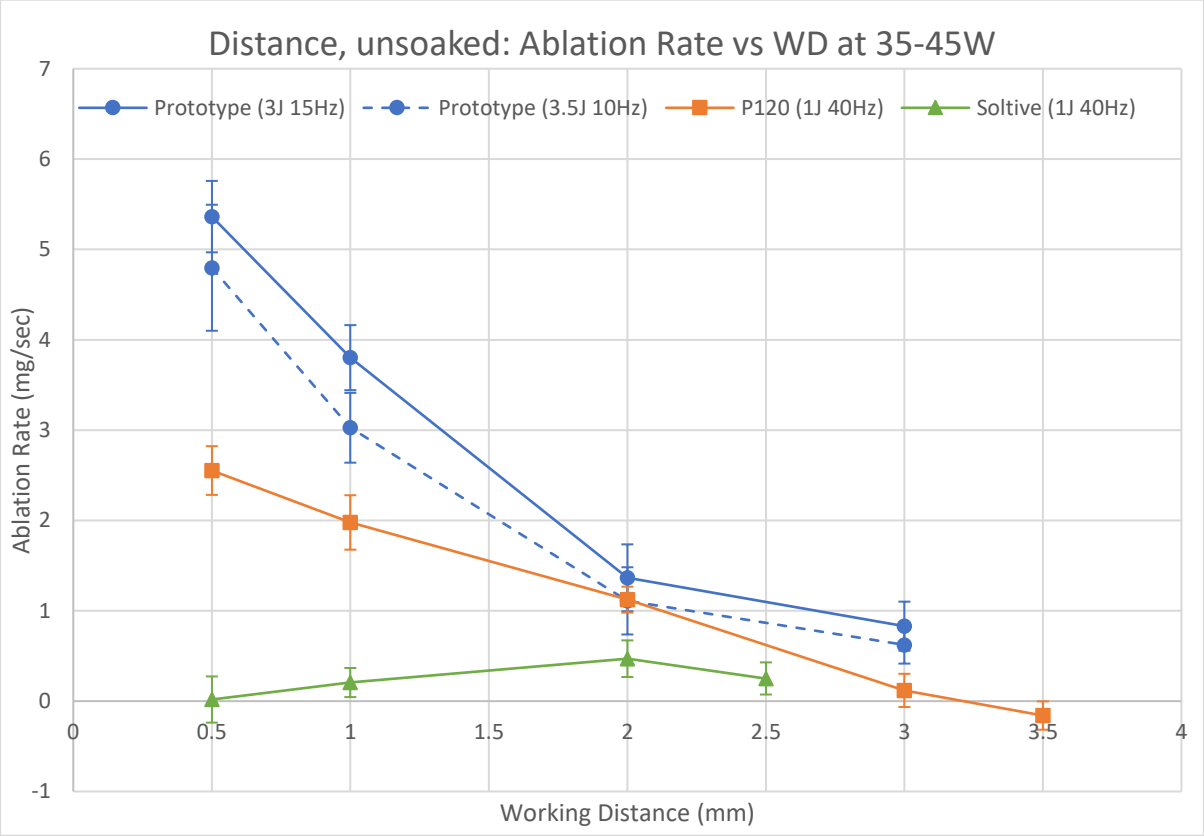


Figure 34. Ablation rate at a distance using unsoaked stones at 35-45W. Error bars indicate one standard deviation.

Both Ho:YAG lasers produce lower ablation rates at longer working distances, as expected. P120 produces a linear looking relationship between working distance and ablation rate, while the prototype graph resembles exponential decay. P120 produces no measurable mass change at 3.5mm working distance, which matches the absence of any visible trench on the stones.

Soltive's working distance graph is different, with ablation rate appearing to increase as the working distance is increased up to 2mm. These experiments were done concurrently with the pseudocontact Soltive ablation rate experiments, so the particular requirements for ablating BegoStone with TFL were not fully understood prior to this set of experiments. The Soltive data here was therefore not optimised for the best performance of this laser. Nevertheless, the effect of increasing working distance in this unoptimized state is interesting and will be discussed in detail later.

Moving to the 20W power level, examples of P120 ablation trenches using 1J 20Hz Moses Distance are shown in Figure 35 and full results in Figure 36.

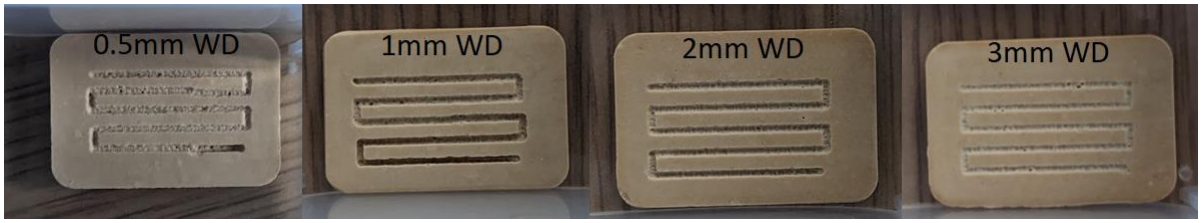


Figure 35. Example ablation trenches for P120, 1J 20Hz Moses Distance. Working distance from left to right: 0.5mm, 1mm, 2mm and 3mm.

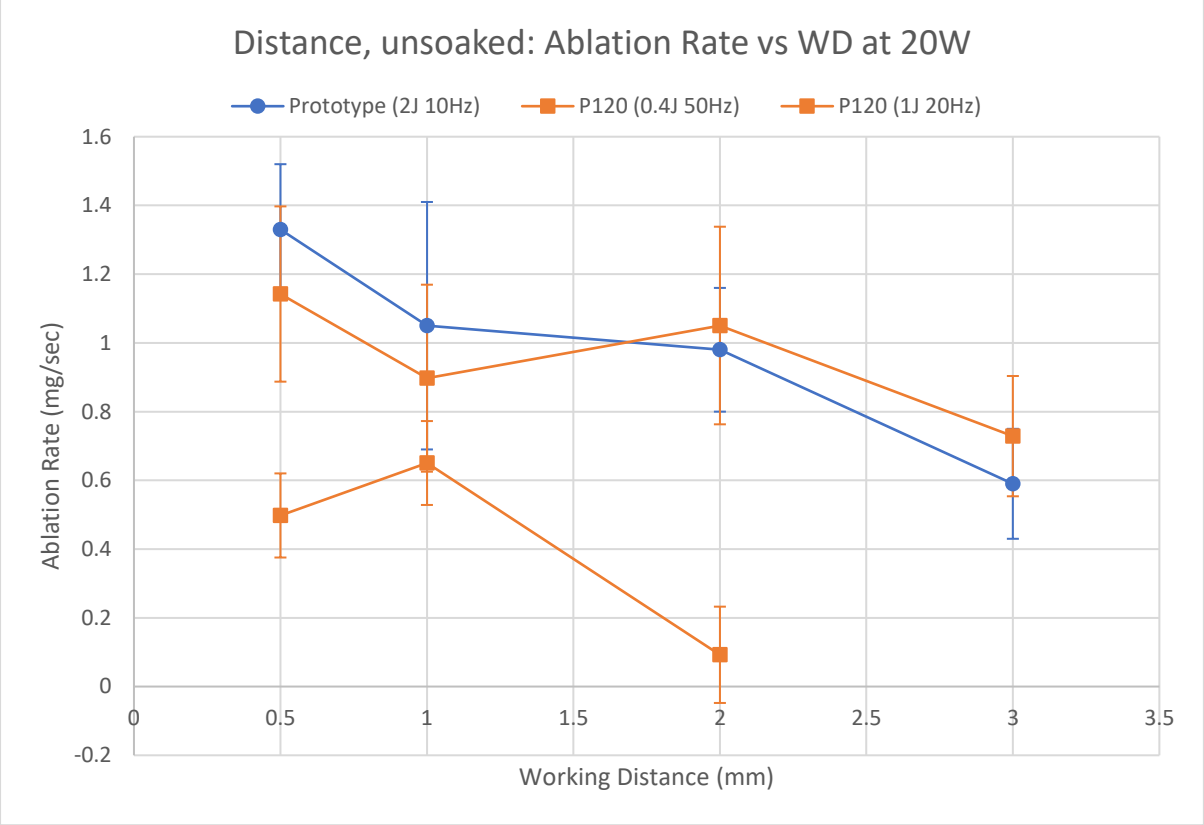


Figure 36. Ablation rate at a distance using unsoaked stones at 20W. Error bars indicate one standard deviation.

Only P120 and prototype laser data was captured at 20W, as it was clear at this point that the Soltive was not optimised with unsoaked stones. As with 40W, a longer working distance appears to result in lower ablation rate for both Ho:YAG lasers. However, the absolute ablation rates are much lower and so the error bars are relatively large and the trends more difficult to establish. The maximum effective working distance of P120 varies depending on the setting used, with the higher pulse energy setting (1J 20Hz) producing effective ablation at a distance of 3mm while the lower pulse energy setting (0.4J 50Hz) was only able produce measurable ablation at a distance of 2mm. It is also

noteworthy that the maximum distance for P120 effective ablation is the same at 1J 20Hz as it was at 1J 40Hz.

Results – pre-soaked stones

The protocol for the second set of experiments, using pre-soaked stones, was informed by the results of both the unsoaked data and the pre-soaked data in pseudocontact. The methodology was unchanged, but only 40W average power settings were used as the mass changes produced by the 20W settings were too low to draw accurate conclusions.

A single setting was selected for each laser. For the Ho:YAG lasers, this was the highest clinically feasible pulse energy at this power level, as this had shown to produce both higher ablation rate in pseudocontact and a longer effective working distance on unsoaked stones. For Soltive, there was again little data to guide the choice of setting and so a high frequency setting was selected, in line with manufacturer recommendations at the time.

Laser	Laser settings at a distance
P120 (Moses Distance)	1J 40Hz = 40W
TFL (short pulse)	0.2J 200Hz = 40W
Prototype (fragmentation mode)	2J 20Hz = 40W

Table 9. Laser settings for ablation rate at a distance experiments using pre-soaked stones.

With pre-soaked stones, Soltive was able to produce even-looking ablation trenches similar to those seen for the Ho:YAG lasers. Examples are shown in Figure 37. It was able to produce some inconsistent trenches at a working distance of 3mm, but many stones had no or minimal visible trenches (Figure 38) and as a result the overall mass change was very small.

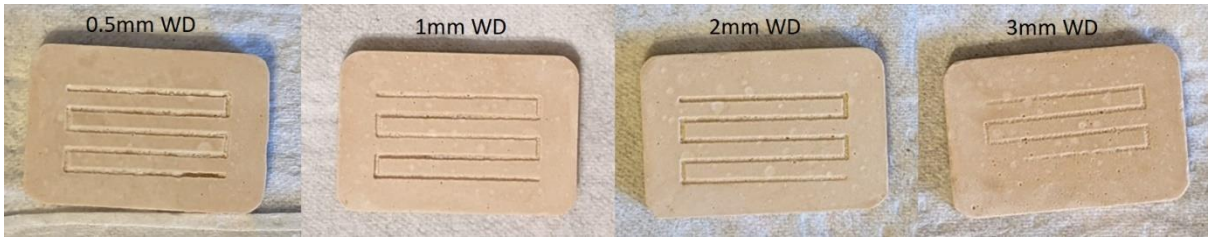


Figure 37. Example ablation trenches for Soltive, 0.2J 200Hz standard short pulse. Working distance from left to right: 0.5mm, 1mm, 2mm and 3mm.



Figure 38. All ablated stones for Soltive, 0.2J 200Hz standard short pulse at a working distance of 3mm.

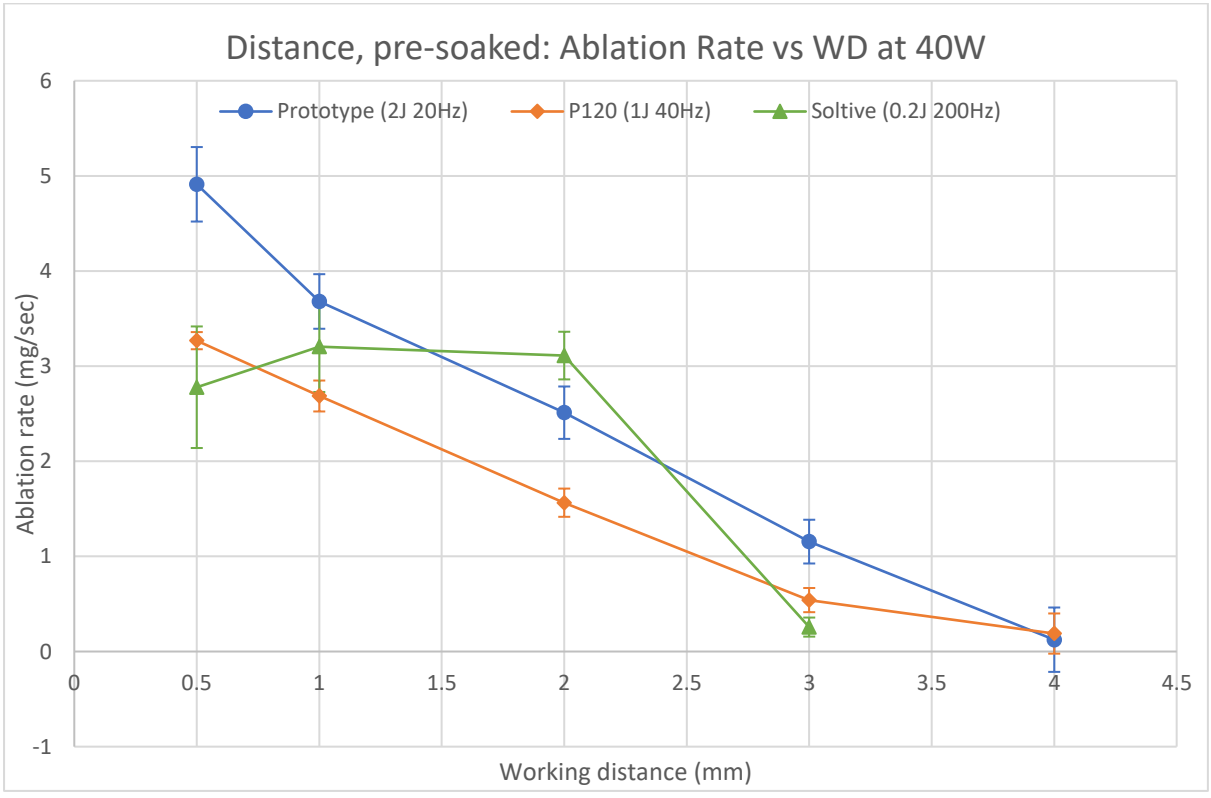


Figure 39. Ablation rate at a distance using pre-soaked stones at 40W. Error bars indicate one standard deviation.

P120 produced higher ablation rates with pre-soaked stones than with unsoaked stones at all working distances. It was not possible to directly compare pre-soaked and unsoaked stones for the prototype and Soltive lasers because of changes in the settings used. However, the pre-soaked prototype setting (2J 20Hz fragmentation mode = 40W) produced very similar ablation rates to both unsoaked settings (3J 15Hz = 45W and 3.5J 10Hz = 35W, both fragmentation mode) with higher ablation rates at 2mm and longer working distances. Despite these slight increases in ablation rate, the effective range of the P120 and prototype lasers was unchanged, with visible ablation trenches and measurable mass changes at 3mm working distance but not at 4mm working distance.

With pre-soaked stones, Soltive was also able to produce both visible ablation trenches and measurable mass changes at a working distance of 3mm, although at these distance the trenches were inconsistent and the mass change was small. At shorter working distances, the ablation rate is essentially constant and does not appear to decay as the fibre goes from 0.5mm to 2mm working distance. This is an interesting observation considering that the high water absorption of the 1940nm TFL laser has been thought to mean it is a contact-only laser. The lack of the expected exponential decay with increasing working distance suggests that there is likely a significant Moses effect with Soltive.

Full results are provided in Table 10 below. As with the pseudocontact results, post-hoc statistical analysis was performed between pairs of lasers and settings using a two-sided t-test. This suggests that the prototype has significantly higher ablation rate than the P120 at all working distances up to 3mm (i.e. within the effective range of these two lasers). Differences with the Soltive laser are not conclusive.

Laser and WD	Ablation rate			Vs laser (p values)		
0.5mm	Mean (mg/s)	S.D. (mg/s)	95% CI (mg/s)	P120	Soltive	Prototype
P120 (1J 40Hz)	3.268	0.117	3.177 – 3.358	-	0.118	**<0.001**
Soltive (0.2J 200Hz)	2.778	0.831	2.139 – 3.417	0.118	-	**<0.001**
Prototype (2J 20Hz)	4.912	0.509	4.520 – 5.303	**<0.001**	**<0.001**	-
1mm						
P120 (1J 40Hz)	2.686	0.211	2.524 – 2.849	-	**0.039**	**<0.001**
Soltive (0.2J 200Hz)	3.205	0.619	2.728 – 3.681	**0.039**	-	0.070
Prototype (2J 20Hz)	3.680	0.373	3.393 – 3.967	**<0.001**	0.070	-
2mm						
P120 (1J 40Hz)	1.565	0.193	1.416 – 1.713	-	**<0.001**	**<0.001**
Soltive (0.2J 200Hz)	3.111	0.326	2.861 – 3.362	**<0.001**	-	**0.002**
Prototype (2J 20Hz)	2.511	0.358	2.235 – 2.786	**<0.001**	**0.002**	-
3mm						
P120 (1J 40Hz)	0.541	0.165	0.414 – 0.668	-	**0.001**	**<0.001**
Soltive (0.2J 200Hz)	0.257	0.130	0.157 – 0.357	**0.001**	-	**<0.001**
Prototype (2J 20Hz)	1.155	0.299	0.925 – 1.385	**<0.001**	**<0.001**	-
4mm						
P120 (1J 40Hz)	0.189	0.286	-0.149 – 0.527	-	-	0.129
Soltive (0.2J 200Hz)	-	-		-	-	-
Prototype (2J 20Hz)	0.124	0.199	-0.028 – 0.277	0.129	-	-

Table 10. Ablation rate at a distance, pre-soaked stones. Statistically significant differences ($p < 0.05$) are in bold, calculated by two-sided t-test.

Discussion

Both P120 and the prototype lasers demonstrated the expected inverse relationship between working distance and ablation rate. Although the number of data points is relatively small, this relationship appears to differ between the two lasers with P120 appearing to be linear while the prototype appears to be exponential. Soltive produces a very different relationship with working distance, with a fairly constant ablation rate up to a 2mm working distance and rapidly falling off beyond this. The two Ho:YAG lasers will be considered first.

The nature of laser attenuation in water can be considered in the context of the pulsed energy delivery of these two lasers. Both Ho:YAG lasers deliver each pulse as a combination of subpulses (two in the case of P120 Moses Distance, and seven for the prototype in fragmentation mode). For both lasers, each subpulse is relatively short as measured in 2. Laser pulse measurement – on the order of 100µs. The state of the surrounding water and any vapour bubble can therefore be assumed to be static relative to any individual Ho:YAG subpulse. Then each subpulse can be considered individually, and will be in one of two states:

- The initial subpulse will have a column of saline between the end of the fibre and the target BegoStone phantom with depth d_{fluid} equal to the working distance.
- Subsequent subpulses will have a column of vapour bubble at the end of the fibre with depth d_{vapour}, and a column of saline with depth d_{fluid} (which may be zero). The sum of d_{vapour} and d_{fluid} is equal to the working distance.

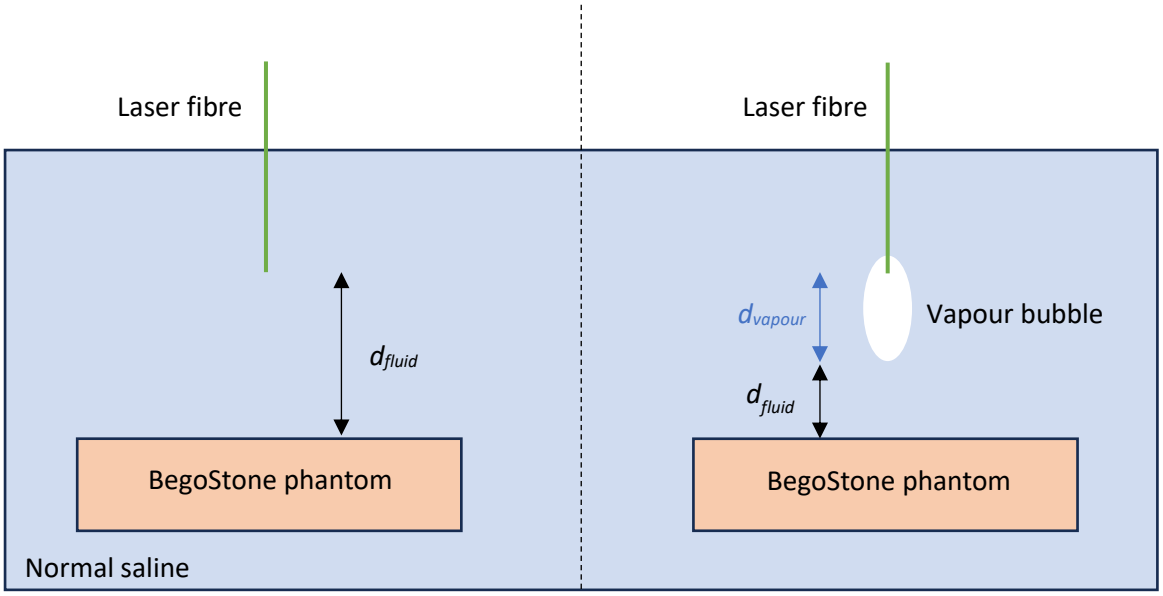


Figure 40. Schematic of laser attenuation for ablation rate at a distance. Left: attenuation without vapour bubble. Right: attenuation with vapour bubble, demonstrating Moses effect.

To keep the model simple, the following assumptions will be made.

- Laser attenuation in vapour is zero (i.e. all energy is transmitted through vapour), i.e. the relevant absorption coefficient $c_{vapour} = 0$.
- Laser absorption in saline is equal to absorption in water.
- The total distance between the laser fibre and the target stone is constant and equal to the initially set working distance $d_{working}$.
- All subpulses deliver equal amounts of energy $E_{subpulse}$ (1/2 of the pulse energy for P120 Moses Distance, and 1/7 of the pulse packet energy for the prototype fragmentation mode).
- All subsequent subpulses feature the same length of vapour bubble column d_{vapour}.
- Ablation rate is directly proportional to the amount of laser energy reaching the stone.

Then the energy delivered to the stone by the initial pulse is as follows, where c is the absorption coefficient (3mm^{-1} for Ho:YAG and 14mm^{-1} for Soltive).

$$E_{initial} = E_{subpulse} \times e^{-c \times d_{working}}$$

The energy delivered to the stone by subsequent pulses is as follows.

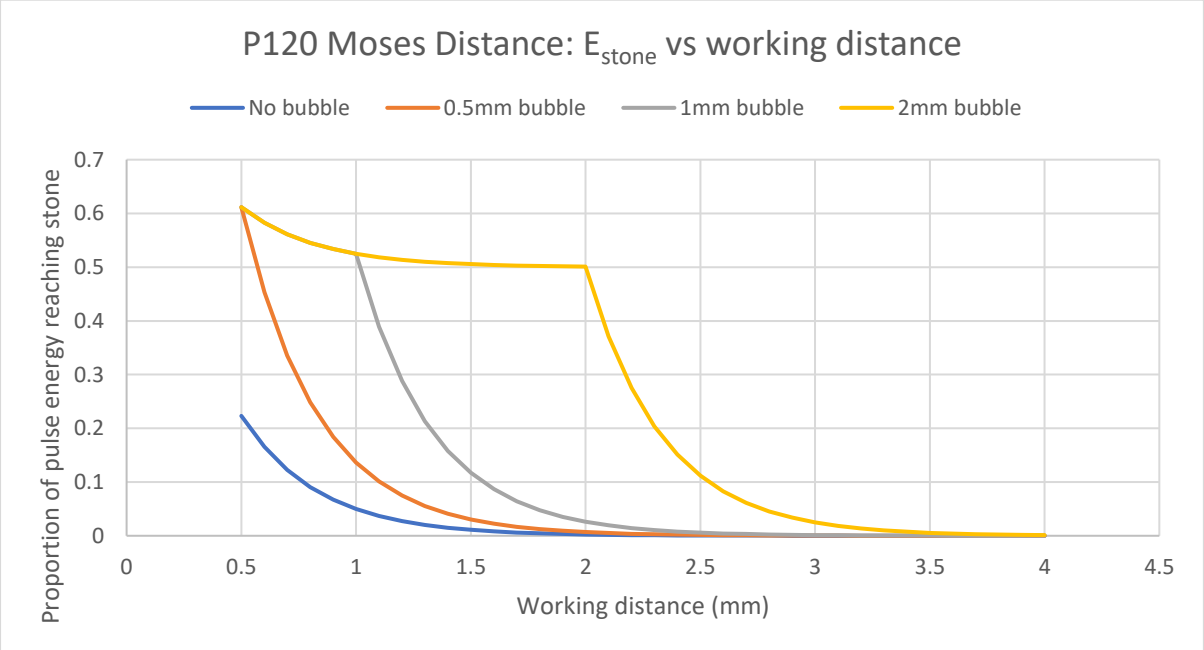
$$E_{subs} = E_{subpulse} \times e^{-0 \times d_{vapour}} \times e^{-c \times d_{fluid}} = E_{subpulse} \times e^{-c \times d_{fluid}}$$

Then the total energy delivered to the stone by all pulses is as follows.

$$P120: E_{stone} = E_{initial} + E_{subpulse} = \frac{1}{2} E_{pulse} \left(e^{-3 \times d_{working}} + e^{-3 \times (d_{working} - d_{vapour})} \right)$$

$$Prototype: E_{stone} = E_{initial} + 6E_{subpulse} = \frac{1}{7} E_{pulse} \left(e^{-3 \times d_{working}} + 6e^{-3 \times (d_{working} - d_{vapour})} \right)$$

Since the pulse energy and working distance are set for each experiment, the only remaining variable is the vapour bubble length. It is convenient to use a pulse energy of 1J so that the energy reaching the stone E_{stone} can be read as a simple ratio. It is then possible to plot E_{stone} against working distance for a variety of anticipated vapour bubble lengths.



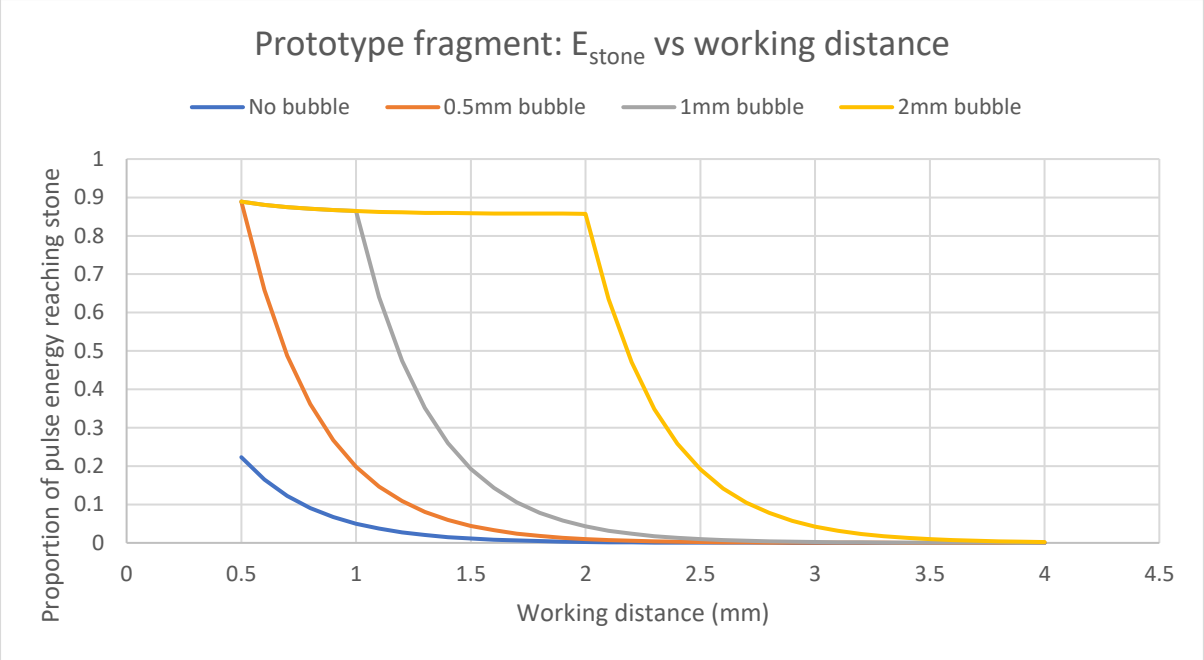


Figure 41. Expected proportion of initial pulse energy reaching the stone at a range of working distances and vapour bubble lengths. Top: P120 Moses distance. Bottom: Prototype fragmentation mode.

As the prototype's fragmentation pulse is divided into 7 subpulses, a higher proportion of energy reaches the stone with the same bubble sizes as P120 Moses distance. This is because the initial pulse (which is subject to the greatest water absorption) is a lower proportion of the total pulse energy. However conversely, as each of the prototype's 7 subpulses is smaller than the P120's 2 subpulses, they are likely to produce smaller vapour bubbles and so one would expect the maximum bubble length to be shorter for the prototype.

In other words, when comparing the effect of working distance on P120 Moses distance and the prototype fragmentation mode, one might expect the following:

- The prototype may deliver a higher proportion of pulse energy when close to the stone than P120.
- The prototype's effectiveness might begin to exponentially decay at a shorter working distance than P120.

These theoretical relationships are consistent with the observed results, with the prototype producing a curve that mostly resembles exponential decay with both soaked and unsoaked stones. Meanwhile the P120's linear-looking decay curve may be a result of a larger initial exponential decay

from the first pulse causing the curve to look flatter at shorter working distances. Attempting to fit this theoretical model to the observed results produces the dotted lines shown in Figure 42. Clearly this over-simplified model is not able to accurately fit all of the observed data points, but it does produce a reasonable fit with R^2 = 0.826 (P120) and R^2 = 0.875 (prototype). These theoretical curves are based on a vapour bubble length of 2.5mm for P120 and 1.8mm for the prototype laser.

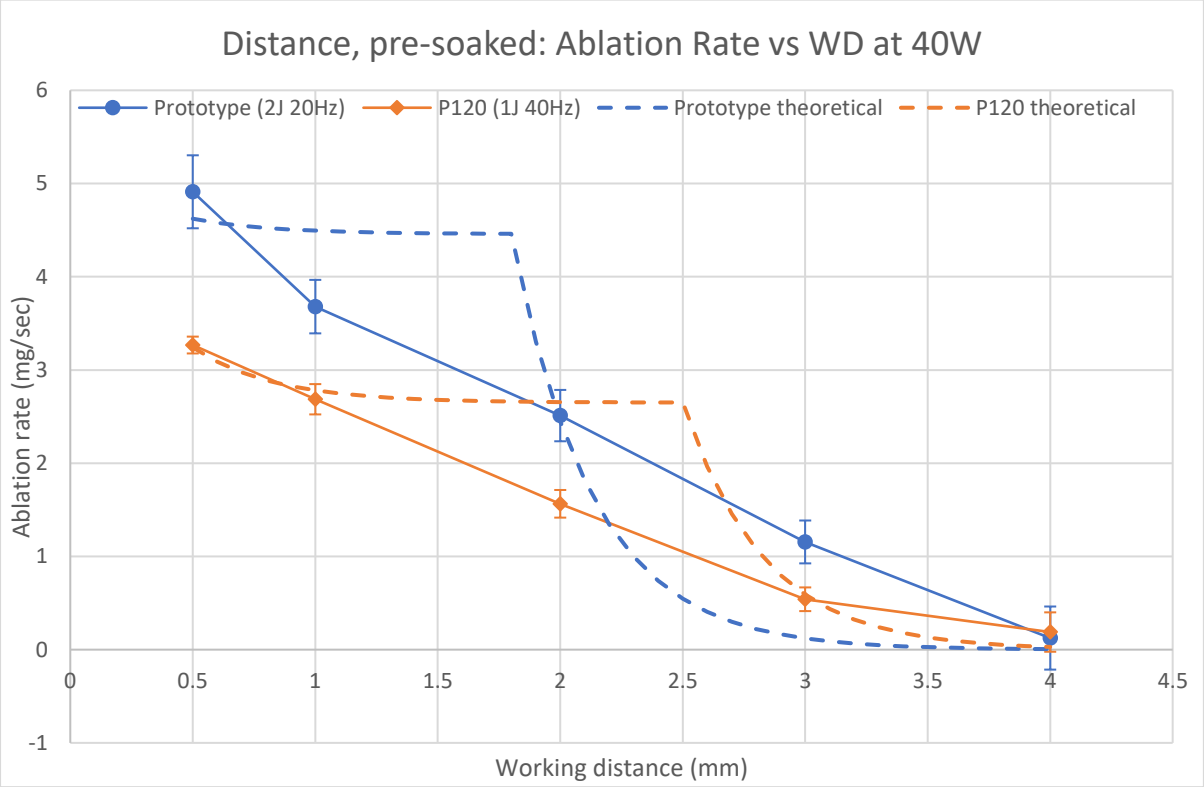


Figure 42. Ablation rates at a distance using pre-soaked stones at 40W. P120 and prototype results with theoretical curves in dotted lines.

This can be correlated with high-speed video photography of the vapour bubbles produced by these lasers. Full details of the experimental setup for capturing these images are provided in Appendix 3: High-speed photography of laser-induced vapour bubbles.

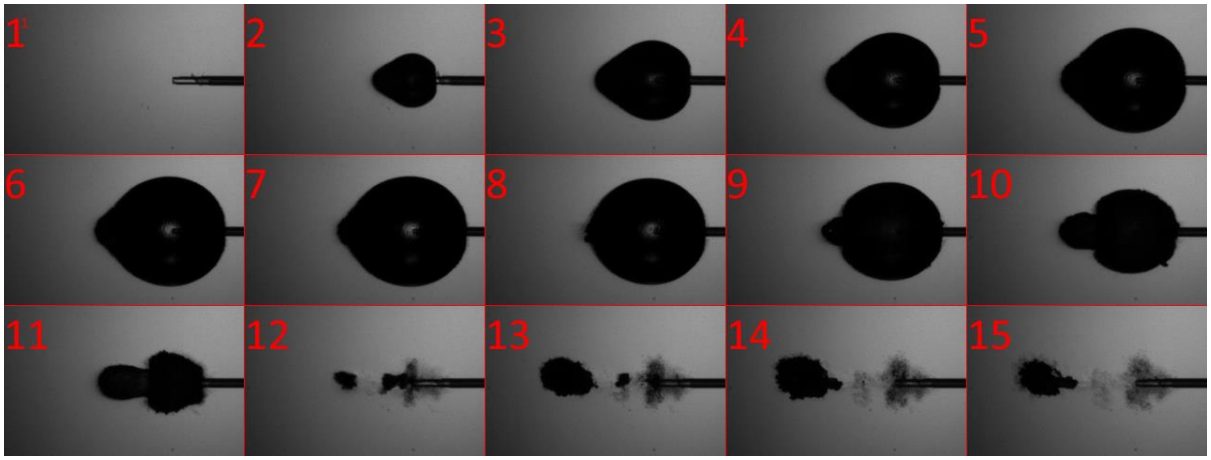


Figure 43. High speed video stills for a single laser pulse from P120 1J, Moses distance. Images are at 50us intervals (10 frames at 200,000 frames per second). The second subpulse can be seen starting in image 8.

The high speed video was calibrated using a transparent ruler in-shot, at 1mm = 28 pixels. At the first frame where the bubble from the second subpulse can be seen to start expanding, the bubble measures 74 pixels from the tip of the laser fibre which converts to 2.64mm. This is remarkably close to the estimated 2.5mm bubble width from fitting the theoretical curve. Further accuracy is likely to be limited by the simplified assumptions made in the model, especially the assumption that the two subpulses are equal (which the pulse measurement data presented earlier shows is not the case for Moses distance).

The behaviour of Soltive at range can now be considered in the context of the above vapour bubble dynamics. The bubble shown required approximately 200µs to expand to its maximum length. The 0.2J pulse energy used for Soltive in these experiments was measured to have a duration of 385µs (although based on the linear relationship between pulse energy and duration at the fixed 500W peak power, the true value is likely to be 400µs). This suggests that vapour bubble dynamics are highly relevant to a single Soltive pulse, and a significant proportion of even a relatively short 0.2J pulse might be delivered with the bubble at maximum length (resulting in a Moses effect). Due to the complexity involved in modelling the non-linear expansion in length of this bubble, a better approach is to observe the vapour bubble and build the model based on measurements.

A single pulse from Soltive 0.2J standard short pulse is shown in Figure 44. Each image is spaced 50µs apart, with the pulse starting immediately after image 1. These images were calibrated at 1mm = 40

pixels. As the total pulse duration should be 400µs, this means the laser is firing during images 2-9 and stops immediately after image 9. The prolonged firing results in the bubble reaching a dynamic equilibrium of partially collapsing and reforming during these images, before eventually collapsing after the pulse ends. It is then possible to plot the maximum bubble length over time.

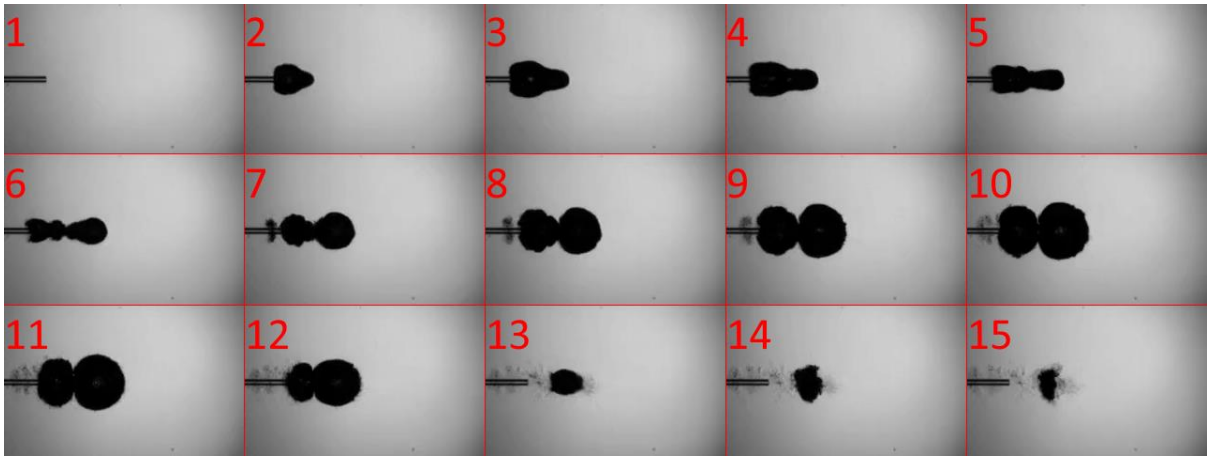


Figure 44. High speed video stills for a single laser pulse from Soltive 0.2J, standard short pulse. Images are at 50us intervals (10 frames at 200,000 frames per second). The duration of the pulse is from immediately after image 1 until image 9.

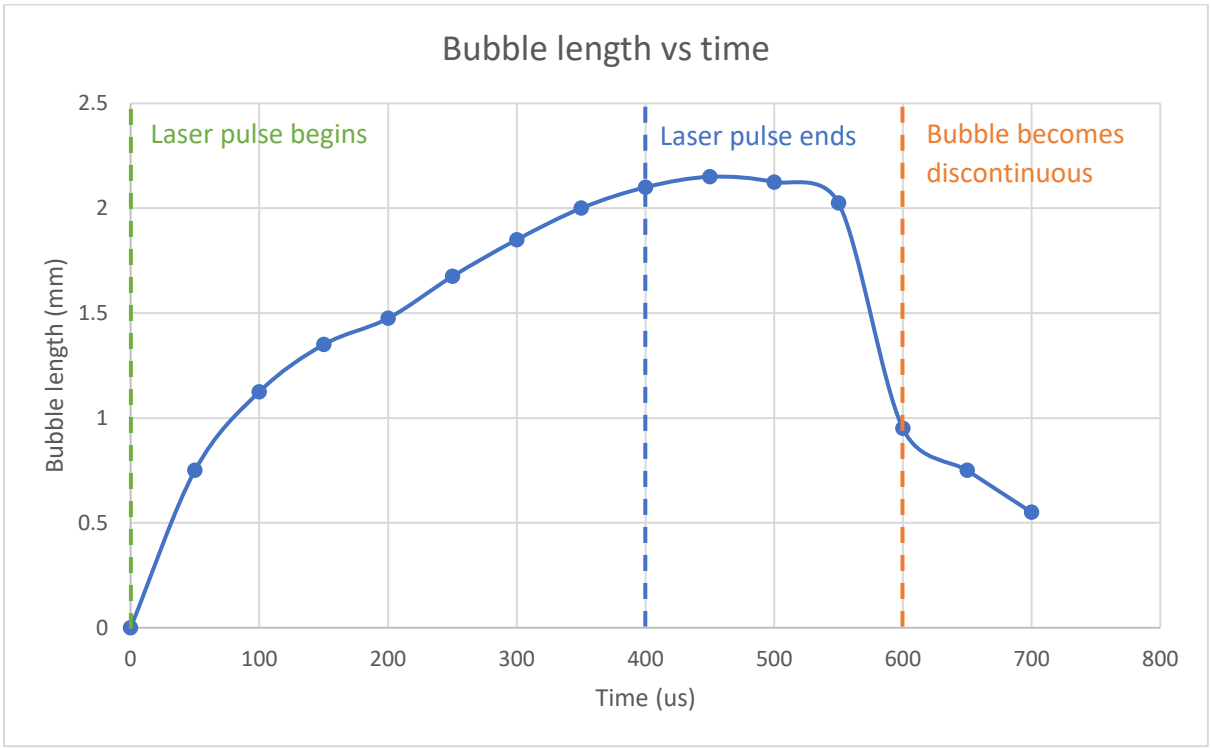


Figure 45. Length over time of the bubble generated by a single pulse of Soltive 0.2J standard short pulse.

By examining the video frame-by-frame, it is possible to establish the time points where the bubble length reaches the working distances used in this set of experiments. It reaches 0.5mm length at 30µs, 1mm length at 80µs and 2mm length at 350µs. The energy delivered to the stone can then be

estimated in a similar manner to that used for the Ho:YAG lasers. A slightly different method will be used, since the pulse duration is extremely long relative to the rate at which the vapour bubble forms and changes.

- Laser attenuation in vapour is zero (i.e. all energy is transmitted through vapour), i.e. the relevant absorption coefficient $c_{vapour} = 0$.
- Laser absorption in saline is equal to absorption in water.
- Since TFL water absorption is extremely high (95% of energy is absorbed by 0.2mm of water), assume that any amount of water column will absorb all energy reaching it.
- The total distance between the laser fibre and the target stone is constant and equal to the initially set working distance $d_{working}$.
- The laser peak power is constant throughout the pulse.
- Ablation rate is directly proportional to the amount of laser energy reaching the stone.
- The length of the vapour bubble varies with time in the same way as observed in Figure 45.
- The total pulse duration is 400µs.

Then no laser energy reaches the stone when the vapour bubble has not reached the stone, and all laser energy reaches the stone when the vapour bubble has reached the stone. The proportion of pulse energy reaching the stone at each working distance can then be calculated as follows.

$$0.5mm\ WD: E_{stone} = E_{pulse}\frac{400-30}{400} = 0.925\ E_{pulse}$$

$$1mm\ WD: E_{stone} = E_{pulse}\frac{400-80}{400} = 0.8\ E_{pulse}$$

$$2mm\ WD: E_{stone} = E_{pulse}\frac{400-350}{400} = 0.125\ E_{pulse}$$

These theoretical values can be plotted against the actual observed Soltive results in Figure 46. Unfortunately this does not appear to accurately model the data, as the theoretical curve appears to be shifted to the left compared to the actual data. In other words, real-world water penetration of

Soltive appears to be about 1mm greater than predicted from the bubble dynamics. Some of this difference will be due to the model slightly over-estimating the effect of water absorption on TFL, but this would not account for 1mm of difference. The high-speed video may not accurately reflect the full extent of the dynamic vapour bubble, or there may be other effects not considered here that enhance laser transmission through the intervening saline.

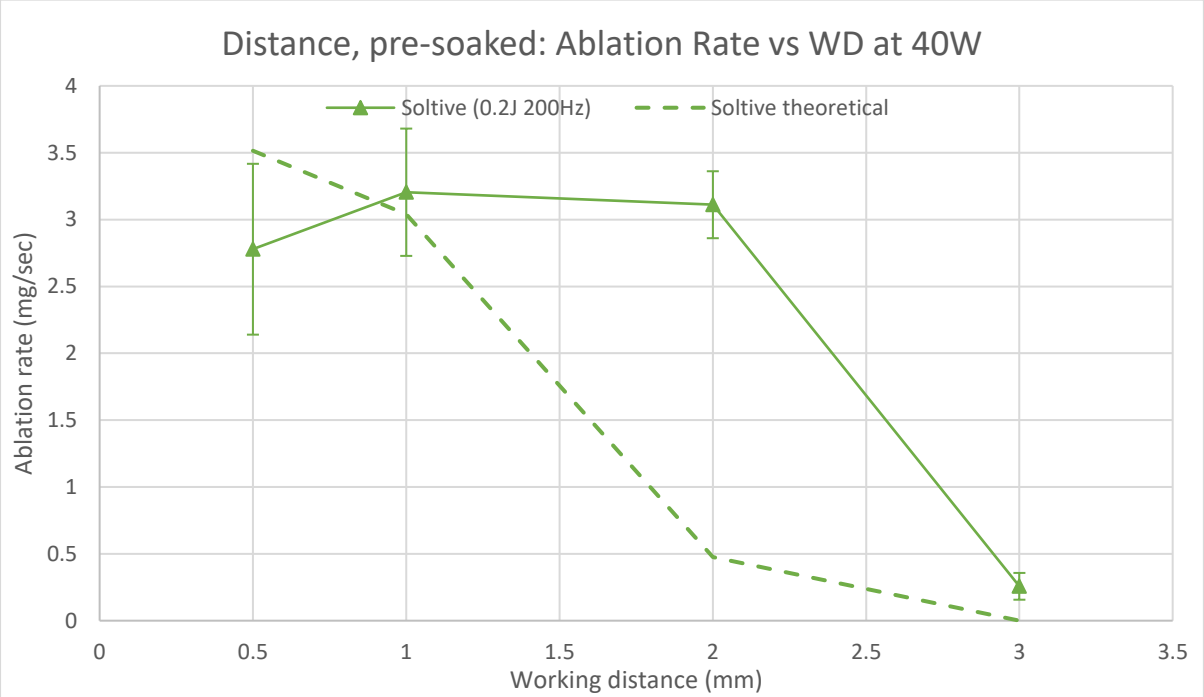


Figure 46. Ablation rates at a distance using pre-soaked stones at 40W. Soltive results with theoretical curve in dotted lines.

Conclusions

All 3 lasers tested were able to effectively ablate BegoStone both in pseudocontact and at a considerable distance. In pseudocontact, the prototype laser produced higher ablation rates at a subset of powers but no single laser or pulse modulation mode was able to demonstrate superiority across the entire range of average powers from 20-60W. When conditions were optimised with pre-soaked stones and appropriate scan speeds, all lasers performed similarly and the biggest determinant of ablation rate was the average power used.

At longer working distances, P120 and the prototype laser were able to ablate visible trenches and produce measurable mass changes at a working distance of 3mm while Soltive was able to do the same at a working distance of 2mm. Soltive was also able to produce some visible trenches at a

working distance of 3mm although these were inconsistent and shallow enough that the mass change was effectively not measurable. All 3 lasers are subject to high water absorption, with 1mm of water absorbing 95% of Ho:YAG energy and 100% of TFL energy. These results are convincing evidence of a significant Moses effect for all 3 lasers.

The relationship between working distance and ablation rate differed for each laser, and this is likely to reflect the nature of the pulses involved. P120 (using Moses distance mode) had a roughly linear relationship between working distance and ablation rate, while the prototype's ablation rate decayed more rapidly and more closely resembled exponential decay (using fragmentation mode). Soltive demonstrated a very different effect, with ablation rate roughly constant at working distance of up to 2mm but rapidly decreasing beyond this range. Some of the difference between P120 and the prototype can be explained by modelling the effect of different numbers of subpulses (2 for P120 and 7 for the prototype) resulting in different shaped curves. Although the prototype produced higher ablation rates than P120 at all working distances, this trend follows the increased ablation rate starting from pseudocontact, and the range for effective ablation remained the same between the two Ho:YAG lasers at 3mm. No clear advantage in working distance could be demonstrated for either of the two Ho:YAG pulse modulation technologies.

The shape of the Soltive's curve can also be explained by considering the much longer pulse duration in relation to the vapour bubble formation. The elongated stream of bubbles has been noted before [91], and the high-speed photography performed here confirms that the bubbles appear to be continuous. This allows the initial part of a Soltive pulse to create a Moses effect for the remainder of the pulse, which is not possible for the much shorter pulses of the Ho:YAG lasers. This suggests that TFLs are not required to maintain full contact for effective ablation in clinical practice, which seems plausible given the difficult of actually achieving fibre-to-stone contact when lasering endoscopically. Soltive's working distance can be modelled by considering the vapour bubble expansion as observed by high-speed photography, but the model presented here underestimates

the effective range by about 1mm. The rate at which the ablation rate decays with increased working distance appears to be accurately modelled, suggesting that the vapour bubble measurements from high-speed photography do not reflect the full degree of the associated Moses effect.

One limitation of these ablation rate data is that the lasers use different settings. As discussed in the methodology, each laser was constrained to only settings that were considered clinically feasible at each average power level, and the setting that was expected to produce the highest ablation rate was selected. This means that, if BegoStone can be considered a suitable model for stone ablation rate, these results can be used as a guide for the upper bound of real-world ablation rate at these average power levels. The disadvantage is that this comparison is less “apples-to-apples” since the lasers use different pulse energies and frequencies. However, in the context of the differing pulse modulation technologies used, a true “apples-to-apples” comparison is not possible, since even if the pulse energy and frequency were matched, the P120 would be delivering each pulse split into two subpulses while the prototype splits each pulse into 7 or more subpulses and the Soltive has no pulse modulation. These results therefore allow comparison of each laser as a unit, rather than matching pulse energy and frequency to isolate the effects of pulse modulation technologies.

Another limitation of these data is that the ablation was performed on BegoStone phantoms. While gypsum stone phantoms (including BegoStone in particular) remain an industry standard, it is not clear whether ablation rate of BegoStone translates accurately to actual stone. However, ablation rate experiments using actual stone are extremely difficult to standardise. The heterogenous and irregular shapes of intact stones make it difficult to make direct comparisons. Furthermore, the effect of differing structures within stones (such as presence or thickness of layers/shells) is not known. If a similar process to the one described here were to be used, then it would require stones large enough to be cut into flat surfaces, which are very rare to obtain intact. It may well be that gypsum stone phantoms are the best available in vtiro option, short of clinical data.

4. Retropulsion

Introduction

Retropulsion is the concept of unwanted stone motion during laser lithotripsy. This originated in the era of photoacoustic lasers such as the Q-switched Nd:YAG laser and pulsed dye laser, which destroyed stones primarily by producing a very high pressure shockwave in the surrounding water medium through vapour bubble formation and collapse to shatter the stone. They produced extremely short (<1µs) pulses with extremely high peak powers (>50kW) but relatively low average powers (<1W for pulsed dye lasers). The effect of these lasers was primarily mechanical and therefore more closely resembled other mechanical devices such as pneumatic and electrohydraulic lithotripters than modern photothermal lasers [47]. It is therefore to be expected that they produced more retropulsion than even the earliest Ho:YAG lasers [125]. As the ability to fragment stones depended on kinetic energy, stone retropulsion was inevitably linked to the efficacy of laser lithotripsy for these early lasers.

The clinical relevance of retropulsion has also changed over time. In the early days of laser lithotripsy in the 1990s, steerable flexible ureteroscopes were not universally available and photoacoustic lasers were mostly used to treat ureteric stones. If the stone or large fragments were retropulsed to the kidney, it would often be impractical or even impossible to access the kidney and the patient would be left with a residual stone. Unwanted stone retropulsion was therefore a significant barrier to successful treatment.

Over the last 30 years, both laser and scope technology have improved significantly and changed the context for stone retropulsion. Adjunct devices such as the Stone Cone or BackStop have been developed to allow clinicians to pre-emptively avoid stone retropulsion from the ureter into the kidney. Meanwhile flexible ureteroscopes are more widely available and smaller diameter, making it feasible to follow and treat stones that are retropulsed to the kidney. The role of the laser itself in avoiding retropulsing a ureteric stone to the kidney is less important than it has historically been. In

the kidney itself, stone baskets are also widely available to allow the clinician to relocate a stone to the calyx of their choice to constrain the stone's motion and aid targeting with the laser.

Modern laser lithotripsy is almost entirely performed using photothermal Ho:YAG and thulium-based lasers (TFL or Tm:YAG). As a result, retropulsion is no longer directly linked to ablation efficacy. These lasers have much longer pulses than photoacoustic lasers (>50μs) with much lower peak powers. The vapour bubbles they generate do not generate enough pressure to damage stone [64, 91], although they are still sufficient to move the stone and generate retropulsion. Combined with the advances in scope and adjunct technology, this means that linear retropulsion is less important than it was historically. Conversely, modern photothermal lasers produce much higher average powers than historical photoacoustic lasers, with average powers of up to 45W being reported in clinical use [99]. Heat dissipation and potential for thermal injury is now a key concern in modern lithotripsy, in contrast to photoacoustic lasers whose low average powers and poor tissue absorption made them incapable of perforating a ureter even with sustained direct emission on ureteric tissue [39]. This means that the ability to maintain the laser beam on the target stone is much more important, as is the impact that stone retropulsion has on this.

The key considerations identified for modern stone retropulsion are therefore as follows:

1. The effect of retropulsion on the ability of the clinician to target the stone is important.
2. The effect of retropulsion on unconstrained linear motion is less important.
3. Stone retropulsion is not as strongly linked to ablation efficacy for photothermal lasers.

A literature review was performed to establish existing methods of measuring and reporting stone retropulsion [83, 92, 96, 120, 125-128]. All studies begin with the laser fibre in direct contact with the target stone phantom. Most studies use an approximately spherical stone phantom that is physically constrained to move in a single horizontal dimension by a variety of mechanisms. Some studies intentionally attempted to reduce friction with spherical phantoms or glass guides, while others such as White et al used intentionally irregular phantoms to mimic real stones.

Most studies quantify retropulsion in terms of a single horizontal distance measurement, with the presumption that a lower value is better. Finley et al instead report on the time taken to produce 8cm of total horizontal movement while Elhilali et al position the laser fibre beneath the stone to propel it upwards against gravity.

A few studies use high-speed photography to capture multiple images during retropulsion. Ventimiglia et al used continuous high-speed video recording to generate displacement and velocity curves for the stones during the period of motion, and this was the only report found that quantified retropulsion in more depth than a single displacement value.

There was a wide variety in the methods of selecting laser settings. Some papers use a single laser pulse for each experiment while others fire continuously for a period. Laser settings are sometimes matched between different lasers for comparison purposes, but often this is not done either because the lasers do not support identical settings or for other reasons.

Most studies used plaster- or gypsum-based stone phantoms, with the exception of Finley et al (ceramic phantoms) and White et al (iron oxalate coated silicate stones "similar in shape to human uroliths"). Ventimiglia et al, who performed the displacement and velocity assessment, used 5x5x5mm cubic BegoStone phantoms and Kang et al used cubic BegoStone phantoms (reported as $5mm^3$ volume, though it is possible they mean 5x5x5mm). All other studies used approximately spherical phantoms.

In terms of constraining motion, Ventimiglia and Andreeva used "hard" constraints that prevented all movement except for a single horizontal dimension. Ventimiglia placed their cubic phantom in a V-shaped guide formed from two steel rulers while Andreeva placed their spherical phantom between two parallel glass rods within a cylindrical cuvette. Elhilali and Kang did not physically constrain the stone motion. The remaining studies used "soft" constraints by placing their spherical phantoms in a cylindrical tube with a larger diameter, allowing some lateral motion but allowing gravity to guide the stone back to the bottom of the cylinder.

Finally, the degree of friction between phantom and the environment was highly variable. At one extreme, Elhilali did not constrain the stone motion at all and the stone was not in contact with any surface during motion, resulting in zero friction other than water resistance. Andreeva used glass rods with only two points of contact to minimise friction (although the process of constraining the phantom's motion would inevitably result in additional friction). On the other end of the spectrum, Ventimiglia used cubic phantoms (presumably incapable of rolling) where the entirety of two faces of each stone appear to be in contact with the steel guides at all times. The remaining studies do not report friction-related details such as surface materials.

Based on the literature review, two retropulsion experiments were designed. Two sets of experiments were planned, to investigate the effect of both a single pulse and sustained laser emission. The decision was made to prioritise reproducibility in results over simulating realism. To that end:

- BegoStone was selected as the phantom material for its well understood and consistent properties.
- Experiments were designed to minimise friction, to reduce the impact on stone motion of elements other than the laser beam.
- For the linear experiment, stone motion was not physically constrained for the same reason as above.
- Cylindrical phantoms were used over spherical phantoms, as the BegoStone casting process was not sufficiently consistent to produce perfect spheres. Imperfect spheres would not roll evenly and small defects in the phantom shape could disproportionately affect results. In contrast, a single flat surface at the base of the cylinder could be cast with high consistency.
- Fluid dynamic factors (such as the physical constraints of a collecting system, or the flow of fluid) were excluded by placing the experiment in the centre of a large water tank, at least 10cm from any wall.

The single pulse “pendulum” experiments were designed and performed first, with the results informing the design of the subsequent “linear” experiments.

Pendulum experiments

Methods

The effect of a single pulse was assessed with pendulum experiments. 6mm diameter cylindrical BegoStone phantoms were prepared as described in Appendix 1: BegoStone preparation, and a thin loop of cotton thread was glued to the curved surface so that the flat base would be vertical when the phantom was suspended by the strings. These phantoms were soaked in water for 24 hours, then suspended by the strings in a water tank with a laser fibre in contact with the flat base of the phantom. A schematic of the experimental setup is shown in Figure 47, and an example still image from the high-speed video in Figure 48.

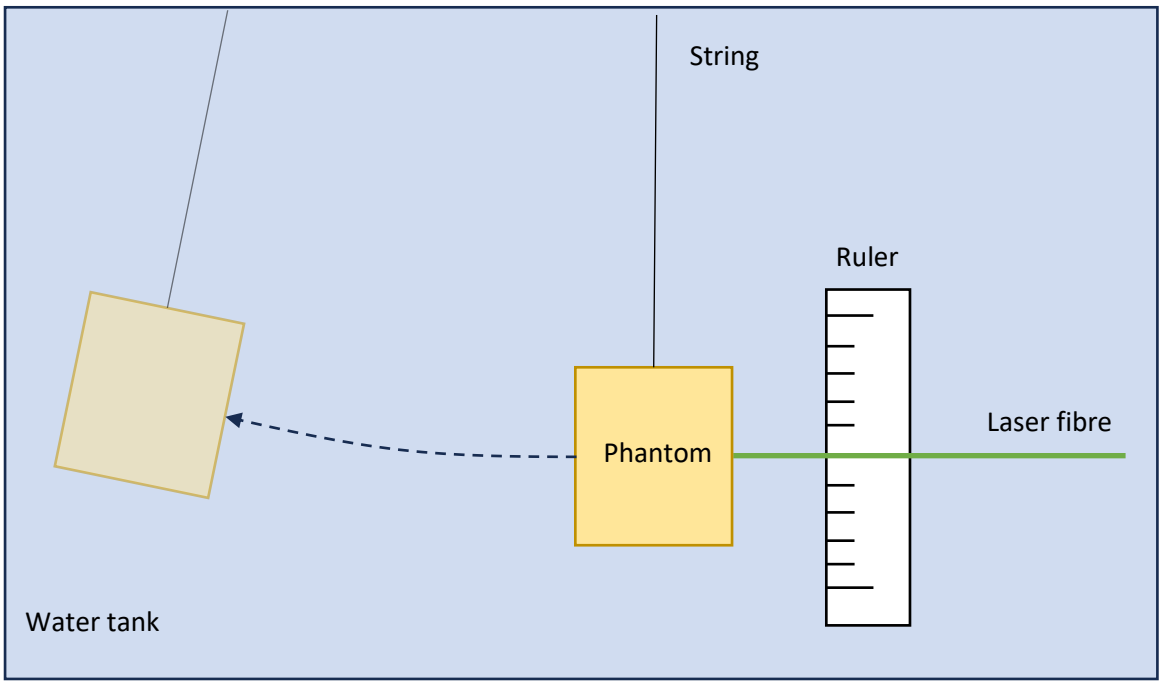


Figure 47. Schematic of retropulsion pendulum experimental setup, from the perspective of the high-speed video camera.



Figure 48. Still image from retropulsion pendulum experiment, taken from high-speed camera recordings using P120 standard short pulse 1J.

A FastCam SA-X2 high-speed camera (Photron, Tokyo, Japan) was aimed towards the phantom so that the laser fibre, camera view and pendulum strings were all perpendicular to each other. This minimised the parallax effect and kept the stone in focus throughout. Light was provided by an F5100 LED microscope light source (Photron, Tokyo, Japan). The laser fibre was renewed prior to each experiment by the same method described in ablation rate experiments, by stripping the cladding using a precision Micro-Strip stripper (Micro Electronics Inc, MA, USA) and cleaving the end of the fibre using a ruby DualScribe optic scribe (THORLABS GmbH, Münchner, Germany). As before, the renewed fibre was checked both by visual inspection of the integrated aiming beam pattern, and by power measurement using a fan cooled thermal laser Ophir power sensir (MKS Instruments, MA, USA). A minimum of 100 pulses was measured and average power within +/- 10% of the selected power setting was considered acceptable.

The laser fibre was then aligned with the centre of the flat base of the cylindrical stone phantom and brought towards the fibre until they were just in contact. A ruler was attached to the laser fibre mount in the same plane for calibrating the images. The laser settings used are shown in Table 11.

Laser	Mode	Pulse energy (J)	Frequency (Hz)
P120	Standard short pulse	0.2	5
P120	Standard short pulse	0.5	5
P120	Standard short pulse	1	5
P120	Standard short pulse	2	5
P120	Standard long pulse	0.2	5
P120	Standard long pulse	0.5	5
P120	Standard long pulse	1	5
P120	Standard long pulse	2	5
P120	Moses contact	0.5	5
P120	Moses contact	1	5
P120	Moses contact	2	5
P120	Moses contact	2	5
P120	Moses distance	0.2	5
P120	Moses distance	0.5	5
P120	Moses distance	1	5
P120	Moses distance	2	5
Prototype	Standard short pulse	0.2	5
Prototype	Standard short pulse	0.5	5
Prototype	Standard short pulse	1	5
Prototype	Standard short pulse	3.5	5
Prototype	Standard long pulse	0.2	5
Prototype	Standard long pulse	0.5	5
Prototype	Standard long pulse	1	5
Prototype	Standard long pulse	3.5	5
Prototype	Dusting	1	5
Prototype	Dusting	3.5	5
Prototype	Fragmenting	1	5
Prototype	Fragmenting	3.5	5
Soltive	Standard short pulse	0.2	5
Soltive	Standard short pulse	0.5	5
Soltive	Standard short pulse	1	5
Soltive	Standard short pulse	2	5
Soltive	Standard long pulse	0.2	5
Soltive	Standard long pulse	0.5	5
Soltive	Standard long pulse	1	5
Soltive	Standard long pulse	2	5

Table 11. Laser settings used for retropulsion pendulum experiments.

The video camera was set to record at 10000 frames per second with a shutter time of 1/10000s. A "start trigger" mode was used so that recording could be started immediately prior to laser emission. The recorded video was then aligned so that the first recorded frame is the final frame prior to laser emission (i.e. laser emission starts on frame 2). The video recording was processed

using a Python script (Python Software Foundation, DE, USA) to track the stone motion across each frame in pixels. This was then converted to measurements in millimetres by calibrating against the ruler in each video. The horizontal and vertical displacements were combined into a single displacement using vector addition.

Retropulsion velocity was calculated as a rolling average of 100 frames, i.e. 10ms intervals. This minimised any image tracking related noise in the stone position.

For a detailed discussion of the technical aspects of this motion analysis, see Appendix 4: High-speed photography of stone motion. The Python script used for image tracking is also presented there.

During experimental design, it was planned to initially collect data for one retropulsion experiment for each setting, to establish the technical limitations of this method and therefore determine the required sample size for accurate data. During collection of this initial data set, it became apparent that these technical limitations (particularly with how the phantom was set up in contact with the laser fibre) had a disproportionate effect on the results compared to the effect of the laser setting variables under test. As a result, only the initial data set was collected and is presented here. The limitations will be discussed as well as potential future methods to mitigate them.

Results

The properties of the BegoStone phantoms used are listed in Table 12 below.

Component	Min	Max	Mean	S.D.
Phantom mass including string (mg)	327	414	371.0	18.9
Suspending string length (mm)	184	219	195.3	5.2

Table 12. Properties of BegoStone phantoms and the suspending strings for retropulsion pendulum experiments.

A set of example output results is presented for P120, 1J 5Hz in standard short pulse mode. The precise stone motion in the first 10 frames (1ms) is shown in Figure 49. Laser emission results in a vapour bubble forming and expanding in frames 4 and 5, with the stone phantom moving away from the fibre tip accordingly. The bubble then collapses in frames 7 and 8, and the phantom is dragged back towards the fibre tip and appears to make contact in frame 10. The phantom subsequently

rebounds away after these first 10 frames, and moves continuously away from the fibre tip thereafter.

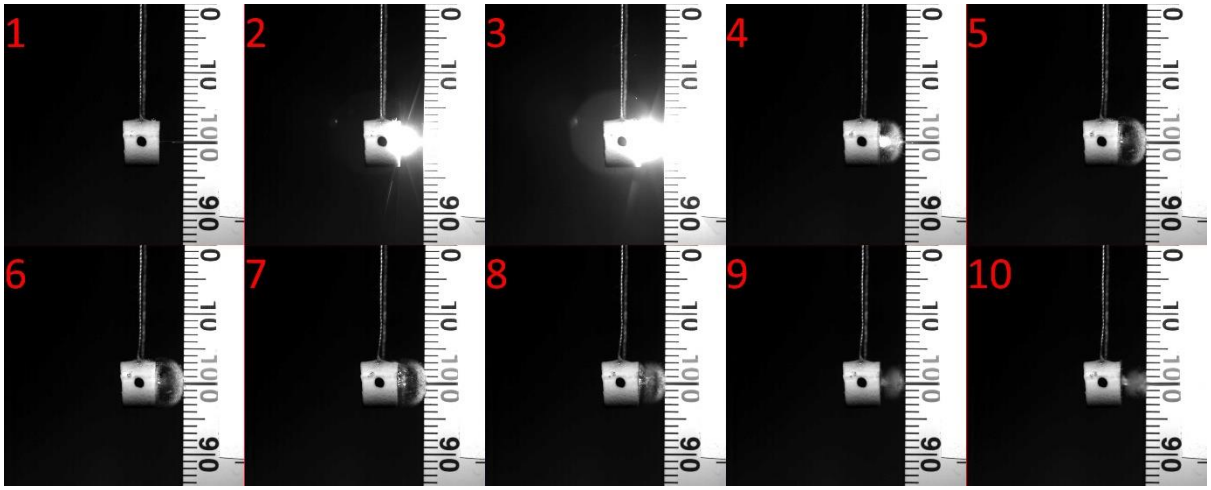


Figure 49. Pendulum retropulsion for P120 1J standard short pulse, high-speed photography of first 1ms.

This motion is captured by analysis of the stone phantom displacement via image tracking, and corresponds to the "bump" seen at the 1ms mark in the graph of phantom displacement in Figure 50.

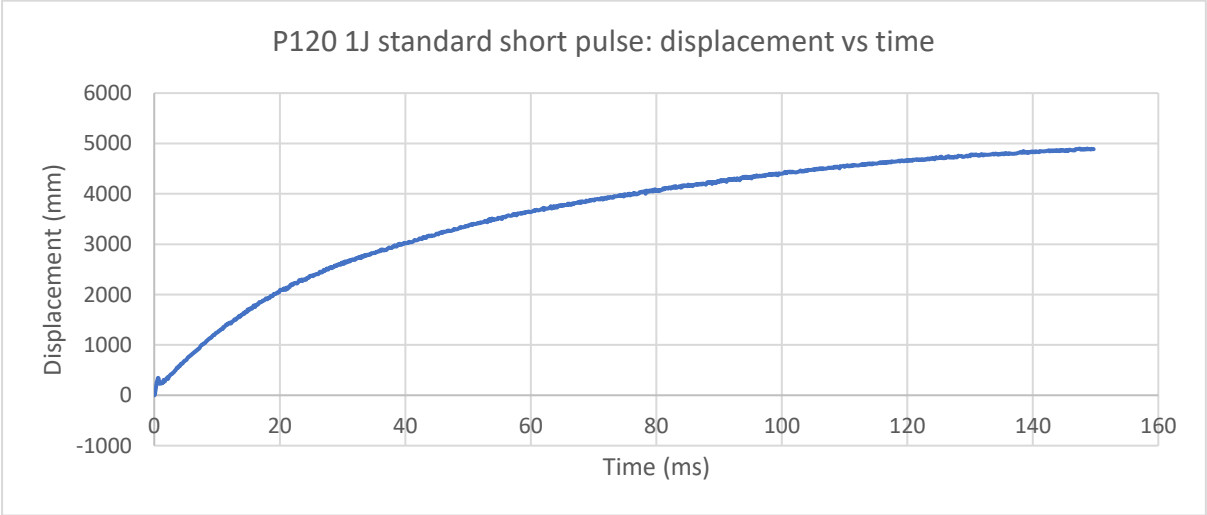


Figure 50. Pendulum retropulsion for P120 1J standard short pulse, stone phantom displacement over time.

It was not possible to precisely calculate the speeds involved in this initial motion as it lasted for just 2-3 frames in each direction, so the limitations on image tracking positions added too much noise to reliably calculate speeds across so few frames. In practice, the speed attained within this first 1ms is of no consequence as it is entirely nullified by the subsequent bubble collapse. However, the effect can still be seen in the rolling average speeds across 100 frames as per the methodology section.

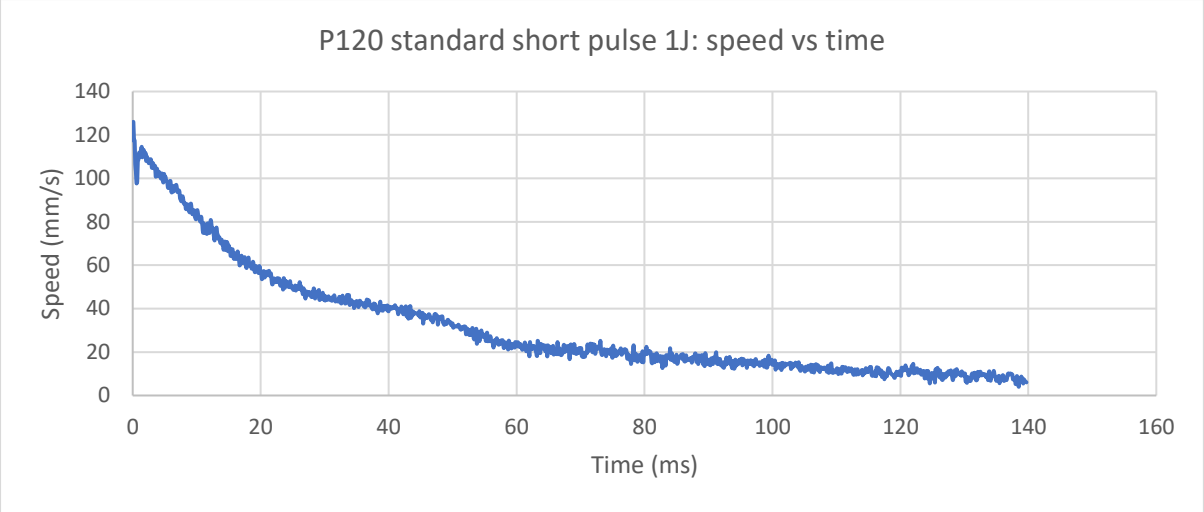


Figure 51. Pendulum retropulsion for P120 1J standard short pulse, stone phantom speed over time.

The maximum speed attained for this setting was 126mm/s. This method of analysis was performed for all the laser settings in Table 11. These experiments featured frequent technical difficulties in both keeping the phantom correctly aligned with the laser fibre (to avoid rotational motion) and inconsistent motion from the phantom rebounding off the laser fibre as seen in Figure 49. Each experiment was repeated if technical issues were observed, and the highest retropulsion speed from each is presented in Figure 52 and Table 13. This represents the single result from each setting that is least impacted by technical issues.

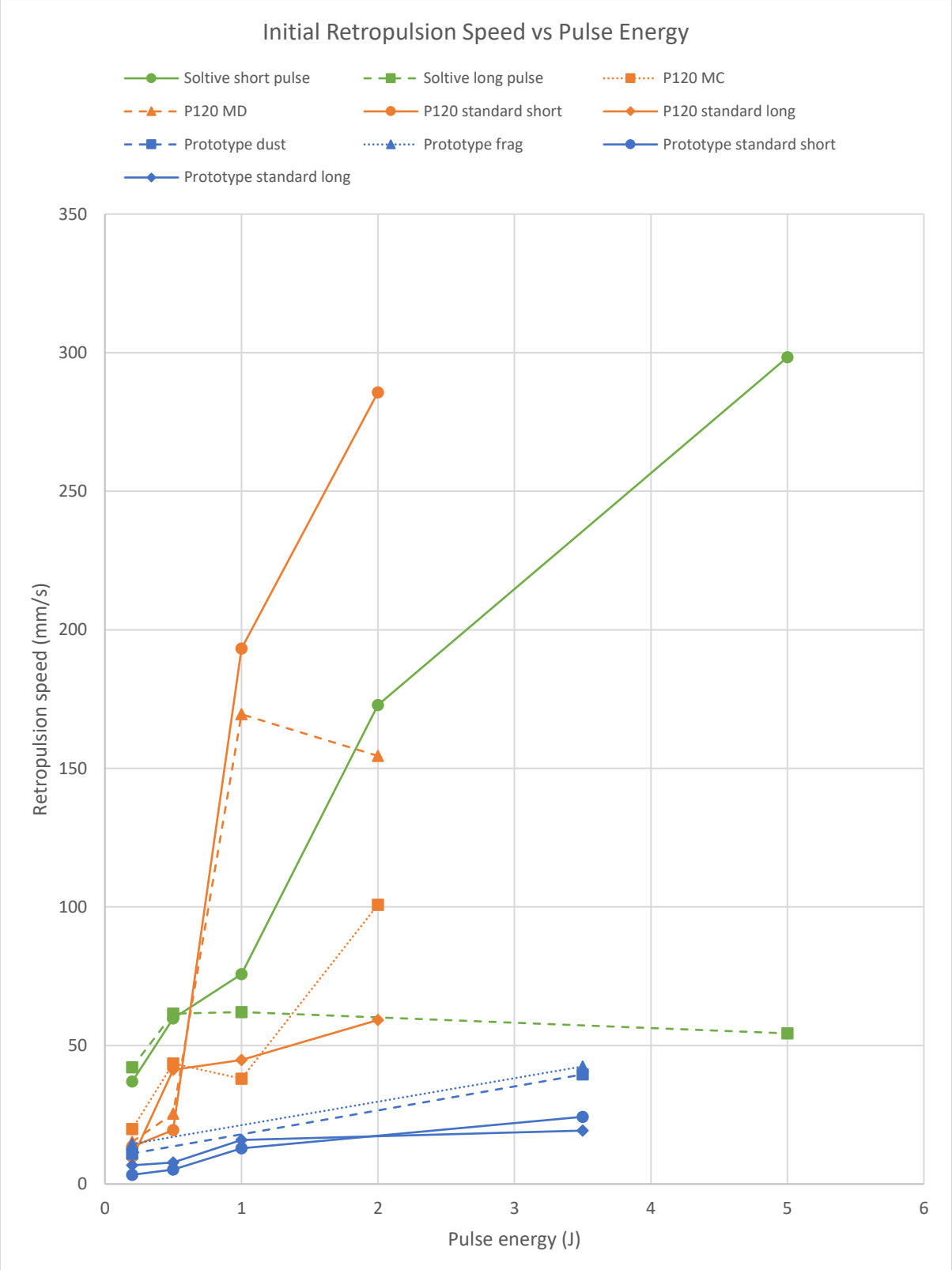


Figure 52. Pendulum retropulsion results. If an experimental setting required repeats for technical issues, only the highest retropulsion speed is plotted here.

Laser	Mode	Pulse energy (J)	Max speed (mm/s)
P120	Standard short pulse	0.2	13.48
P120	Standard short pulse	0.5	19.46
P120	Standard short pulse	1	193.24
P120	Standard short pulse	2	285.66
P120	Standard long pulse	0.2	9.17
P120	Standard long pulse	0.5	41.20
P120	Standard long pulse	1	44.74
P129	Standard long pulse	2	59.17
P120	Moses contact	0.2	19.82
P120	Moses contact	0.5	43.52
P120	Moses contact	1	38.00
P120	Moses contact	2	100.79
P120	Moses distance	0.2	15.24
P120	Moses distance	0.5	25.39
P120	Moses distance	1	169.50
P120	Moses distance	2	154.44
Prototype	Standard short pulse	0.2	3.33
Prototype	Standard short pulse	0.5	5.2
Prototype	Standard short pulse	1	12.84
Prototype	Standard short pulse	3.5	24.25
Prototype	Standard long pulse	0.2	6.75
Prototype	Standard long pulse	0.5	7.77
Prototype	Standard long pulse	1	15.88
Prototype	Standard long pulse	3.5	19.27
Prototype	Dusting	1	11.00
Prototype	Dusting	3.5	39.53
Prototype	Fragmenting	1	14.45
Prototype	Fragmenting	3.5	42.41
Soltive	Standard short pulse	0.2	28.95
Soltive	Standard short pulse	0.5	57.83
Soltive	Standard short pulse	1	112.25
Soltive	Standard short pulse	2	172.85
Soltive	Standard long pulse	0.2	42.13
Soltive	Standard long pulse	0.5	61.51
Soltive	Standard long pulse	1	62.04
Soltive	Standard long pulse	2	54.38

Table 13. Pendulum retropulsion results. Results were not recorded for two of the settings because of difficulties maintaining stone alignment.

These results were initially surprising as TFLs have been reported clinically as producing subjectively less retropulsion than Ho:YAG lasers in clinical trials [89, 129]. This pendulum data shows Soltive short pulse producing higher retropulsion speeds than all P120 modes at pulse energies of 0.2J and 0.5J, and higher retropulsion speeds than Moses contact and standard long pulse at pulse energies of 1J and 2J. Furthermore, the retropulsion speeds for the prototype laser are much lower than the other two lasers and do not increase substantially as the pulse energy is increased.

Discussion – pendulum experiments

The first point of consideration for the pendulum experiments is the technical issues with aligning the stone phantom with the laser fibre, which affected all 3 lasers, and the inconsistent retropulsion velocities which affected only the P120.

The process for attaching the strings to the cylindrical BegoStone phantoms with epoxy resulted in asymmetry in the centres of mass for the resulting pendulums. If the fibre was not precisely aligned with the centre of mass, it would result in rotational movement of the phantom – either twisting along the axis of the strings, or upwards towards the strings. This involved a significant loss of kinetic energy and therefore a corresponding drop in retropulsion speed.

The inconsistent retropulsion velocities affecting P120 appear to be a result of the phantom rebounding from the fibre tip, as shown in Figure 49. This compounds the alignment issues previously mentioned, and results in a huge range of different stone movements depending on how the phantom and fibre tip make contact. Frequently, this resulted in a large amount of rotation. As an extreme example, P120 1J Moses Distance required 5 experiments to achieve a non-rotated retropulsion motion, and the individual results are shown in Table 14 below. Although this setting is clearly capable of producing a retropulsion speed of 169.5 mm/s, the range was 15.7 - 169.5 with a mean of 49.0 mm/s and a standard deviation of 67.4 mm/s. This data is too variable to interpret using the mean.

P120 1J MD retropulsion speeds (mm/s)	15.68	20.13	23.75	169.5	16.13

Table 14. Pendulum retropulsion speeds for P120 1J Moses Distance mode.

This phenomenon was only observed with the P120, and not the Soltive or prototype lasers. Inspecting the high-speed video for the Soltive shows that the phantom only moves away from the fibre, and there is no subsequent contact. TFLs have been shown to produce much lower pressures from both vapour bubble formation and collapse [91], and this lower pressure bubble collapse appears to be insufficient to change the direction of motion of the stone phantom like is seen for P120.

Inspecting the high-speed video for the prototype laser shows very similar motion patterns to Soltive, with the phantom only moving away from the fibre. Checking the laser output pulse powers shows that the first few pulses produced by the laser appear to be much lower power than expected from the selected settings, although the Ophir power meter used did not allow for precise measurement of individual pulses. The lower pulse energies of the initial pulse are the likely explanation for the very low retropulsion speeds seen with the prototype, and it is presumed that the resulting decreased pressure gradients produced by bubble collapse are insufficient to change the stone direction.

Finally, it should be acknowledged that there is some variation in the mass of the BegoStone phantoms, and so velocity alone is not the best physical representation of the energy gained by the phantoms. A better representation of the kinetic energy gain is the change in momentum (in mg·mm/s), as calculated below.

$$\Delta\, momentum = mass \times \Delta\, velocity$$

This calculation was performed for the pendulum retropulsion data presented here, but since the variation in mass was very small relative to the variation in velocity, it did not result in any discernible difference. Since retropulsion speed is a much more intuitive (and observable) outcome than momentum, it was decided to keep speed as the primary outcome provided the variations in mass remained small.

Given the technical difficulties with the pendulum experiments, the reliance on a single (initial) laser pulse and the highly variable results, it is very difficult to draw meaningful quantitative conclusions from this data. The qualitative conclusions are that:

- P120 can produce highly variable stone retropulsion, as bubble collapse can cause the stone to rebound from the laser fibre.

- Soltive produced consistent results with a linear relationship between pulse energy and retropulsion speed, and this consistency may be related to the much longer pulse and lower peak power.
- The prototype laser produced consistent results with a linear relationship between pulse energy and retropulsion speed, but much lower speeds than expected which is likely a result of early laser pulses ramping up in power.

The linear retropulsion experiments were designed to assess a continuous sequence of pulses to overcome some of the problems experienced with the pendulum experiments.

Linear experiments

Methods

A set of linear retropulsion experiments were designed to assess the effect of a series of pulses. The same 6mm diameter cylindrical BegoStone phantoms were used, as these could be cast with a consistently flat base. These were soaked in water for 24 hours, and then placed into a water tank onto a flat 10x10cm borosilicate glass platform with the flat base in contact with the glass. The laser fibre was renewed prior to each experiment by stripping and cleaving as previously described. The phantom was aligned in contact with the laser fibre so that the direction of motion of the stone would be perpendicular to the field of view of the high-speed camera, as shown in Figure 53. An example still image is shown in Figure 54.

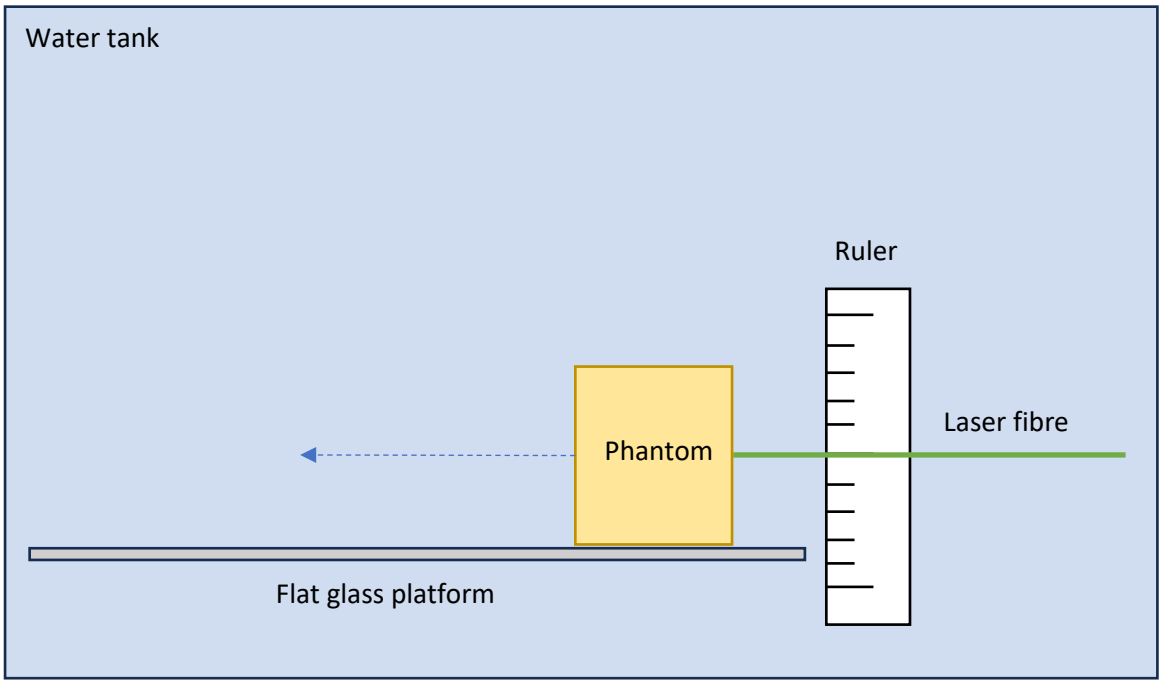


Figure 53. Schematic of retropulsion linear experimental setup, from the perspective of the high-speed camera.

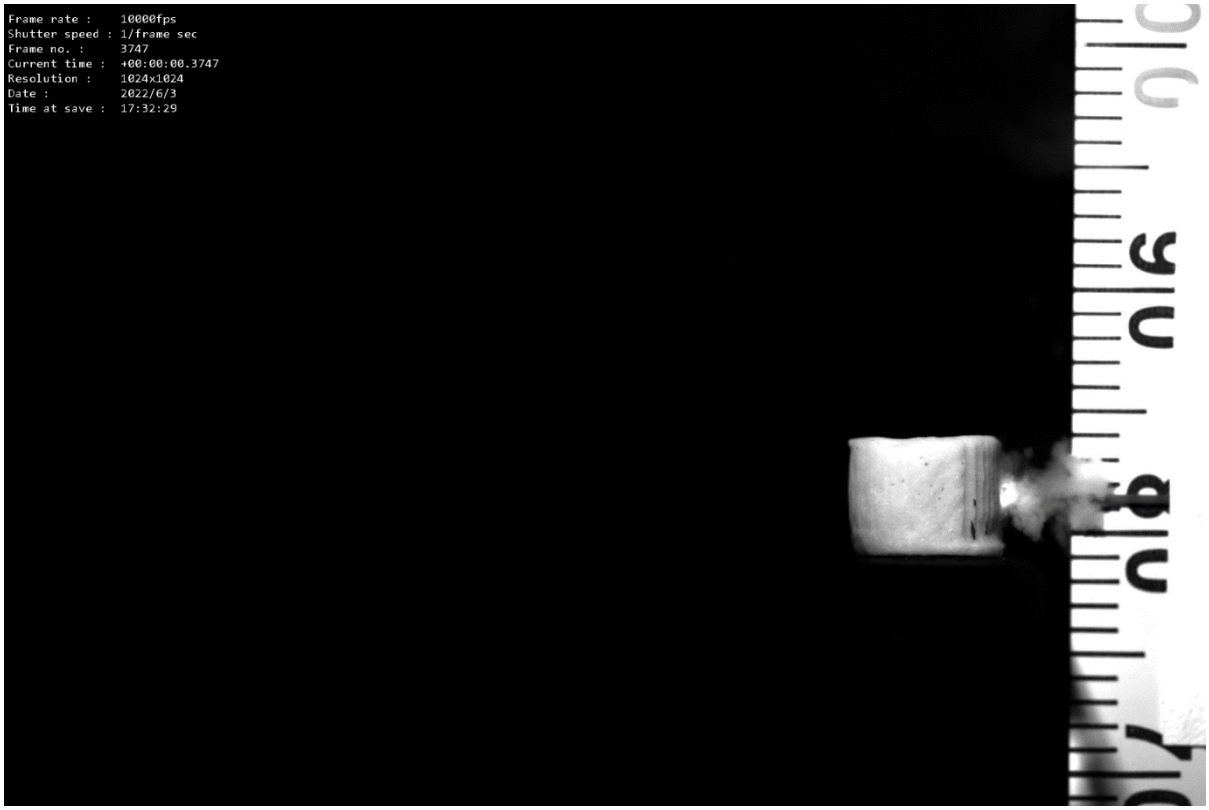


Figure 54. Still image from retropulsion linear experiment, taken from high-speed camera recordings using Soltive short pulse 2J 10Hz.

To facilitate comparisons between different lasers and settings, all laser settings used a 20W average power. This represents a medium level of power that could be applicable in both the ureter and the kidney. The combination of modes and settings is shown in Table 15. Note that 0.2J 100Hz was only

selectable for Soltive, and only pulse energies of >1J were selectable for the prototype in dusting and fragmentation modes. 5 repeats were performed for each setting.

Laser	Mode	Pulse energy (J)	Frequency (Hz)
P120	Standard short pulse	0.5	40
P120	Standard short pulse	1	20
P120	Standard short pulse	2	10
P120	Moses contact	0.5	40
P120	Moses contact	1	20
P120	Moses contact	2	10
P120	Moses distance	0.5	40
P120	Moses distance	1	20
P120	Moses distance	2	10
Soltive	Short pulse	0.2	100
Soltive	Short pulse	0.5	40
Soltive	Short pulse	1	20
Soltive	Short pulse	2	10
Prototype	Standard short pulse	0.5	40
Prototype	Standard short pulse	1	20
Prototype	Standard short pulse	2	10
Prototype	Dusting	1	20
Prototype	Dusting	2	10
Prototype	Fragmentation	1	20
Prototype	Fragmentation	2	10

Table 15. Laser settings used for retropulsion linear experiments.

The camera, lighting and video processing methods were identical to those used for the pendulum experiments. Video was recorded using a FastCam SA-X2 high-speed camera (Photron, Tokyo, Japan) at 10000 frames per second with a shutter time of 1/10000s, using a “start trigger” mode. Light was provided by a F5100 LED microscope light source (Photron, Tokyo, Japan). A ruler was attached to the laser fibre mount in the same plane for calibrating the images.

The recorded video was aligned so that laser emission starts on frame 2, and the stone motion tracked using the Python script (Python Software Foundation, DE, USA) in Appendix 4: High-speed photography of stone motion. This was then converted to measurements in millimetres by calibrating against the ruler in each video. Retropulsion velocity was calculated as a rolling average of 100 frames, i.e. 10ms intervals. The primary outcome measures were the retropulsion displacements and velocities, both for each individual experiment and aggregated averages for all 5 experimental repeats at a given setting.

Results

The masses of the BegoStone phantoms are shown in Table 16. These were consistently around 330mg and so were considered sufficiently uniform to disregard the small relative differences this would have on momentum.

Component	Min	Max	Mean	S.D.
BegoStone phantom mass (mg)	300.8	374.5	330.9	13.6

Table 16. Masses of BegoStone phantoms used for retropulsion linear experiments.

Figure 55 shows an example of the stone motion for P120 2J 5Hz standard short pulse in the first 10 frames (1ms). This demonstrates the same type of motion seen in the pendulum experiments (Figure 49) where the phantom moves away from the fibre in frames 2-4 as the vapour bubble expands, before being dragged back towards the fibre in frames 6-7. Contact is made between the phantom and the laser fibre in frames 8-9 with enough force to deflect the fibre downwards in frames 9-10. Similar frame-by-frame examination of Soltive and prototype laser videos confirms that, like the pendulum experiments, this phenomenon is only seen in P120 linear retropulsion experiments.

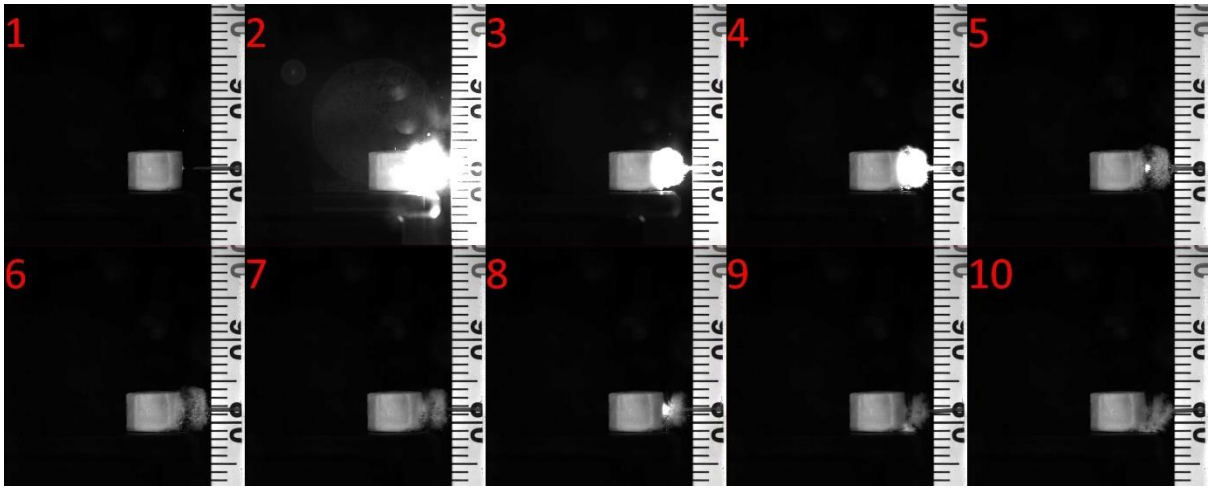


Figure 55. Linear retropulsion for P120 2J 5Hz standard short pulse, high-speed photography of first 1ms.

A set of example output results is presented for 3 example settings:

1. Soltive 0.2J 100Hz short pulse
2. P120 0.5J 40Hz Moses Distance
3. Prototype 1J 20Hz dusting

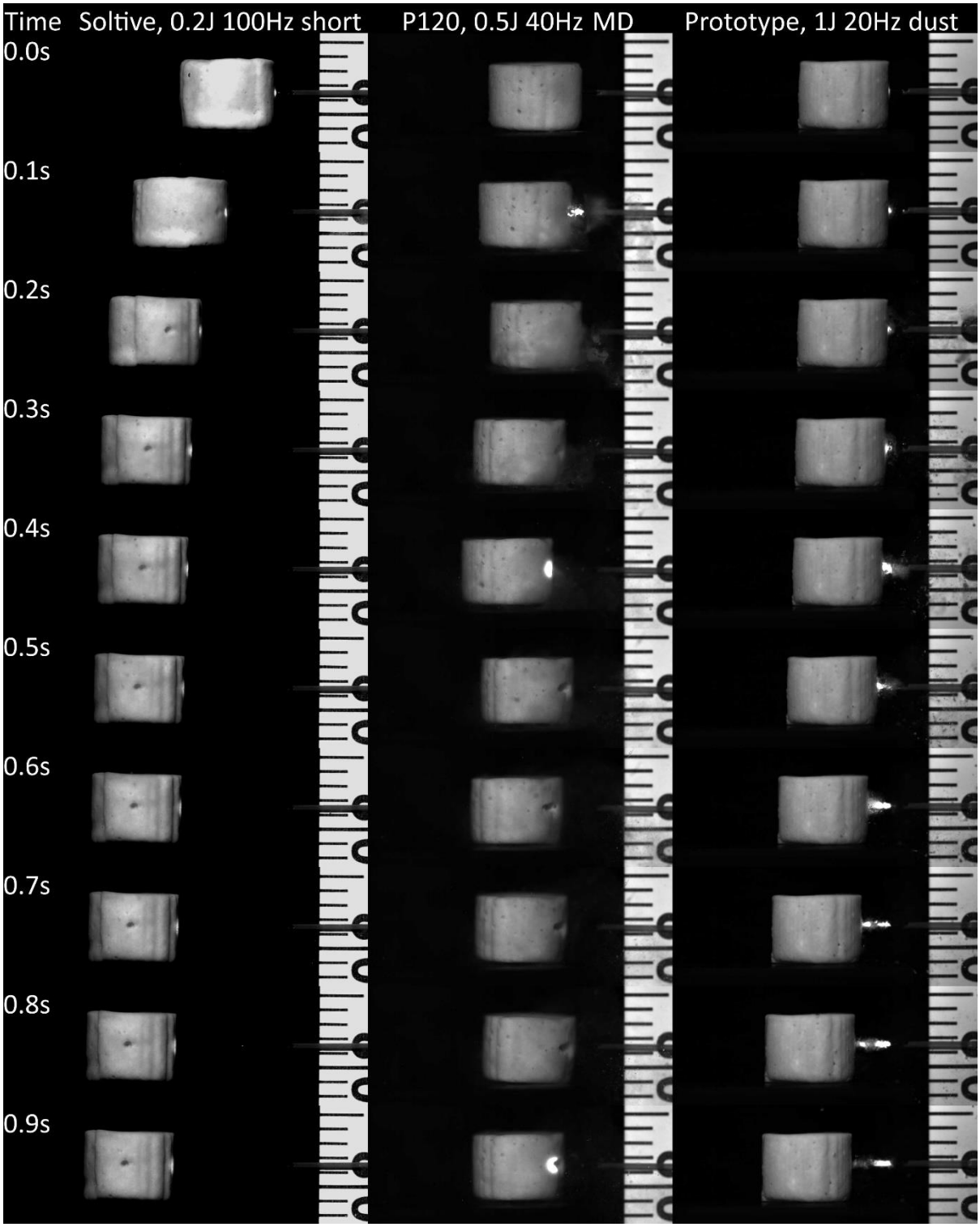


Figure 56. Linear retropulsion examples for Soltive 0.2J 100Hz short pulse, P120 0.5J 40Hz Moses Distance and prototype 1J 20Hz dusting. Still images taken from high-speed video at 100ms intervals.

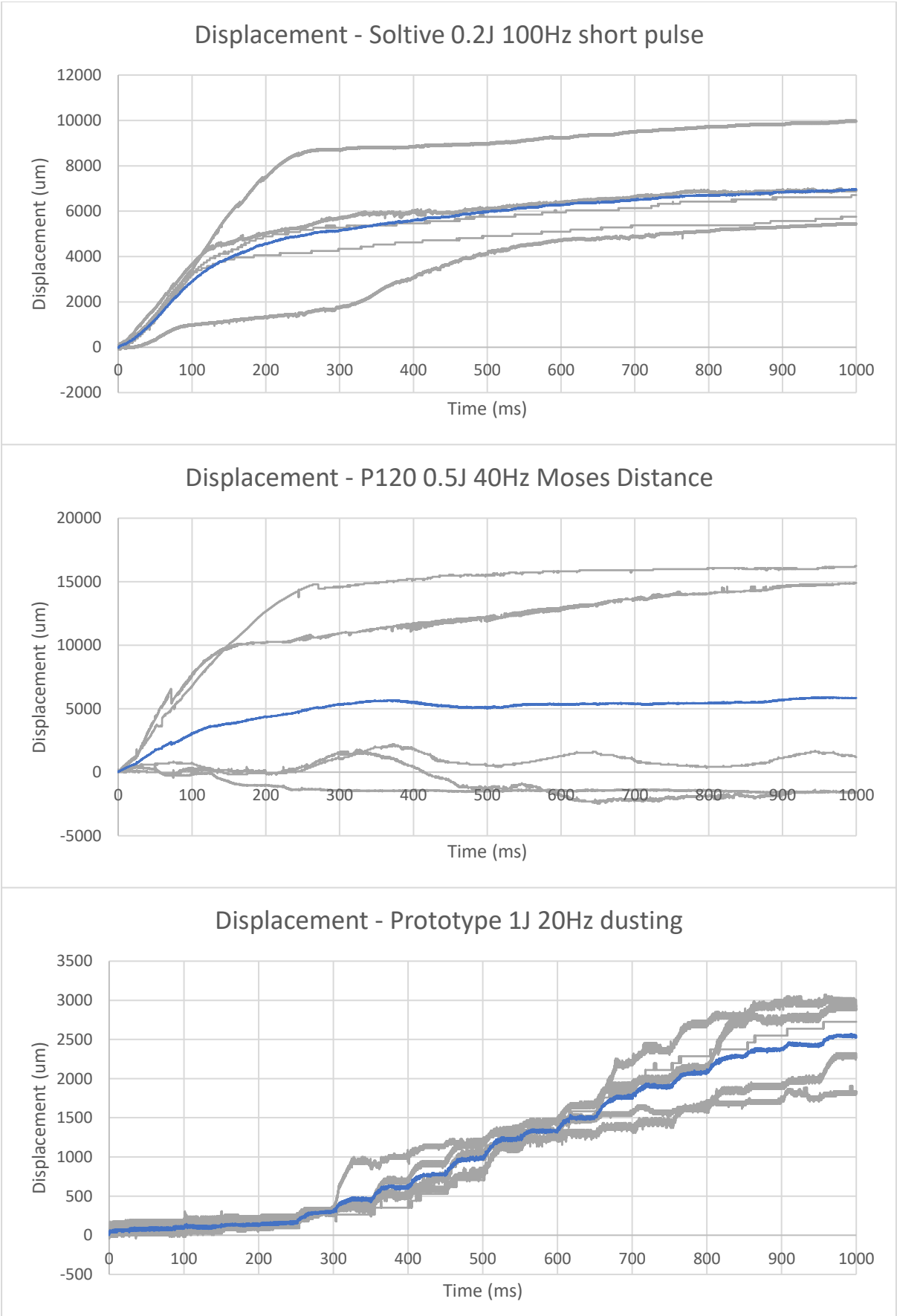


Figure 57. Linear retropulsion examples for Soltive 0.2J 100Hz, short pulse, P120 0.5J 40Hz Moses distance and prototype 1J 20Hz dusting, showing displacement against time. Each grey line is one experiment and the blue line is the average.

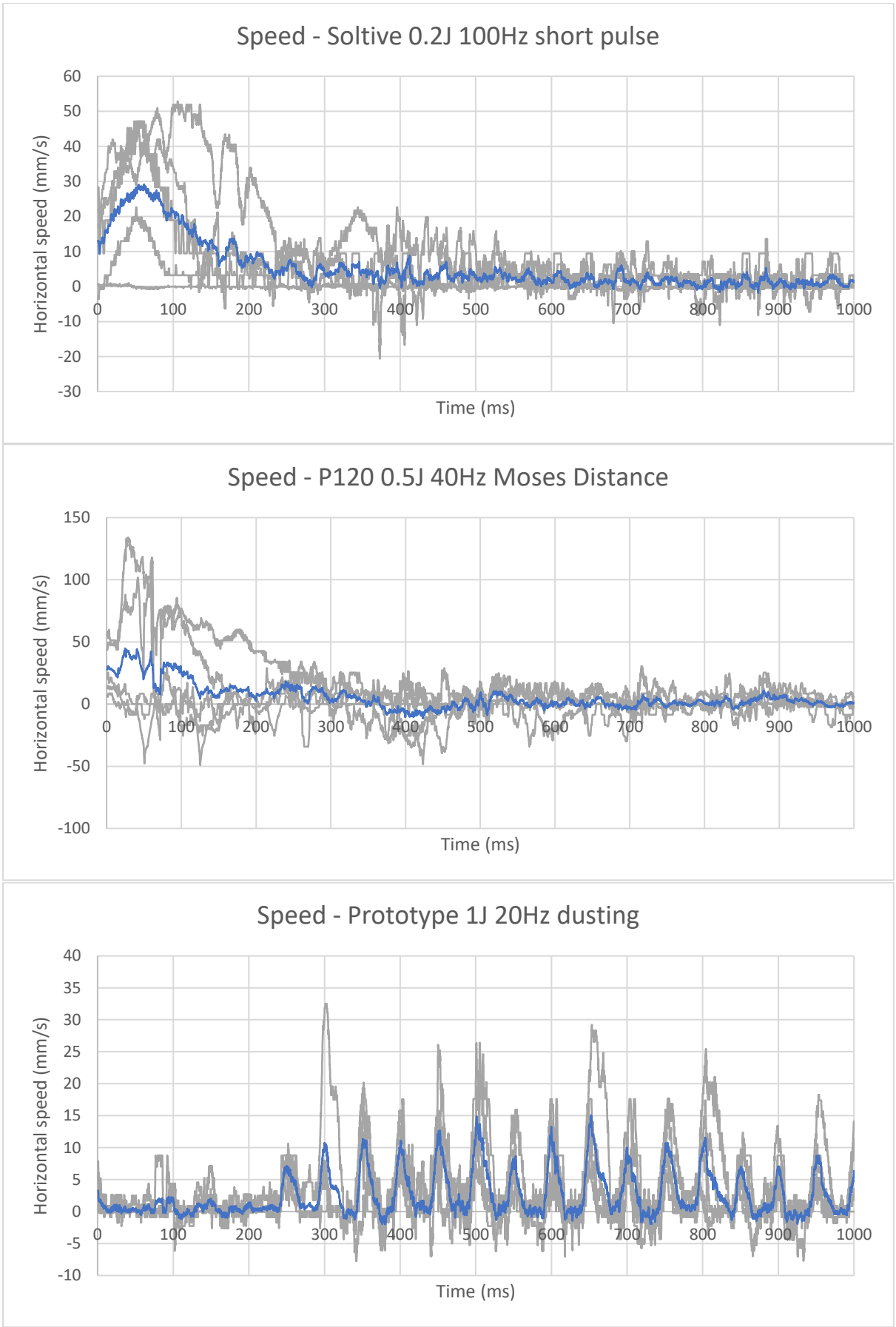


Figure 58. Linear retropulsion examples for Soltive 0.2J 100Hz, short pulse, P120 0.5J 40Hz Moses distance and prototype 1J 20Hz dusting, showing horizontal speed against time. Each grey line is one experiment and the blue line is the average.

Figure 56 shows snapshots from the high-speed video at 100ms intervals for each of the 3 laser/setting combinations. The high frequency Soltive 0.2J 100Hz setting can be seen to quickly accelerate within the first 100ms before gradually slowing down in subsequent images. This contrasts to the prototype 1J 20Hz dusting setting, which moves very slowly at first and accelerates faster after the 300ms mark. The P120 0.5J 40Hz Moses distance setting is different to both, with the stone oscillating away from and towards the laser fibre at different times. This is consistent with previously observed P120 behaviour with pressure gradients from vapour bubble collapse being sufficient to change stone direction. This series suggests that either vapour bubble expansion or collapse can predominantly affect stone motion, depending on the relative position of the stone to the fibre.

Figure 57 shows the displacement over time graphs for the same example laser settings. Each graph contains each experimental repeat (grey lines) and an aggregated average displacement at each moment in time (blue line). This illustrates the degree of consistency between experimental repeats for each setting. The Soltive 0.2J 100Hz trajectories are all fairly consistent, with a very similar trajectory in the first 100ms for 4 of the 5 repeats and similar shapes to all the curves. The same is true for the prototype 1J 20Hz dusting setting, and this graph demonstrates that there is very little motion until the 300ms mark. In contrast, the P120 0.5J 40Hz Moses distance setting results in very different types of motion in the 5 repeats, with some stones only moving away from the fibre and others oscillating away from and towards the fibre. This makes the retropulsion trajectory difficult to predict with a single curve such as the average displacement curve.

Figure 58 shows the horizontal speed graphs for the sample example laser settings (curves have been smoothed to improve visual clarity). Again, each experimental repeat is shown in grey and the aggregated average speed at each time point is shown in blue. For Soltive 0.2J 100Hz, the frequency is too high to see effects of individual pulses but almost all horizontal speeds are positive, indicating motion away from the fibre. The speeds approach 0 after around 300-500ms as the phantom moves

too far from the fibre for the pulses to reach. P120 0.5J 40Hz Moses distance is still too high frequency to clearly see individual pulses, but this demonstrates more frequent and larger negative horizontal speeds (i.e. motion towards the laser fibre). It is difficult to predict what the speed change from any given pulse will be, or even if that change will be positive or negative. Finally the prototype 1J 20Hz dusting mode clearly shows the effect of individual pulses. Early pulses in the first 300ms have almost no retropulsion effect, but subsequent pulses generate relatively uniform positive speed changes that are consistent across all 5 repeats.

Laser and mode	Energy (J)	Freq (Hz)	Phantom mass (mg)		Initial speed (mm/s)		Max speed (mm/s)		Distance (mm)	
			Mean	S.D.	Mean	S.D.	Mean	S.D.	Mean	S.D.
P120, standard short	0.5	40	334.2	8.5	24.1	23.4	61.7	30.1	2.02	5.02
P120, standard short	1	20	335.1	12.0	94.9	68.5	133.2	53.8	11.62	2.97
P120, standard short	2	10	327.7	6.8	175.5	85.2	175.5	85.2	13.09	5.67
P120, Moses contact	0.5	40	329.3	10.3	17.6	10.1	49.4	19.8	4.15	3.21
P120, Moses contact	1	20	330.1	11.2	42.0	4.6	74.8	16.1	8.66	3.24
P120, Moses contact	2	10	332.7	6.3	111.9	17.1	120.6	13.8	12.16	3.05
P120, Moses distance	0.5	40	330.9	18.2	38.3	23.0	96.2	38.4	6.28	9.49
P120, Moses distance	1	20	336.3	11.3	75.6	35.2	147.0	51.6	4.52	6.86
P120, Moses distance	2	10	329.3	16.4	111.3	44.1	120.9	34.9	7.09	5.62
Soltive, short pulse	0.2	100	333.9	15.2	25.3	7.91	48.2	9.6	7.03	1.50
Soltive, short pulse	0.5	40	331.3	9.4	39.2	15.2	46.2	12.7	5.18	1.42
Soltive, short pulse	1	20	328.4	11.4	83.7	18.2	83.7	18.2	5.39	0.99
Soltive, short pulse	2	10	347.2	15.9	193.8	39.0	193.8	39.0	10.64	3.17
Prototype, std. short	0.5	40	326.5	7.3	10.4	4.0	46.5	15.6	3.87	1.24
Prototype, std. short	1	20	324.4	3.2	19.4	4.4	52.6	18.2	5.44	1.53
Prototype, std. short	2	10	331.8	9.2	27.7	12.5	71.2	28.3	6.82	3.26
Prototype, dusting	1	20	314.1	9.2	11.8	5.2	34.2	4.4	2.72	0.34
Prototype, dusting	2	10	327.1	8.2	24.6	22.2	54.8	9.7	4.63	1.07
Prototype, fragment	1	20	312.4	8.4	14.6	11.7	34.1	7.1	3.28	1.18
Prototype, fragment	2	10	317.5	11.7	26.7	13.9	61.6	12.0	5.71	1.83

Table 17. Linear retropulsion results, including initial horizontal speed (in first 10ms), maximum horizontal speed and final displacement after 1s.

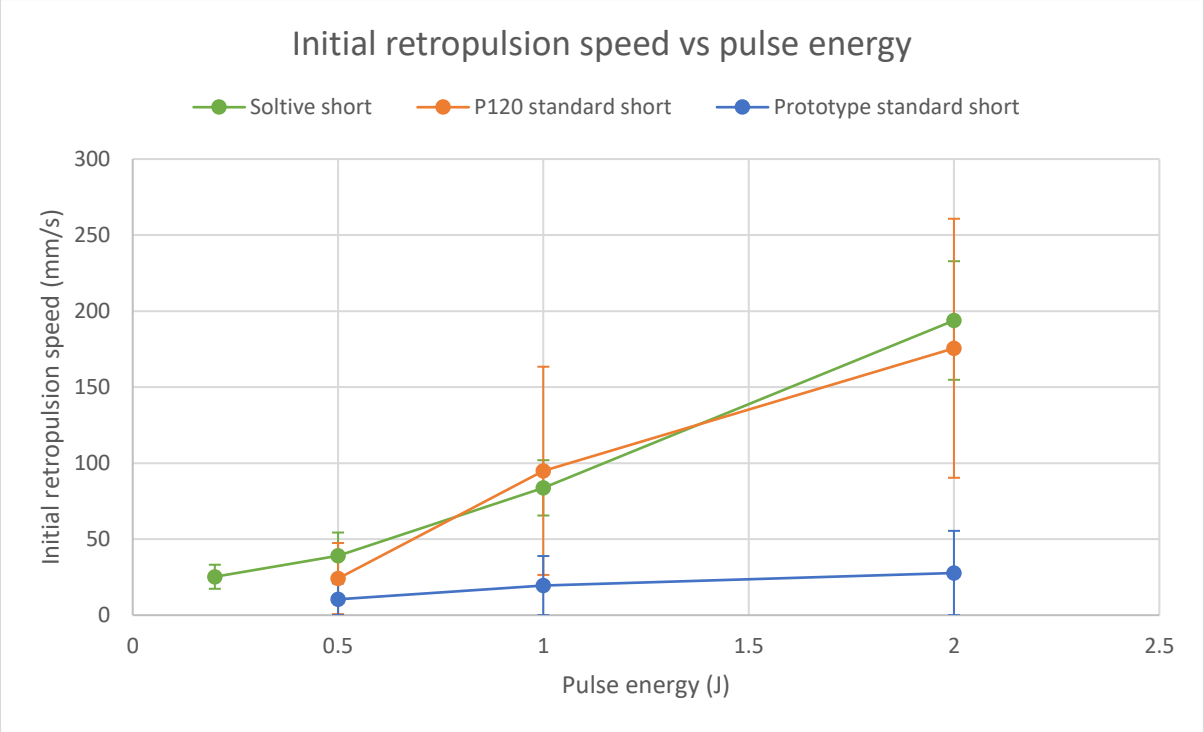


Figure 59. Linear retropulsion initial horizontal speed for all lasers in short pulse operation. Error bars indicate one standard deviation.

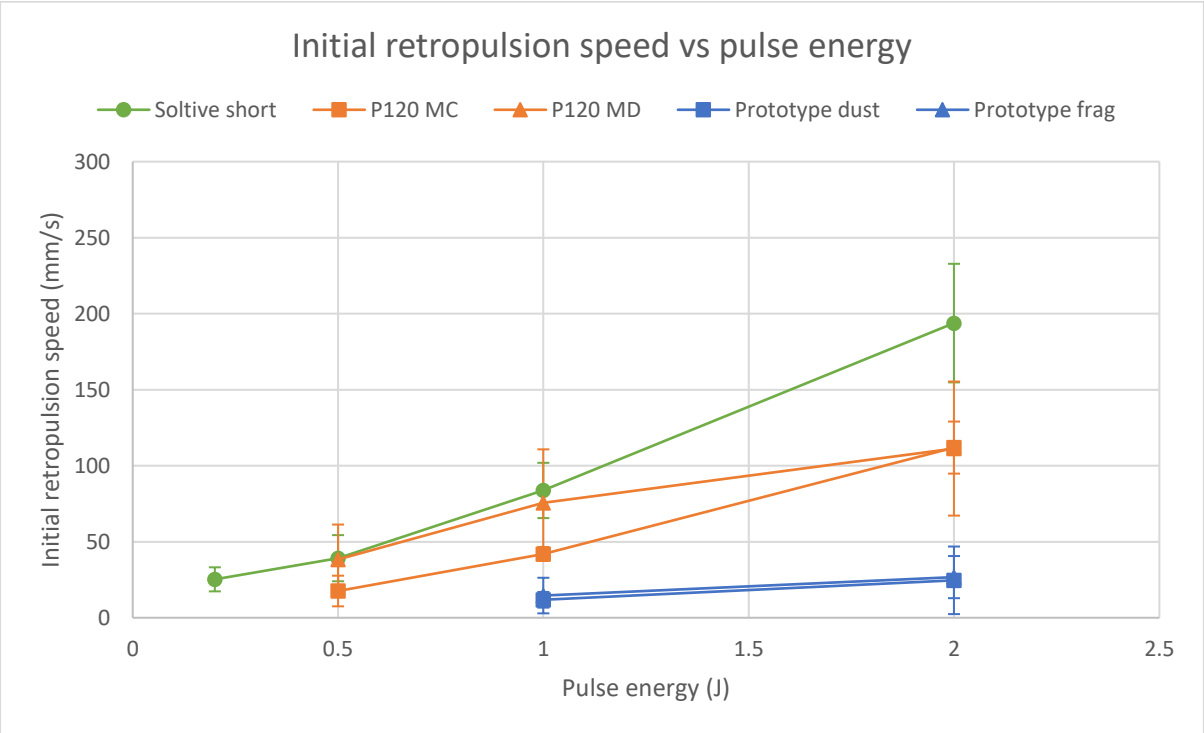


Figure 60. Linear retropulsion initial horizontal speed for all lasers in pulse modulated modes. Soltive does not have pulse modulation so the short pulse data is included for reference. Error bars indicate one standard deviation.

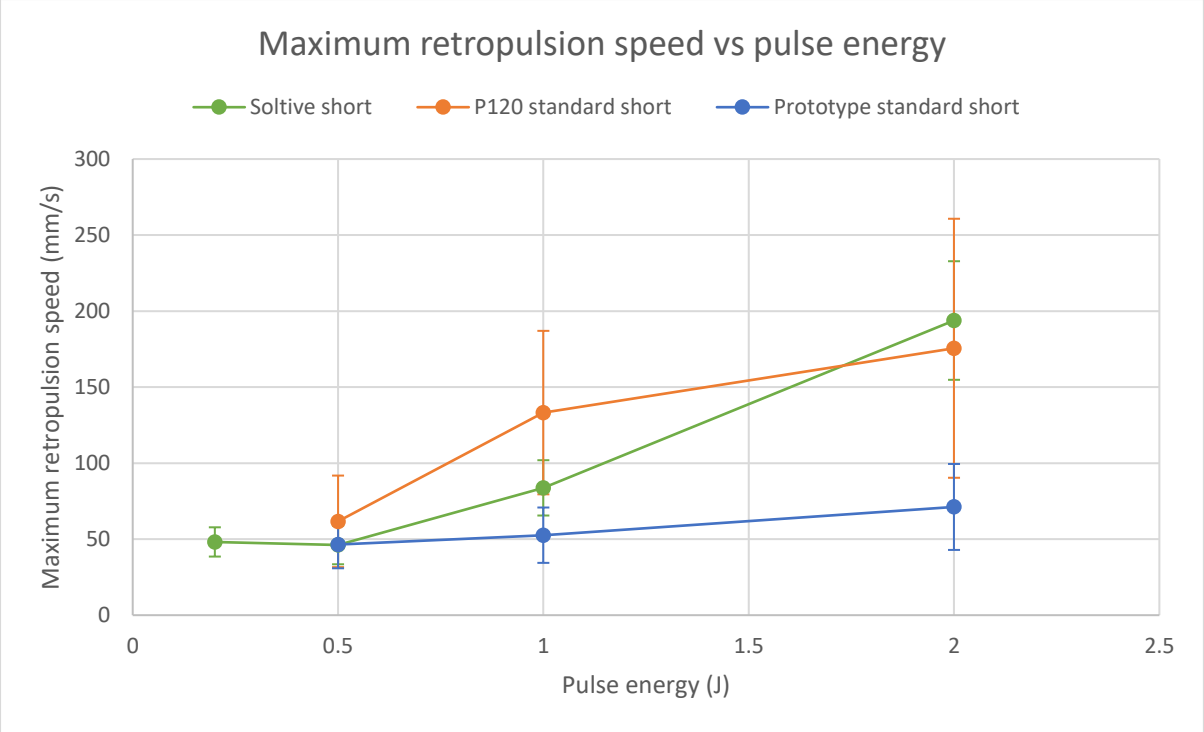


Figure 61. Linear retropulsion maximum horizontal speed for all lasers in short pulse operation. Error bars indicate one standard deviation.

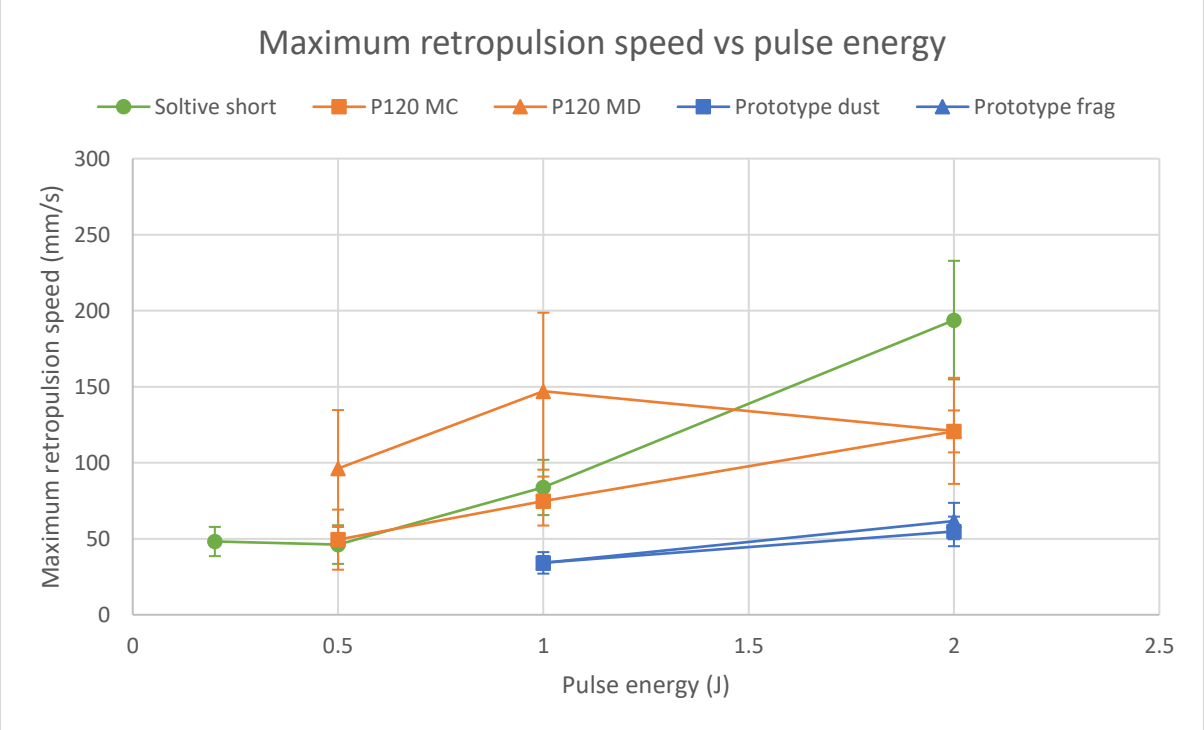


Figure 62. Linear retropulsion maximum horizontal speed for all lasers in pulse modulated modes. Soltive does not have pulse modulation so the short pulse data is included for reference. Error bars indicate one standard deviation.

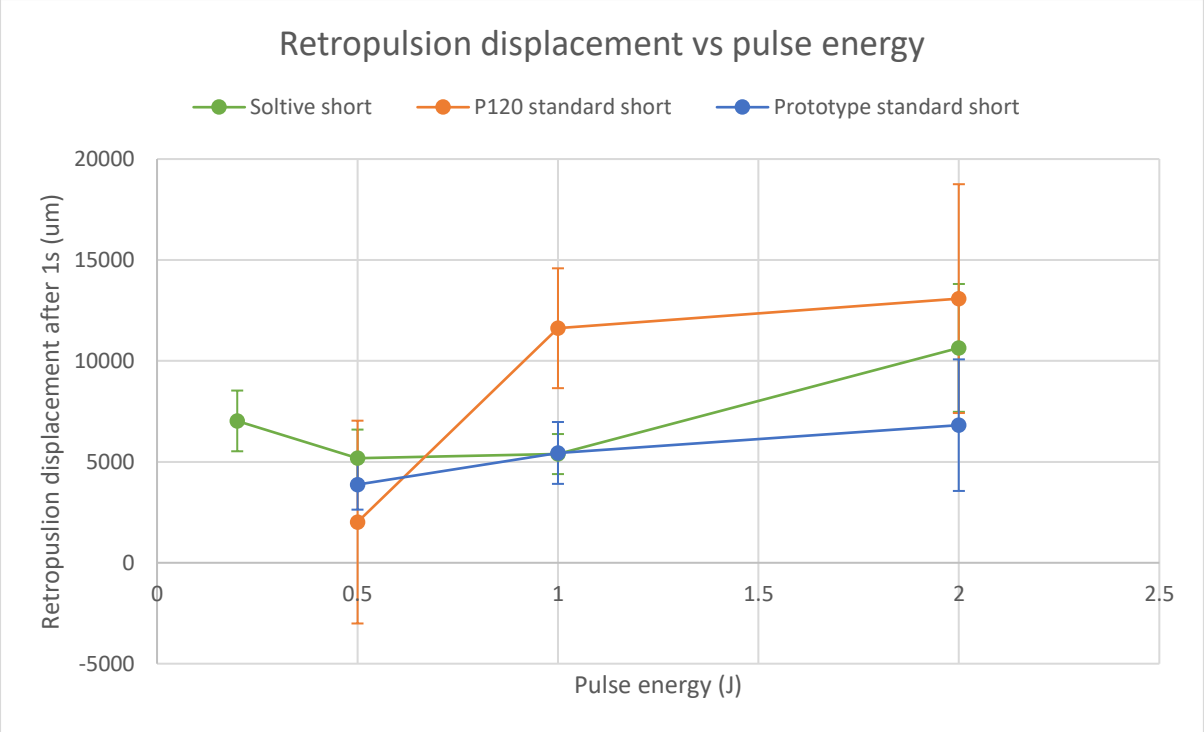


Figure 63. Linear retropulsion horizontal displacement after 1s for all lasers in short pulse operation. Error bars indicate one standard deviation.

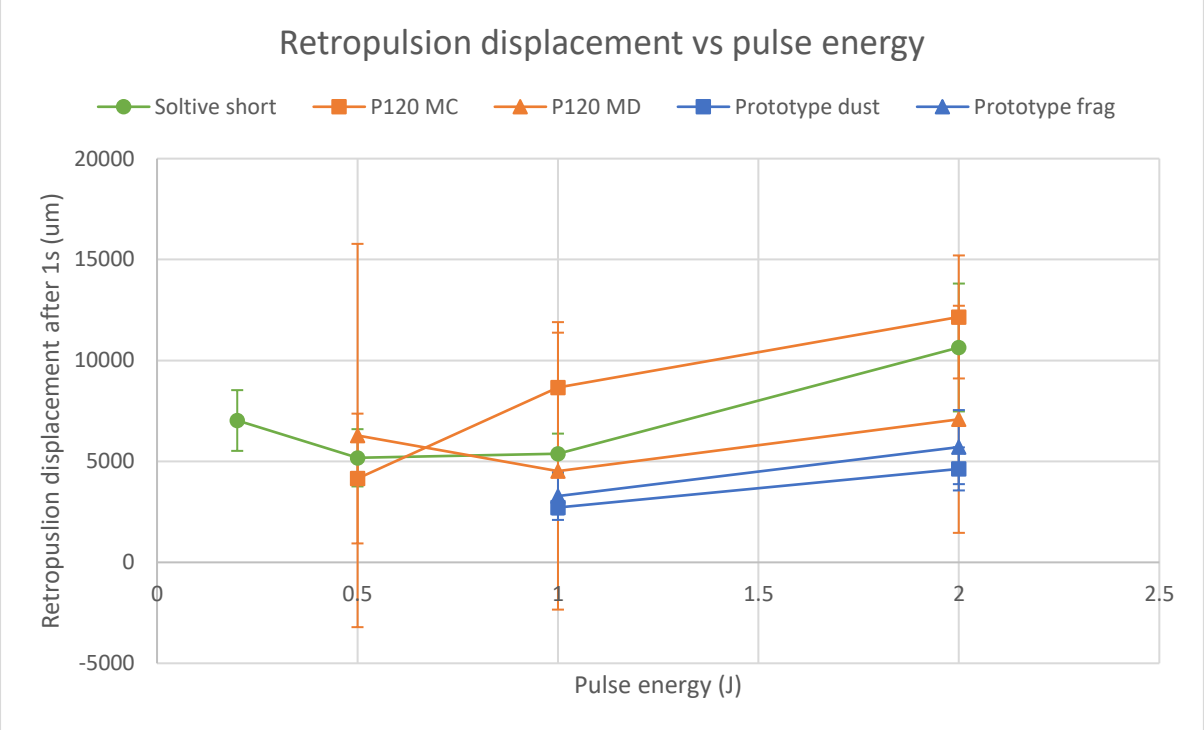


Figure 64. Linear retropulsion horizontal displacement after 1s for all lasers in pulse modulated modes. Soltive does not have pulse modulation so the short pulse data is included for reference. Error bars indicate one standard deviation.

The results for the initial retropulsion speeds (Figure 59 and Figure 60) are analogous to the results for the pendulum model. Similar to those results, both P120 and Soltive in standard short pulse mode generated relatively high initial retropulsion speeds, with very similar means. However, P120 had a much higher variance than Soltive. In pulse-modulated modes, P120 generated slightly lower initial retropulsion speeds in Moses contact and Moses distance modes than standard short pulse. The prototype had extremely low initial retropulsion speeds and this is likely due to the low initial pulse energies previously demonstrated, so it cannot be directly compared to P120 or Soltive.

Looking at the maximum retropulsion speed (Figure 61 and Figure 62), lower pulse energy/higher frequency settings result in a maximum retropulsion speed that is higher than the initial retropulsion speed. For P120 this is the case for 0.5J 40Hz and 1J 20Hz in all modes, and for Soltive this is the case for 0.2J 100Hz and 0.5J 40Hz. At these settings, subsequent pulses after the first are still able to reach the stone and accelerate it to a higher speed. As a result, the relationship between maximum retropulsion speed and pulse energy (or frequency) is not linear or otherwise easily modelled. In the cases of Moses distance, the effect of these subsequent pulses is more complex still and will be further explored later.

The final retropulsion displacement (Figure 63 and Figure 64) also does not have a straightforward linear relationship with the pulse energy. High frequency settings such as Soltive 0.2J 100Hz and P120 0.5J 40Hz MD are able to accelerate the phantom with consecutive pulses and achieve a relatively long displacement, while high pulse energy settings such as 2J 10Hz (all lasers) generate a high initial retropulsion speed with the initial pulse resulting in a lot of momentum that carries the phantom a long distance. The standard deviations are also very high relative to the actual displacements, as shown by the corresponding error bars.

Discussion

The initial retropulsion speeds seen in these linear experiments were similar to those seen during the pendulum experiments. It was somewhat unexpected to see Soltive producing similar speeds in

short pulse mode to P120 standard short pulse, given the reputation and published subjective data of TFL producing lower retropulsion than Ho:YAG lasers in clinical practice. From the physics perspective, these results appear plausible as they arise from a single pulse of equal energy from the P120 or Soltive. Since the laser fibre starts in contact with the stone phantom, it can be assumed that no energy will be absorbed by the fluid medium and the entire pulse energy E_{pulse} will reach the stone phantom. The immediate outcome will be that some amount will be reflected (and lost as heat) and the rest $E_{phantom}$ will be absorbed by the phantom. Some of this absorbed energy will directly break chemical bonds in the phantom, some will be converted into movement as kinetic energy, and the rest will heat the phantom.

$$E_{phantom} = E_{chemical} + E_{kinetic} + E_{heat}$$

While there is published data on the surface reflectivity of gypsum on infrared light, no data could be found that differentiated reflectivity at 1940nm wavelength compared to 2120nm wavelength. Nor is it well documented how much of absorbed energy goes towards breaking chemical bonds, though measurements of decomposition products suggests that the proportion is low for Ho:YAG lasers [26]. However, it is clear that if these values are comparable between Ho:YAG lasers and TFLs, the end result will be a similar amount of kinetic energy gained by the phantom from equivalent energy pulses, which would manifest experimentally as equal initial retropulsion speeds. Clinical reports comparing retropulsion in these lasers [97, 100, 101, 130, 131] do not always use matched settings between Ho:YAG lasers and TFLs, and can be complicated by other factors. The most significant of those is the difficulty in judging the distance between laser fibre and stone [124], which would have a much larger impact on TFL energy than Ho:YAG, as it the water absorption is far higher.

It is also noteworthy that clinical retropulsion comparisons are universally performed using Likert scales reported by the operating clinician, meaning that what is being compared is the subjective experience of retropulsion rather than objective measurements. This is important as the two may not directly correlate. For example, if 2 settings both produce a mean initial retropulsion speed of

100 mm/s, this objective data may be interpreted as both settings producing “equal” or “equivalent” retropulsion. However, if one laser produces a consistent 100 mm/s every time while the other laser randomly produces 0 mm/s or 200 mm/s retropulsion speeds, the subjective experience of using these lasers will likely be extremely different. This is approximately the case for Soltive short pulse 1J 20Hz when compared to P120 standard short pulse 1J 20Hz in the linear model, and it would be misleading to describe their retropulsion profiles as similar despite the mean values being very close.

These results indicated that the retropulsion generated by these lasers was more complex than could be described by a single parameter such as initial or maximum retropulsion speed, and that additional analysis was required to provide context to these speeds. Particular factors that needed to be considered were:

- A measurement was needed to quantify the variability between experimental repeats, to represent how predictable the motion would be, as this would be a factor in the subjective experience of retropulsion.
- Initial retropulsion speed and maximum retropulsion speed are both relevant to experienced retropulsion, but not sufficient on their own. For example, high retropulsion speeds are meaningless if the stone is immediately slowed or stopped by the next laser pulse before the operator experiences the motion.
- Retropulsion displacement does not correlate well with retropulsion speeds, and a low displacement can hide clinically disruptive behaviour such as highly variable motion.
- The stone phantom might still be moving at 1s, meaning that it may not represent the endpoint of stone motion.

Analysis of trajectory and variability

In order to quantify the variability of retropulsion of a given laser setting, a measurement was required that was analogous to standard deviation for a scalar variable, but which could be applied to an entire sequence of values that formed a complete stone phantom trajectory. The objective was

to enumerate how accurately the motion of the stone could be predicted by the clinician prior to firing the laser, as this is likely to have a significant effect on both the ability to mitigate the retropulsion and its subjective perception. This can be done using the residual sum of squares method, using the clinician's prediction as the model for comparison.

The residual sum of squares measures the discrepancy between a model and the actual observed data set as follows.

$$RSS = \sum_{i=1}^{n} (x_i - p_i)^2$$

Here x_i is the ith value of the observed data set and p_i is the ith value of the predicted data set. The RSS is zero if and only if the model perfectly predicts every element of the observed data set. A larger RSS indicates more deviation from observed data, i.e. a less accurate model.

The raw RSS is well suited for comparing different models of a single data set, but cannot be used to compare the accuracy of models for different data sets. This is because the value is related to both the number of data points within the set, and the value of those data points. It is easy to see that if a model for a data set produces an RSS of R_1, then if every point in the data set is duplicated (resulting in twice as many points) then the RSS doubles to $2R_1$. Similarly, if the values of each data point and model point are doubled, then the RSS increases by a factor of 2^2 to $4R_1$, even though the model describes the data set equally well in relative terms. Therefore, in order to allow comparisons between RSS values for different data sets, it must first be normalised to exclude these factors.

The normalised RSS (NRSS) is defined as follows, where n is the size of the data set (i.e. the number of frames of video), and $\bar{p}$ is the mean value of the model across all frames.

$$NRSS = \frac{RSS}{n \times \bar{p}^2}$$

The NRSS is a unitless measurement that, like the RSS, equals zero if and only if the model perfectly predicts every element of the observed data set, but which can also be used to compare the

goodness-of-fit of models for different data sets. The two examples in the previous paragraph, with twice as many points (but an equally good fit) and with the values doubled (but an equally good relative fit) would result in the same NRSS as the original data set.

The NRSS makes it possible to quantify the variability of stone phantom trajectories by using the mean trajectory (shown in blue in Figure 57) as the model. A laser setting that produces consistent trajectories will result in a mean trajectory that accurately models each experimental trajectory, and hence NRSS values close to zero. The more inconsistent the experimental trajectories, the more they will differ from the mean trajectory and the larger the NRSS will be. The NRSS can therefore be thought of as analogous to the coefficient of variation for a scalar variable (which is S.D./mean) but applied to the entire set of data points that make up a stone phantom trajectory. It reports the extent to which experimental outcomes vary, but it is agnostic to when those differences occur.

Illustrative examples of the NRSS are shown in Figure 65. These are the same data sets presented in Figure 57. The prototype laser 1J 20Hz dusting setting has very consistent stone phantom trajectories that are well described by the mean trajectory (in blue), and this results in a low NRSS value of 0.011. In other words, an experienced clinician could expect the stone trajectory to closely match the mean trajectory prior to firing, and adjust accordingly.

The Soltive 0.2J 100Hz short pulse setting also produces relatively consistent trajectories, especially at the start. Although the shapes of the trajectories are all similar, the values differ as some travel further than others, and this results in a higher (but still relatively low) NRSS of 0.058. Conversely, the P120 0.5J 40Hz Moses distance setting produces widely divergent trajectories, so the mean trajectory does not describe any of the observed trajectories well. This produces a very high NRSS of 1.340, meaning that the motion is extremely variable. An experienced clinician might know the range of possible retropulsion trajectories, but still would be unable to accurately predict the actual stone motion on any given experiment. This highly variable retropulsion is very difficult to mitigate.

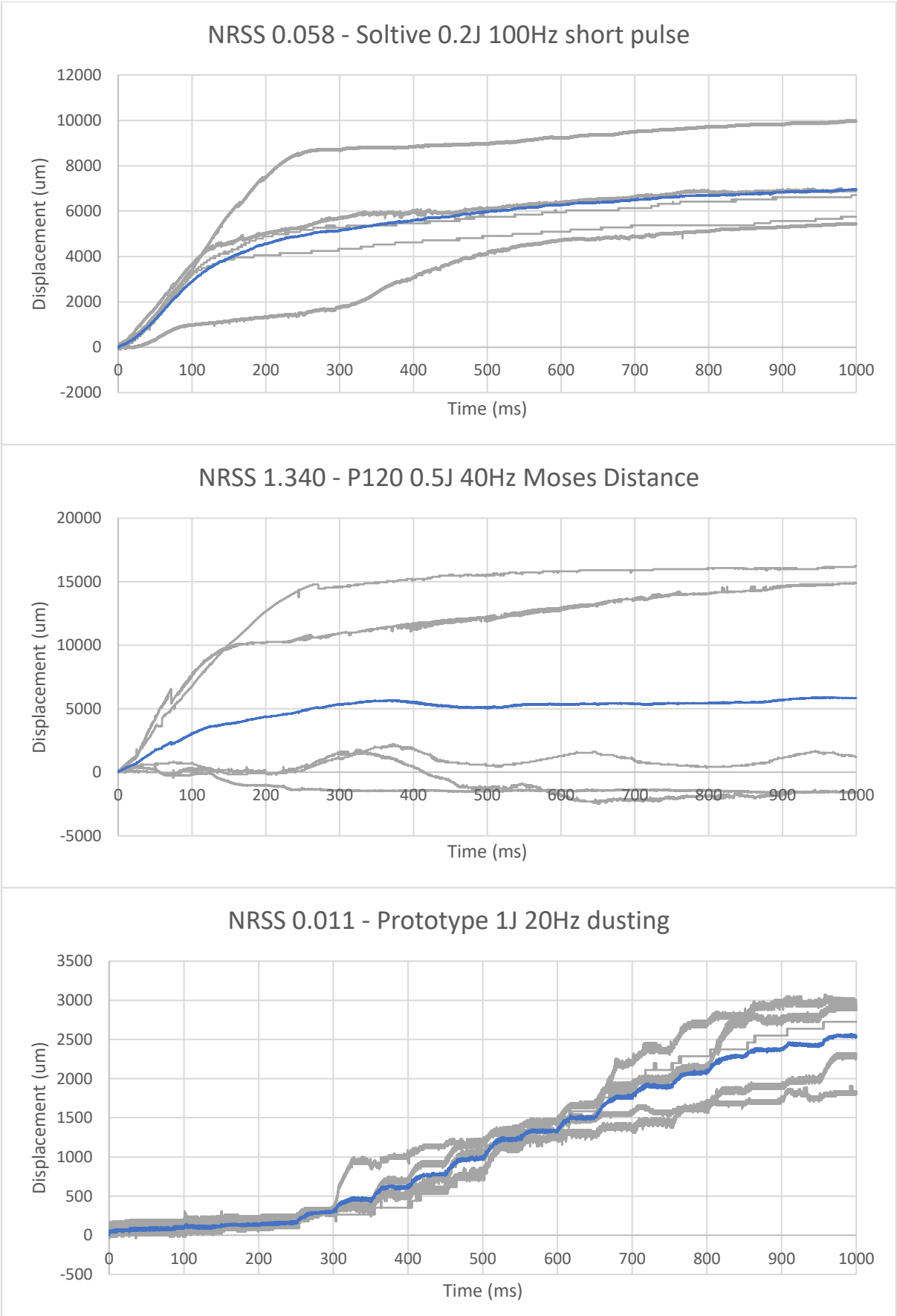


Figure 65. Linear retropulsion examples for Soltive 0.2J 100Hz, short pulse, P120 0.5J 40Hz Moses distance and prototype 1J 20Hz dusting, showing displacement against time with the calculated average NRSS values

Laser and mode	Energy (J)	Freq (Hz)	Initial speed (mm/s) Mean	Initial speed (mm/s) S.D.	Max speed (mm/s) Mean	Max speed (mm/s) S.D.	Distance (mm) Mean	Distance (mm) S.D.	NRSS
P120, standard short	0.5	40	24.1	23.4	61.7	30.1	2.02	5.02	2.445
P120, standard short	1	20	94.9	68.5	133.2	53.8	11.62	2.97	0.152
P120, standard short	2	10	175.5	85.2	175.5	85.2	13.09	5.67	0.096
P120, Moses contact	0.5	40	17.6	10.1	49.4	19.8	4.15	3.21	0.389
P120, Moses contact	1	20	42.0	4.6	74.8	16.1	8.66	3.24	0.070
P120, Moses contact	2	10	111.9	17.1	120.6	13.8	12.16	3.05	0.023
P120, Moses distance	0.5	40	38.3	23.0	96.2	38.4	6.28	9.49	1.340
P120, Moses distance	1	20	75.6	35.2	147.0	51.6	4.52	6.86	1.585
P120, Moses distance	2	10	111.3	44.1	120.9	34.9	7.09	5.62	0.372
Soltive, short pulse	0.2	100	25.3	7.91	48.2	9.6	7.03	1.50	0.058
Soltive, short pulse	0.5	40	39.2	15.2	46.2	12.7	5.18	1.42	0.036
Soltive, short pulse	1	20	83.7	18.2	83.7	18.2	5.39	0.99	0.025
Soltive, short pulse	2	10	193.8	39.0	193.8	39.0	10.64	3.17	0.062
Prototype, std. short	0.5	40	10.4	4.0	46.5	15.6	3.87	1.24	0.036
Prototype, std. short	1	20	19.4	4.4	52.6	18.2	5.44	1.53	0.033
Prototype, std. short	2	10	27.7	12.5	71.2	28.3	6.82	3.26	0.089
Prototype, dusting	1	20	11.8	5.2	34.2	4.4	2.72	0.34	0.011
Prototype, dusting	2	10	24.6	22.2	54.8	9.7	4.63	1.07	0.052
Prototype, fragment	1	20	14.6	11.7	34.1	7.1	3.28	1.18	0.032
Prototype, fragment	2	10	26.7	13.9	61.6	12.0	5.71	1.83	0.024

Table 18. Linear retropulsion results, average NRSS values. Other results (initial horizontal speed (in first 10ms), maximum horizontal speed and final displacement after 1s) are repeated for reference.

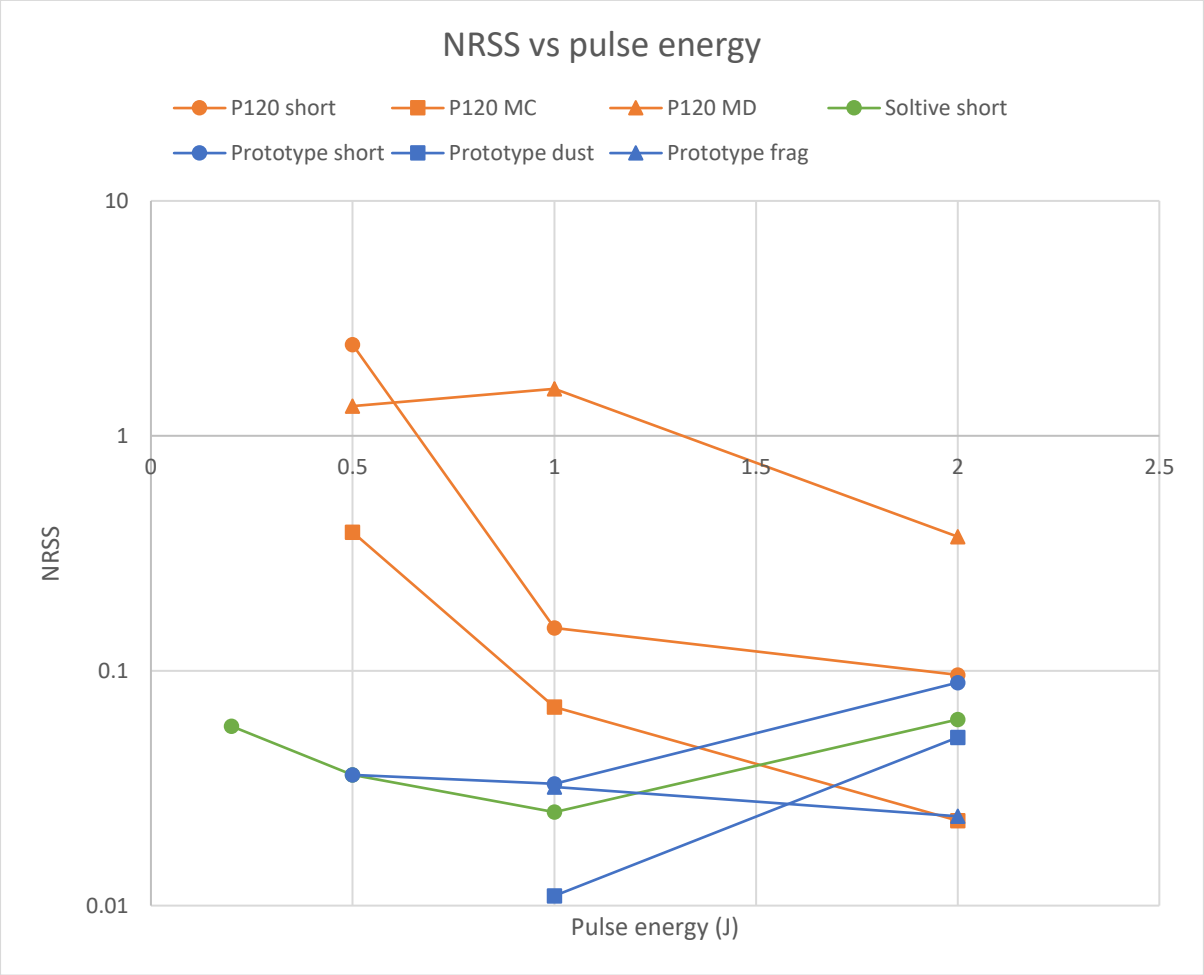


Figure 66. Linear retropulsion results, average NRSS values. The y-axis is presented on a logarithmic scale for visual clarity.

The calculated average NRSS values for each laser and setting combination in the linear experiments is presented in Table 18, and the relationship with pulse energy in Figure 66. For P120, it appears that higher frequency settings (0.5J 40Hz and 1J 20Hz) result in higher variability in all firing modes compared to 2J 10Hz, and the variability at 0.5J 40Hz is extremely high in all modes. The pulse-modulated modes also have very different effects, with Moses contact reducing variability compared to standard short pulse at all settings but Moses distance appearing to increase overall variability (except at 0.5J 40Hz, where variability is similarly extremely high in both short pulse and Moses distance modes).

In comparison, Soltive has low variability (NRSS < 0.062) at all settings. With the exception of 2J 10Hz compared to P120 standard short pulse, all other Soltive settings had lower variability than equivalent P120 settings, and in most cases the difference was very large.

The prototype laser also has low variability (NRSS < 0.089) at most settings, similar to Soltive. As before, it should be kept in mind that the initial pulses from the prototype appear to deliver lower energy than expected before ramping up to the selected value, which will have implications for ablation efficacy.

Results with NRSS

The same linear retropulsion results are now presented with the context of the accompanying NRSS to quantify the variability of the setting, in Figure 67, Figure 68 and Figure 69. Note that while both the error bars (one standard deviation each) and the NRSS quantify variability, the standard deviation only captures variability of the specific measured parameter while the NRSS captures all variability across the retropulsion trajectory. It is possible that two phantoms might have different trajectories but the same initial speed, maximum speed and position at 1s, resulting in low standard deviations. The difference would then only be measurable via the NRSS.

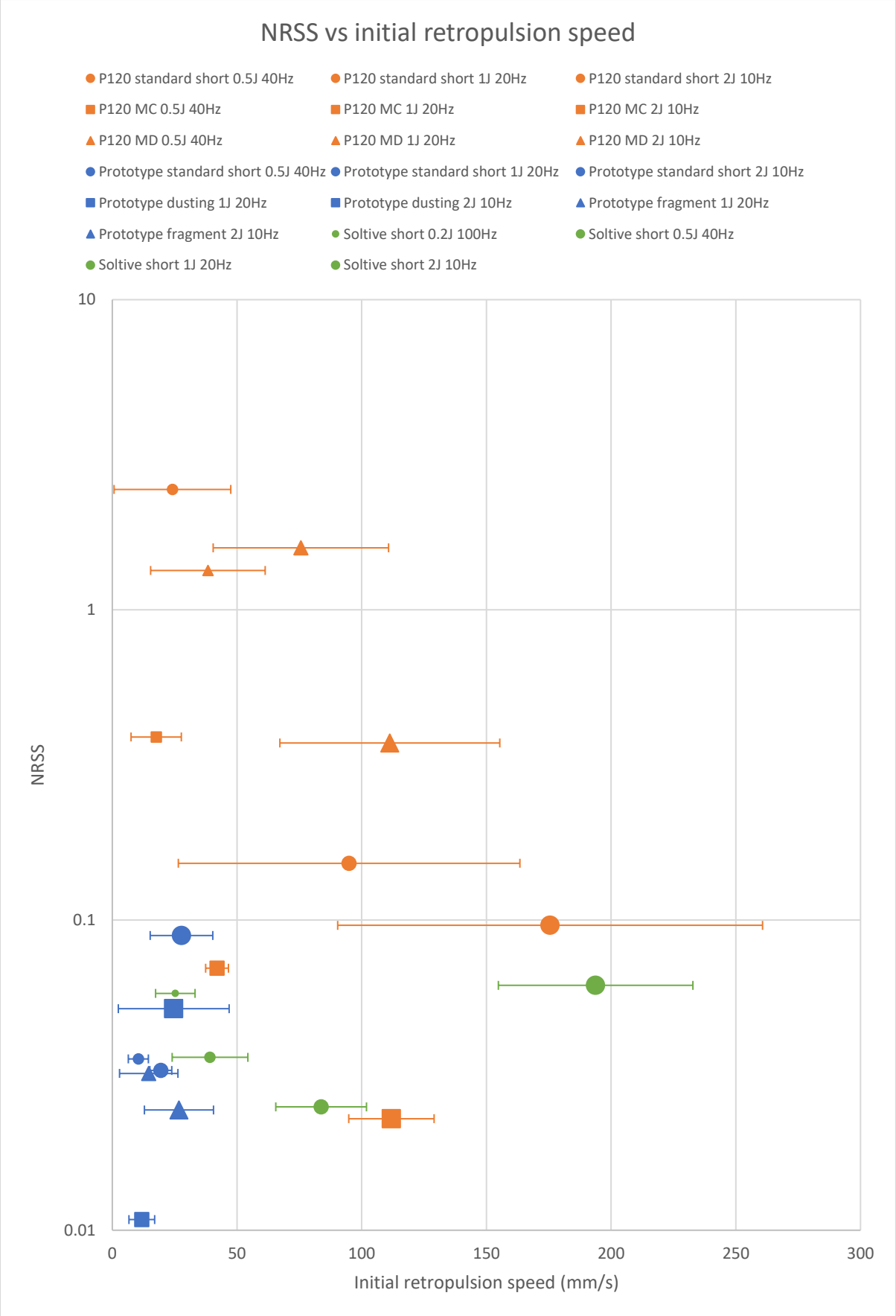


Figure 67. Linear retropulsion, NRSS vs initial horizontal speed for all lasers. The size of the data point indicates the pulse energy, with the largest mark corresponding to 2J pulse energy. Error bars indicate one standard deviation.

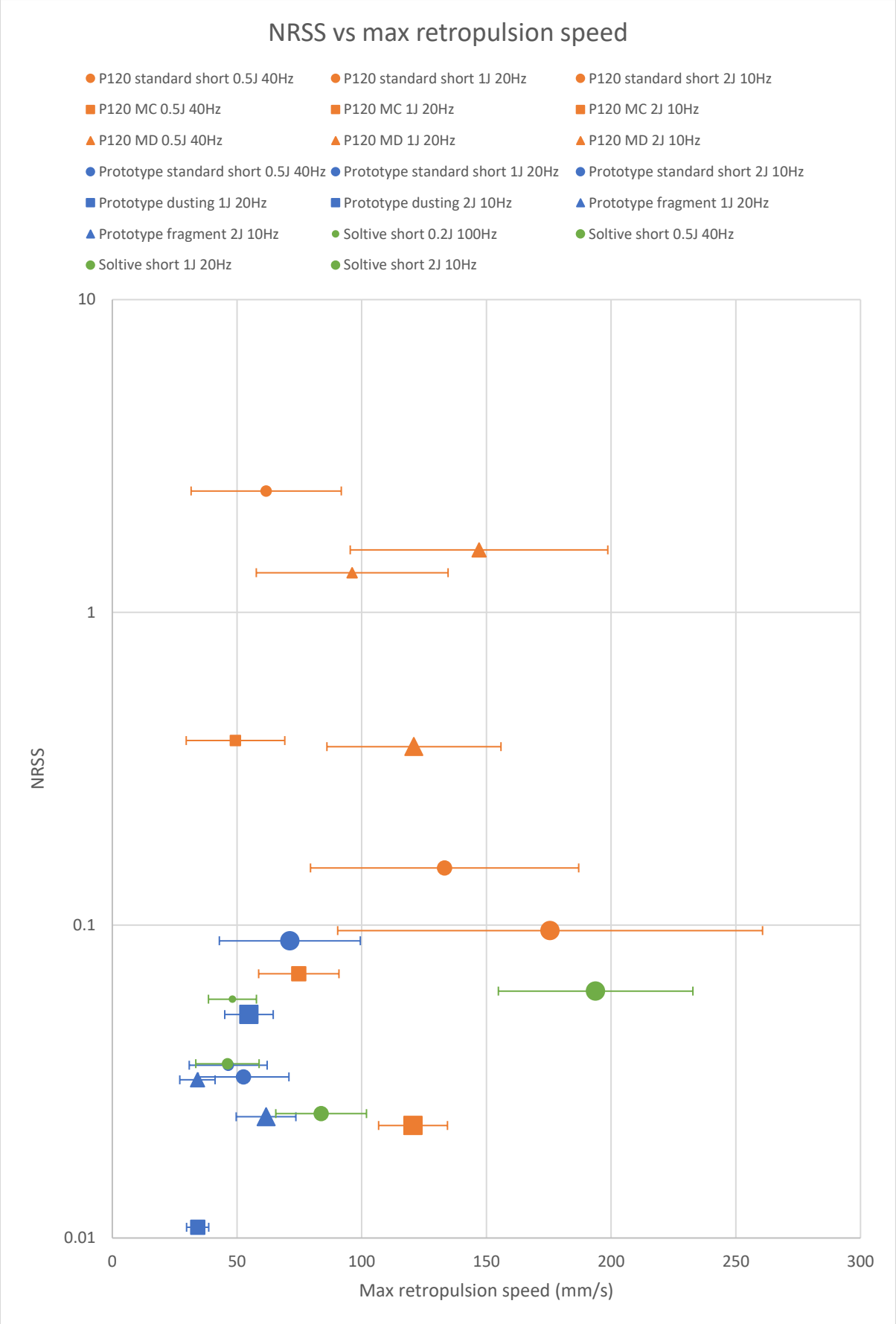


Figure 68. Linear retropulsion, NRSS vs maximum horizontal speed for all lasers. The size of the data point indicates the pulse energy, with the largest mark corresponding to 2J pulse energy. Error bars indicate one standard deviation.

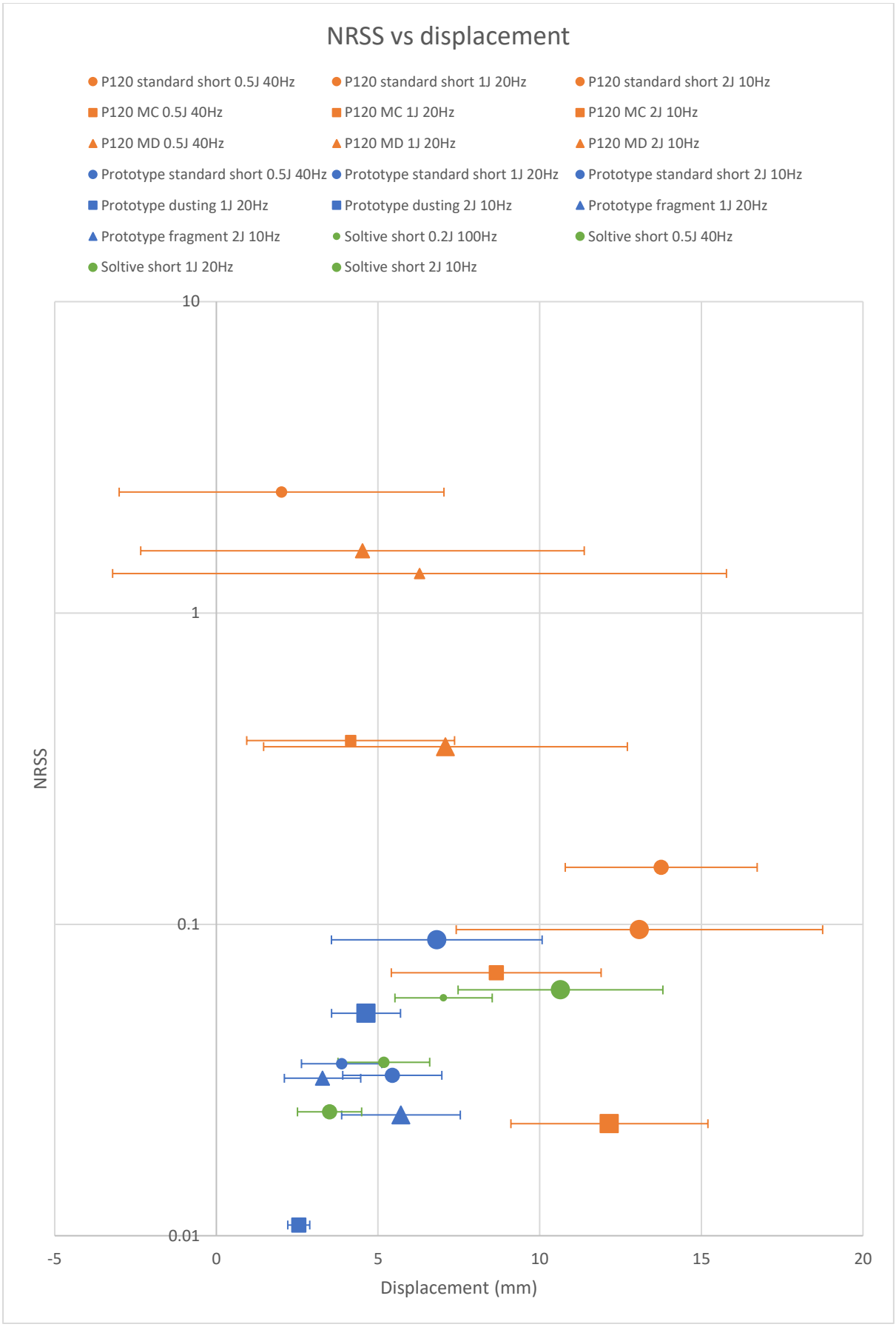


Figure 69. Linear retropulsion, NRSS vs horizontal displacement after 1s. The size of the data point indicates the pulse energy, with the largest mark corresponding to 2J pulse energy. Error bars indicate one standard deviation.

It can now be seen clearly that although P120 and Soltive standard short pulse produced similar initial retropulsion speeds, the P120 results had much higher variability. Both the variability and initial speed of P120 standard short pulse were reduced when changing to Moses contact mode. Moses distance mode reduced the initial speed but did not reduce variability. The same is seen for maximum retropulsion speeds, as per previous analysis.

Looking at the horizontal displacement, the P120 settings can be divided into two types. All 2J 10Hz settings plus 1J 20Hz standard short pulse produced large displacements which are relatively consistent, with a low or intermediate NRSS. Meanwhile, all P120 0.5J 40Hz settings plus 1J 20Hz in Moses contact/Distance modes produced extremely variable trajectories, with high variances in the endpoint. The exception is 1J 20Hz Moses contact, which produced highly variable trajectories but a relatively consistent displacement at 1s. In contrast, all Soltive settings produced consistent trajectories (low NRSS) with a consistent displacement at 1s (low standard deviations).

Conclusions

There appears to be an approximately linear relationship between initial retropulsion speed and pulse energy for all lasers. The magnitude of this initial speed seems to depend on the pulse energy rather than the laser type, which would suggest a similar proportion of laser light energy is converted to kinetic energy for both Ho:YAG and TFLs. Pulse-modulated P120 modes result in a lower average initial retropulsion speed than standard short pulse, which may be due to the first subpulse (when the stone is in contact) only delivering a proportion of the total pulse energy. Maximum retropulsion speed is not as clearly related to pulse energy, as lower pulse energy/higher frequency settings can result in subsequent pulses accelerating the stone above the initial retropulsion speed. It is further complicated by laser settings that can cause the stone to move towards the fibre. This has been reported in literature for both Ho:YAG lasers and TFLs [132] but only observed here in P120 standard short pulse and Moses distance settings. This limits the application of retropulsion speeds alone to compare retropulsion.

Stone displacement was extremely variable and did not appear to correlate well with pulse energy or retropulsion speeds (partly because of the movement towards the fibre for some P120 settings). While this is the outcome that will be most directly observed by a clinician, it is also limited by the fact that many stone phantoms were not yet stationary at the 1s limit of the high-speed video. It should also be kept in mind that these experiments were designed in a low friction environment to minimize variance and exaggerate differences, so these displacements are unlikely to be observed when friction from urothelium and fluid dynamics from a constrained space are in play. Follow-up experiments may introduce these fluid dynamics aspects by performing similar experiments within a 3D space that models a human kidney collecting system, with fluid flow to simulate irrigation through a ureteroscope.

Considering individual lasers, the P120 demonstrated more variable retropulsion outcomes than both Soltive and prototype lasers, both in terms of variance of the individual parameters being measured and in terms of higher NRSS values when evaluating retropulsion trajectories. Both variance and NRSS were reduced when switching from standard short pulse to Moses contact mode, and this setting appears to result in more consistent, repeatable retropulsion. Switching from standard short pulse to Moses distance resulted in slightly lower variances in initial/maximum speeds and displacement, but more variable overall trajectories as calculated by NRSS. This setting may be more suited to techniques such as popdusting, where inconsistent retropulsion directions and speeds may be beneficial.

The Soltive demonstrated consistent retropulsion outcomes at all settings. The variance of individual parameters was lower than P120 standard short pulse or Moses distance modes, and similar to Moses contact mode. The variability of trajectories via NRSS was lower than all P120 settings. This consistency makes the retropulsion behaviour of Soltive very easy to predict at all settings tested, and may contribute to an improved subjective experience of retropulsion as the clinician is able to compensate for retropulsion with a high degree of accuracy.

The prototype laser also demonstrated consistent retropulsion at all settings, with low variance of individual parameters and low NRSS values. However, this is in the context of trajectories and pulse energy measurements that suggest that the first few laser pulses are significantly lower power than expected, so the results cannot be directly compared to P120 and Soltive. It was not possible to prove in these experiments if the expected energy was achieved by 1s or not. This reduced power will inevitably have a corresponding effect on reduced the ablation efficacy. It is not known if this behaviour is by design – however, the effect on retropulsion is nevertheless interesting as it results in low absolute measurements of retropulsion with low variability. There is therefore a potential clinical use case for lasers with this effect, if it is desirable to minimise retropulsion even at the cost of some ablation efficacy.

Measuring stone retropulsion is a complex task. Easily computed, objective measurements such as retropulsion speed and displacement fail to capture differences in retropulsion trajectories, even when combined. The only complete data set that describes a stone's retropulsion is the complete video of the trajectory, and while this can be translated to displacement and velocity over time graphs without information loss, it is not feasible to compare these graphs across laser settings.

The combination of retropulsion speeds, displacement and NRSS allows a more comprehensive objective description of retropulsion in a way that allows comparison of different lasers and settings, by also quantifying variability. However, this inevitably results in some loss of information. Based on the data presented here, two laser settings with similar initial/maximum retropulsion speeds, displacements and NRSS appear to produce similar looking and similarly consistent retropulsion trajectories. This is most clearly seen when comparing Soltive short pulse to the prototype laser standard short pulse settings.

The NRSS value is important in differentiating laser settings that produce similar speeds/displacement but with different levels of variability. This is most clearly seen when

comparing P120 standard short pulse with Soltive short pulse, where the retropulsion speeds appear similar but the NRSS demonstrates the massive difference in variability.

This combination of initial retropulsion speed, maximum retropulsion, displacement and NRSS is therefore proposed as a minimum set of objective measurements to adequately describe laser stone retropulsion. There are no assumptions made on how these measurements translate to the clinical, subjective experience of retropulsion – it is presumed that settings with similar objective measurements result in similar subjective experiences of retropulsion, but this needs to be assessed in future work. This would involve simultaneous assessment of both objective (via high-speed video) and subjective (via clinician reported experience) aspects of retropulsion, to allow for correlation between the two. The natural follow-up to these experiments would be to establish this correlation in vitro, by adding clinicians' subjective experiences of retropulsion for each setting.

These experiments are limited by the starting conditions discussed in the introduction to facilitate reproducibility.

- The stone phantom is a regular, cylindrical BegoStone phantom instead of an actual stone.
- Friction is minimised by using a flat glass platform with no physical constraints to stone motion.
- The experiments are performed in the centre of a large tank, so any fluid dynamics of restricted flow are not considered.

Future experiments may attempt to remove individual limitations, but given the high degree of variation observed in this section and the complex interactions between each factor, it may be preferable to eliminate as many as possible simultaneously by using actual stones in an anatomical kidney model. Such models based on CT scans of real kidneys are already available commercially, although the materials used are often selected to match compliance of the kidney rather than the friction coefficients of urothelium. It would then be necessary to modify the model with a transparent surface to film video and obtain objective data as well as subjective.

5. Particle size

Introduction

The final component of laser lithotripsy is the nature of the dust, particles and fragments produced by stone destruction. The clinical interest in this outcome is that it is presumed (although not proven) that smaller particles are more likely to pass out of the kidney spontaneously than larger particles.

There is evidence that smaller stones/stone fragments <4mm [133] are more likely to pass spontaneously in clinical settings than larger fragments. Evidence for the behaviour of smaller fragments is scant and inconclusive, and clinical evidence for <1mm particles is essentially non-existent. This is presumably because of imaging-related limitations; computed tomography (CT) scans typically use slices ranging from 0.3mm to 2mm apart, and <1mm particles would not be detected reliably on even the smallest of the slices. Many clinical trials use ultrasound or roentgenography instead of CT scans, which are even less reliably at detecting smaller stones. Therefore, much of the assumption that smaller fragments are more desirable than larger fragments is based on extrapolation rather than direct evidence. Similarly, there is no evidence to show if there is an “optimal” size of particle or fragment, or if smaller is always better as presumed.

Much of the existing evidence on particle size has focused on relatively large fragments >1mm. Some of these studies were performed on calcium sulfate based phantoms [134-136] while others used real stones [65, 114, 137, 138]. Most of these studies involved lithotripsy by hand, where the laser fibre was moved manually across the stone surface to emulate clinical lithotripsy. Where endpoints where defined, they were subjective assessments that lithotripsy was “complete”, presumably corresponding to when a clinician would consider lithotripsy to be complete intraoperatively. This definition is likely to vary both by the individual making the assessment, and also over time as clinicians have become less tolerant of 2-4mm residual fragments. Some studies did not define the endpoints for lithotripsy, making comparisons more difficult.

Every study except Pal et al separated the resulting particles by size using some kind of sieving process. Each of these papers except Bader et al used a 1mm sieve size as one of their boundary conditions, with some adding further size categories. It is not clear if there is any clinical significance to this 1mm size separation; no evidence could be found in a literature search so this may simply be a matter of convenience.

The way in which particle size outcomes were reported was highly variable. Teichman et al reported the complete histogram of particle masses by size category (>4mm, 2-4mm, 1.4-2mm, 1-1.4mm and <1mm) for each stone type. Pal et al took a different approach in reporting a particle size distribution from a particle size analyser. This resulted a much smoother curve with more size categories, but relatively opaque methodology in that it was not stated how the particle size analyser produced this data (e.g. whether it reported mass or number of particles). Similarly, the analyser reported a single "average particle size" for each stone, but without information on how this was calculated. This data was therefore not comparable to any other data set, which all reported particle mass.

Particle size histograms are objective and easy to interpret, but the collection of categorical outcomes makes it very difficult to compare two data sets. Most of the literature performed comparisons by selecting a single size threshold (of presumed clinical significance), and comparing the mass above and below this threshold. Teichman et al also proposed a method to estimate an "average" size, based on allocating a fixed 100 fragments to each size category proportionate to the mass in that category, and assuming that each fragment size was the midpoint of its category's limits. They then reported the "average" size of one of those assumed 100 fragments. This method would work relatively well for uniform data sets, but unfortunately data sets of particle sizes are extremely skewed. If a particle's diameter is halved then the mass of each particle is reduced by a factor of $2^3 = 8$, and the number of particles for the same category mass is increased by the same factor. The exponentially increasing number of smaller particles is not modelled by Teichman et al's

method, resulting in “average” size estimates that bear no correlation with the actual average particle size or any skew of the particle mass data, and that are very difficult to correlate with the corresponding particle mass histograms. This method of calculating an “average” size was therefore not considered viable.

In addition to this literature on particle size from lithotripsy, Keller et al reported on a modern method of separating human stone dust by size for analysis using wet sieving [76]. This method is similar to Teichman et al’s methods but using wet sieving instead of freeze drying, and with a much higher granularity of particle sizes going down to <63µm at regular intervals.

Alternative methods of calculating a single “average” particle size include the mean particle size, the median particle size (both of which would require an accurate count of the number of particles in each size category) and the centre of mass. These methods can be assessed on a selection of simulated data. The size categories are set to <63µm, 63-125µm, 125-250µm, 250-500µm, 500-1000µm and 1000-2000µm (corresponding to Keller et al’s reported methodology). For simplicity, particles are modelled as spheres at midpoint of each size category. In other words, all particles included in the 63-125µm category are exactly 94µm in diameter. The distributions used as examples are:

- Uniform number of particles (every size category contains the same number of particles)
- Uniform particle mass (every size category contains the same mass of particles)
- Skewed distribution based on preliminary calcium oxalate data

These distributions are shown in Figure 70, Figure 71 and Figure 72. Bars indicate particle mass while the orange line indicates the particle number. The vertical coloured lines indicate the four calculated “average” values – mean μ, median m, Teichman’s “average” t and the centre of mass c.

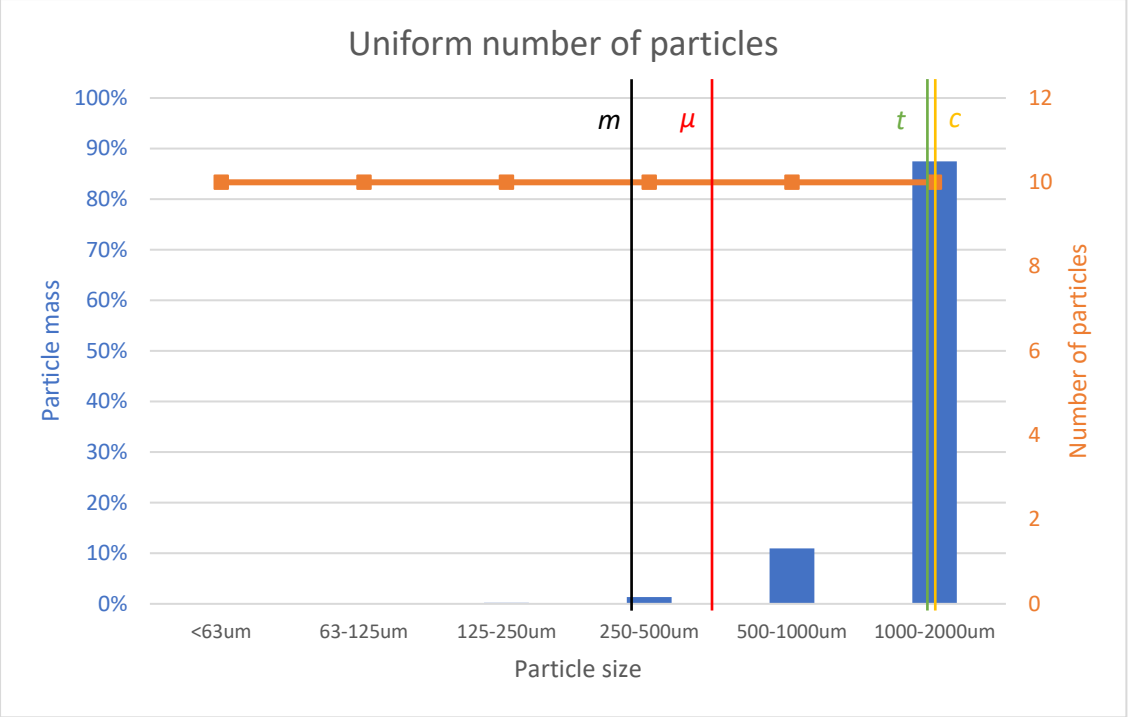


Figure 70. Particle size model with uniform number of particles in each size category. Mean μ = 0.49. Median m = 0.28. Teichman "average" t = 1.40. Centre of mass c = 1.5.

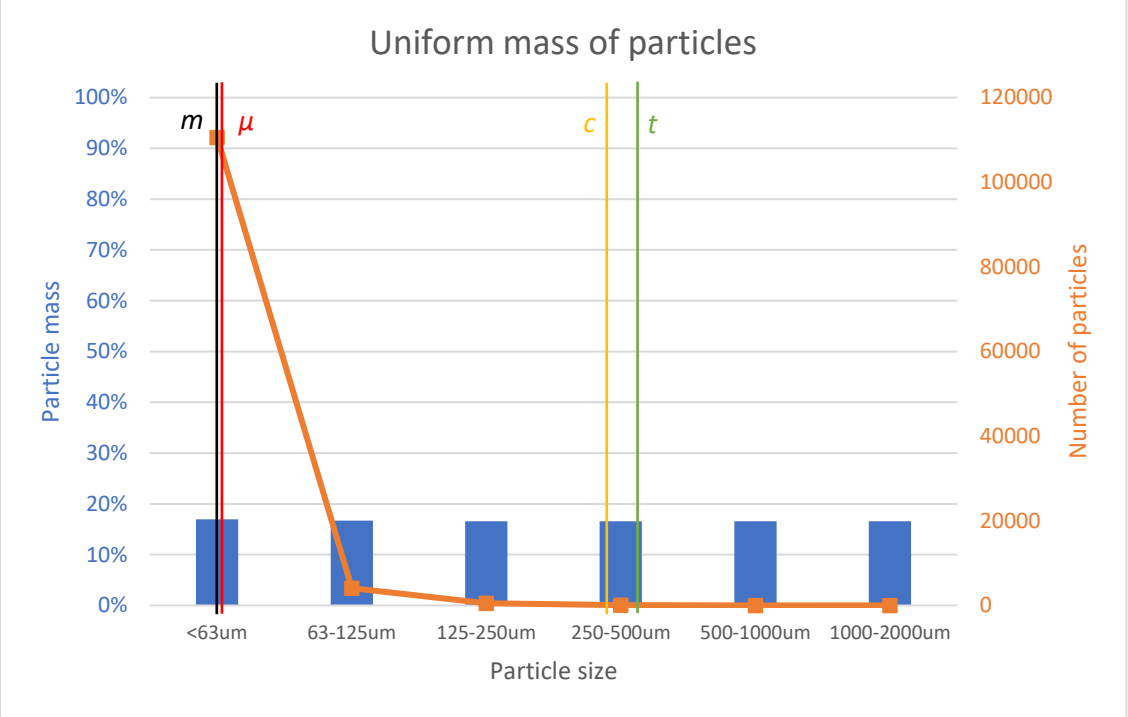


Figure 71. Particle size model with uniform mass of particles in each size category. Mean μ = 0.035. Median m = 0.032. Teichman "average" t = 0.49. Centre of mass c = 0.28.

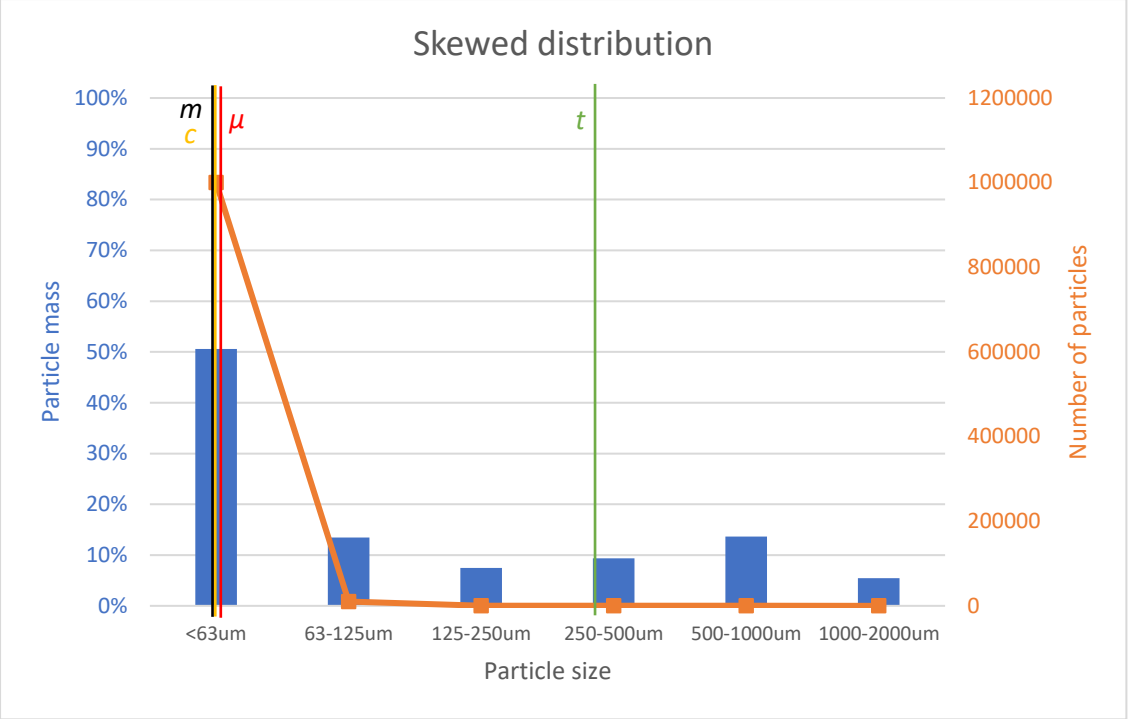


Figure 72. Particle size model with skewed distribution of particles. Mean μ = 0.033. Median m = 0.032. Teichman "average" t = 0.26. Centre of mass c = 0.032.

It is clear that all four of these "average" values have significant problems due to the highly skewed nature of this data, with the number of particles heavily skewed towards the extremely numerous smaller particles and the particle mass skewed in the opposite direction, towards the larger particles.

The mean μ is well understood and works well for distributions where the number of particles in each category is similar (e.g. Figure 70), but the expected skewed distributions with much greater numbers of smaller particles make μ essentially useless for discriminating relatively small numbers of massive fragments. The same problem applies to the median m.

The centre of mass c presents an intuitive and potentially helpful measurement for the uniform distributions, but breaks down when the distribution is skewed as in Figure 72 as it is unaffected by changes in mass distribution that do not alter the centre of mass.

Finally, the Teichmann "average" t is not dependent on the number of particles (which are calculated from arbitrarily assigned values) so it is not affected by skewed particle number data. However, this method of calculation results in some counterintuitive behaviour. For example, in the case of uniform number of particles shown in Figure 70, t = 1.406, calculated with 10 particles in

each size fraction. If a single particle increases in size from 200µm to 300µm (moving it from the 125-250µm fraction up to the 250-500µm fraction), then the resulting particle distribution is made strictly larger. However, the Teichmann "average" *t* actually decreases to 1.395. This is because the absolute total mass increases and the absolute mass in the largest size categories is unchanged, meaning that the proportion of mass in the largest size categories decreases. As *t* is calculated from particle mass, it is heavily influenced by the largest particle sizes and this results in a decrease in *t*. This result holds more generally where any increase in a particle's size below *t* will actually result in a decrease in *t*. This counterintuitive behaviour makes the Teichmann "average" unsuitable for comparisons between particle size distributions.

Given these inherent problems with summarising particle size distribution data, only complete particle size distribution data will be reported here without any summarisation. Simple calculations such as the proportions above/below clinically relevant size thresholds may also be reported where relevant. The existing literature suggests that 2mm is one such threshold, and there is bench evidence to support 250µm as a second potential threshold.

Objectives

As with ablation rate and retropulsion, one objective of this work was to quantify the particle size results of the P120, Soltive and prototype lasers on common stone types with representative laser settings.

The paucity of evidence behind particle size highlighted a gap in understanding, as it does not appear to have been proven to be an optimal particle size (or if one even exists). Instead, there appears to have been an assumption without evidence than smaller is necessarily better even for fragments <2mm. Therefore, another objective was to understand the expected behaviour of small fragments and particles following laser lithotripsy – in particular, which particles (if any) could be expected to wash out spontaneously intraoperatively.

Particle size distribution of canine stones

Canine stones were used as the model to quantify particle size outcomes. These were ablated in a controlled environment and all the resulting particles and fragments collected for analysis. Throughout this section, “particles” will be used to refer to all products of stone ablation regardless of size (encompassing colloquial terms such as dust, sand, grit, rubble, fragments, etc).

Methods

Canine stones were obtained from a stone analysis laboratory. These were labelled with the chemical composition of each stone based on a sample from both the shell and the core. Only stones labelled as 100% pure were used for experiments. The stone compositions used were calcium oxalate monohydrate (COM), struvite (magnesium ammonium phosphate hexahydrate, MAPH) and ammonium acid urate (AAU). COM is the most common human stone type, accounting for about 80% of stones. Struvite is a relatively common stone type in humans accounting for about 10%. AAU is extremely rare in humans, and was included instead of the chemically similar uric acid stones (which were not available in this stone library). Unfortunately, post-hoc analysis of AAU particles suggests that it behaves in a chemically distinct way to uric acid, so the results cannot be extrapolated. Nevertheless, the results are included here to illustrate the range of particle size outcomes.

Stones were weighed dry on a precision Entris II electronic balance (Sartorius, Goettingen, Germany). 3 stones of each type with a dry weight of at least 300mg were selected, to ensure a reasonable amount of particles produced (corresponding to a diameter of approximately 5mm). Selected stones were pre-soaked in water for 24 hours and then ablated in water in a Petri dish. Saline could not be used because the salt would re-crystallise when the resulting particles were dried and affect the results. The stone was held fixed with a pair of soft plastic forceps, and a 200µm-class laser fibre was manually guided to ablate the stone using a “painting” technique. This is a commonly used clinical technique where the fibre is moved across the surface of the stone maintaining a

constant depth, with the aim of ablating the stone into finer dust while avoiding events such as "drilling" that are more likely to result in the creation of larger fragments [139]. A visual size threshold of 2mm was set to determine if ablation was complete. If a particle was visually judged to be >2mm, it was further ablated until all resulting particles were visually judged to be <2mm. This represented the expectation that a clinician would not intentionally leave a particle of >2mm during ureteroscopy, and would instead either extract or continue to ablate it. The water and particles were periodically rinsed into a container to prevent re-circulation and maintain clear vision of the stone. Figure 73 illustrates the appearance of the stone and resulting particles.

In these experiments, the P120 laser was used with 2 settings:

- Standard short pulse, 1J 10Hz (10W)
- Standard short pulse, 0.2J 50Hz (10W)

These were selected to represent a power-matched pair of fragmentation and dusting settings.

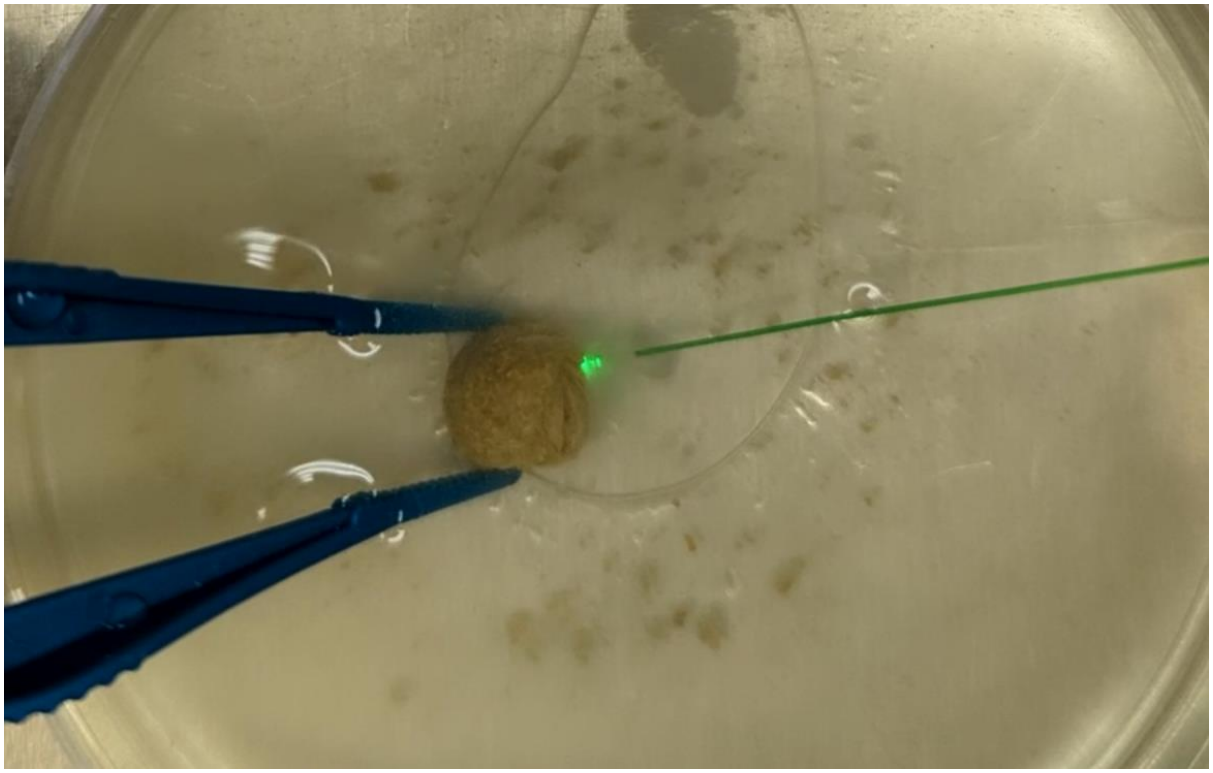


Figure 73. Particle size experiment in Petri dish, using a calcium oxalate monohydrate canine stone with P120 standard short pulse 1J 10Hz.

Once ablation was complete, the particles were separated by size using a wet sieving technique. A series of ISO 3310-1:2016 certified sieves (Endecotts Ltd, London, UK) was used with aperture sizes of 2mm, 1mm, 500µm, 250µm, 125µm and 63µm. The particles and water were separated using each sieve in turn as per the manufacturer's manual wet sieving instructions, starting with the largest aperture size. Wet sieving was performed manually for 1 minute at each sieve size. The particles retained from each sieve size were recovered on 11µm particle retention filter paper (Whatman Grade 1, Danaher Corporation, DC, USA). Each 110mm filter paper disc was weighed dry prior to use as it was not possible to separate smaller particles from the paper even after drying, to get a starting mass m_{start}. In addition, since the filter paper dry weight was highly sensitive to environmental conditions such as humidity, 3 filter paper discs were used as environmental controls. These were weighed dry and a similar amount of water passed through them (250ml) without any stone particles. These were then dried alongside the experimental samples.

After 24 hours of drying at room temperature, all filter papers (along with their captured particles) were weighed for a final mass m_{final}. The environmental mass change Δm_{env} was calculated as the mean mass change of the 3 control filter papers. The mass of each particle size fraction $m_{particles}$ was then calculated as follows.

$$m_{particles} = m_{final} - m_{start} - \Delta m_{env}$$

The size fraction masses were then summed to calculate the total recovered mass, both as an absolute value and as a proportion of the starting stone mass.

Results

Examples of the resulting particles from each of the 3 stone types (COM, struvite and AAU) are shown in Figure 74, Figure 75 and Figure 76 respectively.

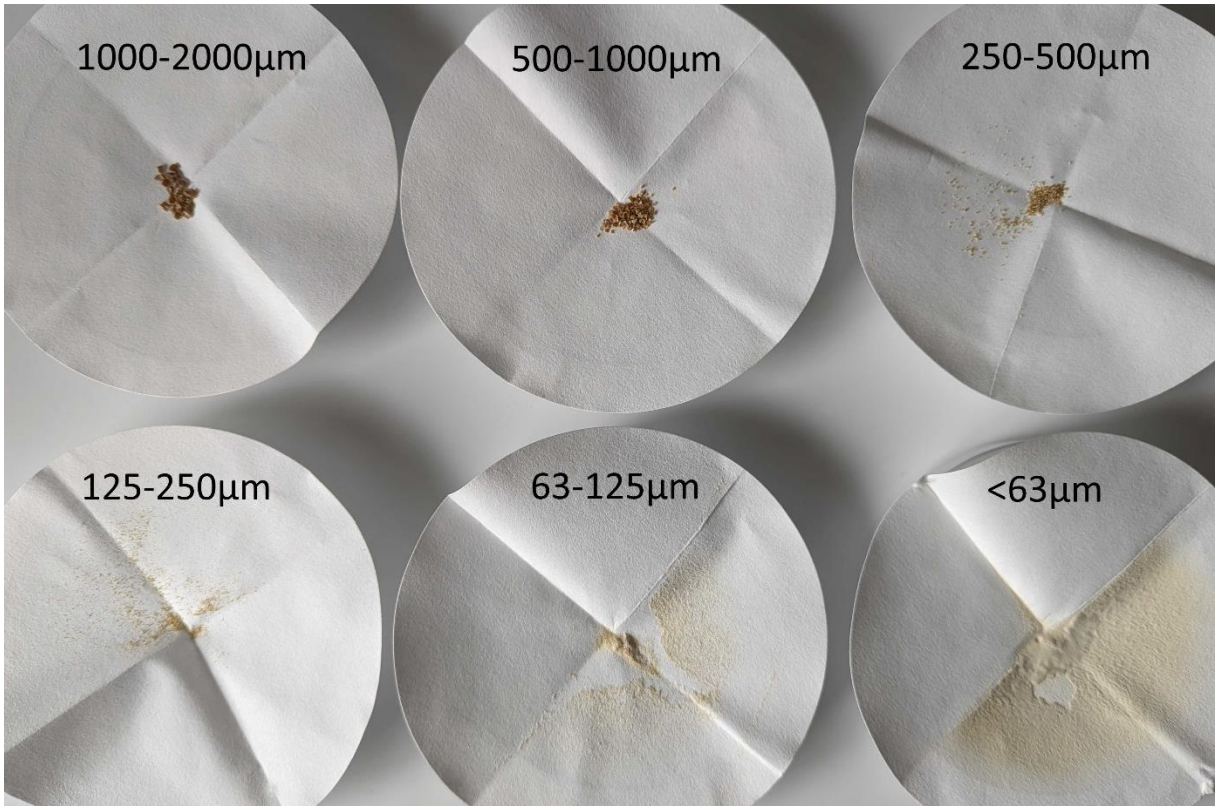


Figure 74. Particle size results from canine calcium oxalate monohydrate stone using P120 1J 10Hz standard short pulse.

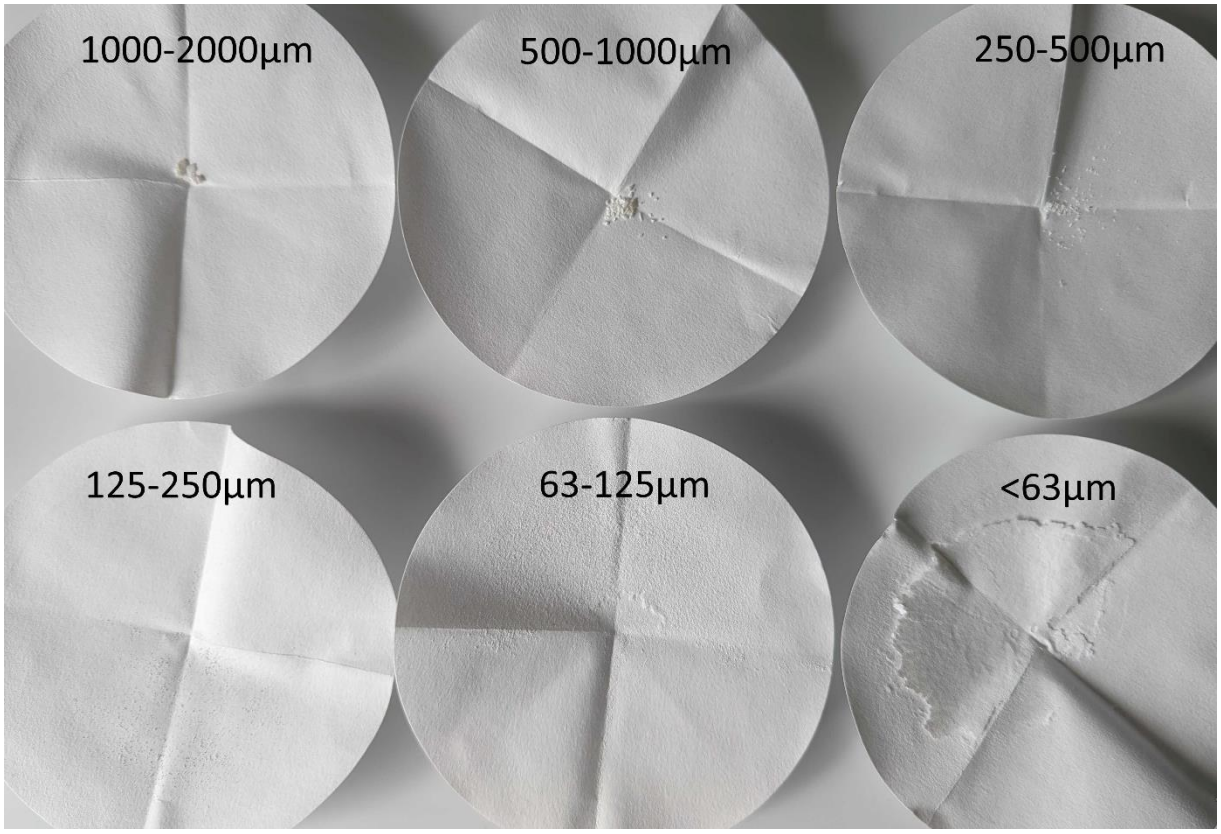


Figure 75. Particle size results from canine struvite stone using P120 1J 10Hz standard short pulse.

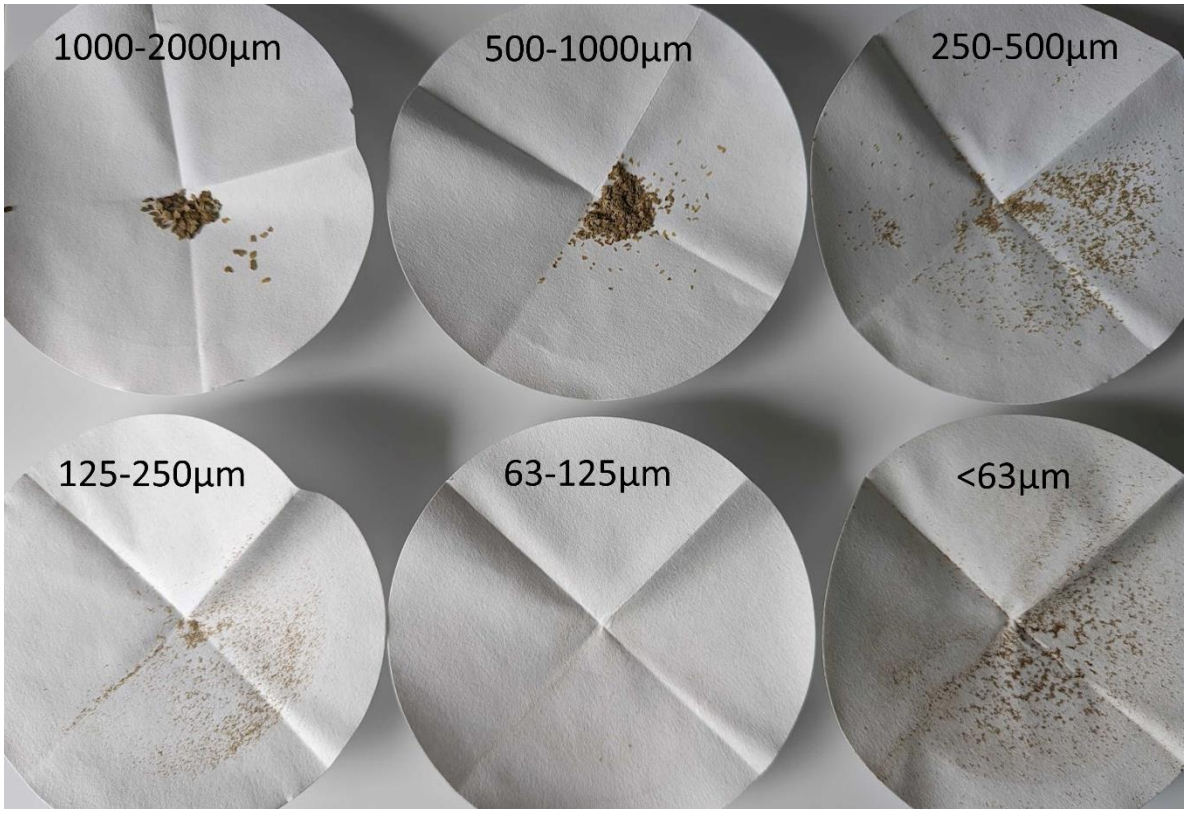


Figure 76. Particle size results from canine ammonium acid urate stone using P120 1J 10Hz standard short pulse.

Both COM and struvite stones result in large amounts of fine dust <63µm, with variable but moderate quantities of larger fragments >500µm and very little in between. Results for each stone type are in Figure 77, Figure 78 and Figure 79 with numerical data in Table 19, Table 20 and Table 21.

Almost all COM particles were retrieved using the sieving methodology, with over 90% of the starting mass recovered in all cases. Only about 60% of the starting mass of struvite was recovered, and even less of the AAU stone with only 39% of the starting mass recovered. The low rate of AAU recovery suggested that the behaviour was different to uric acid stone, where a high rate of recovery was expected. Therefore, dusting setting experiments were not performed with AAU.

The mass of particles >2000µm is still reported despite the methodology being designed to remove all such particles. There were no visible particles of >2000µm in the COM or struvite samples, and so this data serves to validate the accuracy of the methodology. There were some visible particles of >2000µm in the AAU samples but this is not plotted in the graphs as it reflects the operator's ability to visually estimate size, rather than the capabilities of the laser.

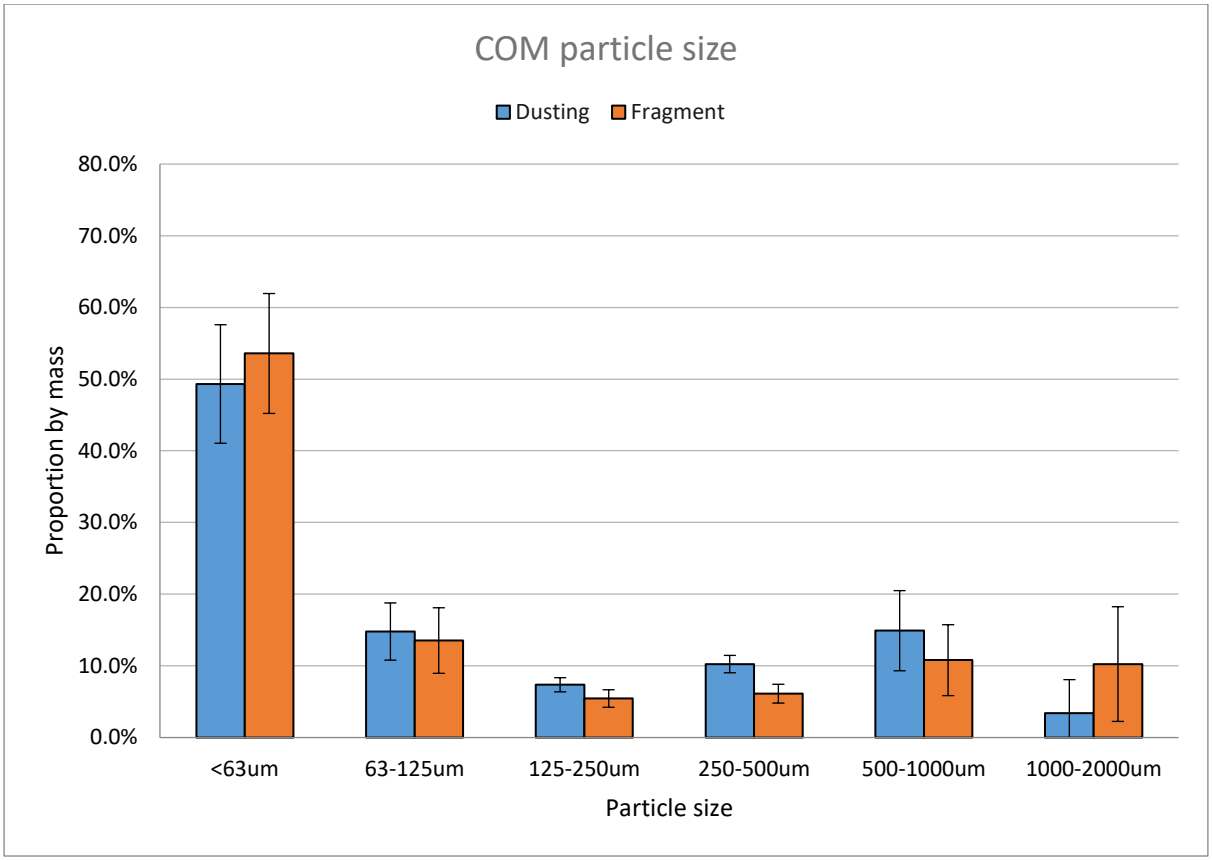


Figure 77. Particle size of calcium oxalate monohydrate stones after ablation with P120 using dusting (0.2J 50Hz) and fragment (1J 20Hz) standard short pulse settings. Error bars indicate one standard deviation.

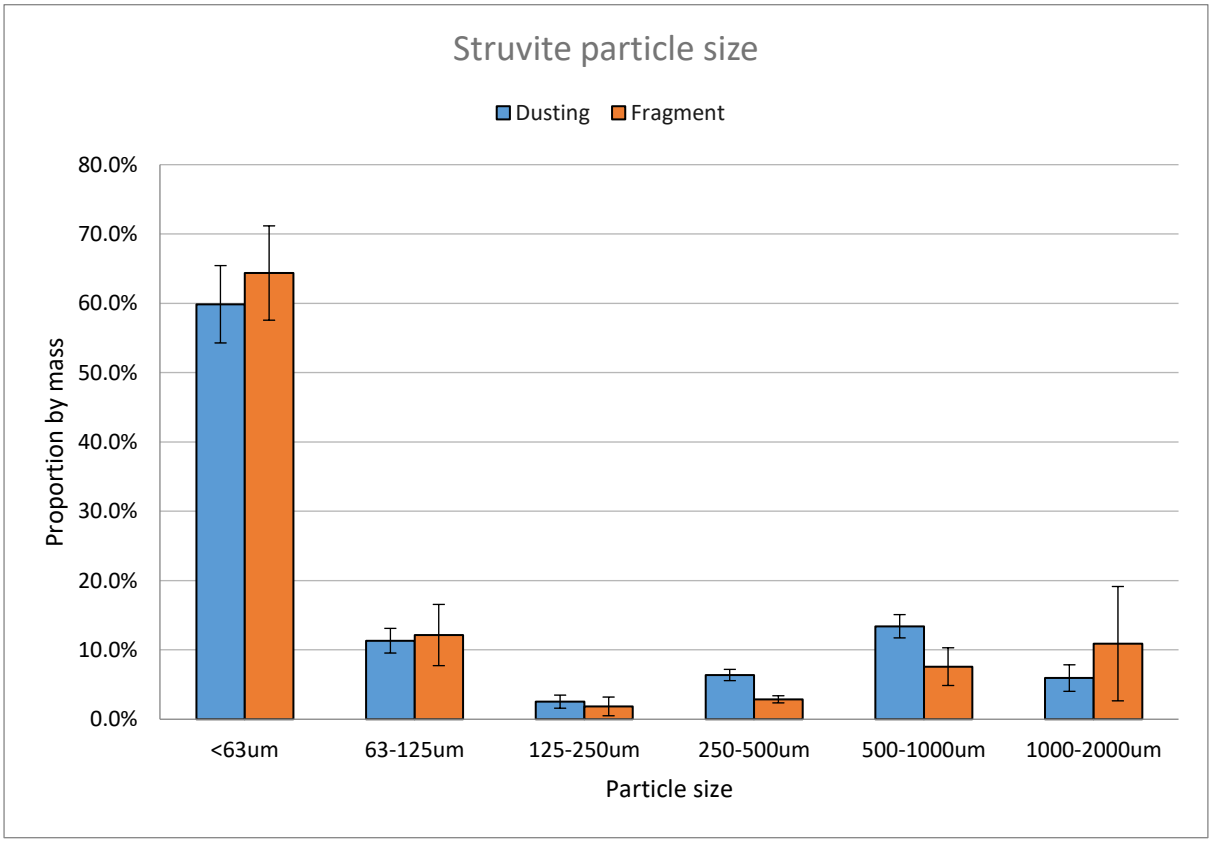


Figure 78. Particle size of struvite stones after ablation with P120 using dusting (0.2J 50Hz) and fragment (1J 20Hz) standard short pulse settings. Error bars indicate one standard deviation.

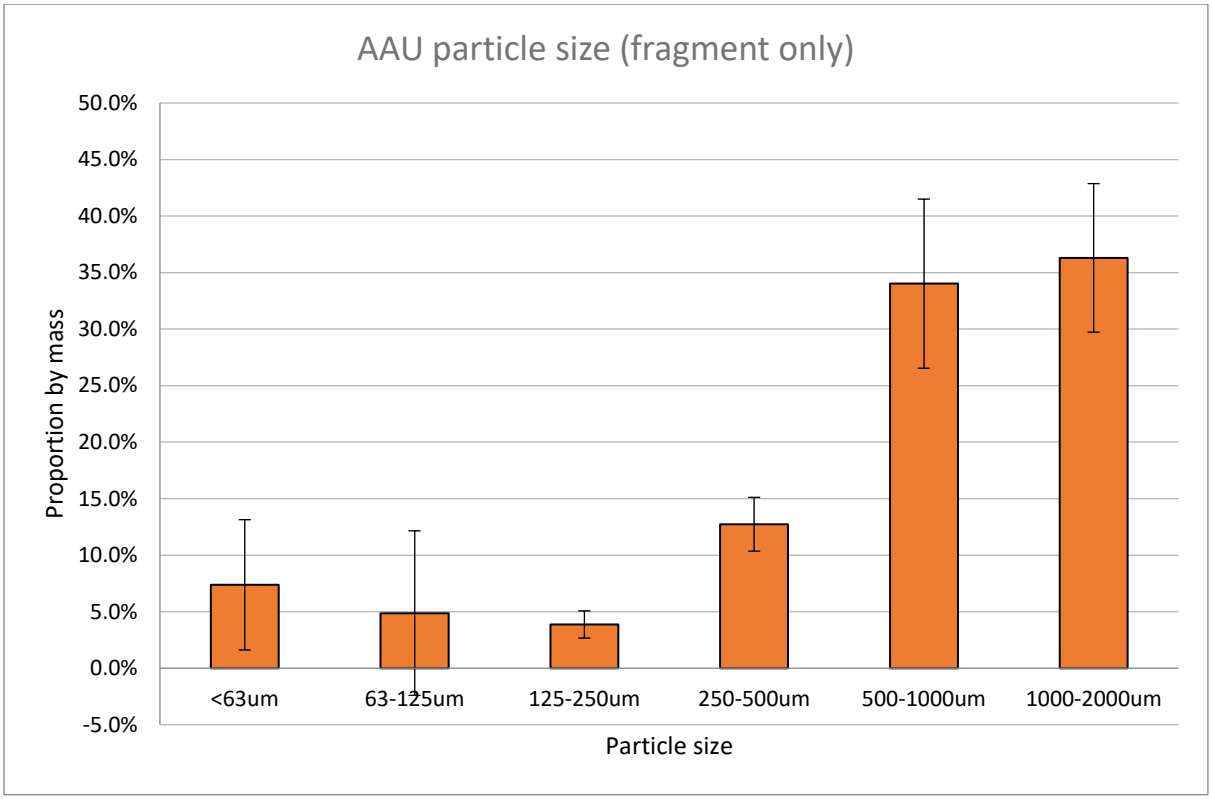


Figure 79. Particle size of ammonium acid urate stones after ablation with P120 using fragment (1J 20Hz) standard short pulse settings. Error bars indicate one standard deviation.

COM canine stone results	**P120 1J 10Hz ("frag")**		**P120 0.2J 50Hz ("dust")**	
Size fraction	**Mean**	**S.D.**	**Mean**	**S.D.**
<63µm	53.6%	8.3%	49.3%	8.4%
63-125µm	13.5%	4.0%	14.8%	4.6%
125-250µm	5.4%	1.0%	7.4%	1.2%
250-500µm	6.1%	1.2%	10.2%	1.3%
500-1000µm	10.8%	5.6%	14.9%	4.9%
1000-2000µm	10.2%	4.7%	3.4%	8.0%
>2000µm*	0.3%	0.1%	0.0%	0.5%
Total mass recovered	90.4%	2.9%	91.7%	6.2%

*Table 19. Particle size of calcium oxalate monohydrate stones after ablation with P120 using dusting (0.2J 50Hz) and fragment (1J 20Hz) standard short pulse settings. Results for each size fraction are a proportion of total recovered mass, and the ratio of total recovered mass to starting mass is included separately. * indicates that there were no visible particles of >2000µm.*

Struvite canine stone results	**P120 1J 10Hz ("frag")**		**P120 0.2J 50Hz ("dust")**	
Size fraction	**Mean**	**S.D.**	**Mean**	**S.D.**
<63µm	64.4%	5.6%	59.9%	6.8%
63-125µm	12.1%	1.8%	11.3%	1.4%
125-250µm	1.9%	0.9%	2.5%	1.4%
250-500µm	2.9%	0.8%	6.4%	0.5%
500-1000µm	7.6%	1.7%	13.4%	2.7%
1000-2000µm	10.9%	1.9%	5.9%	8.2%
>2000µm*	0.3%	0.2%	0.5%	0.3%
Total mass recovered	61.3%	1.4%	56.6%	3.9%

*Table 20. Particle size of struvite stones after ablation with P120 using dusting (0.2J 50Hz) and fragment (1J 20Hz) standard short pulse settings. Results for each size fraction are a proportion of total recovered mass, and the ratio of total recovered mass to starting mass is included separately. * indicates that there were no visible particles of >2000µm.*

AAU canine stone results	P120 1J 10Hz ("frag")	
Size fraction	**Mean**	**S.D.**
<63µm	7.4%	5.8%
63-125µm	4.9%	7.3%
125-250µm	3.9%	1.2%
250-500µm	12.7%	2.4%
500-1000µm	34.0%	7.5%
1000-2000µm	36.3%	6.6%
>2000µm	0.8%	1.1%
Total mass recovered	39.0%	11.9%

Table 21. Particle size of ammonium acid urate stones after ablation with P120 using fragment (1J 20Hz) standard short pulse settings. Results for each size fraction are a proportion of total recovered mass, and the ratio of total recovered mass to starting mass is included separately.

The differences in mass recovery between the stone types preclude direct comparisons between different stone types, as it is not known which particles were lost in each case.

Both COM and struvite resulted in a bimodal particle size distribution. About half the resulting particulate mass consisted of the smallest <63µm particles (about 50% for COM and about 60% for struvite).

About 20% of the resulting mass consisted of larger particles >500µm (18.3%-21.0% for COM and 18.5%-19.3% for struvite), but variation between stones was relatively high with large error bars relative to the means. For both COM and struvite, changing the laser settings from "frag" (1J 10Hz) to "dust" (0.2J 50Hz) does not seem to have an obvious impact on the resulting particle size distribution. The proportion of larger particles >500µm is not significantly different between the two laser settings for either COM ($p = 0.786$) or struvite ($p = 0.905$).

The distribution for AAU is less clear, especially considering the large amount of mass loss, but may be a similar bimodal distribution if it is assumed that most of the mass loss comes from the smallest particles.

Discussion

This method of ablating stones in a controlled environment appears to result in relatively consistent particle size distributions for COM and struvite stones, especially for smaller particles <500µm. These distributions appear to be bimodal, with very fine particles <63µm making up about half the

recovered mass and another peak for larger particles >500µm which make up approximately 20% of recovered mass.

COM stones had a high rate of mass recovery which indicates that in the right conditions (i.e. a very insoluble stone type), the experimental methodology is capable of recovering >90% of initial mass and up to 95.4% for some stones. The lower rate of recovery for struvite and AAU stones implies that another, non-mechanical factor is responsible, and this is mostly likely to be solubility. All urinary tract stones are composed of soluble components, since they form by precipitating out of urine. COM has a very low solubility in water of 0.61mg/100g H_2O at 20 centigrade [140] which explains the high rate of mass recovery. In contrast, struvite (magnesium ammonium phosphate hexahydrate) has a solubility of 16.92 mg/100g H_2O at 25 centigrade [141], more than an order of magnitude higher. Since the particles consist mostly of extremely small particles, the surface area to volume ratio is extremely high especially for the smallest particles. It is therefore likely that most of the mass lost results from solubility of smaller particles, with minimal impact to the larger particles. Uric acid was expected to have an intermediate solubility of 6 mg/100g H_2O at 25 centigrade, but AAU appears to behave differently with a much higher mass loss than struvite. The relative paucity of small particles from AAU is also consistent with a higher solubility having a much larger impact on small particles with a high surface area to volume ratio.

The experimental methodology appears to be sound and capable of accurately measuring particles in each size fraction. The measurements of visually empty >2000µm fractions were consistent and very close to zero, and the control weights and weight changes were also very consistent despite the very small absolute mass values. Attempts were initially made to dessicate the stone and filter paper to eliminate the need for controls, but the filter paper was found to rapidly re-hydrate immediately in air, resulting in a rapidly changing weight measurement that could not be performed consistently.

It is interesting that the choice of laser setting did not appear to make any difference to the particle size distribution in these experiments. All experiments were performed with the stone held directly

with forceps, allowing for a consistent “painting” technique throughout ablation. It may be that technique is more important to particle size than the laser setting itself – in which case, it is necessary to explore other scenarios where this (unrealistically well-controlled) technique is not possible.

The canine stone is assumed to be an accurate model for chemically identical human stone. While this assumption is reasonable based on the chemistry, it should also be noted that urinary stones contain a small amount of protein matrix (up to 5% by mass) which may not be identical in either chemical composition or location.

Similarly, stones themselves may be chemically identical but vary in terms of their physical structure. While the struvite stones used appeared relatively homogenous, COM stones often had distinctive physical structures such as individual concentric shells. The exact physical structures (such as thickness of each shell) are likely to have an impact on the particles produced from ablation, but lacking any standardised means in which to quantify this physical structure (or detect it in clinical scenarios) it was not necessary or possible to assess this impact.

Washout of stone particles

The second objective of the particle size work was to understand the expected behaviour of stone particles following laser lithotripsy, especially in terms of whether they would wash out of the kidney spontaneously. This would help establish potential goals for particle size based on objective data.

Based on both the underlying physics and clinical data for larger stone sizes >4mm, it has been assumed that there is an inverse relationship between particle size and likelihood of spontaneous washout. An experiment was designed to investigate this relationship by introducing particles of known sizes into a simulated kidney model and measuring the extent of washout under controlled bench conditions.

Quartz-based stone dust model

Large quantities of stone dust particles of known sizes were required for these experiments. Although actual stone dust would have been the most authentic model, initial prototyping experiments revealed a number of problems. On the practical side, the uneven size distributions of particles meant that very large quantities of stone would need to be dusted to generate sufficient amounts of dust at all sizes. For example, generating 83mg of 125-250µm struvite dust (enough for one washout experiment) would require 5.9g of raw struvite stone – corresponding to 15-20 stones of 6mm diameter. This was clearly not feasible and instead a suitable stone model was sought.

The density and solubility in water of the most common human stone types (calcium oxalate monohydrate and dihydrate, struvite, uric acid, cystine, and the calcium phosphate-based brushite and hydroxyapatite) are shown in Table 22 [116, 140-147]. Since there is no ablation in these experiments, other properties such as hardness, compressive strength and tensile strength are not relevant.

Material	**Density (g/cm^3)**	**Solubility (mg/100g H_2O)**
Calcium oxalate	1.84 – 2.08	0.61
Struvite	1.701	16.92
Uric acid	1.89	6
Cystine	1.677	11.2
Calcium phosphate	3.14	2
Brushite	2.32	8.52
Hydroxyapatite	3.05 – 3.16	0.44
BegoStone	1.563 – 1.995	260
Glass (vitreous silica)	2.4 – 2.8	0
Quartz (crystalline silica)	2.65	1.08
Polyethylene	0.88 – 0.96	0
Polystyrene	0.96 – 1.05	0
Polypropylene	0.855	0
Aluminium	2.7	0

Table 22. Density and solubility of types of kidney stone and proposed stone dust phantom materials. Properties of the monohydrate and dihydrate forms of calcium oxalate are reported together.

Both the densities and solubilities of the different chemicals in urinary stones are heterogeneous. Density ranges from 1.7 – 3.2 g/cm^3 while solubility ranges over several orders of magnitude from 0.44 – 16.9 mg/100g H_2O. In addition, most stones are not chemically pure but instead a

combination of multiple chemical components plus a small proportion of proteins. With that in mind, BegoStone is similar in density to the least dense stone components while the silica-based models are in the middle of the range, though denser than the most abundant stone component (calcium oxalate).

The solubility of the model is a more difficult question to answer. Calcium-based stones are highly insoluble, with the exception of the rare calcium phosphate-based component, brushite. Uric acid and cystine stones are still relatively insoluble, but struvite has a much higher solubility that has already been shown to be problematic for high precision experimental measurement in the previous section. Trial experiments using BegoStone that was ablated into fragments by laser resulted in up to 90% of the starting mass being lost to solution. This is consistent with contemporary literature such as Black et al [136] who reported 40-60% of mass "lost in fluid" when attempting to measure BegoStone dust produced from lasering. For these reasons, it was decided that instead of trying to match the solubility of actual stone, the stone dust model should have minimal water solubility to ensure experimental accuracy. BegoStone was therefore rejected as a possible candidate.

The potential stone dust model required a large range of particle sizes from <63µm to >1mm, spanning at least 2 orders of size magnitude. This required either commercially available particles of suitable sizes, or a material that could be ablated to these sizes by laser or other means.

Both silica- and plastic-based materials are available as microspheres at suitable sizes. Unfortunately, all common plastic microbead materials (polyethylene, polystyrene and polypropylene) had a density of < 1g/cm^3. This meant that not only were they unrepresentative of stones, but also that they would likely float in water resulting in significantly different behaviour. Plastics were therefore also rejected as possible candidates. Glass microspheres were available down to 10µm sizes, but no suitable vendor could be found that offered a complete range of sizes up to 2mm. Aluminium data is also presented here as a metal with similar density to quartz, but neither this nor any other metal was available as microspheres. It was expected that the malleable

nature of metals would make them unsuitable for lasering into dust, and so metals were not considered further.

Other avenues of acquiring a silica-based model were then considered. River sands are widely available at a range of particle sizes, but contain an unknown quantity of unknown impurities that may differ in density. Manufactured sands are made artificially using a starting substrate material such as granite, so there is greater control over the resulting chemical composition. Quartz sand was identified as a potential model fitting all of the required criteria. Quartz sand:

- Is chemically pure crystalline quartz (SiO_4)
- Has a density within the range of human stones (2.65 g/cm^3)
- Is almost completely insoluble in water
- Is available at particle sizes ranging from <63µm to >1mm

Quartz sand was therefore selected as the model for stone dust. Graded quartz sand (Sika AG, Baar, Switzerland) was purchased at 3 grain sizes: 0.06-0.3mm, 0.3-0.8mm and 0.7-1.2mm.

Quartz dust sedimentation experiments

A set of sedimentation experiments were designed in order to verify the expected fluid dynamics of quartz dust. This was based on the sedimentation experiment described by Keller et al [76] where particles of each size category (<63µm, 63-125µm, 125-250µm, 250-500µm, 500-1000µm and 1000-2000µm) were placed in water in 10 x 1cm closed cuvettes and rapidly rotated 180˚. The time taken for each size of particle to sediment a distance of 10cm could then be recorded.

Two experiments were performed – one using quartz dust and one using COM dust. Keller et al's methodology was adhered to as closely as possible in an attempt to produce comparable results to their reported data on COM, calcium oxalate dihydrate, uric acid, carbapatite, brushite and cystine.

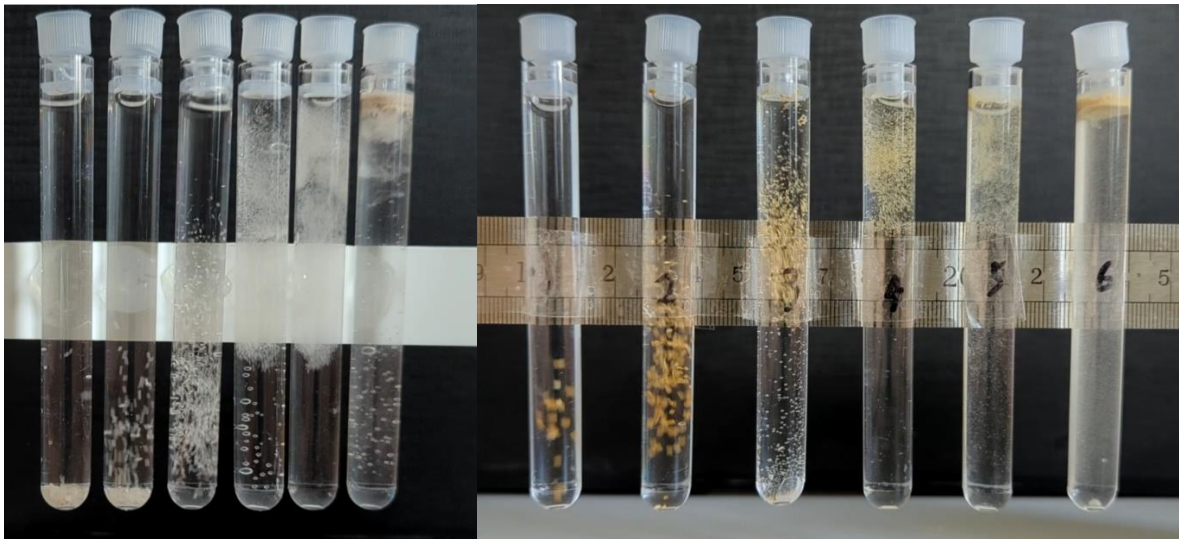


Figure 80. Sedimentation experiments. Left: quartz sand. Right: calcium oxalate monohydrate. Cuvettes for each experiment from left to right: 1000-2000µm, 500-1000µm, 250-500µm, 125-250µm, 63-125µm, <63µm.

5 repeats were performed for each stone type. The sedimentation time for the first particle to reach the far end of the cuvette is presented below. Reference COM sedimentation data from Keller et al is included in orange in Figure 81.

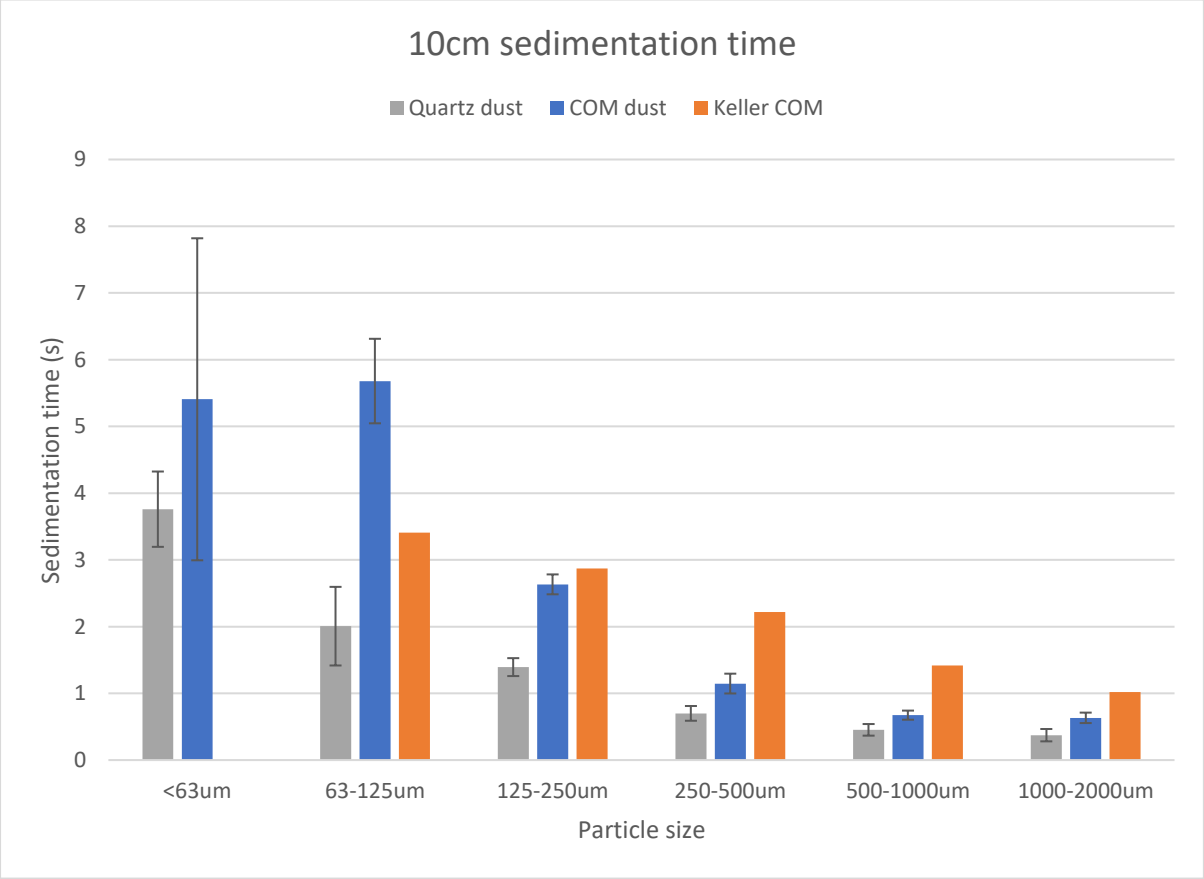


Figure 81. 10cm sedimentation times for quartz and calcium oxalate monohydrate particles. Error bars indicate one standard deviation. Reference COM data from Keller et al is included in orange.

Sedimentation time (s)	Quartz		COM	
Particle size	**Mean**	**S.D.**	**Mean**	**S.D.**
<63µm	3.76	0.56	5.41	2.41
63-125µm	2.01	0.59	5.68	0.63
125-250µm	1.39	0.13	2.63	0.15
250-500µm	0.70	0.11	1.15	0.15
500-1000µm	0.45	0.09	0.67	0.68
1000-2000µm	0.37	0.09	0.63	0.78

Table 23. 10cm sedimentation times for quartz and calcium oxalate monohydrate particles.

In these experiments, quartz sediments more rapidly than COM. This is to be expected from quartz's higher density, as terminal sedimentation velocity V_g is determined by Stokes' law:

$$V_g = \frac{d^2(\Delta\rho)g}{18\eta}$$

where d is the diameter of the particle, $\Delta\rho$ is the density difference between the particle and the fluid medium, g is Earth gravity and η is the viscosity of the fluid. Stokes' law holds under the assumptions of:

- Laminar flow
- No inertial effects
- Spherical particles
- Smooth (frictionless) surfaces
- Particles do not interact with each other

It can be seen from Stokes' law that a denser particle results in a higher terminal velocity. If the density of COM is taken to be 1.96 g/cm^3, then the difference in density from water is 1.65 g/cm^3 for quartz and only 0.96 g/cm^3 for COM. Thus, quartz is only about 35% more dense than COM, but the terminal velocity is 72% higher. Since these terminal velocities are relatively small (well under 1m/s), the acceleration time under Earth gravity of 9.81 m/s^2 is extremely short and it is reasonable to make the simplifying assumption that small particles attain their terminal velocity instantaneously.

As expected, larger particles sediment more rapidly. Stokes' law indicates that halving the particle diameter will reduce the terminal velocity to a quarter, which in turn would approximately

quadruple the sedimentation time. This is not reflected in these results, which show a lower-order relationship between particle size and velocity, and implies that at least some of the assumptions of Stokes' law are not valid. Most obviously the assumption of smooth, frictionless surfaces cannot be valid in reality, and the implication is that friction has a proportionately larger impact on the velocity of larger particles than smaller particles.

For particles >125µm, the difference in quartz and COM sedimentation time appears to fit well with this ratio as expected. For smaller particles <125 µm, this difference does not hold, with COM having an abnormally short sedimentation time. Close inspection of the video reveals that this is because the particles are clumping together, delaying initial sedimentation and then descending as a single, larger clump. This is also seen for the smallest quartz particles <63µm. Sedimentation data should therefore be treated with caution at extremely small particle sizes.

Quartz sedimentation results were more consistent than COM, with proportionately lower standard deviations compared to means. This is beneficial for experimental purposes.

Finally, it is clear that despite best efforts to replicate the methodology, the results from these experiments are not comparable to the results reported by Keller et al. This can be seen from the differences in COM results in Figure 81, which cannot be corrected by a simple 0^{th} order or 1^{st} order conversion (i.e. addition or multiplication by a constant).

These results can be used to model sedimentation of quartz and COM dust based on well-understood physical constraints. It can easily be calculated that a frictionless particle under Earth gravity takes 0.14s to fall 10cm without any resistance, and therefore there must be a horizontal asymptote at 0.14s as no particle can physically sediment faster than this. Within this constraint, a non-linear regression can be performed on these results as shown in Figure 82.

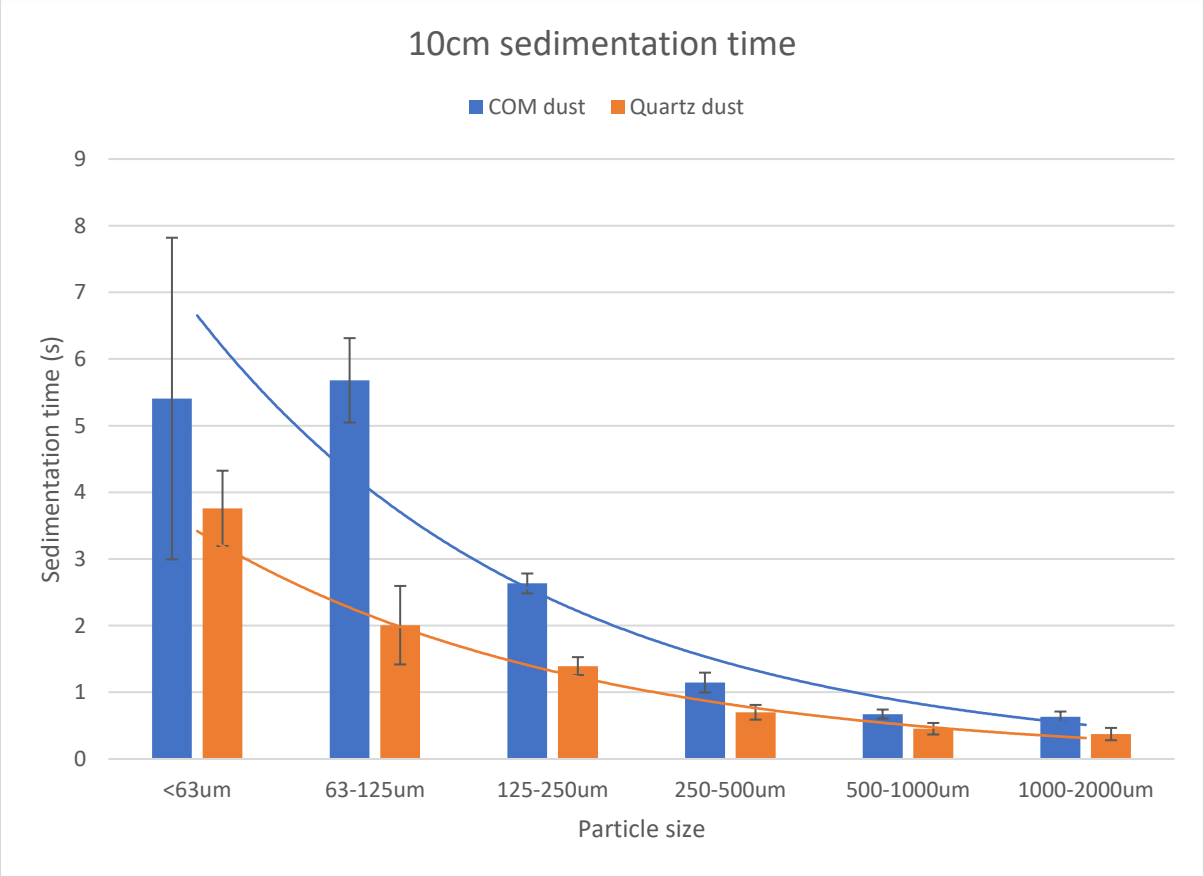


Figure 82. 10cm sedimentation times for quartz and calcium oxalate monohydrate particles with non-linear regression curves. Error bars indicate one standard deviation.

The resulting regression curves for sedimentation times have the following equations:

$$t_{quartz} = 0.14 + 91d^{0.8}$$

$$t_{COM} = 0.48 + 4552d^{1.4}$$

where d is the particle diameter in micrometres, giving the 10cm sedimentation time in seconds. The corresponding R^2 is 0.982 for quartz and 0.997 for COM.

It is noteworthy that neither exponent in the sedimentation time regression curves (0.8 and 1.4) have an obvious physics-based explanation. This suggests that the observed sedimentation behaviour results from more complex interactions involving not just particle size and density, but also friction, particle-particle interactions and fluid dynamics (including turbulence).

For the purposes of particle size experiments, this establishes quartz as a suitable model for stone dust. It satisfies the most important requirement that sedimentation time increases as particle size

decreases. Compared to COM, it is more dense and so has a lower sedimentation time. This is acceptable since any situation where quartz particles can be suspended or moved should mean that stone dust of equivalent size can also be suspended or moved. The quartz sedimentation results are also more consistent than COM dust which is beneficial for experimental purposes.

Microscopy of quartz and stone dust particles

Light microscopy was performed on the common COM and struvite stone particles as well as quartz particles, in order to determine any differences in morphology that may affect fluid dynamics. COM and struvite particles were generated in a Petri dish by the methods described earlier in this section. Pure canine stones of the respective types were soaked in water and then ablated by hand using a P120 laser with a 230µm fibre using a "painting" technique. The particles were then separated by size by wet sieving, as previously described. Quartz particles did not require ablation as they were supplied in a heterogeneous mixture of sizes from 60µm to 1.2mm diameter, and only required separation by the same wet sieving technique.

Particles from each size fraction (<63µm, 63-125µm, 125-250µm, 250-500µm, 500-1000µm and 1000-2000µm) were placed in turn on a Petri dish and illuminated with an LED light source. A FastCam SA-X2 high-speed camera (Photron, Tokyo, Japan) was used for photography with a 12x zoom Navitar microscope lens and 2x F-mount adapter tube (Navitar, NY, USA). The camera distance and focus was kept constant in order to maintain the same magnification for each picture, so the relative sizes are comparable within and between Figure 83, Figure 84 and Figure 85.

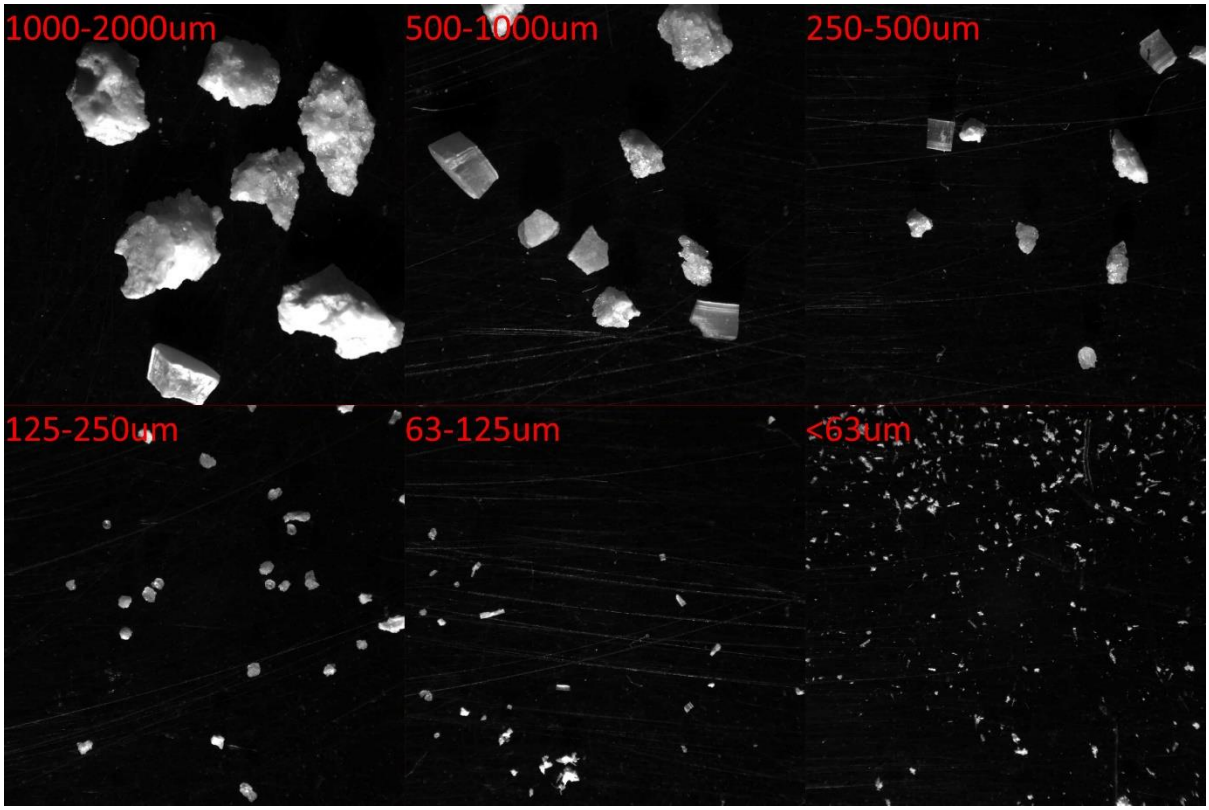


Figure 83. Light microscopy of calcium oxalate monohydrate particles.

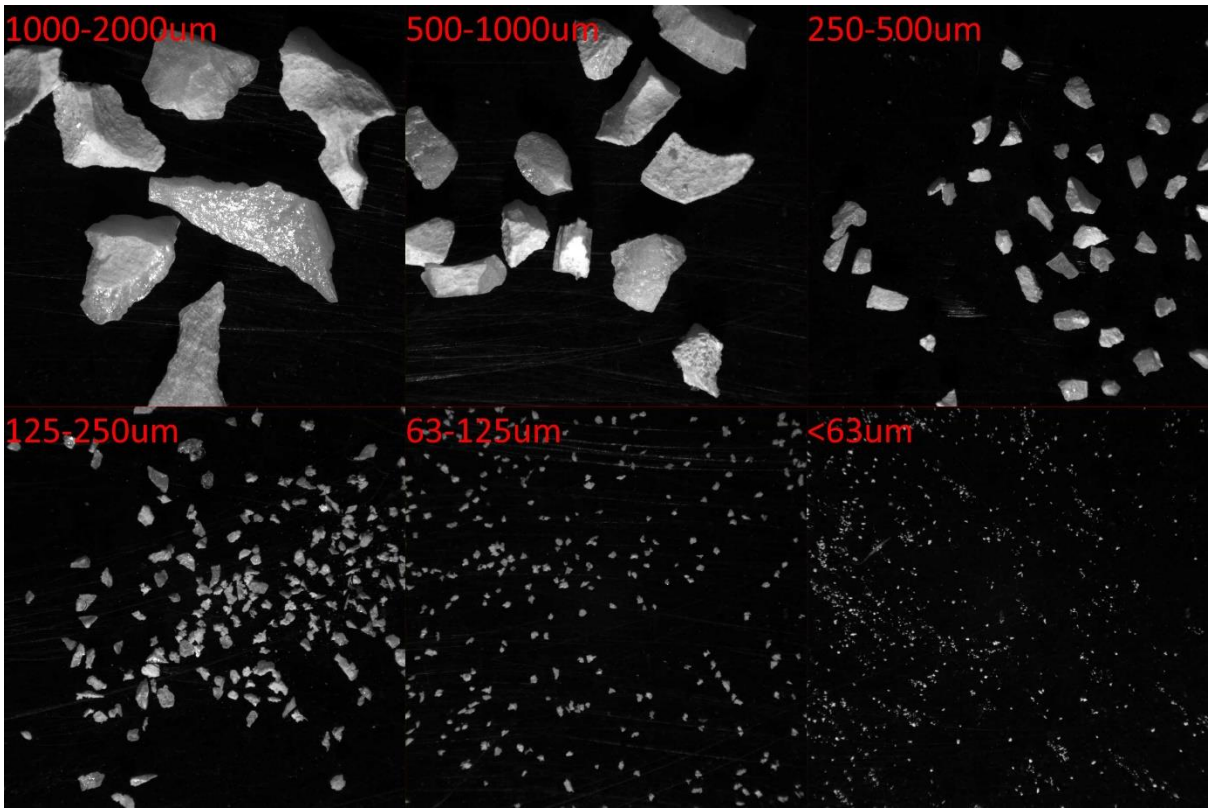


Figure 84. Light microscopy of struvite particles.

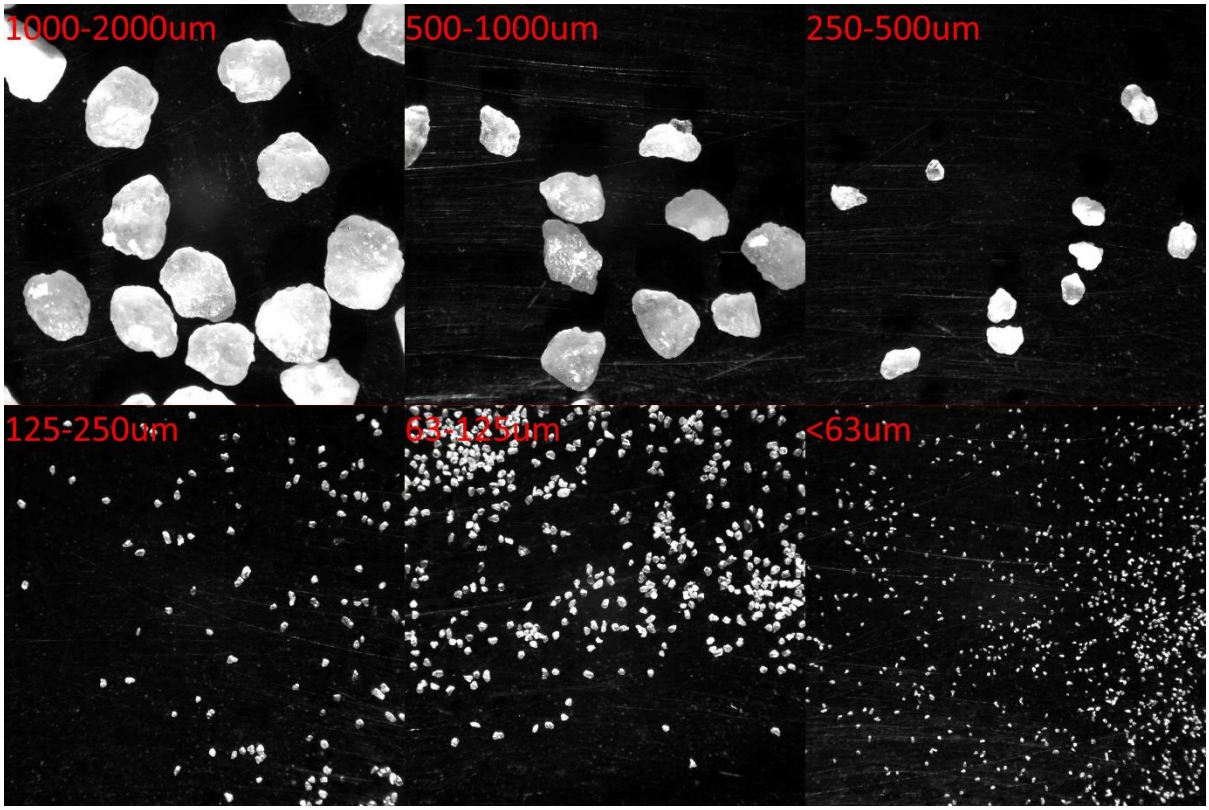


Figure 85. Light microscopy of quartz particles.

Since these particles are separated by sieving, the size measurements correspond to the sieve aperture size through which they can pass. In other words, a particle categorised as 250-500µm can pass through a sieve with square 500µm x 500µm apertures, but not through a sieve with square 250µm x 250µm apertures. This is a practical (and widely adopted) notation, and reflects the clinical interest in whether these particles can pass through apertures of certain diameters. For spherical particles, it will correspond exactly to the particle dimensions, but irregular particles with a single larger dimension may pass through these sieves in the same way that a sofa may be manoeuvred through a doorway.

The COM and struvite images clearly show that these particles are usually irregular. Larger particles in both can be seen to have two kinds of surface: some extremely flat/planar surfaces where presumably the crystal has sheared along a plane, and other irregular surfaces which look like the cumulative effect of many small craters. As a result, COM particles are mostly irregular oblong shapes, with many consisting of very straight sides, and struvite particles are more often elongated or spindle shaped. Meanwhile quartz particles are almost all irregular rounded shapes, which is

presumably a result of being produced by artificially eroding quartz down from larger chunks. The irregular shapes of COM and struvite particles mean that their orientation can have a significant effect on their fluid dynamics, which is less important for the more regularly shaped quartz particles.

Finally it should be noted that the smallest COM and struvite particles <63µm can reach extremely small sizes. The 12x magnification of the microscope lens used here does not allow for precise size measurements on the order of microns, but if it is assumed that the maximum width of a particle passing through the 63µm sieve is indeed 63µm then the smallest particle width measured was approximately 15µm for both COM and struvite. This is consistent with the filter paper used to recover these particles which is rated to capture particles of 11µm diameter. Meanwhile the smallest quartz particle measured was approximately 30µm in diameter, which is significantly larger.

In conclusion, light microscopy does reveal some interesting morphological differences between quartz and stone particles. The most relevant of these are that:

1. The smallest quartz particles <63µm are larger on average than the smallest stone particles <63µm.
2. Stone particles are more irregularly shaped than quartz particles, which is likely to impact their fluid dynamics. This is expected to have a smaller effect on larger particles with a lower surface area to volume ratio.

These findings support the sedimentation rate findings, that the quartz model is a more accurate model at larger particle sizes but less accurate at smaller particle sizes (particularly <63µm).

Kidney washout experiment

Washout introduction and objectives

With a quartz dust model established and an understanding of the basic physical properties of this model, an experiment was designed to measure dust washout from a simulated kidney. Two sets of

experiments were performed; one set using the quartz model, and one set using canine stone dust for validation.

Washout of stone dust and fragments is a combination of intraoperative washout from ureteroscopic irrigation, immediate post-operative drainage from gravity (over minutes/hours) and delayed post-operative drainage from patient activity (over days/weeks). Interoperative washout could be easily controlled, and immediate post-operative drainage could also be modelled in a controlled and consistent manner. There is no way to accurately model the wide range of patient movements and positions in the days or weeks following an operation, and so these experiments were restricted to investigating the intraoperative and immediate post-operative period.

The principles of these experiments were to place a representative quantity of quartz particles of a known size distribution in the calyx of a kidney model, irrigate the particles as they would be during ureteroscopy, and collect both the particles that are washed out of the kidney model and those that are retained in the kidney. These would then be analysed to determine how effectively particles of different sizes wash out at different irrigation rates.

Methods

An anatomical kidney and ureter model was used based on a pre-existing medical teaching model (Pulse Medical Demonstration Models, PA, USA). This silicone-based model was modified to feature a transparent anterior surface to allow for direct vision of the collecting system, and with a dark blue posterior surface to maximise contrast with white/brown coloured stones. The inner diameter of the PUJ at the narrowest point was 8mm, for a cross-sectional area of 50.26mm^3 at this point. The internal volume of the collecting system was 31.5ml, up to the point where the silicone portion of the model ended at the PUJ. The model was not compliant to any measurable extent.

The dust was prepared using quartz sand as the model and struvite dust as the reference data. A stock sample of quartz particles was prepared at <63µm, 63-125µm, 125-250µm, 250-500µm, 500-

1000µm and 1000-2000µm sizes. Equivalent sized struvite particles were recovered from ablating pure struvite canine stone with a P120 laser using 1J 10Hz standard short pulse, using the methodology documented earlier in this chapter. 83mg of particles from each of these 6 size fractions was measured on an Entris II balance (Sartorius Lab Instruments GmbH, Goettingen, Germany), combined and mixed thoroughly to make 500mg of uniform dust mixture. As it was not always possible to measure exactly 83mg, variation of up to +/- 10% was considered acceptable (74.7 – 91.3mg). The mass of each size fraction was recorded so that the exact starting particle size distribution was known. This uniform dust mixture was then introduced into the interpolar calyx of the kidney model, and the model carefully filled with sterile water without disturbing the dust. Saline could not be used as the salt would crystallize out of solution and interfere with particle size analysis.

A ureter adapter tube was constructed to capture all particles washing out of the kidney model while minimising potential for backflow. The proximal end of the adapter tube fitted over the end of the kidney's pelviureteric junction (PUJ) so that there was a step down from the PUJ into the adapter tube that would act as a gravity trap to prevent particles washing back up into the kidney. The distal end of the adapter tube drained into a container to collect the particles and fluid for analysis. The adapter tube also featured another port to allow a flexible ureteroscope to be introduced to the system via a long flexible tube.

The arrangement of the kidney and adapter tube is shown in Figure 86. The model was placed horizontally, representing a patient in the prone position. A LithoVue single-use digital flexible ureteroscope (Boston Scientific Corporation, MA, USA) was introduced via the secondary port of the adapter tube, and positioned in the interpolar calyx looking directly at the dust.

Irrigation was performed using a peristaltic pump (120 drive pump with 114DV pump head, Watson Marlow, Cornwall, UK). This allowed delivery of constant flow rates regardless of fluctuations in resistance up to 2 bars (200 kPa), which would be well above resistances from tubing and scopes in this experimental design. Irrigation time was fixed at 30 minutes to represent a typical ureteroscopy time. Irrigation rates were set at 15 ml/min, 30 ml/min and 120 ml/min with a 0 ml/min control set of experiments (i.e. no irrigation). These were selected with 30 ml/min representing a typical irrigation rate with modern flexible ureteroscopes with a completely open working channel [148, 149], 15 ml/min representing a typical irrigation rate with a 200µm-class optical fibre in the working channel [112, 148], and 120 ml/min to investigate the effects of (currently unachievable) very high irrigation rates. Note that 15 ml/min and 30 ml/min are likely to be on the optimistic over-estimates of what can be achieved clinically, as flow will be reduced further in practice by leakage from pressure cuffs, kinked tubing, occlusions in scopes, raised intrarenal pressure, etc. These results are therefore expected to represent a "best-case scenario" of the washout achieved by ureteroscopic irrigation.



Figure 86. Kidney model with ureter adapter tube. Fluid drains out of the primary port at the bottom for collection, and a flexible ureteroscope can be introduced via the secondary port to the left.

Prior to each experiment, the pump was calibrated to the required irrigation rate by adjusting the pump speed and measuring the amount of fluid pumped through the scope in 60 seconds. Irrigation was then directed towards the stone dust by an operator holding the ureteroscope. The ureteroscope was repositioned if no visible dust motion was observed on the endoscopic display, or at 5 minute intervals (whichever came sooner). The ureteroscope could be deflected, advanced deeper into the calyx or withdrawn up to the entrance of the calyx to maintain effective agitation of the stone dust. For the control experiments (0 ml/min irrigation rate), the ureteroscope was introduced and positioned as usual but the pump was not turned on and the scope was left stationary for 30 minutes instead.

Once 30 minutes of irrigation was complete, the pump was turned off and the ureteroscope gently removed from the kidney model. The horizontal kidney model was then rotated into the vertical position, to represent a patient sitting up or standing in the post-operative period, allowing the fluid and particles to drain under gravity. After this manoeuvre, any particles remaining in the kidney were considered to be retained, and any particles that had washed out (into the washout container or the adapter tube) were considered to be washed out. Any particles in the adapter tube were rinsed into the washout container. Particles from the two separate samples (washed out and retained) were separated by size by wet sieving using the same method previously described in this section, and weighed. Video data of the entire irrigation period was recorded from two sources. A 50 megapixel video camera (Pixel 6, Google LLC, CA, USA) was positioned above the kidney to record movement of particles through the transparent anterior surface of the kidney model. The endoscopic video feed was also duplicated and recorded on a UR-4MD surgical video recorder (TEAC Europe GmbH, Germany).

3 experiments were performed using quartz dust for each irrigation rate (0 ml/min, 15 ml/min, 30 ml/min and 120 ml/min) for a total of 12 experiments. A further 3 experiments were performed

using struvite dust at 15 ml/min to provide reference data, limited by the available quantity of struvite stone.

Results

Example still images from endoscopic views of struvite and quartz washout experiments are shown in Figure 87. Although the quartz model was not designed for the purpose of simulating the visual appearance of stone dust, it nevertheless does have a similar appearance both when settled in the kidney, and when agitated in turbulent flow.

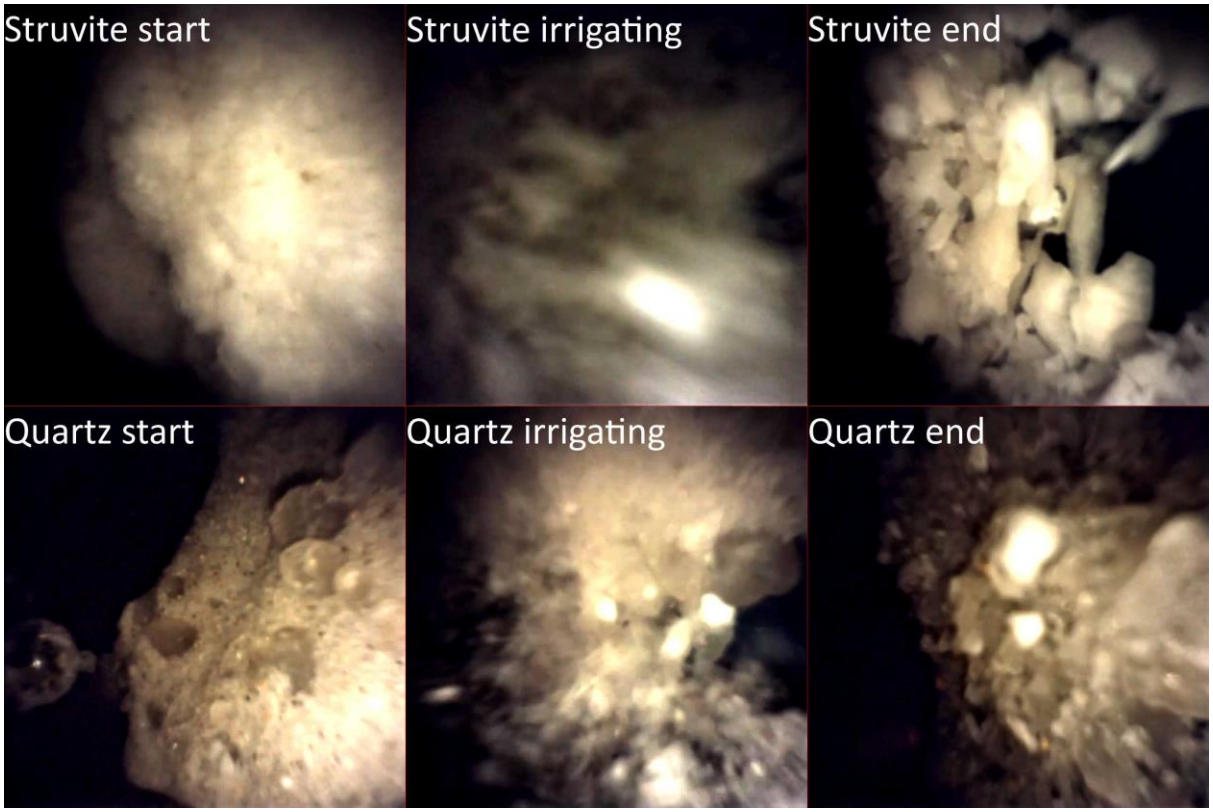


Figure 87. Quartz and struvite particle washout experiments - endoscopic appearances before, during and after irrigation. The irrigation rate was 15 ml/min for both particle types.

The subjective observations from endoscopic video of washout experiments were as follows.

At 15 ml/min irrigation rate, particles of all sizes could be agitated but larger particles could not be agitated into suspension, nor could they be displaced out of the calyx regardless of the angle at which they were irrigated. Smaller particles were seen suspended in a turbulent vortex being carried both out of and back into the calyx. Subjectively, the appearance of this vortex resembled clinical

appearances with high dust densities. At the end of irrigation, most smaller particles were cleared from the calyx but larger particles remained. Inspecting the renal pelvis showed a thick carpet of fine dust leading towards the PUJ and ureter, but with few particles reaching as far as the PUJ.

At 30 ml/min irrigation rate, larger particles still could not be agitated into suspension although some larger particles could be displaced out of the calyx. Particles were seen suspended in a similar turbulent vortex as was seen at 15 ml/min. At the end of irrigation, appearances of the calyx were similar to those seen at 15 ml/min. Inspecting the renal pelvis showed the same thick carpet of fine dust leading to the PUJ but with a few scattered larger particles. The carpet reached further and wider than at 15 ml/min but still few particles reached the PUJ.

At 120 ml/min irrigation rate, all particles were rapidly and almost immediately washed out of the calyx within a few seconds. A vigorous vortex was seen with larger particles in suspension, though within about 30 seconds no further particles were seen in the vortex. Despite this effective initial clearance of the calyx, a dense carpet of particles could still be seen settled in the renal pelvis and repositioning the scope (along with the irrigation jet) had almost no appreciable effect. Inspecting the carpet after irrigation showed that it contained more large particles than at lower irrigation rates, but did not obviously extend further towards the PUJ.

With no irrigation (i.e. control experiments), no agitation or displacement of particles was seen during the 30 minutes of experimental time.

Overhead video recording was also performed for all washout experiments. Example still images from these recordings are shown in Figure 88, taken from the start (immediately prior to commencing irrigation), mid-washout (after 15 minutes of irrigation) and end (after 30 minutes of irrigation, immediately after ceasing irrigation). In all cases, the final appearance was essentially unchanged from the mid-washout appearance, suggesting that all experiments had reached a state of equilibrium by the end where no further washout out of the kidney could be expected. These

overhead views illustrate the extent to which particles were displaced into the renal pelvis, as previously described.

At 120 ml/min, re-positioning of the tip of the ureteroscope did allow for some movement of particles from the renal pelvis. This can be seen in Figure 88 when comparing the mid-washout and end images, as a tiny amount of dust at the entrance to the lower pole calyces was displaced between these two images and there is a greater amount of dust at the PUJ. However, the volume of dust displaced here appeared to be very small.

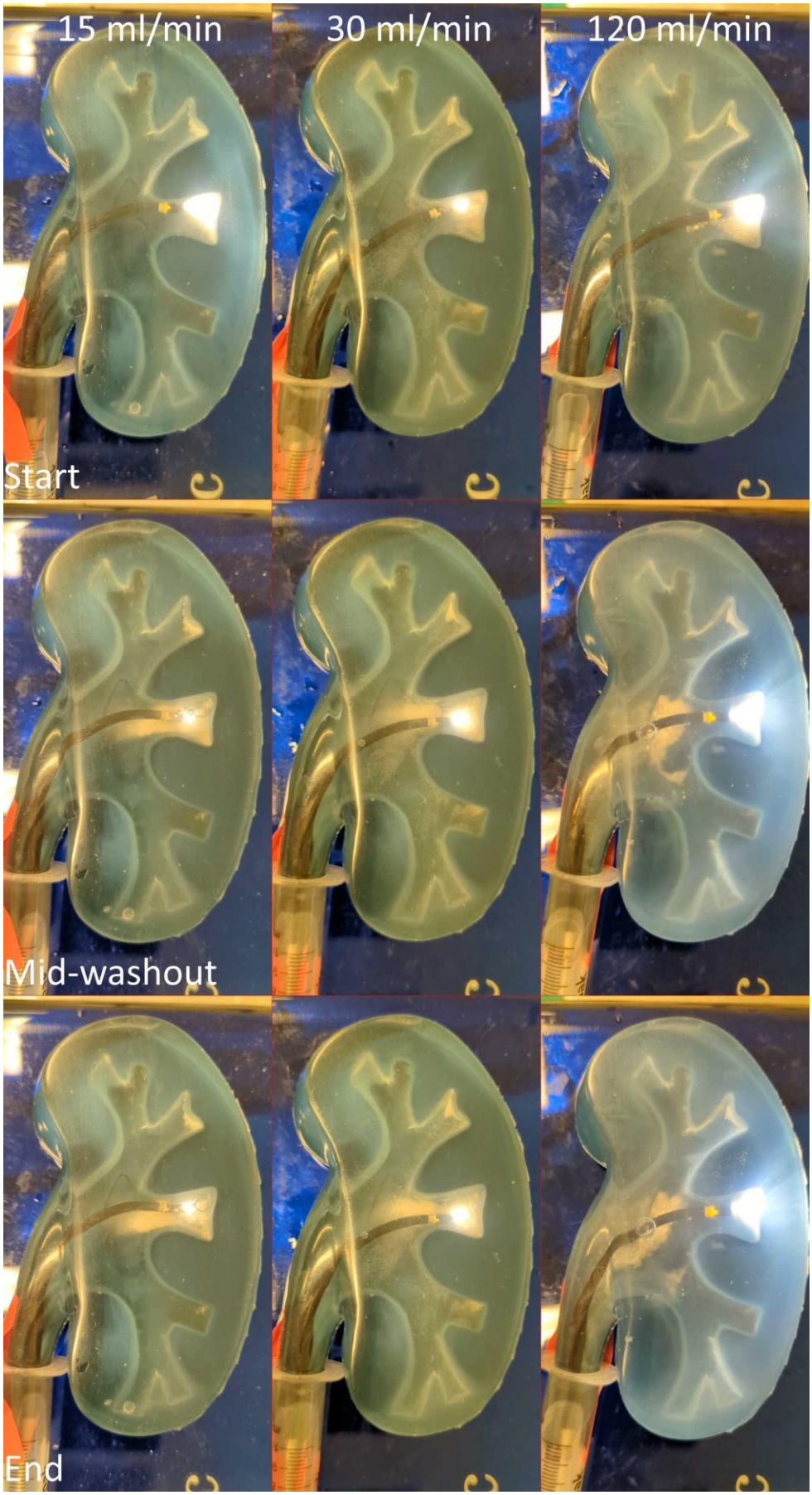


Figure 88. Quartz washout experiments. Columns represent different irrigation rates. Rows are different times before, during and after 30 minutes of irrigation.

Results for these washout experiments are shown in Figure 89, Figure 90 and Figure 91, with numerical results in Table 24. Each solid line represents a quartz washout result at the specified irrigation rate, and the dashed line represents the struvite result (at 15 ml/min only). Lost particles are calculated as the difference between the total recovered particles of a particular size (i.e. retained plus washed out) and the starting mass. This provides an estimate for the potential measurement error in the results, as it is not possible to retrospectively prove whether particles were lost from the retained sample or the washed out sample.

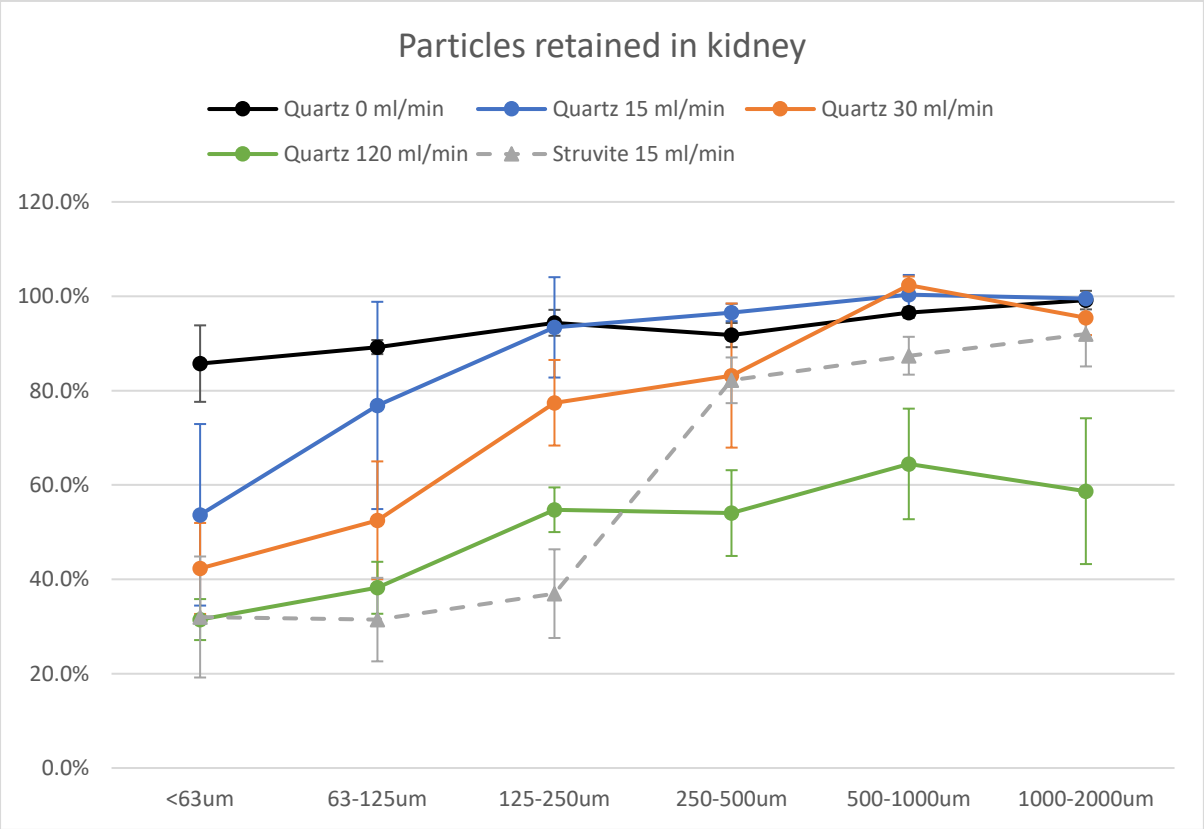


Figure 89. Washout results showing particles retained in the kidney after 30 minutes of irrigation. Results for each size fraction are a proportion of the respective size fraction's starting mass. Error bars indicate one standard deviation.

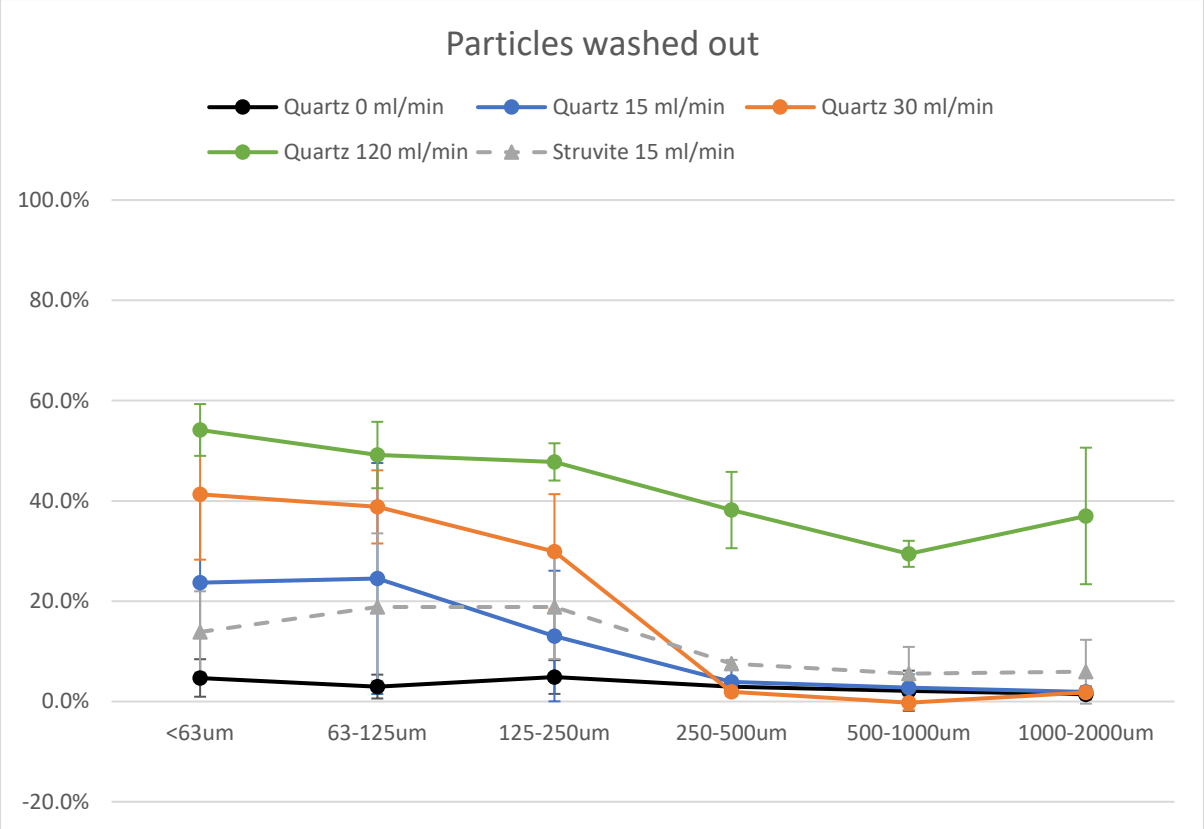


Figure 90. Washout results showing particles washed out of the kidney after 30 minutes of irrigation. Results for each size fraction are a proportion of the respective size fraction's starting mass. Error bars indicate one standard deviation.

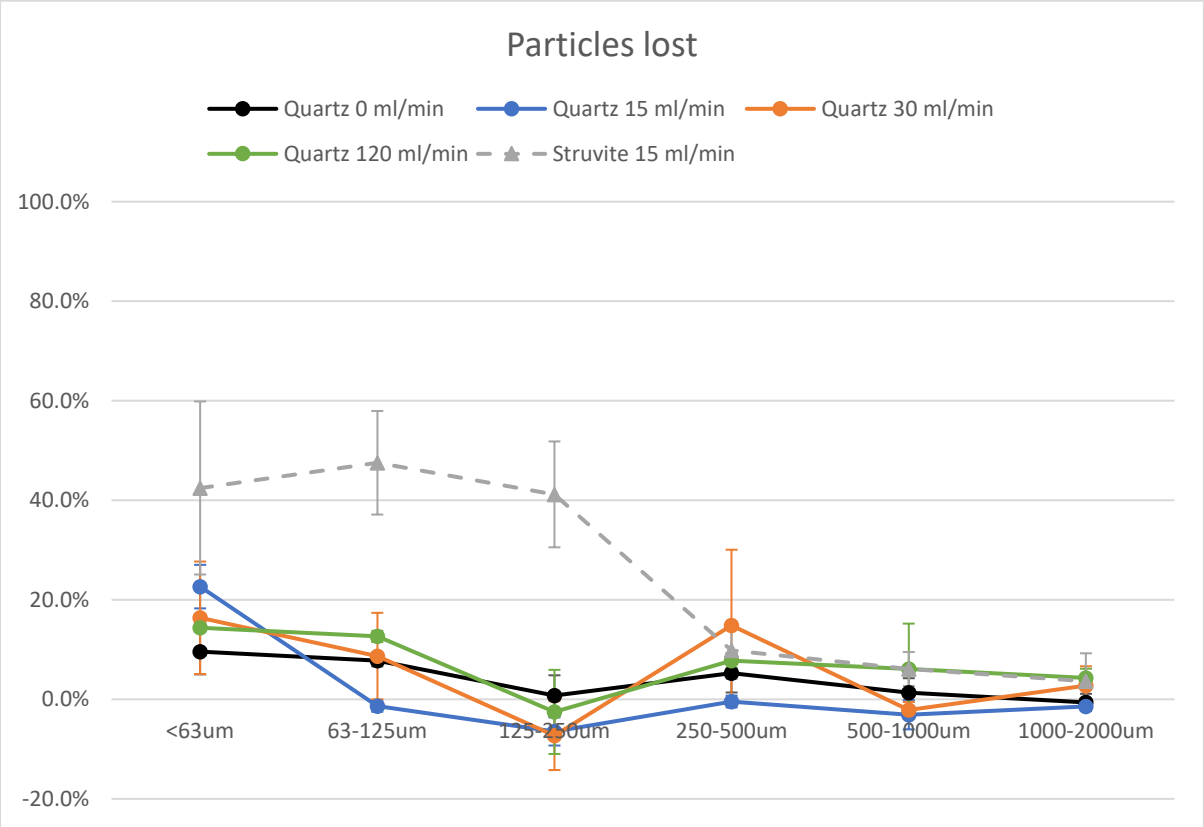


Figure 91. Washout results showing particles unaccounted for after 30 minutes of irrigation. Results for each size fraction are a proportion of the respective size fraction's starting mass. Error bars indicate one standard deviation.

As expected, there appears to be a relationship between irrigation rate and the efficacy of washout, with higher irrigation rates resulting in a greater proportion of particles washed out and lower proportion of retained particles at almost all particle sizes. The only exceptions to this are as follows:

- Quartz particles of size 250-1000µm are retained at a higher rate at 15 ml/min compared to the control, although the difference is not significant ($p = 0.06$ for 250-500µm, $p = 0.26$ for 500-1000µm).
- Quartz particles of size 500-1000µm are retained at a higher rate at 30 ml/min compared to 15 ml/min or the control. This difference is significant for the control ($p = 0.02$) but not for 15 ml/min.
- Quartz particles of size >250µm are washed out at a lower rate at 30 ml/min compared to 15 ml/min or the control. None of these differences were statistically significant. For 250-500µm particles, $p = 0.37$ for 15 ml/min and $p = 0.34$ for control. For 500-1000µm particles, $p = 0.18$ for 15 ml/min and $p = 0.41$ for control. For 1000-2000µm particles, $p = 0.92$ for 15 ml/min and 0.70 for control.

The only statistically significant exception is therefore that particles of size 500-1000µm are retained at a higher rate at 30 ml/min irrigation rate compared to control. Examining the individual experimental data, the difference appears to mostly result from a single experiment at 30 ml/min with a -3.7% particle loss at this size and simultaneous 32% particle loss at the next smallest size, 250-500µm. In other words, a greater mass of 500-1000µm particles was recovered than was introduced to the system, and there was a simultaneous unexplained and higher than average loss of smaller 250-500µm particles. There is no obvious scientifically plausible explanation for why an irrigation rate of 30 ml/min would cause more particles to be retained than no irrigation, and the observed data would be explained by some smaller particles being misattributed to the 500-1000µm size fraction during analysis. This difference is therefore unlikely to reflect a true underlying difference.

In terms of retained particles, it is noteworthy that >54% of particles in size fractions >125µm were retained in the kidney at all irrigation rates. When restricted to clinically achievable irrigation rates of up to 30 ml/min, this proportion increases to >77% of particles >125µm. However, there were negative lost particle calculations for some of these sizes, indicating that there must be some degree of measurement error resulting in a greater recovered mass than starting mass, as seen in Table 24. Once these are taken into account, the appropriate cut-offs are that >52% of particles >125µm were retained at all irrigation rates, and >70% of particles >125µm at clinically achievable irrigation rates.

Analysis of washed out particles confirms that these differences are a result of differences in washout rather than particle loss. When restricted to irrigation rates of up to 30 ml/min, <4% of particles in size fractions >250µm were collected from the washout, though it must be noted that particle losses of up to 15% were recorded for 250-500µm sizes. Once particle losses are taken into account, the appropriate cut-offs are that at clinically achievable irrigation rates of up to 30 ml/min, <19% of particles >250µm were washed out, and only <4% of particles >500µm.

Comparison of struvite and quartz washout at 15 ml/min shows that struvite has a lower proportion of retained particles at all size fractions, and this difference is more pronounced for smaller particles <250µm. However, the proportion of washed out particles is similar at all size fractions and this suggests that the difference mostly a result of particle loss rather than (or in addition to) differences in fluid dynamics, as seen in Figure 91. This likely stems from struvite's relatively high water solubility, which would explain why smaller particles (with a higher surface area to volume ratio) are disproportionately affected. This limits the usefulness of struvite as a reference point.

Examining the quartz particle losses shows that <6.9% of particle mass was lost (i.e. that >93.1% was recovered). This is in line with recovery rates for low solubility COM stone in previous experiments, and does not reveal any concerns regarding technical quality. Slightly higher proportions of particles <125µm were lost, which likely reflects the mechanical challenges in sieving and recovering these extremely small particles.

Quartz – Retained	0 ml/min		15 ml/min		30 ml/min		120 ml/min	
Size fraction	Mean	S.D.	Mean	S.D.	Mean	S.D.	Mean	S.D.
<63µm	85.7%	8.1%	53.7%	19.2%	42.3%	9.6%	31.5%	4.3%
63-125µm	89.2%	1.5%	76.9%	22.0%	52.5%	12.5%	38.2%	5.5%
125-250µm	94.4%	2.7%	93.4%	10.6%	77.4%	9.1%	54.7%	4.7%
250-500µm	91.8%	2.6%	96.6%	1.8%	83.2%	15.3%	54.0%	9.1%
500-1000µm	96.5%	1.1%	100.3%	4.2%	102.4%	1.8%	64.5%	11.7%
1000-2000µm	99.2%	2.0%	99.5%	0.2%	95.4%	3.7%	58.7%	15.5%
Total mass recovered	92.8%	2.3%	87.2%	8.7%	75.8%	7.4%	50.9%	8.1%

Quartz – Washed out	0 ml/min		15 ml/min		30 ml/min		120 ml/min	
Size fraction	Mean	S.D.	Mean	S.D.	Mean	S.D.	Mean	S.D.
<63µm	4.7%	3.7%	23.7%	18.1%	41.3%	13.0%	54.2%	5.2%
63-125µm	3.0%	2.4%	24.5%	23.0%	38.8%	7.3%	49.2%	6.6%
125-250µm	4.9%	3.4%	13.1%	13.0%	29.9%	11.5%	47.8%	3.7%
250-500µm	3.0%	1.3%	3.9%	2.8%	1.9%	0.8%	38.2%	7.6%
500-1000µm	2.1%	4.0%	2.8%	2.7%	-0.2%	1.5%	29.5%	2.6%
1000-2000µm	1.4%	1.0%	1.9%	0.8%	1.8%	1.2%	37.0%	13.6%
Total mass recovered	3.2%	2.0%	11.7%	9.6%	18.9%	4.6%	42.3%	4.8%

Quartz – Lost	0 ml/min		15 ml/min		30 ml/min		120 ml/min	
Size fraction	Mean	S.D.	Mean	S.D.	Mean	S.D.	Mean	S.D.
<63µm	9.6%	4.6%	22.7%	4.4%	16.4%	11.3%	14.4%	0.8%
63-125µm	7.8%	1.2%	-1.4%	1.1%	8.7%	8.7%	12.6%	1.1%
125-250µm	0.7%	4.1%	-6.5%	2.8%	-7.3%	6.9%	-2.5%	8.5%
250-500µm	5.3%	3.9%	-0.4%	1.2%	14.9%	15.2%	7.8%	1.5%
500-1000µm	1.3%	2.9%	-3.1%	2.9%	-2.1%	1.6%	6.1%	9.1%
1000-2000µm	-0.6%	1.7%	-1.5%	0.6%	2.7%	3.9%	4.3%	1.8%
Total mass recovered	4.0%	2.2%	1.6%	1.1%	5.5%	2.8%	6.9%	3.2%

Table 24. Quartz particle results for washout experiments after 30 minutes of irrigation at the indicated irrigation rate. Results for each size fraction are a proportion of the respective size fraction's starting mass. Total mass recovered is a proportion of the total starting mass. "Lost" particles indicates the difference between all recovered particles and the starting mass.

Struvite – 15 ml/min	Retained		Washed out		Lost	
Size fraction	Mean	S.D.	Mean	S.D.	Mean	S.D.
<63µm	32.0%	12.8%	13.9%	8.1%	42.5%	17.4%
63-125µm	31.5%	8.9%	18.8%	14.7%	47.5%	10.4%
125-250µm	37.0%	9.4%	18.8%	10.4%	41.2%	10.6%
250-500µm	82.2%	4.8%	7.6%	0.7%	9.8%	5.7%
500-1000µm	87.4%	4.0%	5.6%	5.3%	6.1%	3.4%
1000-2000µm	92.0%	6.9%	5.9%	6.4%	3.6%	5.6%
Total mass recovered	60.7%	3.9%	11.8%	4.8%	27.5%	4.9%

Table 25. Struvite particle results for washout experiments after 30 minutes of irrigation at the indicated irrigation rate. Results for each size fraction are a proportion of the respective size fraction's starting mass. Total mass recovered is a proportion of the total starting mass. "Lost" particles indicates the difference between all recovered particles and the starting mass.

Discussion

There are a number of limitations to these experiments are results. First, the limitations of the materials required (in particular the limited number of kidney models) meant that only 3 experimental repeats were performed for each irrigation rate. Although the standard deviations do not raise any concerns regarding the quality of data, future work should expand the quantity of data.

Quartz was used as the model for stone dust, and while this chapter documents the reasons for considering this as a valid model, there are nevertheless physical differences including the higher density of quartz, subtle differences in particle shape and differences in particle-to-particle interactions. The attempts to validate quartz against a canine struvite model were limited by the high solubility of struvite, resulting a high rate of particle loss and therefore an excessive scope for error. Further attempts to validate quartz should be made using an insoluble stone material for reference, such as calcium oxalate monohydrate, calcium phosphate or hydroxyapatite. In the meanwhile, it is reasonable to assume that any scenario where quartz particles are displaced would also be sufficient to displace equivalent sized, lower density stone particles.

The wet sieving method for particle size analysis also has some limitations. Although the sieve size is fixed, whether each particle passes through the sieve is an essentially stochastic process and therefore has some variability. This was seen in the results where on some rare occasions, a negative mass of lost particles was recovered (i.e. a greater mass of particles was recovered than was originally introduced), often accompanied by a greater than average lost particle mass in an adjacent size fraction. The most likely interpretation of this is that some recovered particles were being sieved to a different size fraction than their original category. For larger size categories, even a small number of such particles can result in measurable differences in the results, given the small absolute masses involved. Alternative methods of particle sizing could be considered to avoid this, though as previously discussed, sieving is the most well established method in the literature as well as having direct clinical relevance and being intuitive to understand.

Finally, as discussed in the introduction to this chapter, it is extremely difficult, if not impossible, to compare two particle size distributions in a meaningful fashion to determine if one is “larger” than the other. The methods described here are not suitable for drawing such broader conclusions, and restricted to narrow comparisons between individual size fractions or describing behaviour around specific size cut-offs.

Conclusions

These experiments demonstrate that a wet sieving technique is feasible (when performed diligently) for accurately and precisely separating stone and quartz dust by size for quantities on the scale of milligrams for the purpose of measurement. For insoluble particles such as COM and quartz, over 90% of starting mass could be recovered at the end of experiments, even with mechanically intensive interventions such as lasering and high flow irrigation.

When canine stone was ablated by hand in a Petri dish, characteristic particle size distributions were recorded for COM and struvite stones that did not appear to vary substantially with the laser settings used, with the majority of mass consisting of very fine particles <63µm in diameter but also approximately 20% consisting of larger particles >500µm.

Quartz is proposed as a widely available model for stone dust for the purpose of fluid dynamic experiments. It is insoluble in water and has a density (2.65 g/cm^3) between denser stone types such as calcium phosphate (3.14 g/cm^3) and less dense types such as struvite (1.7 g/cm^3). Commercially available water-weathered quartz has an irregular microscopic shape that is a better approximation for stone dust than spherical beads.

The results from the washout experiments provide convincing evidence that ureteroscopic irrigation at clinically achievable rates of up to 30ml/min is not effective at washing out quartz particles >250µm. Almost no such particles were recovered from washed out fluid, and over 70% were recovered from the kidney (once uncertainty from lost particles was factored in). Overall technical accuracy of the experimental process was satisfactory, with over 93% of starting particle mass

recovered from either the kidney or the washed out fluid. It was also noteworthy that increasing irrigation rate to 120 ml/min was still not sufficient for complete particle clearance, with 31.5 – 64.5% of particles still remaining in the kidney depending on size, and 51% of overall particle mass remaining in the kidney.

These experiments suggest that, although a substantial proportion of stone dust is likely to be very fine dust, a significant minority is likely to be produced as larger particles >500µm in diameter regardless of laser settings, and that those large particles are unlikely to be washed out from intraoperative irrigation or immediate post-operative drainage. Increasing the rate of irrigation to 120 ml/min may allow approximately half of these particles to be washed out, but achieving complete stone clearance is unlikely to be achievable using irrigation techniques alone.

6. Integrated model

Introduction

Chapter 5 demonstrated the expected particle size produced from laser ablation of stone in a bench setting under controlled circumstances, and the expected subsequent behaviour of those particles. However, that degree of control is rarely (if ever) achievable in clinical settings, and the lack of difference between dusting and fragmentation results raised the possibility that the results might be significantly different when laser ablation is performed in a kidney via a ureteroscope. In particular, it can be expected that laser emission is likely to contribute to driving turbulent fluid flow in a way that may differ in important ways from the irrigation flow, and this may in turn affect the movement of particles.

To investigate these effects, a set of experiments was designed to mirror clinical ureteroscopic laser lithotripsy as closely as possible, while maintaining a bench environment to enable precise measurement of particle size. It is envisioned that this experimental platform can be extended to measurement of ablation rate and retropulsion as well in future.

Methods

The same canine stone library from previous chapters was used in these experiments. Stones labelled (from chemical analysis) as 100% pure calcium oxalate monohydrate were used for these experiments, as these were the available stones with the lowest water solubility.

COM stones were selected with a diameter of at least 6mm, and weighed dry on a precision Entris II electronic balance (Sartorius, Goettingen, Germany). They were then pre-soaked in water for 24 hours and placed in the interpolar calyx of the same bespoke silicone kidney model described in Chapter 5 (Pulse Medical Demonstration Models, PA, USA). The model was then filled with sterile water and fitted with the same ureter adapter tube previously described in order to allow a

ureteroscope to be introduced while simultaneously collecting all particles washing down the ureter. The model was then laid horizontally, to simulate a patient in the supine position.

A single-use flexible digital ureteroscope (LithoVue, Boston Scientific, MA, USA) was introduced through the appropriate channel of the adapter tube. Sterile water irrigation was delivered via a 120D peristaltic pump with 114DV pump head (Watson Marlow, Cornwall, UK) connected to the irrigation port of the ureteroscope via a Tuohy-Borst adapter. As with previous particle experiments, saline could not be used as it would interfere with particle size analysis.

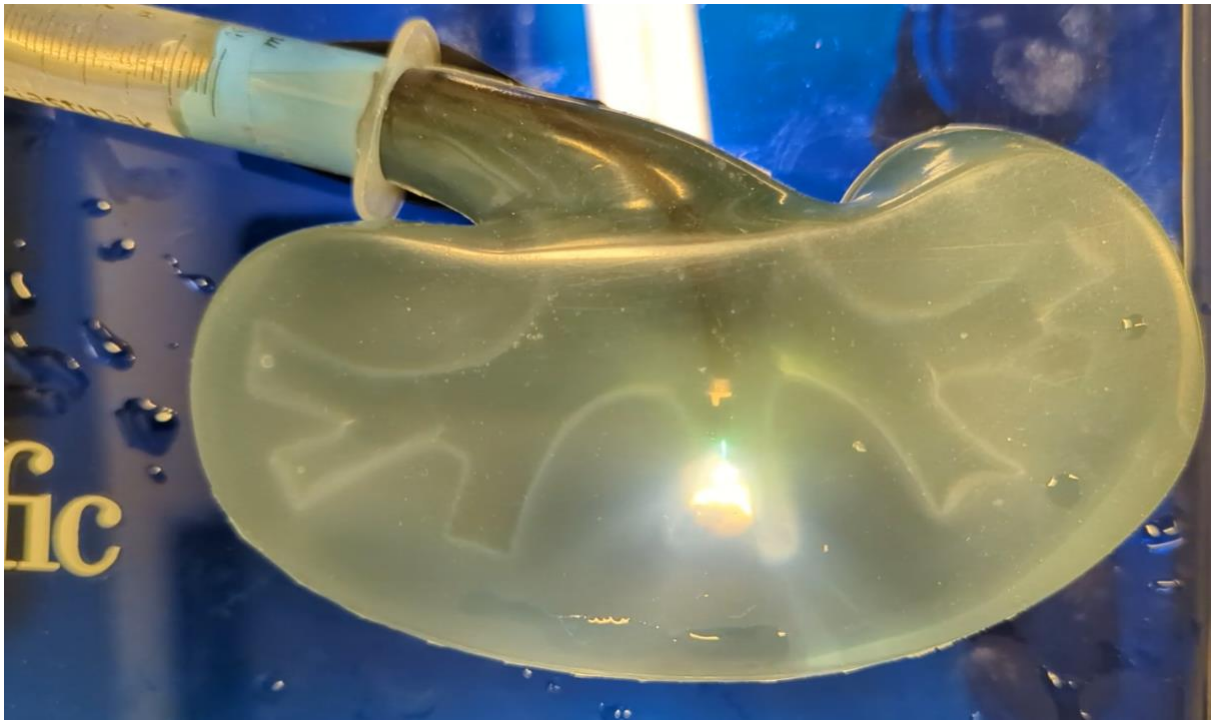


Figure 92. Integrated kidney model experiment. A canine calcium oxalate monohydrate stone is in the interpolar calyx, and a single use digital flexible ureteroscope with a 230um laser fibre is positioned ready to begin lithotripsy. Additional sealant has been added to the adapter tube to ensure a watertight seal.

The ureteroscope was directed towards the COM stone in the interpolar calyx, and the laser system was prepared. The P120 was used for these experiments in standard short pulse mode, with settings of 1J and 10Hz and a 230µm laser fibre. This allowed for direct comparisons with the corresponding Petri dish particle size experiments. The laser fibre was introduced down the port in the Tuohy-Borst adapter and the fibre/ureteroscope positioned in preparation for laser lithotripsy. Once setup was complete, a 50 megapixel video camera (Pixel 6, Google LLC, CA, USA) was positioned over the model to record video at 4K resolution and 30 frames per second. An illustrative still image of the

initial experimental setup is shown in Figure 92. Endoscopic video was also recorded by a UR-4MD surgical video recorder (TEAC Europe GmbH, Germany).

At the start of the experiment, the irrigation was initiated by turning on the pump and the operator (BY) performed laser lithotripsy in this simulated clinical environment, with the following restrictions to maintain consistency:

- Irrigation continued at the pre-determined rate until the end of the experiment.
- The laser settings were not modified at any point.
- The laser could be withdrawn to the tip of the ureteroscope to assist in repositioning, but was not withdrawn further so as not to interfere with fluid dynamics.

The endpoint was determined as the point when either all stone particles/fragments were visually judged to be <2mm in diameter, or when it was deemed by the operator that further laser lithotripsy was futile (at the pre-set settings and with the above restrictions).

Once lithotripsy was deemed to be complete by this definition, the irrigation was stopped by turning off the pump and the ureteroscope gently removed from the kidney model. In the same way as the quartz washout experiments, the horizontal kidney model was rotated into the vertical position to represent a patient sitting up or standing in the post-operative period, allowing the fluid and particles to drain under gravity. After this manoeuvre, any particles remaining in the kidney were considered to be retained, and any particles that had washed out (into the washout container or the adapter tube) were considered to be washed out. Any particles in the adapter tube were rinsed into the washout container. Particles from the two separate samples (washed out and retained) were separated by size by wet sieving using the method described in Chapter 5, and weighed.

Initially it was planned to perform 3 experimental repeats each at 15 ml/min, 30 ml/min and 120 ml/min irrigation rates, to match the quartz washout experiments. It was not thought to be feasible to perform a control experiment without irrigation, as thermal effects of prolonged lasering in a

31ml collecting system were anticipated to be unacceptable. However, early experience from initial experiments suggested that uncontrolled factors such as stone properties, surgical technique and movement of large fragments would have an excessive impact on lithotripsy and results, to the point where quantitative differences could not confidently be attributed to differences in controlled variables with the planned sample sizes and techniques. The full set of experiments was therefore not performed, but instead the limited data set obtained is presented here as qualitative data illustrating the differences from the methods described in Chapter 5. This data set consists of one experiment at each of 15 ml/min and 120 ml/min irrigation rates.

Results

Figure 93 shows still images from the overhead video recording of laser lithotripsy of COM stone at 15 ml/min irrigation rate. The images are at 2 minute intervals. The dry stone mass was 0.472g.

In the first 4 minutes, lithotripsy was rapid and the volume of stone rapidly decreased, with corresponding large quantities of fine dust produced and washed into the renal pelvis and PUJ. By 6 minutes, the initial stone was entirely fragmented but the fragments were relatively large and displaced into the renal pelvis. This is presumed to be a result of turbulent flow produced by laser emission, as this irrigation rate was insufficient to wash similarly sized quartz particles out of the calyx. Dust and larger fragments also began to accumulate towards the upper and lower pole calyces, presumably carried by the natural flow of irrigation fluid.

From 6 minutes to 16 minutes, laser lithotripsy proceeded in the renal pelvis on the remaining large fragments. It was not possible to re-locate these fragments back into the interpolar calyx with the actions of the ureteroscope, irrigation and/or laser. The size of these fragments decreases over this time, and an increased amount of dust and fragments was deposited towards the upper and lower pole calyces.

Following the images in this series, the scope was positioned in the lower and upper pole calyces to further ablate those fragments to completion, for a further 13 minutes (total 29 minutes).

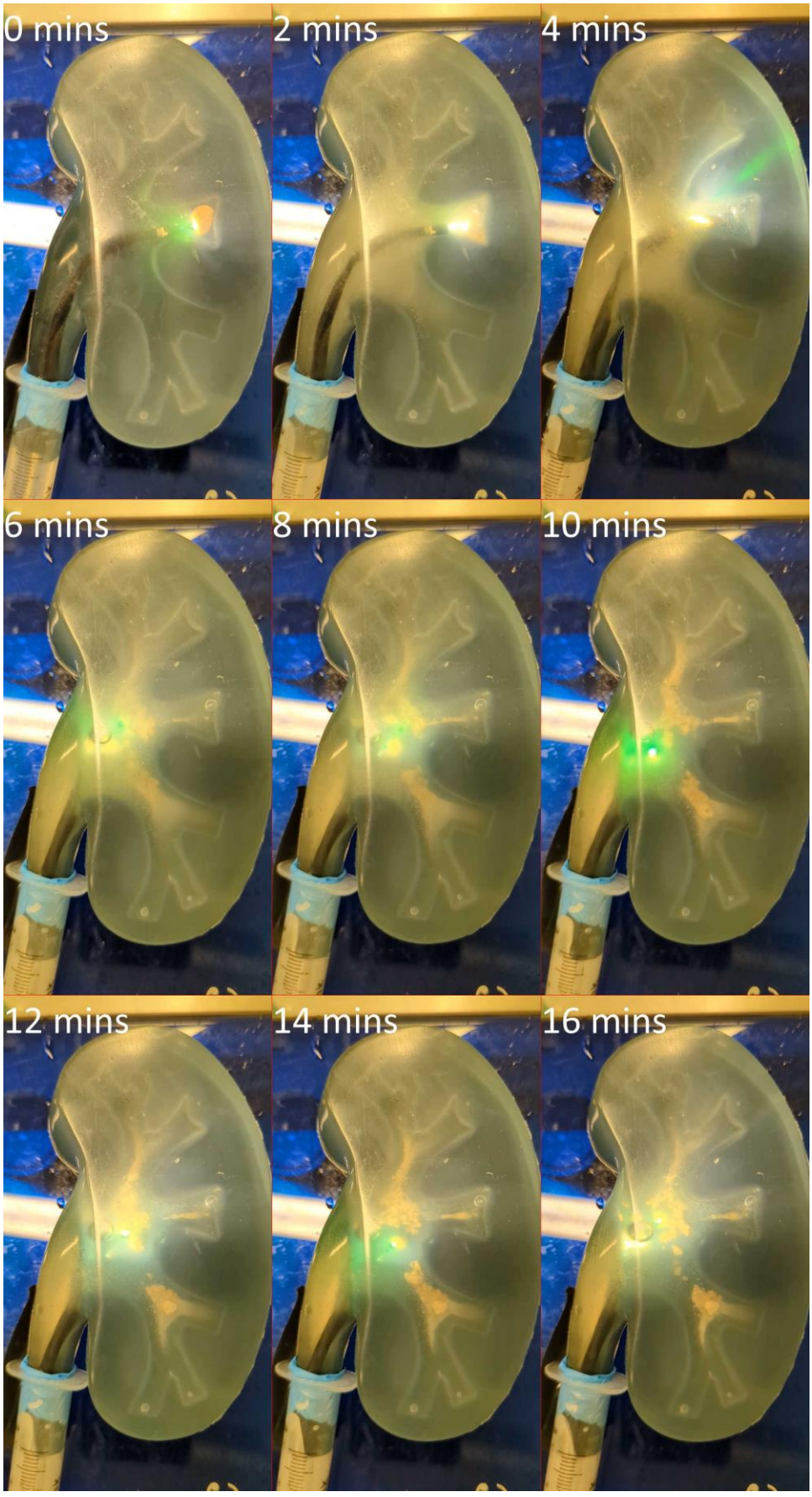


Figure 93. Laser lithotripsy of canine calcium oxalate monohydrate stone at 15 ml/min irrigation rate. Images are taken at 2 minute intervals.

Figure 94 shows the corresponding still images from the overhead video recording of laser lithotripsy of canine COM stone at 120 ml/min irrigation rate. Again, the images are at 2 minute intervals. The dry stone mass was 0.469g, almost identical to the previous experiment.

Similar to the previous experiment, initial lithotripsy rapidly decreased the visible stone volume. However, this phase took approximately 8 minutes compared to just over 4 minutes at the lower 15 ml/min irrigation rate, despite the similarly sized stone. The high 120 ml/min irrigation rate resulted in constant stone motion which impaired aiming of the laser beam, and likely reduced the rate of effective energy delivery to the stone.

During this initial phase of lithotripsy, the high rate of irrigation rapidly carried away fine dust and this was reflected with clear views in both the overhead and endoscopic videos. The effectiveness of the irrigation flow at removing larger particles and fragments was limited, and these particles were seen accumulating in the renal pelvis during these first 8 minutes. After this point, the stone split into two large fragments which were rapidly carried into the renal pelvis.

From 10 minutes to 16 minutes, the ureteroscope was withdrawn into the renal pelvis to ablate the remaining large fragments. During this period there was no noticeable decrease in the amount of particles in the renal pelvis despite the close proximity of both the high flow irrigation jet and the laser fibre tip. The fragments being ablated were gradually displaced towards the upper pole calyx which facilitated lithotripsy. This suggests that the flow generated by the high flow irrigation (which is necessarily away from the PUJ from the limited motion of the ureteroscope) counteracts any flow towards the ureter that might be produced by laser emission.

Following the images in this series, the fragments in the upper pole calyx were ablated to completion, for a further 8 minutes (total 24 minutes).

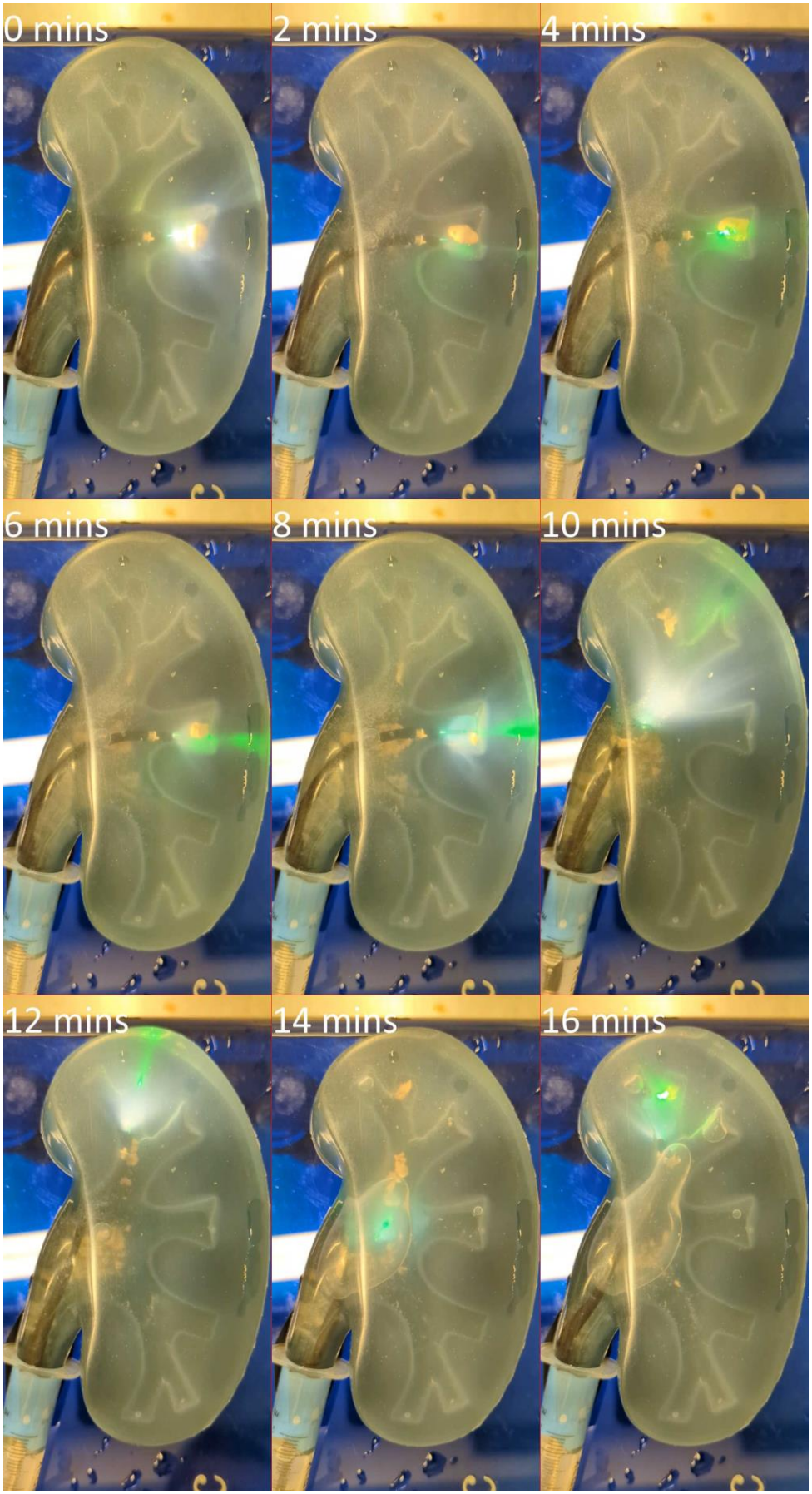


Figure 94. Laser lithotripsy of canine calcium oxalate monohydrate stone at 120 ml/min irrigation rate. Images are taken at 2 minute intervals.

Figure 96 shows the size and location of COM particles in the 15 ml/min irrigation rate experiment, with numerical results in Table 26. In total, 412mg of particles were recovered (87.5% of the starting 472mg dry mass). The size distribution of all particles had a similar bimodal distribution to that demonstrated in Chapter 5, except with a higher proportion of large particles in the 500-2000µm range (35.4% of recovered mass, compared to 21.0% when ablating in a Petri dish with the same 1J 10Hz P120 standard short pulse settings). There were also 22.3% of recovered particles >2000µm, indicating incomplete ablation, and correspondingly a smaller proportion 31.2% of particles <63µm. It is not possible to prove which particles were lost, but previous data in Chapter 5 showed a higher proportion of smaller particles lost for quartz and this is likely also the case for COM.

Analysis can also be performed on the rate of washout by particle size, similar to that done for quartz particles in Chapter 5. Some assumptions must be made here as, unlike with the quartz experiments, the true size distribution of all particles is not known. As 87.5% of the starting mass is recovered, the size of these particles is known but the size of the 12.5% of lost mass is not known. For the purpose of analysis, it was assumed that this mass was lost pro rata (i.e. that the proportions of each size fraction were unchanged from particle loss). The proportion of particles retained in the kidney is presented alongside data from Chapter 5 for quartz and struvite particle washout at the same 15 ml/min irrigation rate in Figure 97. It should be noted that these data sets are not directly comparable as the experimental protocols differed beyond inclusion of a laser for COM. The quartz and struvite data used a fixed duration of 30 minutes with the ureteroscope position restricted to one calyx, while the COM laser experiment continued for 29 minutes of irrigation and the ureteroscope was repositioned multiple times including into the renal pelvis. Nevertheless, the COM laser lithotripsy and washout curve closely resembles the struvite washout curve and it is not immediately apparent from this very limited data that the addition of an active laser has any impact on particle washout.

The COM particles retained in the kidney are shown in Figure 95.

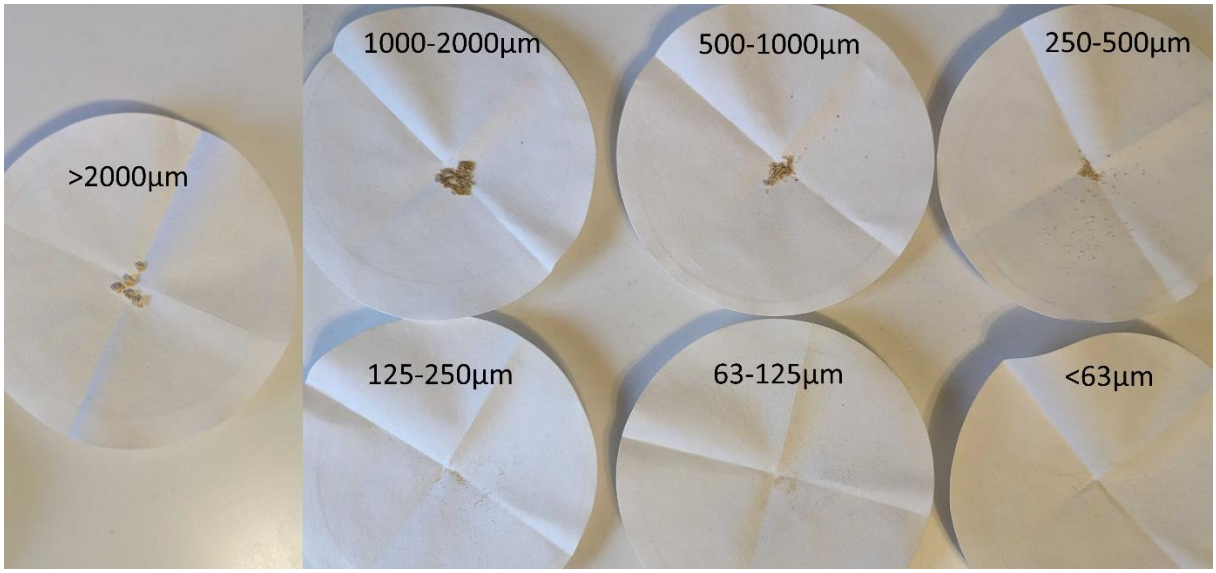


Figure 95. Calcium oxalate monohydrate particles retained in the kidney after laser lithotripsy and washout at 15 ml/min irrigation rate.

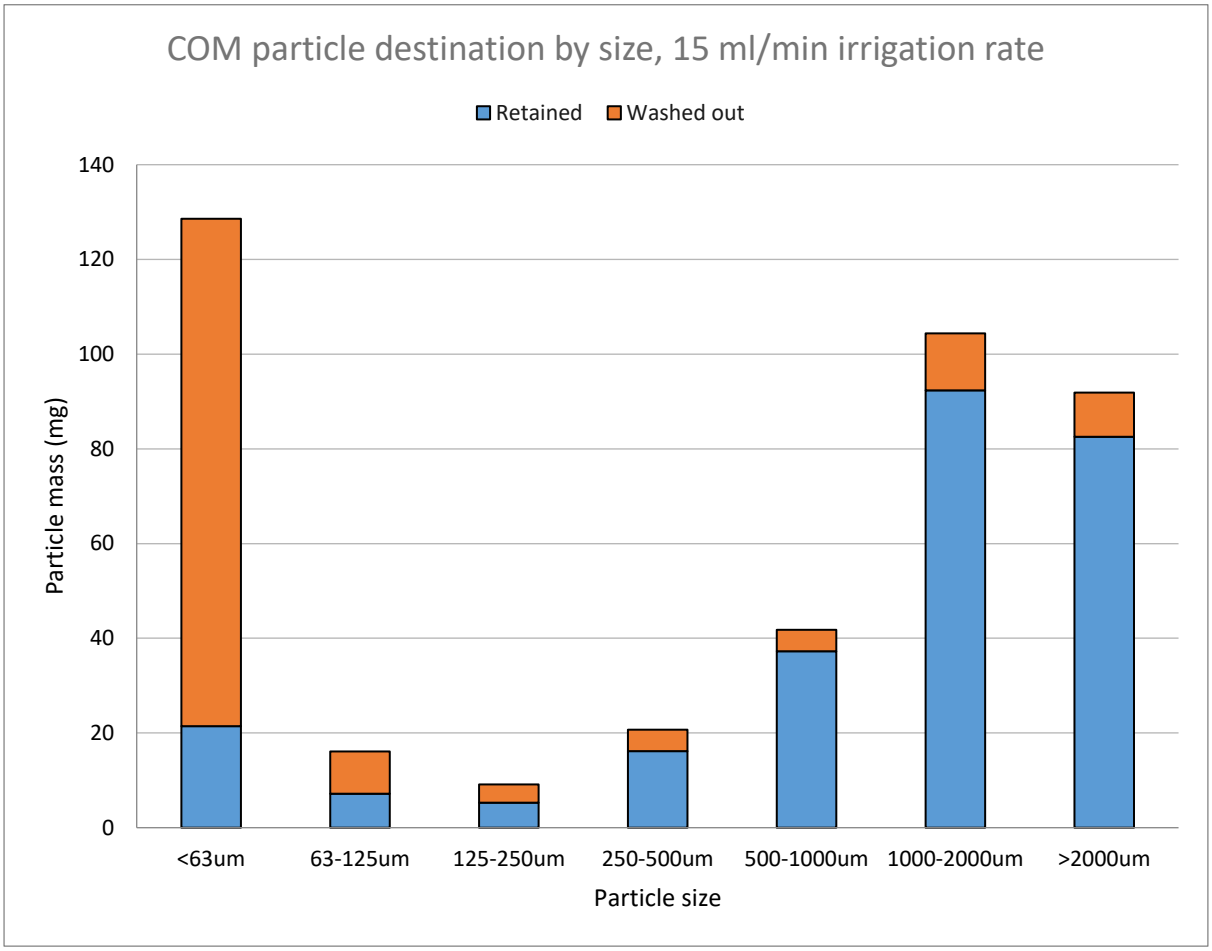


Figure 96. Calcium oxalate monohydrate particles produced from laser ablation in kidney model at 15 ml/min irrigation rate, by size and location.

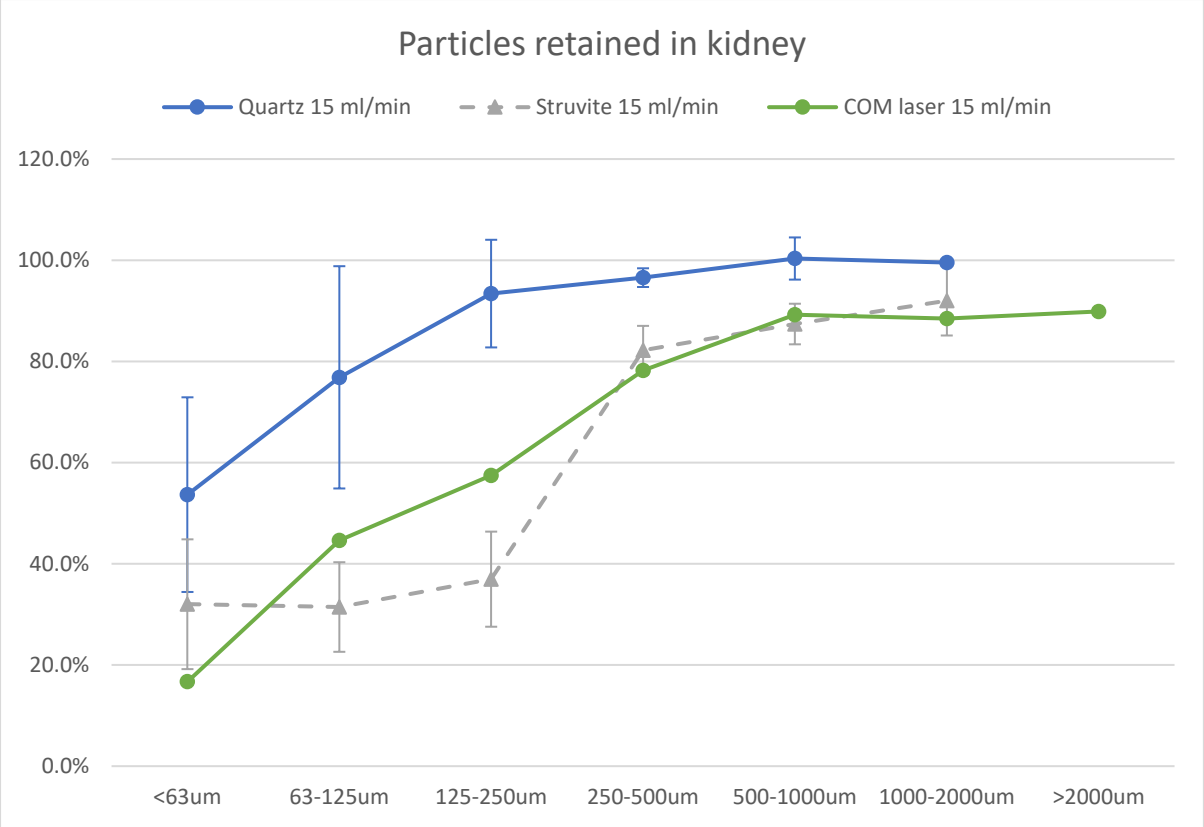


Figure 97. Particles retained in kidney. Data from COM laser ablation in the kidney model is presented alongside data from washout only for quartz and struvite.

The corresponding data for size and location of COM particles in the 120 ml/min irrigation rate experiment is shown in Figure 99, with numerical results in Table 26. In total, 313mg of particles were recovered (66.7% of the starting 469mg dry mass). The size distribution of all particles still had a bimodal distribution, but compared to previous results there was a much lower proportion of particles <63µm (10.2%, compared to 53.6% when ablating in a Petri dish with the same 1J 10Hz P120 standard short pulse settings) and a significant 59.0% of recovered particles >2000µm, indicating incomplete ablation. This is presumably related to the technical challenges involved in aiming the laser beam at the stone at an effective distance with the agitation produced by the 120 ml/min irrigation jet. It is unclear why the rate of particle recovery was so low compared to previous results, despite COM being relatively insoluble. The very low quantities of particles recovered from the washout (just 4.9%, compared to 31.9% from washout at 15 ml/min irrigation rate) suggests that this was where most particles were lost, and so it was not reasonable to assume that particles were lost pro rata or to attempt to perform analysis of proportions retained/washed out.

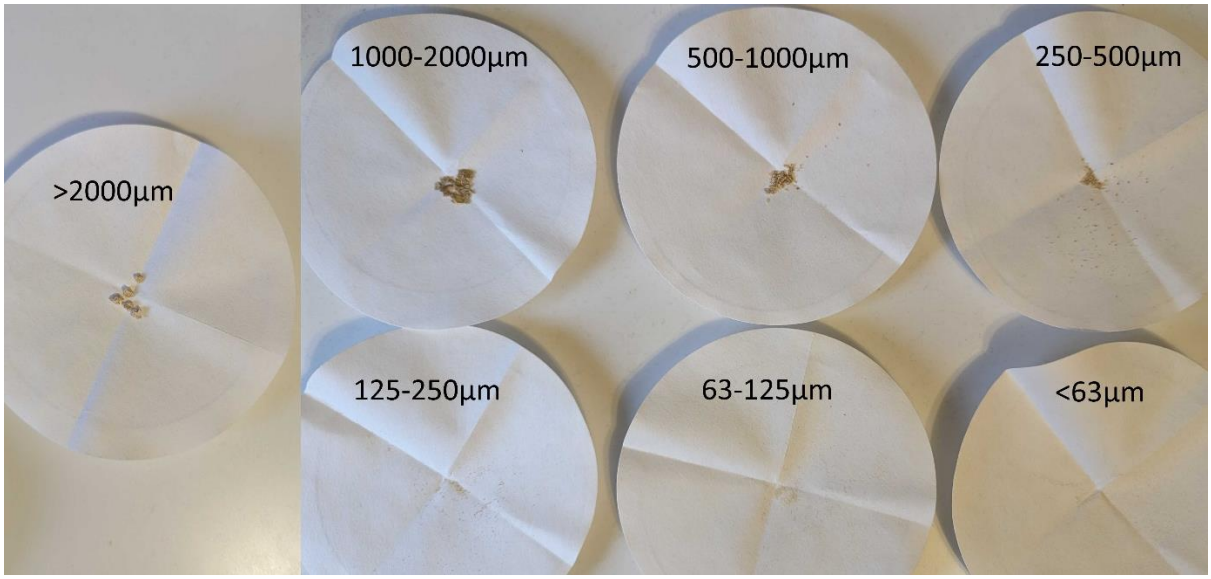


Figure 98. Calcium oxalate monohydrate particles retained in the kidney after laser lithotripsy and washout at 120 ml/min irrigation rate.

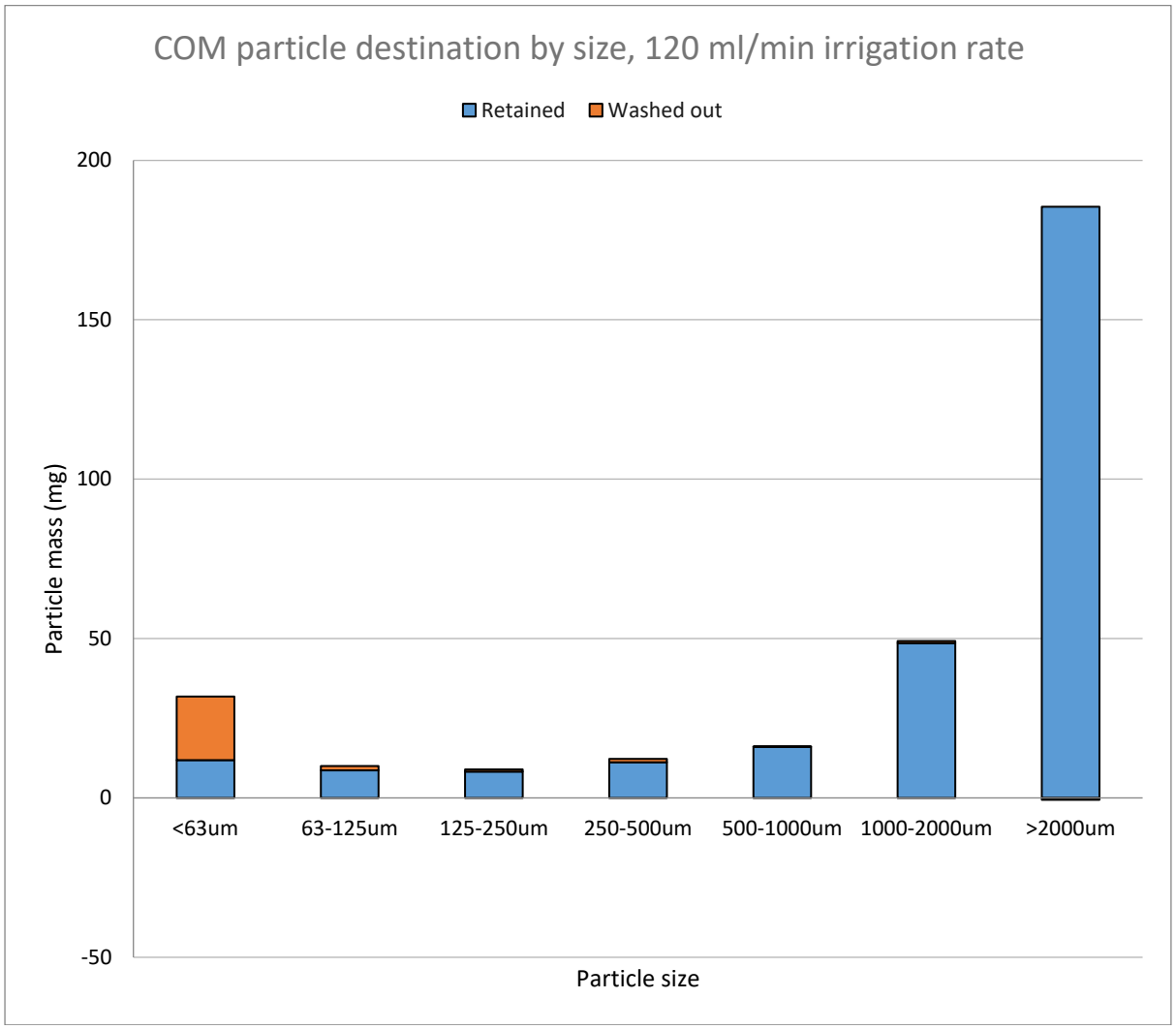


Figure 99. Calcium oxalate monohydrate particles produced from laser ablation in kidney model at 120 ml/min irrigation rate, by size and location.

COM – 15 ml/min irrigation	Retained (mg)	Washed out (mg)	Total (mg)
<63µm	21.5	107.1	128.6
63-125µm	7.2	8.9	16.1
125-250µm	5.3	3.9	9.2
250-500µm	16.2	4.5	20.7
500-1000µm	37.3	4.5	41.8
1000-2000µm	92.4	12.0	104.4
>2000µm	82.6	9.3	91.9
Total mass recovered	55.6%	31.9%	87.5%

COM – 120 ml/min irrigation	Retained (mg)	Washed out (mg)	Total (mg)
<63µm	11.8	20.0	31.8
63-125µm	8.6	1.4	10
125-250µm	8.2	0.7	8.9
250-500µm	11.1	1.1	12.2
500-1000µm	16.0	0.1	16.1
1000-2000µm	48.5	0.7	49.2
>2000µm	185.4	0.0	185.4
Total mass recovered	61.8%	4.9%	66.7%

Table 26. Calcium oxalate monohydrate particles produced from laser ablation in kidney model, by size and location.

Discussion

Laser lithotripsy and washout experiments in the bespoke kidney and ureter model appear to be technically feasible, with the potential to recover up to 87.5% of starting COM stone mass. This is comparable to the rates for washout alone (using quartz) or laser lithotripsy in a Petri dish (using COM).

The very limited data from these two experiments should be interpreted with caution, especially at 120 ml/min irrigation rate where the rate of particle recovery was abnormally low at just 66.7%. It is likely that technical issues contributed to this, as it was impractical for one person to perform the lithotripsy while simultaneously managing the irrigation fluid and outflow collection at such high flow rates. However, the data at 15 ml/min irrigation rate looks technically satisfactory and can be compared cautiously to the COM particle size data from lithotripsy in a Petri dish. The distribution of COM particles <2000µm can be plotted together in Figure 100. The data for lithotripsy in the kidney model bears a similar bimodal shape to the corresponding Petri dish “fragment” data (collected with the same P120 1J 10Hz standard short pulse laser lettings). However, lithotripsy in the kidney produced slightly fewer small particles (<250µm) than ablation in the Petri dish, and considerably

more very large particles 1000-2000µm. This is despite identical laser settings, fibre size, stone chemical composition, particle recovery method and similar rates of particle loss.

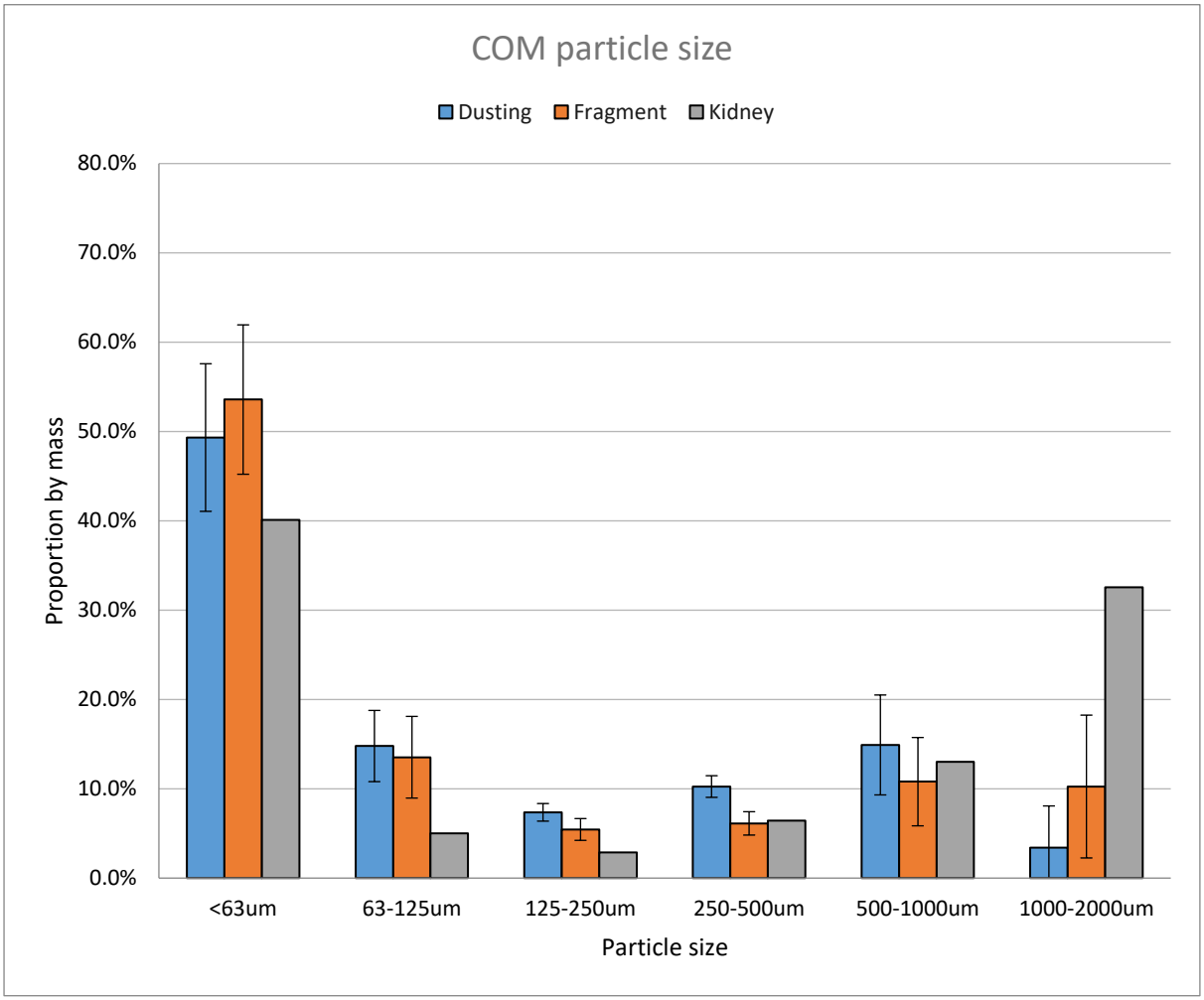


Figure 100. Calcium oxalate monohydrate particle distribution from laser lithotripsy. Dusting and fragment data was collected in a Petri dish while the kidney data was collected in the bespoke kidney model.

A potential explanation for this difference is that laser lithotripsy is the combined effect of (at least) two distinct underlying mechanisms:

1. A “dusting” action where the energy from a laser pulse is distributed relatively evenly throughout the ablated volume, resulting in the simultaneous formation of a large number of relatively small (mostly <250µm) particles.
2. A “fragmenting” action where the energy from a laser pulse is distributed unevenly through a line or plane, resulting in the majority of the ablated volume being ejected as a single,

intact, large (usually >250µm) particle accompanied by a smaller amount of relatively small particles.

Both these principles are well established in clinical practice, and both have also been observed in COM laser lithotripsy both in the Petri dish and in the kidney model. This would explain how laser lithotripsy in the kidney model could produce different COM particle size distributions. In the Petri dish, the painting technique could be maintained with a high degree of consistency and this may have skewed the laser mechanism of action towards dusting, as relatively few larger fragments were seen being ejected from the stone. It is possible that stabilising the stone using the forceps may have also had an effect on how energy was dissipated throughout the stone. Meanwhile, in the kidney model (or in clinical environments) it is often not possible to consistently maintain a painting technique, and this may have skewed the laser action towards fragmenting as larger fragments were frequently seen.

It is therefore hypothesised that "particle size distribution is a function of the physical constraints/movement of the stone" (in addition to stone properties and laser properties). Establishing the truth or falsehood of this hypothesis is critically important to understanding the relationship between lasers and particle size. If it is true, then bench experiments for particle size must be done in physical conditions that match clinical environments in order to produce relevant results.

It would be possible to test this hypothesis by designing a set of experiments similar to the Petri dish lithotripsy experiments in Chapter 5. Two sets of experiments could be performed with matched stone types and laser settings. In the first set, the stones would be fixed and immobile (for example, by being partially embedded in a resin), and in the second set the stones would be free to move within a designated space (such as a small round flask). The stones would then be ablated using matched laser settings under a suitably designed protocol, such as the visual <2mm size target

protocol used in these experiments, and the resulting particles sized by a suitable method such as wet sieving.

Conclusions

The limited data from these two lithotripsy experiments visually illustrates the products of laser lithotripsy in the form of fine dust and larger fragments, and their distribution within the collecting system of the kidney. It suggests that high proportions of retained particles following washout seen with the quartz washout experiments (especially larger particles >250µm) is likely to also be the case for COM stone with concurrent laser lithotripsy.

This set of experiments may be extended to additional stone types and laser types/settings, but the sample size must be calibrated for the expected high degree of variance. Regrettably, the available library of canine stones was thought to be insufficient for a meaningful sample size in these experiments.

The size distribution of COM particles from laser lithotripsy in the kidney model resembles, but does not exactly match that seen when lithotripsy is performed in the Petri dish. This raises the possibility that particle size is a function not only of the stone type and laser settings, but also the physical constraints of the stone. This question must be answered for future bench particle size experiments to be designed robustly, and a possible experimental method is outlined in the discussion.

7. Conclusions

The data from these experiments point to some high level conclusions on the lasers commonly used for modern stone surgery. Although three specific models were used (the P120 as an example of a Ho:YAG laser, the Soltive as an example of a TFL and the prototype as an example of a Ho:YAG laser with next-generation pulse modulation), it is likely that conclusions for standard, non-pulse-modulated pulses are likely to also hold for other models, based on the similarities between reported pulse measurements.

The following sections will correlate the findings from each these experiments to contemporary literature and clinical outcomes.

Ablation rate

All 3 lasers tested produced broadly similar, high levels of ablation rate on BegoStone models that scaled close to linearly with average power. All lasers' ablation rates were influenced by experimental setup, primarily the speed at which the laser was moved across the surface of the stone. This was particularly true for the Soltive laser, where very high scan speeds of >5mm/s were required for optimal ablation rate, and where failure to do so resulted in substantial reductions in ablation rate or even failure to ablate altogether. These findings corroborate those of other authors who report using similarly high scan speeds for TFL [89, 121].

The ablation rate at distance experiments demonstrated a significant Moses effect for all 3 lasers. This is well known for Ho:YAG lasers but not expected for TFLs, which have a much higher water absorption and were expected to behave as contact-only lasers. Instead, clear and deep ablation trenches were demonstrated for TFL at a working distance of up to 2mm (at 0.2J 200Hz short pulse). High speed video photography of the vapour bubble produced by TFL and some mathematical modelling suggests that the prolonged duration of the TFL pulse results in a significant amount of

the energy being delivered during bubble expansion, leading to a Moses effect even without any of the pulse modulation that is required for Ho:YAG lasers.

These experiments have been unable to replicate the findings of some other in vitro experiments that showed a significantly higher (sometimes double or more) ablation rate for TFL compared to Ho:YAG lasers in vitro on both BegoStone [89, 121] and actual stones [96, 114]. The largest differences were reported with actual stones, while the differences with BegoStone were smaller. This may therefore be a limitation of the BegoStone model for ablation rate.

Early data from clinical use of TFLs is now being reported. Many of these are non-comparative case series [97-101] though there are also a handful of randomised controlled trials (RCTs). Haas et al report a single centre RCT comparing a 120W Moses 2.0 laser from Boston Scientific/Lumenis (presumably the P120h) with the Soltive for 108 patients [150]. This is of particular interest since these are two of the exact lasers used in Oxford. They used Moses contact for Ho:YAG fragmentation, Moses distance for Ho:YAG dusting, and short pulse for the Soltive throughout. Starting laser settings were defined but changes were left to the surgeons' discretion. They reported no significant differences in stone-free rate (by two different measurement methods), laser-on time, total operating time, complications or post-operative quality of life.

Ulvik et al report a single centre prospective RCT comparing a Medilas H Solvo 30W with the Soltive for 120 patients [151]. They restricted laser settings to a maximum of 0.4J 6Hz in the ureter (2.4W) and 0.8J 20Hz in the kidney (16W). They reported no significant difference in laser-on time or total laser energy, but a significantly shorter total operating time for Soltive. They also reported significantly more intraoperative complications for Ho:YAG including bleeding impairing vision. This specific complication is rarely found or reported on in other literature, so it is not clear whether this is a wider problem. They hypothesise that the shorter total operating time for Soltive is a result of "superior endoscopic vision" but it is not clear whether they are referring to the lower rate of bleeding impairing vision or something else.

Taratkin et al report a single centre RCT comparing an unspecified Ho:YAG laser from Lumenis to a superpulsed TFL from NTO IRE-Polus for 94 patients [101]. This has been reported elsewhere as being a 50W average power TFL with a maximum 500W peak power, able to operate in both pulsed and continuous wave modes [97]. The primary goal of this paper appears to be the comparison between 150µm and 200µm fibres for the TFL, and details of the Ho:YAG laser are scant other than it being "a conventional Ho:YAG without pulse modulation". Laser settings were recommended to surgeons but left to their discretion, so it is not known if the available average power was comparable between the Ho:YAG and TFL arms. They reported a significantly lower laser-on time for TFL with 200µm compared to Ho:YAG, but again no significant difference in total operating time between these two groups, with a reported p value of 0.054. For unclear reasons, the text states "Both [150µm and 200µm fibre TFL total operation time] durations were shorter than that in the Ho:YAG group (90.0 ± 31.8 min, p = 0.006)" but this pooled comparison is not referenced in their methods and the corresponding p value does not appear in their results tables. No direct comparison was reported (or planned) between the 150µm fibre TFL and Ho:YAG groups.

No doubt there will be more direct RCT comparisons of Ho:YAG lasers to TFLs in the future. However, the limited data from the handful of RCTs published so far suggests that, at the very least, the dramatic in vitro ablation rate advantage of TFL has not translated into a consistent difference in total operating time or even laser-on time. It remains to be seen if greater familiarity with the TFL will change this, but if it does not then the conclusion must be that non-laser factors limit (and potentially even eliminate) the benefit from increased in vitro ablation rate. Some of these limitations may result from TFL's affinity for higher scan speeds, which may be impossible in clinical use. Others factors include:

- Laser fibre to stone distance
- Stone motion requiring re-positioning
- Visibility

- Patient factors including respiratory motion
- Stone chemical and physical structure
- Surgeon familiarity with the laser
- Surgeon skill with ureteroscopy

None of these factors are truly independent of the choice of laser, but will be impacted by different lasers (and laser settings) in different ways that are not readily modelled in vitro.

Although the evidence is not yet conclusive, a tentative and forward-thinking interpretation of the experimental and clinical data would be that laser ablation rate has reached a "saturation point" where current generation Ho:YAG and TFLs such as the P120 and Soltive are able to provide sufficient ablation rate to achieve near-maximal ablation rate in clinical use (with the appropriate settings and used by a sufficiently experienced surgeon), and future research would be better directed towards other parameters.

Retropulsion

Clinicians' understanding of retropulsion has evolved over time, and is still evolving. Early photoacoustic lasers such as the pulsed dye laser and Q-switched Nd:YAG laser relied on plasma formation, producing almost no heat but large amounts of mechanical energy. This mechanical retropulsion could be used to disimpact stones but sometimes required concurrent use of alternative treatments such as extracorporeal shockwave lithotripsy or antegrade access if a stone was retropulsed into the kidney [152, 153]. Retropulsion was often acknowledged [39], but rarely discussed as a target for intervention – presumably due to the lack of alternatives, with electrohydraulic lithotripters described as inferior and very limited options for ultrasonic endoscopic lithotripters at that time.

The rise of Ho:YAG laser lithotripsy raised the importance of retropulsion as kinetic energy delivery to the stone was no longer integral to the mechanism of lithotripsy. This necessitated methods of measuring and quantifying retropulsion. Many early methods involved modelling retropulsion as a

single instantaneous force which could then be quantified by measurement of a single retropulsion distance.

The recent popularity of TFLs has produced a consistent subjective experience that was often presented as “TFL produces less retropulsion”, using these single measure methods of quantifying retropulsion. The data from these experiments shows that the true picture is more complex, where a single laser at a given setting that starts in contact with a stone can be expected to produce a range of retropulsion trajectories. Individual parameters such as retropulsion distance or initial velocity are often related, but do not always correlate with each other. For example, at 0.5J 40Hz settings, Soltive in short pulse mode generates a similar average initial retropulsion speed and final retropulsion distance to P120 in Moses distance mode in these experiments, but the trajectories differ dramatically. Soltive produces a constantly accelerating stone with little variation between consecutive pulses or between experimental repeats, while P120 Moses distance produces an erratically accelerating and decelerating stone with sometimes unrecognisable trajectories between experimental repeats.

The methods described in these experiments provide a method to characterise and quantify these differences in an objective manner.

- The NRSS provides a single numerical value that represents all variability between experimental repeats. In other words, it quantifies how predictable or unpredictable the trajectory will be, with a value of 0 being completely predictable.
- The collated retropulsion trajectories for each laser and laser setting combination shows the range of motions a clinician might expect.
- The individual parameters of initial retropulsion speed, maximum retropulsion speed and displacement can be used in conjunction with the NRSS to categorise similar retropulsion patterns.

This work provides an objective framework for describing stone retropulsion with minimal data loss (as opposed to summarising retropulsion with a single parameter such as speed or displacement, which loses large amounts of potentially critical data). It is hoped that using this framework, clinicians and technologists will be able to identify patterns of retropulsion that are clinically advantageous in certain settings, and find other lasers or settings that produce similar retropulsion patterns.

Today the conversation on retropulsion is moving away from the overly simplistic "TFL produces less retropulsion" and towards more nuanced interpretations such as "TFL produces a better retropulsion pattern for dusting" or "Ho:YAG produces a better retropulsion pattern for pop-dusting". Further work needs to be done to translate from the objective measurements produced by these methods, to the subjective benefits associated with certain clinical techniques. Although not the focus of this work, the hypotheses formed to explain clinical experience are that:

- Low NRSS (i.e. low variability) results in more predictable behaviour which can be compensated for more easily, and may result in less perceived retropulsion.
- High NRSS (i.e. high variability) results in more unpredictable behaviour which may break up laminar flow and may assist with pop-dusting.
- Accelerating stone motion (i.e. initial retropulsion speed is much less than maximum retropulsion speed) occurs when the stone is accelerated by a series of consecutive pulses, and is associated with lower NRSS and more predictable behaviour.

Future work should consider the effects of ureteroscopic irrigation, the altered fluid dynamics within a ureter or kidney, and friction from urothelium. From a technical feasibility perspective, this work has demonstrated that high speed video photography can be performed in the bespoke kidney model at 10,000 frames per second, which is sufficient for the computer vision-based trajectory analysis described here. However these factors are all individually complex, and a high degree of variability was seen even in the simplified, unconstrained low-friction model. Serious consideration

therefore needs to be given to whether any of these can be reasonably modelled in vitro, and if so what experimental adaptations would be required to produce meaningful results.

Finally, it is noteworthy that the prototype laser was able to produce retropulsion trajectories that resembled the Soltive in dusting mode, regardless of the pulse modulation or laser settings. Pulse energy measurements (as well as the changes in retropulsion velocity from each pulse) suggest that initial pulses especially in the first 300ms after emission begins have lower energy than the setting selected on the console. The equipment available was not able to accurately measure the extent of this "ramp-up" such as the exact amount of energy or the time when ramp-up was completed, other than then steady-state pulse energy matching the selected setting. It is also not known if this was intended behaviour. Regardless, this ramp-up results in a retropulsion profile with features similar to Soltive dusting settings (0.2J 100Hz short pulse and 0.5J 40Hz short pulse), in that the trajectories are consistent and predictable with a low NRSS, the initial retropulsion velocity is low, and there are no significant negative retropulsion velocities seen. Even if unintentional, this behaviour merits further investigation as clinicians may find the trade-off of reduced initial energy delivery (that will inevitably result in reduced ablation rate) worth the benefit of a retropulsion profile that is anticipated to be well suited to dusting.

Particle size

Particle size is a difficult parameter to research experimentally primarily because of the dearth of high quality evidence on the scientific objectives. Even the clinical objectives are somewhat contentious – at a high level, clinicians wish for the patients they treat to become and remain stone- and symptom-free, but there is no universal agreement on the specific targets. A recent review [154] highlighted the relatively orthogonal nature of using clinical outcomes (such as stone-free rate, SFR) versus patient-reported outcomes (such as quality of life) versus cost-effectiveness, as methods to quantify treatment success. Although it was once popular to leave "clinically insignificant residual fragments" up to 4mm in diameter [155], both the concept (of leaving known stone behind) and the

size limit have come under greater scrutiny, particularly as changes in technology and clinical practice have lead to clinicians treating stones that might have been considered insignificant by this definition. There has been greater interest in leaving patients truly stone free, sometimes referred to as a zero fragment rate. While it is not clear if this improves clinical outcomes or re-intervention rates, it does provide an incentive to understand the behaviour of these smaller particles.

This work has focused on one aspect of laser lithotripsy induced particle size, which is the size distribution of particles in “stone dust”. This is an ill-defined term that is used by clinicians in diverse ways, but generally refers to products of laser lithotripsy that are thought to be clinically inconsequential and therefore do not require further treatment or removal. Attempts have been made to define stone dust based on in vitro behaviour [76], but it is not known whether this translates to clinical outcomes. Clinical research on such fine particles is hampered by the limitations of post-operative assessment – even the gold standard of computed tomography (CT) scanning is limited by the distance between individual radiological cross-sectional slices. Even modern ultra-high-resolution CT scans are only able to acquire slices of 0.2-0.3mm [156] and are generally reserved for specific clinical indications that do not include urinary calculi. Conventional CT scans used most commonly for stone disease usually have a distance between radiological slices of 0.6-0.8mm [157, 158] before reconstructing the image by combining radiological slices for an effective slice distance of 2-5mm [159]. This means that particles smaller than 0.6mm in diameter may be completely missed by the tomography slices, and particles smaller than 2mm might be missed in the computational slice reconstruction process (or impossible to positively identify as calculi). These numbers are already on the most optimistic side as they assume that the long axis of the stone lies perpendicular to the slices, and that image quality is not further impaired by the desire to reduce radiation dosage by further increasing slice distance.

Because of the difficulty in measuring particles in vivo, it is anticipated that future stone particle size research will follow these experiments in being predominantly based in vitro. This work has

demonstrated the expected washout behaviour of a range of stone and quartz dust particles from <63µm diameter to 2mm diameter in a simulated kidney model. It has shown a “transition point” at a diameter of 250µm, with smaller particles being mostly washed out at clinically achievable ureteroscopic irrigation rates of 15-30ml/min, and larger particles mostly being retained in the kidney. Despite the drastic differences in both methodology and endpoints, this mirrors the findings of Keller et al [76] in their sedimentation experiments on a range of stone dust types. This supporting evidence suggests that the 250µm transition point for dust behaviour is likely to represent real stone dust behaviour and may represent a target for future laser development.

These experiments also present quartz sand as a potential robust model for stone dust for future experiments. It is readily available and has similar physical properties to many stone types. While not identical to struvite or calcium oxalate monohydrate dust, the behaviour was qualitatively similar to actual stone dust and it may represent the best alternative model for scientists who do not have access to an inexhaustible supply of correctly sized, homogenous stone dust of known chemical composition.

Two sets of these experiments aimed to measure the particle size produced by laser lithotripsy. One set was performed in a highly artificial and highly controlled environment where a stone held by forceps was ablated by hand in a Petri dish, while the other set was performed in a simulated kidney model that closely resembled clinical ureteroscopy. Although the data set for the latter was limited, it was nevertheless surprising to see apparent differences in the particle size distribution between these two data sets despite identical lasers, laser settings and stone compositions. The most notable difference was a dramatic increase in large 1-2mm fragments in the latter set. Anecdotally, there was also a large increase in the amount of >2mm fragments in the latter, though the experimental protocol of the former did not allow for accurate measurement of these particles. It is unclear from the limited data if there are any differences in the distribution of smaller <250µm particles. Further work needs to be done to establish whether there is a relationship between physical constraint of

the stone and the size of particles produced by laser lithotripsy. The tentative hypothesis formed from this limited data is that:

- Laser lithotripsy is the composite effect of (at least) 2 different underlying mechanisms, which correspond to the concepts of “dusting” and “fragmentation”.
- The “fragmentation” action of laser lithotripsy is influenced by the physical mobility/constraints of the target stone.

The existence of these two mechanisms could be proven by demonstrating that part of the particle size distribution can be altered by physically constraining the stone, while another part is unchanged. This would necessarily imply that one mechanism is dependent on physical constraint while the other is not. If this is proven, then further work should also be done to investigate the effect of laser settings on these two mechanisms, as there is no data from these experiments to answer this question.

Related to these mechanisms, the question of fragmentation is another target for future work. Over the years since the start of this project, the limitations of TFLs have become apparent and one of them is a relative inability to fragment stone. As with many of the concepts used by clinicians, this poorly defined but refers to the concept where a relatively small total amount of energy is delivered rapidly to the stone (usually with a high pulse energy) with the objective to break the stone into a small number of relatively large particles and a minimal amount of fine dust. In order to quantify fragmentation in any meaningful way, it is necessary to first define it. In Chapter 6, a proposed definition is given as “where the majority of the ablated volume being ejected as a single, intact, large (usually >250µm) particle accompanied by a smaller amount of relatively small particles”. No doubt alternative (and perhaps better) definitions will be suggested, that lend themselves to experimental design.

The current state of urological lasers

"Almost every new technique initially evokes a euphoric reaction among surgeons and patients. This period is often followed by indifference and rejection when long-term effects and limitations become obvious."

- Markolf Niemz, *Laser-Tissue Interactions (Fourth Edition)*

At the start of this project, TFLs were just beginning to enter widespread clinical use and clinician excitement at this novel technology was at its most euphoric. The potential for higher ablation rate and "lower" retropulsion appeared well demonstrated in vitro. Today, the benefits and limitations of these lasers are better understood. While Niemz's interpretation of this cycle as "indifference and rejection" is perhaps an exaggeration, it is clear that TFLs have not made Ho:YAG lasers obsolete. TFLs retain technological advantages in size, portability, noise and accessibility of power which have made them popular lasers of choice in low- and middle-income countries such as India. They retain situational benefits in ablation rate or "dusting" performance which may be preferred by certain clinicians or for the treatment of certain stones, even if the effect on outcomes is not yet clear. On the other hand, Ho:YAG lasers appear to be more effective when "fragmentation" is desired, even though the scientific basis for this has yet to be robustly established. Although not the focus of this thesis, this preference is most apparent when lasers are used in percutaneous nephrolithotomy, where the vast majority of clinicians would prefer the Ho:YAG laser to a TFL. There are also soft tissue applications of these lasers that are beyond the scope of this work, such as prostate enucleation or tumour ablation.

When the TFL first became commercially available, there was much debate about the relative benefits or disadvantages of the slightly shorter wavelength compared to Ho:YAG and resulting increased water absorption. The experiments in this work have demonstrated that the limitations in effective working range are not as draconian as the water absorption would imply. With the benefit of some hindsight, it would appear that this debate was largely irrelevant to the effectiveness of

these lasers. Contemporary lasers have remained in the near-infrared part of the spectrum, but differences in localised peaks are probably not significant. Ho:YAG and TFL represent one of the largest differences in water absorption coefficient found in the near-infrared spectrum, which is less than one order of magnitude. Meanwhile, the difference between their water absorption coefficients and pulsed dye lasers is 4-5 orders of magnitude (10,000-100,000x difference). Conservative urologists might be reluctant to stray beyond the near-infrared to avoid the dependence on stone chemical composition that plagued early lasers, but the minimum water absorption for stone composition-agnostic laser lithotripsy is not known and researchers should not constrain their thinking to a small, safe rock pool in the ocean of the electromagnetic spectrum.

The TFL has raised awareness of “peak power” as a concept amongst urologists, mostly in response to its inability to effectively fragment. This must be seen as a positive development, as up to this point, most commercially available lasers do not expose “peak power” as a user-selectable setting. The P120 offers a selection of short, medium and long pulse and this work has shown that, while the pulse widths do indeed increase in length going from short to medium to long at the same pulse energy, there are still areas of overlap where, for example, a 1.5J medium pulse is longer than a 0.8J long pulse. Whether this is intuitive is a subjective matter, but meanwhile the TFL employs a completely different meaning for its short, medium and long pulse selection where the effect of the selection is to alter the peak power from 500W (short pulse) to 250W (medium pulse) or 125W (long pulse). It would be arguably much more intuitive and transparent to instead label this setting as high, medium or low peak power. Even in 2024, lasers are now coming to market that use this labelling scheme as clinicians become more familiar with the concept of peak power and its implications.

In the last year, a new pulsed Tm:YAG laser has become commercially available. Although details of this laser are still relatively scarce, this appears to be an electrically modulated, continuous wave, diode-pumped bulk crystal laser. It has been marketed as a “halfway house” between TFL and

Ho:YAG, advertising peak powers up to 3.7kW and pulse widths of 150-1200µs. Clinical results are still awaited.

On a historical note, it is interesting to note that the Tm:YAG laser was first introduced to urology in the mid-2000s as a device for BPH and tumour ablation. Commercially available lasers at the time (such as the Revolix) were able to output a 200W continuous beam at a 2000nm wavelength, but there was no interest from clinicians of the time in trialling these lasers on stone. The prevailing opinion of the time was that continuous wave lasers were fundamentally unsuitable for stone surgery. Less than a decade later, researchers were able to demonstrate that a 100-110W continuous beam at 1920nm wavelength was able to effectively ablate urinary calculi [115], and that it was a relatively simple matter to electrically modulate the laser to produce a pulsed output and thereby maintain the average power at acceptable levels. No doubt the reader has concluded that this laser was indeed the precursor to the modern TFL, although advances in the diode pumping lasers since then have permitted increases in the power output up to 500W.

This inflexibility of thought mirrors another that occurred about a decade earlier, when photoacoustic lasers were becoming established in use. During this era, the prevailing and consistent opinion in published literature was that lasers for lithotripsy needed to be incapable of causing soft tissue injury to reduce ureteric injury, and that average powers could not exceed a few single digits of Watts in order to maintain safe temperatures. Pulse widths needed to be under 1µm to facilitate plasma formation, and wavelength was critical to ensure good absorption by stone. The Ho:YAG laser violated every established principle of the time for a lithotripsy laser, except for the fact that it effectively ablated stones of any chemical composition. Fortunately, the initial “euphoric reaction” to this new technology was able to break past established dogma and drove innovation to mitigate the disadvantages that Ho:YAG brought – or even turn those into advantages in soft tissue applications.

The future of lasers in stone surgery

If there is one lesson that can learned from the development of urological lasers over the past 40 years, it is that nobody truly knows what the “best” laser for lithotripsy looks like. Numerous properties once thought to be absolute contraindications have already been overcome, and there is no knowing what dogma of today might be overthrown tomorrow.

One aspect of optimising the lasers of today is the approach taken in this thesis. This is to investigate lasers currently in use, examine the relationship between their properties and the desired outcomes of lithotripsy. Those relationships can then be extrapolated to inform the development of future lasers, as refined versions of lasers currently in use. The pulsed Tm:YAG laser is an example of this kind of technological progress. This approach is helpful for identifying areas of diminishing returns such as ablation rate, where in vitro improvements are not matched by corresponding gains in clinical data, and under-researched areas such as particle size, where much of the science is extrapolated from clinical data on much larger >2mm particles and direct research is required.

However, technologists must also consider de novo technologies. One obvious avenue is to investigate lasers used in related industries and consider if they can be used or adapted for stone surgery. This might be from related medical fields such as dentistry, orthopaedic surgery and veterinary medicine (as was the case for the Ho:YAG laser), or from academic laser research. Another key related field is industrial deep-sea drilling, where lasers are often used in conjunction with conventional drills, on material with similar properties to urinary stones, in submerged environments that more closely resemble urology than any of the related medical fields. Urologists must be attentive and opportunistic in monitoring these industries, and open minded in testing potential candidates. There is no knowing when the next Ho:YAG laser might come along and revolutionise the principles of laser lithotripsy.

While it is impossible to predict the future, the findings and knowledge gained from these experiments can form a hypothesis for the next step in incremental laser development for lithotripsy. The anticipated technical properties of this hypothetical laser are as follows:

- Diode-pumped, to benefit from the increased efficiency and form factor benefits compared to flashlamp-pumped.
- Solid state (most likely bulk crystal based, given the more stringent technical limitations that fibre lasers impose on laser design).
- Wavelength between 1500-2000nm (the author anticipates a gradual decrease towards the lower water absorption end of the near-infrared spectrum, based on the unclear benefit and potential charring consequences of higher water absorption TFLs. Notably, there is a fraction of Er:YAG at 1540nm).
- A user-selectable peak power between 100W and 15000W (regrettably, these high peak powers are probably technologically incompatible with being diode-pumped at present but it is anticipated that diode technology will progress in future).
- A user-selectable pulse shape ranging from the “shark-fin” shape seen with Ho:YAG lasers, a square wave such as those seen with TFLs, and any other pulse shapes thought to be clinically beneficial such as a triangular “ramp” shape. This should be selectable independent of the peak power, and once again is dependent on a suitable diode laser to pump the laser in the correct way.
- Sensibly designed presets to allow clinicians to easily select appropriate combinations of pulse energy, frequency, peak power and pulse shape for the intended use case. These should display all underlying settings and suggest the outcomes of modifying each setting. For example, a dusting preset might label increasing pulse energy as “faster ablation, more retropulsion”.

In terms of the performance of the laser:

- Common clinical outcomes in terms of safety/complications, stone-free rate (by any definition), re-intervention rate and patient reported outcomes will be non-inferior to existing lasers.
- Clinical laser-on time and total operating time will be non-inferior to existing lasers. It is anticipated that this will not necessitate in vitro ablation rate to be non-inferior to existing lasers.
- In vitro and when dusting-optimised settings are used, the laser will produce a non-inferior proportion by mass of small particles <250µm compared to existing lasers. In other words, at least as much of the resulting particles is in the form of fine dust that is more likely to wash out.
- In vitro and when fragmenting-optimised settings are used, the laser will produce a non-inferior quantity of fragments compared to existing lasers. Since no universal definition of fragments or protocol to assess fragmentation exists, it is not possible to be any more specific at present.
- When “low retropulsion”-optimised settings are used, the clinical experience of this laser will be non-inferior compared to existing lasers (whether by subjective clinician report or by quasi-objective measurements such as the need to reposition the ureteroscope).
- When “high retropulsion”/”popdusting”-optimised settings are used, the clinical experience of this laser will be non-inferior compared to existing lasers (whether by subjective clinician report or by quasi-objective measurements such as the total energy required to complete popdusting).

It is expected that dusting-optimised and low retropulsion settings will initially mirror popular clinician-reported TFL dusting settings, with low peak powers of 500W, relatively low pulse energies of <0.5J and square or “ramp” shaped pulses. The relationship between laser settings and particle size was not conclusively established in these experiments, as the Petri dish experiments (suggesting no link) were contradicted by the experiments in the kidney model.

Technologists must also consider non-laser technologies for the treatment of urinary stones. At present, these technologies are limited by the requirement to transmit the energy from the source to the target stone in a precise and localised manner, usually through the working channel of a ureteroscope. This requirement largely limits the types of energy to light and electricity – in other words, lasers and electrohydraulic lithotripsy. However, this could be bypassed by introducing the energy source itself into the patient, which would open up alternative types of energy as well as radically changing the manner in which light and electricity could be used for lithotripsy. For example, if it were possible to introduce a miniaturised ultrasonic transducer on the tip of a ureteroscope, it might be possible to enjoy all the benefits of direct contact shockwave lithotripsy while keeping the control and direct vision from ureteroscopy.

If this thesis can be summarised in a single sentence, then it is the following:

"Incremental advances in laser lithotripsy will come from the careful application of the scientific method to what we know, but leaps forward require us to be diligent to advances outside urology and open-minded to technologies that might at first sound impossible"

Bingyuan Yang

Appendix 1: BegoStone preparation

BegoStone plus type 4 (BEGO GmbH & Co. KG, Bremen, Germany) was used as the base for artificial stone phantoms used in these experiments.

BegoStone mixture

A 15:3 ratio of BegoStone powder to deionised water was used, in order to produce a harder stone phantom with similar physical properties to calcium oxalate stones.

The mixture was prepared as per manufacturer instructions as follows:

1. One scoop of BegoStone powder was weighed out using the provided spoon, and the spoon weight subtracted (5.9g)
2. The required amount of deionised water was calculated by dividing the powder weight by 5
3. The deionised water was placed in a dry ceramic mixing bowl
4. The powder was added to the water and mixed by hand with a stainless steel spatula for 30 seconds

Once then mixture was evenly mixed to a paste-like consistency, it was added to the appropriate mould depending on the shape required.

Flat BegoStone preparation

Flat BegoStone phantoms were prepared using the silicone mould shown below in Figure 101. This consists of 12 separate wells, each measuring 30mm x 20mm x 4mm with rounded corners.

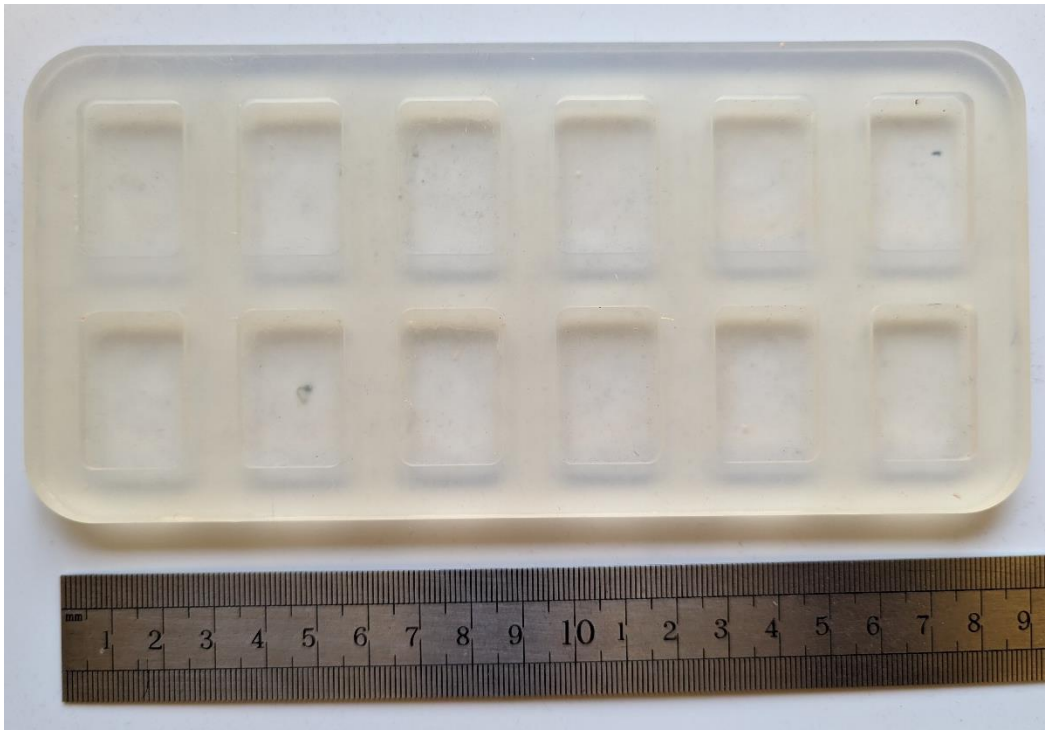


Figure 101. Silicone mould for producing flat BegoStone phantoms

The BegoStone mixture was moulded as follows:

1. An even amount of mixture was placed into each well, aiming to completely fill each well
2. The entire mould was placed on a hard surface and tapped firmly and repeatedly from below, to allow the viscous mixture to flow into the corners of the wells
3. If necessary, any unfilled wells were topped up with additional mixture and step 2 repeated
4. Any excess mixture was carefully scraped off the top of the mould using a sharp stainless steel blade
5. Step 2 was repeated for 1 minute, to ensure that as many air bubbles as possible were expelled from the mixture
6. The mixture was left for 24 hours at room temperature to dry and harden

Once dried, the phantoms were removed and prepared as follows.

1. Any excess stone from overflowing the mold was filed down using a fine-tooth file. Only the sides of the stone were filed, being careful to preserve the top surface (which would be used for ablation)

2. The stone was examined for the following defects. Any stone with these defects was discarded.
    a. Visible bubbles on the top (experimental) surface
    b. Large bubbles on any surface that could interfere with ablation
    c. Cracks or other defects
    d. Concavity or convexity of the top surface
    e. Any slope in the top surface
3. Stones free of defects were stoned in a dry container at room temperature until 24 hours prior to experimentation

Cylindrical BegoStone preparation

Cylindrical BegoStone phantoms were prepared using the 3D-printed mould shown below in Figure 102. This is a 2 part mould consisting of 10 separate wells, each having a cylindrical shape with a diameter of 6mm and a height of 5mm. The two halves of the mould are attached to each other by 3 bolts.

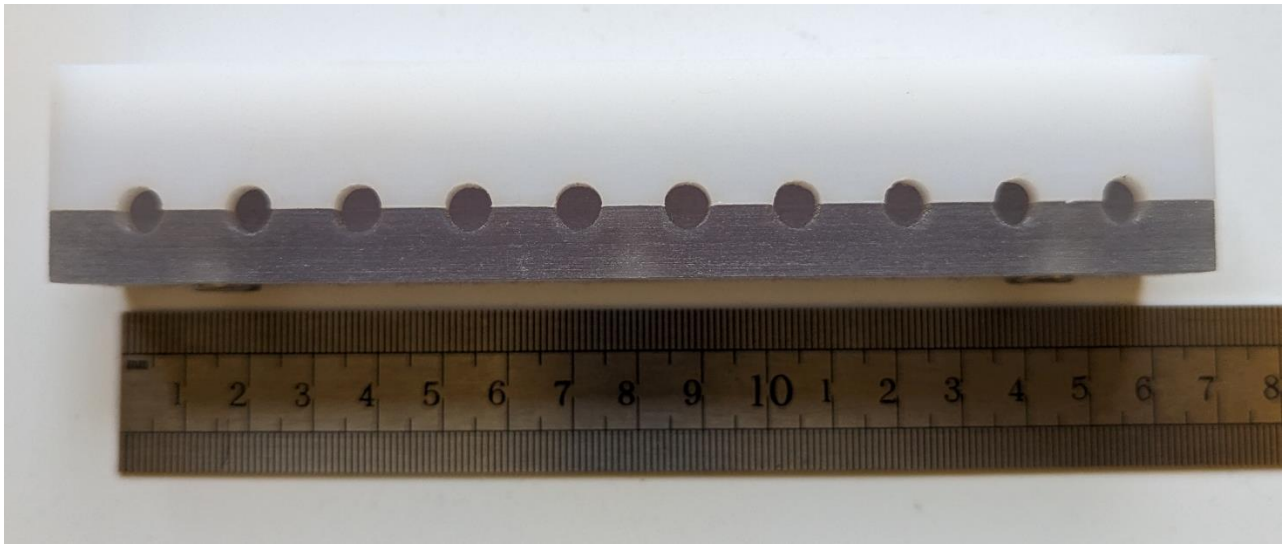


Figure 102. 3D-printed mould for producing cylindrical BegoStone phantoms

The BegoStone mixture was moulded as follows:

1. An even amount of mixture was placed into each well, aiming to completely fill each well

2. The entire mould was tapped firmly and repeatedly down onto a hard surface, to allow the viscous mixture to flow into the bottoms of the wells
3. If necessary, any unfilled wells were topped up with additional mixture and step 2 repeated
4. Any excess mixture was carefully scraped off the top of the mould using a sharp stainless steel blade
5. Step 2 was repeated for 1 minute, to ensure that as many air bubbles as possible were expelled from the mixture
6. The mixture was left for 24 hours at room temperature to dry and harden

Once dried, the phantoms were removed by separating the two halves of the mould and prepared as follows.

1. Any excess stone from overflowing the mold was filed down using a fine-tooth file. Only the sides of the stone were filed, being careful to preserve the top surface (which would be used for ablation)
2. The stone was examined for the following defects. Any stone with these defects was discarded.
    a. Misalignment of the two mould halves (leading to a non-cylindrical phantom)
    b. Visible bubbles on any surface
    c. Cracks or chips
    d. Concavity or convexity of the top surface
3. Stones free of defects were stoned in a dry container at room temperature until 24 hours prior to experimentation

Appendix 2: Software used for stone ablation volume analysis

Stone ablation volume was calculated using micro-CT volumetric scans. Software was written in Perl version 5 (ActiveState, Vancouver, Canada) to extract the ablation trench heights from the side-on trench profiles, and trench widths from the top-down trench profiles.

The format for the profile images is monochrome bitmap images where white indicates stone and black indicates ablated trench. The side-on profile should be aligned so the top of the image is level with the top of the stone (so all black pixels represent ablated stone, and white pixels indicate the base of the trench). The top-down profile should be aligned so that white pixels (indicating the sides of the trench) are visible at both the top and bottom of the image, with black pixels in-between (indicating the width of the trench).

Perl script for analysing ablation trenches

```
#!/usr/bin/perl

#-------------------------------------------------------------------------------
# MicroCT.pl
#
# Open a flattened BMP image of an ablation trail and output a CSV file with the
# height (for landscape images) or width (for topdown images) of the trench.
#
# Usage: perl MicroCT.pl <mode> <filename> (<microns per pixel>)
#
# <mode>:  1 = landscape
#          2 = topdown
#
# Copyright Bingyuan Yang 2020.
#
# Changelog
# 1.1 - added a mode to analyse width on a topdown image
# 1.0 - initial version
#-------------------------------------------------------------------------------

#-------------------------------------------------------------------------------
# Standard pragmas.
#-------------------------------------------------------------------------------
use 5.010_001;
use strict;
use English;
use warnings;

#-------------------------------------------------------------------------------
# Included modules.
#
# BMP for bitmap processing
#-------------------------------------------------------------------------------
use Image::BMP;

#-------------------------------------------------------------------------------
# Globals.
#-------------------------------------------------------------------------------
```

```
#-------------------------------------------------------------------------------
# Debug mode?
#-------------------------------------------------------------------------------
my $cDEBUG = 0;

#-------------------------------------------------------------------------------
# Script return code.
#-------------------------------------------------------------------------------
my $cRC_OK = 0;
my $cRC_NO_FILE = 1;
my $cRC_FILE_ERROR = 2;
my $cRC_MODE_ERROR = 3;

my $gRC = $cRC_OK;

#-------------------------------------------------------------------------------
# Operation modes.
#-------------------------------------------------------------------------------
my $cMODE_LANDSCAPE = 1;
my $cMODE_TOPDOWN = 2;

my $gMODE;

#-------------------------------------------------------------------------------
# BMP file name and file object.
#-------------------------------------------------------------------------------
my $gBMP_FILENAME;
my $gBMP_FILE;

#-------------------------------------------------------------------------------
# Default conversion from pixels to microns to 40 microns.
#-------------------------------------------------------------------------------
my $gPIXEL_TO_MICRON = 40;

#-------------------------------------------------------------------------------
# Do the work.
#-------------------------------------------------------------------------------
&Main();
exit($gRC);

#-------------------------------------------------------------------------------
# Main function.
#-------------------------------------------------------------------------------
sub Main
{
  #-----------------------------------------------------------------------------
  # Local variables.
  #-----------------------------------------------------------------------------
  my @lPixels = ();

  #-----------------------------------------------------------------------------
  # Turn off output buffering.
  #-----------------------------------------------------------------------------
  $| = 1;

  #-----------------------------------------------------------------------------
  # Command line arguments.
  #-----------------------------------------------------------------------------
  &ParseCLAs();

  #-----------------------------------------------------------------------------
  # Open the input file.
  #-----------------------------------------------------------------------------
  $gBMP_FILE = new Image::BMP(file => $gBMP_FILENAME,
                              debug => $cDEBUG);
  $gBMP_FILE or &ErorAndDie($cRC_FILE_ERROR);

  #-----------------------------------------------------------------------------
  # Set up the widths or depths array depending on operation mode.
  #-----------------------------------------------------------------------------
  if ($gMODE == $cMODE_LANDSCAPE)
  {
    #---------------------------------------------------------------------------
    # Landscape mode - get depths.
    #---------------------------------------------------------------------------
    @lPixels = &GetBMPDepths();
  }
```

```
  elsif ($gMODE == $cMODE_TOPDOWN)
  {
    #-------------------------------------------------------------------------
    # Top down mode - get widths.
    #-------------------------------------------------------------------------
    @lPixels = &GetBMPWidths();
  }
  else
  {
    &ErrorAndDie($cRC_MODE_ERROR);
  }

  #-------------------------------------------------------------------------
  # Output the depths array.
  #-------------------------------------------------------------------------
  &OutputBMPArray(@lPixels);

  #-------------------------------------------------------------------------
  # Close the input file.
  #-------------------------------------------------------------------------
  $gBMP_FILE->close();
}

#-------------------------------------------------------------------------------
#
# Sub:       ParseCLAs
#
# Purpose:   Parse the command line arguments
#
# Params:    None
#
# Returns:   Nothing
#
# Operation: Reads, checks and saves the command line arguments.
#            1: Operation mode is mandatory
#            2: BMP file name is mandatory.
#            3: Pixel to micron conversion is optional
#
#-------------------------------------------------------------------------------
sub ParseCLAs()
{
  #-------------------------------------------------------------------------
  # Local variables.
  #-------------------------------------------------------------------------
  my @lDepths;
  my $lWidth;

  #-------------------------------------------------------------------------
  # Operation mode.
  #-------------------------------------------------------------------------
  $ARGV[0] or &ErrorAndDie($cRC_MODE_ERROR);
  $gMODE = $ARGV[0];
  $cDEBUG and print " Op mode is " . $gMODE . "\n";
  if (($gMODE != $cMODE_LANDSCAPE) && ($gMODE != $cMODE_TOPDOWN))
  {
    $cDEBUG and print " Invalid operation mode " . $gMODE . "\n";
    &ErrorAndDie($cRC_MODE_ERROR);
  }

  #-------------------------------------------------------------------------
  # BMP file name.
  #-------------------------------------------------------------------------
  $ARGV[1] or &ErrorAndDie($cRC_NO_FILE);
  $gBMP_FILENAME = $ARGV[1];
  $cDEBUG and print " Input file is " . $gBMP_FILENAME . "\n";

  #-------------------------------------------------------------------------
  # Pixel to micron conversion constant.
  #-------------------------------------------------------------------------
  if ($ARGV[2])
  {
    $gPIXEL_TO_MICRON = $ARGV[2];
    $cDEBUG and print " Set pixel to micro conv to " . $gPIXEL_TO_MICRON . "\n";
  }

  return;
}
```

```
#-------------------------------------------------------------------------------
#
# Sub:       GetBMPDepths
#
# Purpose:   Get the heights at each column from the input BMP.
#
# Params:    None
#
# Returns:   Array of depths of ablation in pixels
#
# Operation: Read each column of the BMP starting from the top, and count the
#            number of black pixels to work out the depth of that column.
#
#-------------------------------------------------------------------------------
sub GetBMPDepths()
{
  #-----------------------------------------------------------------------------
  # Local variables.
  #-----------------------------------------------------------------------------
  my @lDepths;
  my $lWidth;
  my $lHeight;
  my $lColID;
  my $lRowID;
  my $lColour;
  my $lBlackPixels;

  $gBMP_FILE or &ErrorAndDie($cRC_FILE_ERROR);

  #-----------------------------------------------------------------------------
  # Get image parameters.
  #-----------------------------------------------------------------------------
  $lWidth = $gBMP_FILE->{Width};
  $lHeight = $gBMP_FILE->{Height};
  $cDEBUG and print " Width:  " . $lWidth . "\n";
  $cDEBUG and print " Height: " . $lHeight . "\n";

  #-----------------------------------------------------------------------------
  # Cycle through each column.
  #-----------------------------------------------------------------------------
  for ($lColID = 0; $lColID < $lWidth; $lColID++)
  {
    #---------------------------------------------------------------------------
    # Start at the top and count downwards.  These bitmaps start in the top
    # left.
    #---------------------------------------------------------------------------
    $lBlackPixels = 0;

    for ($lRowID = 0; $lRowID < $lHeight; $lRowID++)
    {
      #-------------------------------------------------------------------------
      # Break out when we find a non-black pixel.
      #-------------------------------------------------------------------------
      $lColour = $gBMP_FILE->xy($lColID, $lRowID);
      $cDEBUG and print " Pixel " . $lColID . ", " . $lRowID . " is " .
                        $lColour . "\n";

      if ($lColour == 0)
      {
        $lBlackPixels++;
      }
      else
      {
        $cDEBUG and print " Not black pixel - move to next column\n";
        $cDEBUG and print " Height of col " . $lColID . " was " .
                          $lBlackPixels . "\n";
        last;
      }
    }

    #---------------------------------------------------------------------------
    # Save the height.
    #---------------------------------------------------------------------------
    $lDepths[$lColID] = $lBlackPixels;
  }
```

```
  return @lDepths;
}

#-------------------------------------------------------------------------------
#
# Sub:       GetBMPWidths
#
# Purpose:   Get the widths at each column from the input BMP.
#
# Params:    None
#
# Returns:   Array of widths of ablation in pixels
#
# Operation: Read each column of the BMP starting from the top, find the first
#            black pixel to determine the start of the trench, and count the
#            number of black pixels to determine the width.
#
#            If there is more than one stretch of black pixels in any single
#            column, the largest is assumed to be the trench.
#
#-------------------------------------------------------------------------------
sub GetBMPWidths()
{
  #-----------------------------------------------------------------------------
  # Local variables.
  #-----------------------------------------------------------------------------
  my @lWidths;
  my $lWidth;
  my $lHeight;
  my $lColID;
  my $lRowID;
  my $lColour;
  my @lBlackPixels;
  my $lChunkIndex;
  my $lWidestChunk;

  $gBMP_FILE or &ErrorAndDie($cRC_FILE_ERROR);

  #-----------------------------------------------------------------------------
  # Get image parameters.
  #-----------------------------------------------------------------------------
  $lWidth = $gBMP_FILE->{Width};
  $lHeight = $gBMP_FILE->{Height};
  $cDEBUG and print " Width:  " . $lWidth . "\n";
  $cDEBUG and print " Height: " . $lHeight . "\n";

  #-----------------------------------------------------------------------------
  # Cycle through each column.
  #-----------------------------------------------------------------------------
  for ($lColID = 0; $lColID < $lWidth; $lColID++)
  {
    #---------------------------------------------------------------------------
    # Start at the top and count downwards.  These bitmaps start in the top
    # left.
    #---------------------------------------------------------------------------
    $lChunkIndex = 0;
    $lBlackPixels[$lChunkIndex] = 0;

    #---------------------------------------------------------------------------
    # Each time we find a stretch of black pixels, save off how wide it is.
    #---------------------------------------------------------------------------
    for ($lRowID = 0; $lRowID < $lHeight; $lRowID++)
    {
      #-------------------------------------------------------------------------
      # Break out when we find a non-black pixel.
      #-------------------------------------------------------------------------
      $lColour = $gBMP_FILE->xy($lColID, $lRowID);
      $cDEBUG and print " Pixel " . $lColID . ", " . $lRowID . " is " .
                        $lColour . "\n";

      if ($lColour == 0)
      {
        $lBlackPixels[$lChunkIndex]++;
      }
      else
      {
        $cDEBUG and print " Not black pixel - start next chunk\n";
```

```
        $cDEBUG and print " Width of col " . $lColID .
                          " chunk " . $lChunkIndex . " was " .
                          $lBlackPixels[$lChunkIndex] . "\n";
        $lChunkIndex++;
        $lBlackPixels[$lChunkIndex] = 0;
      }
    }

    #-------------------------------------------------------------------------
    # Find the largest stretch and assume that is the width.
    #-------------------------------------------------------------------------
    $lWidestChunk = 0;
    for (@lBlackPixels)
    {
      $cDEBUG and print " Check next chunk width " . $_ . "\n";
      if ($_ > $lWidestChunk)
      {
        $cDEBUG and print " This is the widest chunk so far\n";
        $lWidestChunk = $_;
      }
    }

    #-------------------------------------------------------------------------
    # Save the width.
    #-------------------------------------------------------------------------
    $cDEBUG and print " Widest chunk at col " . $lColID .
                      " was " . $lWidestChunk . "\n";
    $lWidths[$lColID] = $lWidestChunk;
  }

  return (@lWidths);
}

#-------------------------------------------------------------------------------
#
# Sub:       OutputBMPArray
#
# Purpose:   Output the array of ablation measurements in microns
#
# Params:    IN     $xiPixels    - Array of measurements in pixels
#
# Returns:   Nothing
#
# Operation: Converts each measurement from pixels to microns and outputs it as
#            a comma separated list.
#
#-------------------------------------------------------------------------------
sub OutputBMPArray()
{
  #-------------------------------------------------------------------------
  # Local variables.
  #-------------------------------------------------------------------------
  my (@xiPixels) = @_;

  my $lColID;
  my $lPixels;
  my $lMicrons;

  #-------------------------------------------------------------------------
  # Loop through measurements, converting to microns and printing to screen.
  #-------------------------------------------------------------------------
  foreach $lPixels (@xiPixels)
  {
    $lMicrons = $lPixels * $gPIXEL_TO_MICRON;
    $cDEBUG and print $lPixels . " pixels = " . $lMicrons . " microns\n";
    print $lMicrons . ",";
  }
}

#-------------------------------------------------------------------------------
#
# Sub:       ErrorAndDie
#
# Purpose:   Reports and error and dies.
#
# Params:    IN     $xiCode      - error code to report.
#
```

```
# Returns:   Does not return.
#
# Operation: Report the error and next action depending on the code.
#
#-------------------------------------------------------------------------------
sub ErrorAndDie()
{
  #-----------------------------------------------------------------------------
  # Local variables.
  #-----------------------------------------------------------------------------
  my ($xiCode) = @_;

  my $lInput;

  #-----------------------------------------------------------------------------
  # Report error.
  #-----------------------------------------------------------------------------
  if ($xiCode == $cRC_NO_FILE)
  {
    #---------------------------------------------------------------------------
    # No input file specified.
    #---------------------------------------------------------------------------
    print " No input file specified\n\n" .
          " Press return to exit\n";
    $lInput = <STDIN>;
    die " \n Error";
  }
  elsif ($xiCode == $cRC_FILE_ERROR)
  {
    #---------------------------------------------------------------------------
    # Error with the specified file.
    #---------------------------------------------------------------------------
    print " Error reading " . $gBMP_FILENAME . "\n\n" .
          " Press return to exit\n";
    $lInput = <STDIN>;
    die " \n Error";
  }
  elsif ($xiCode == $cRC_MODE_ERROR)
  {
    #---------------------------------------------------------------------------
    # Error with the operation mode
    #---------------------------------------------------------------------------
    print " Invalid operation mode " . $gMODE . "\n\n" .
          " Press return to exit\n";
    $lInput = <STDIN>;
    die " \n Error";
  }
  else
  {
    #---------------------------------------------------------------------------
    # Script error, doh.
    #---------------------------------------------------------------------------
    print " Script error, sorry!\n\n" .
          " Press return to exit\n";
    $lInput = <STDIN>;
    die " \n Error";
  }
}
```

Appendix 3: High-speed photography of laser-induced vapour bubbles

To better understand the vapour bubbles produced during laser emission and therefore the expected Moses effects, these bubbles were recorded using high-speed video photography.

A FastCam SA-X2 high-speed camera (Photron, Tokyo, Japan) was used for video recording with a 12x zoom Navitar microscope lens and 2x F-mount adapter tube (Navitar, NY, USA). Light was provided by a F5100 LED microscope light source (Photron, Tokyo, Japan). Recording was done using PFV 4.0 software (Photron, Tokyo, Japan).

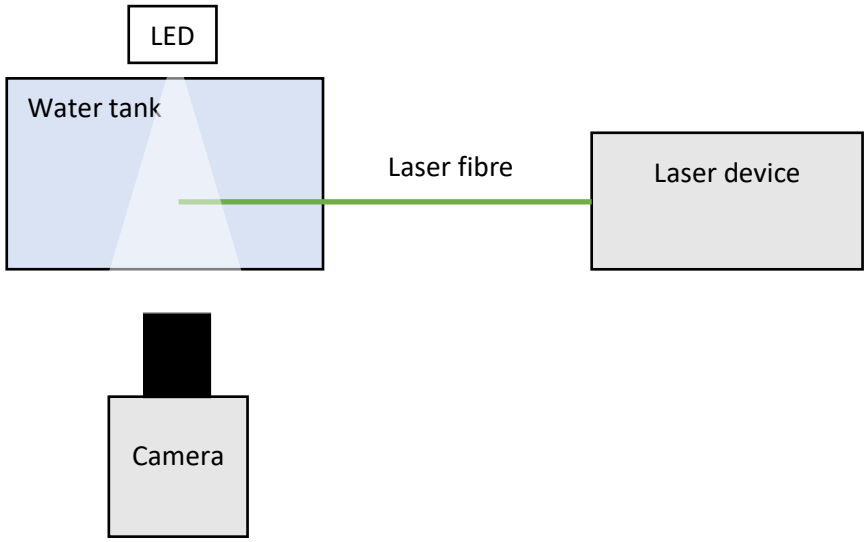


Figure 103. Experimental setup for high-speed photography of laser-induced vapour bubbles.

The apparatus was set up as shown in Figure 103. The laser fibre was taped to a metal holder to keep it still, and the camera placed perpendicularly 18cm from the fibre tip. For spatial calibration, a set of 1mm ruled lines was printed on overhead transparency film. A series of these lines was then fixed adjacent to the laser fibre to allow precise calibration of distance within the recording, as shown in Figure 104. The film was then cut away to avoid any potential interference with vapour bubbles, and the position and focus was kept constant for all recordings.

Vapour bubble recording was performed at 200,000 frames per second (FPS), shutter speed of 5µs and a resolution of 256x160 pixels. The recording parameters were constrained by the on-board

memory of the camera, as a higher frame rate resulted in a lower spatial resolution and vice versa. Preliminary experiments indicated that these settings provided the best balance of having sufficient spatial resolution to resolve individual bubbles clearly in individual images, while maintaining enough temporal resolution to smoothly track changes over time. It was not necessary to lower the shutter speed from the default (5µs at 200,000 FPS) as the movement artifact was minimal. This high frame rate required that the bubble was backlit (with the bubble between the LED and the camera) as shown in the setup.

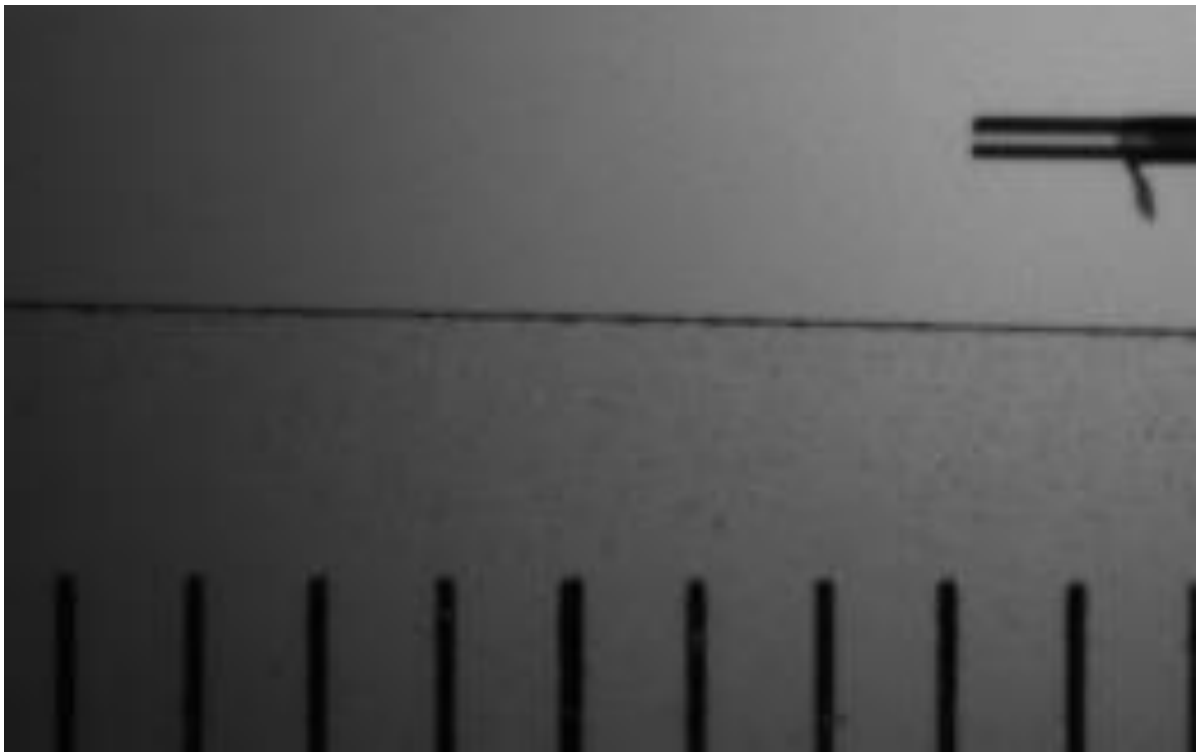


Figure 104. Transparent 1mm ruled lines for spatial calibration.

Once recorded, the high-speed video was converted to H.265 format using PFV 4.0, with video metadata included on the side of each frame including timestamps. Still images were obtained by playing the video back in VLC 3.0 (VideoLAN, Paris, France) at a 1:1 zoom ratio to ensure that pixel size was maintained. Spatial calibration was done by counting the number of pixels between midpoints of the 1mm lines in Paint.net 5.0 (dotPDN LLC, USA) to determine the conversion from pixels to millimetres. Still image processing of vapour bubbles was also performed by counting pixels using Paint.net 5.0.

Appendix 4: High-speed photography of stone motion

Stone retropulsion was measured using high-speed video photography for both pendulum and linear experiments. Initial experiments were performed using an ZV1 camera (Sony, Tokyo, Japan) with room lighting. This was able to record at 1000 frames per second, but the resulting stone tracking was too noisy at this limited frame rate. All subsequent retropulsion experiments were performed using a high-speed FastCam SA-X2 camera (Photron, Tokyo, Japan) with a 105mm F2.9 EX DG Macro OS lens (Sigma Corporation, Kanagawa, Japan) and a F5100 LED light source (Photron, Tokyo, Japan). Recording was performed with PFV 4.0 software (Photron, Tokyo, Japan). Full details of the experimental setups are provided in Chapter 4. Retropulsion.

Geometric considerations in calculating motion

Parallax error

The pendulum experiment involved a stone suspended on strings being propelled by a single laser pulse. The motion was therefore expected to be in the arc of a circle, and so it was necessary to position the camera perpendicular to both the direction of motion and the radius of the circle as shown in Figure 105. The camera was aligned so that the starting position of the stone was centred in the camera's field of view in both horizontal and vertical directions. The same physical layout was used for the linear experiment to maintain consistency.

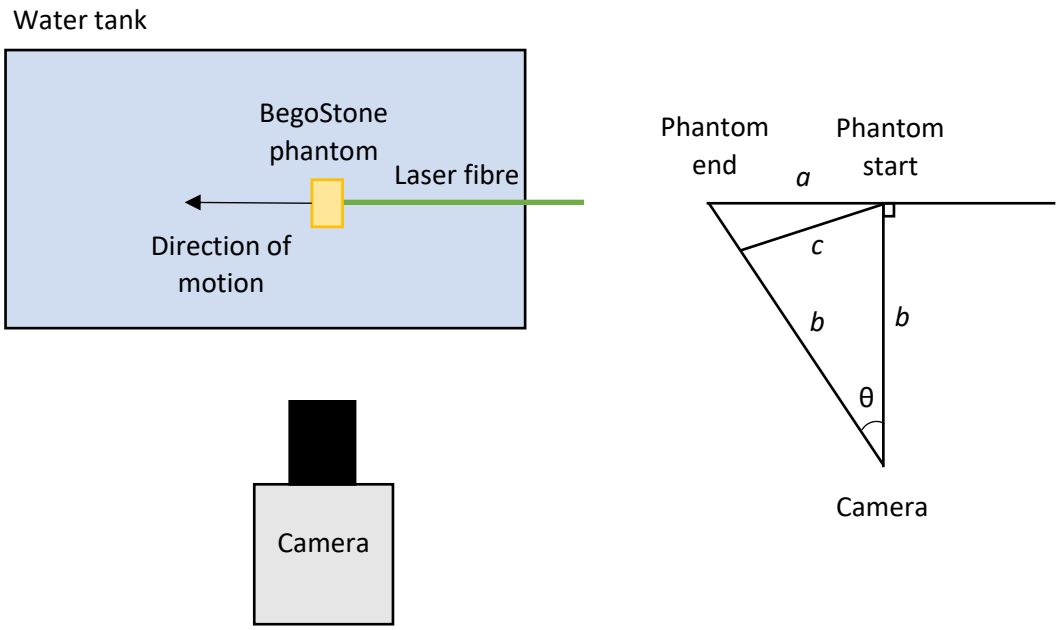


Figure 105. Top-down view of experimental setup for retropulsion experiments, showing alignment of the camera and direction of motion. A schematic of the geometric layout and distances is provided on the right.

The camera is only able to capture 2D images by flattening the (curved) image captured at the camera's focal distance. The stone phantom will actually move slightly further away from the camera, and therefore some amount of parallax error will inevitably be introduced in the process of estimating the actual distance moved *a*. The exact amount of error can be calculated from the geometric layout. The starting distance between the camera and phantom is *b*. As it is not possible to measure the end distance between the camera and phantom from a 2D image, it will appear that the end point of the stone forms an isosceles triangle with the starting point (when the reality is that it should be a right-angled triangle). The angle of view moved by the phantom is θ. The calculated distance moved *c* will underestimate the actual distance *a*, and this is the parallax error. This can be calculated by bisecting the isosceles triangle into 2 right-angled triangles with a hypotenuse of *b*.

$$\tan\theta = \frac{a}{b}$$

$$\sin\frac{\theta}{2} = \frac{c}{2b}$$

$$b = \frac{a}{\tan\theta}$$

$$\frac{c\tan\theta}{2a} = \sin\frac{\theta}{2}$$

$$\frac{c}{a} = \frac{2\sin\frac{\theta}{2}}{\tan\theta}$$

Then *c*/*a* is the ratio between the estimated motion and the actual motion i.e. a measurement of the parallax error. The parallax effect can then be plotted as shown in Figure 106.

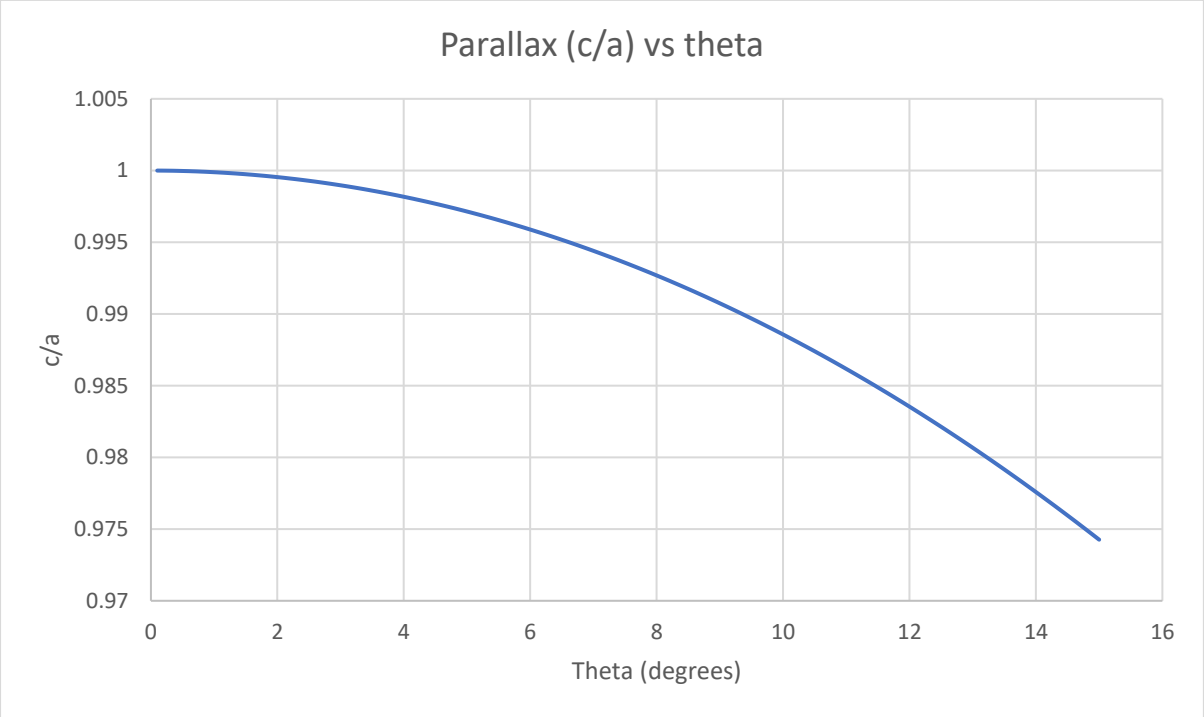


Figure 106. Parallax error vs the angle of motion of the stone theta (in degrees). A ratio of c/a of 1 corresponds to perfect accuracy in estimating actual distance moved.

A ratio *c*/*a* of 1 indicates perfect accuracy in estimating the actual distance moved, i.e. no parallax error. The pendulum experiment was used to calculate the initial stone phantom velocity, so the images being compared were consecutive frames of high-speed video footage. The changes in angle of view θ were therefore extremely small (< 1 degree) and so parallax error was essentially non-existent in the pendulum experiment.

The linear experiment measured displacements both between each consecutive frame and between the positions at time 0s and 1s. The starting distance between camera and stone phantom was 200mm, and the field of view was approximately 40mm. Since the phantom was centred in the view

initially, the maximum actual distance moved that could be measured was 20mm. This corresponds to a maximum change in angle of view θ of 5.7 degrees, which creates a parallax error of about 0.4% when the final stone position is compared to the start position.

The only way to accurately exclude parallax error is with knowledge of the exact distances between the stone phantom and the camera at each point. In theory this could be estimated by assessing the stone size in each frame, but this would be complicated by the stone phantom rotating, uneven casting, the limited video resolution and the extremely small changes in size. Attempting to compensate for parallax is likely to introduce more error than the <0.4% parallax error itself, and therefore it was decided to accept the known, very small amount of parallax error.

Movement out of plane

In both the pendulum and linear retropulsion experiments, the stone was aligned with the laser fibre so that the direction of motion would be perpendicular to the direction of the camera, as shown in Figure 105. However, it was possible for small imperfections in the setup to result in movement of the stone outside this plane.

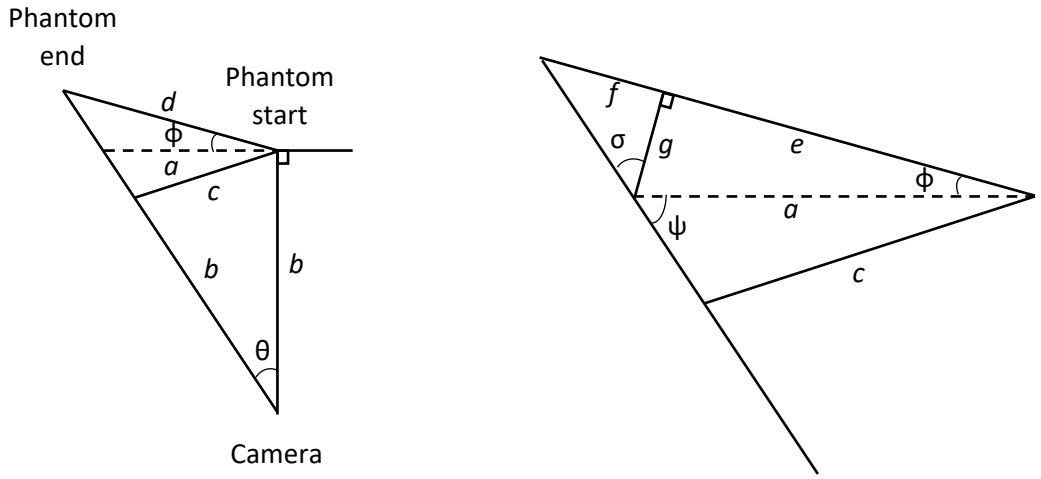


Figure 107. Schematic of geometric layout when phantom trajectory deviates away from camera. The intended trajectory is shown as a dotted line. An expanded view is shown on the right.

The error introduced by lateral stone motion can be calculated by considering motion away from the camera and motion towards the camera separately. Note that motion away from the camera exacerbates the parallax error calculated in the previous section, and will therefore result in greater errors between calculated and actual motion. Conversely, motion towards the camera will (at least initially) counteract parallax error and result in reduced errors between calculated and actual motion.

Figure 107 shows the geometric layout when the stone deviates away from the camera. The angle by which the stone is deflected is ϕ. The actual distance moved is *d*, while the apparent distance moved (calculated from camera images) is *c*. To calculate *d*, the triangle formed between the actual and intended motion needs to be divided as shown in the expanded view. Then:

$$d = e + f$$

Using the larger right-angled triangle formed above:

$$\cos\varphi = \frac{e}{a}$$

$$e = a\cos\varphi$$

Note that ψ is part of a larger right-angled triangle with sides *a*, *b* and the line from the camera towards the phantom end position. Then:

$$\psi = 90 - \theta$$

$$\sigma = 180 - \psi - (90 - \varphi)$$

$$\sigma = 90 + \varphi - (90 - \theta)$$

$$\sigma = \varphi + \theta$$

The length of the subdivision *g* can be calculated:

$$g = a\sin\varphi$$

Then:

$$f = g \tan \sigma$$

$$f = a \sin \varphi \tan(\varphi + \theta)$$

The actual distance moved by the stone is therefore:

$$d = e + f$$

$$d = a \cos \varphi + a \sin \varphi \tan(\varphi + \theta)$$

$$d = a(\cos \varphi + \sin \varphi \tan(\varphi + \theta))$$

This gives an expression for the intended trajectory *a*:

$$a = \frac{d}{\cos \varphi + \sin \varphi \tan(\varphi + \theta)}$$

From the previous section, the ratio of the estimated motion *c* to the intended trajectory *a* is:

$$\frac{c}{a} = \frac{2 \sin \frac{\theta}{2}}{\tan \theta}$$

Therefore the ratio of the estimated motion *c* to the actual motion *d* is:

$$\frac{c(\cos \varphi + \sin \varphi \tan(\varphi + \theta))}{d} = \frac{2 \sin \frac{\theta}{2}}{\tan \theta}$$

$$\frac{c}{d} = \frac{2 \sin \frac{\theta}{2}}{\tan \theta \, (\cos \varphi + \sin \varphi \tan(\varphi + \theta))}$$

This ratio can be plotted for a range of θ (the angular motion of the stone) and ϕ (the angular deviation of the stone away from the camera) as shown in Figure 108.

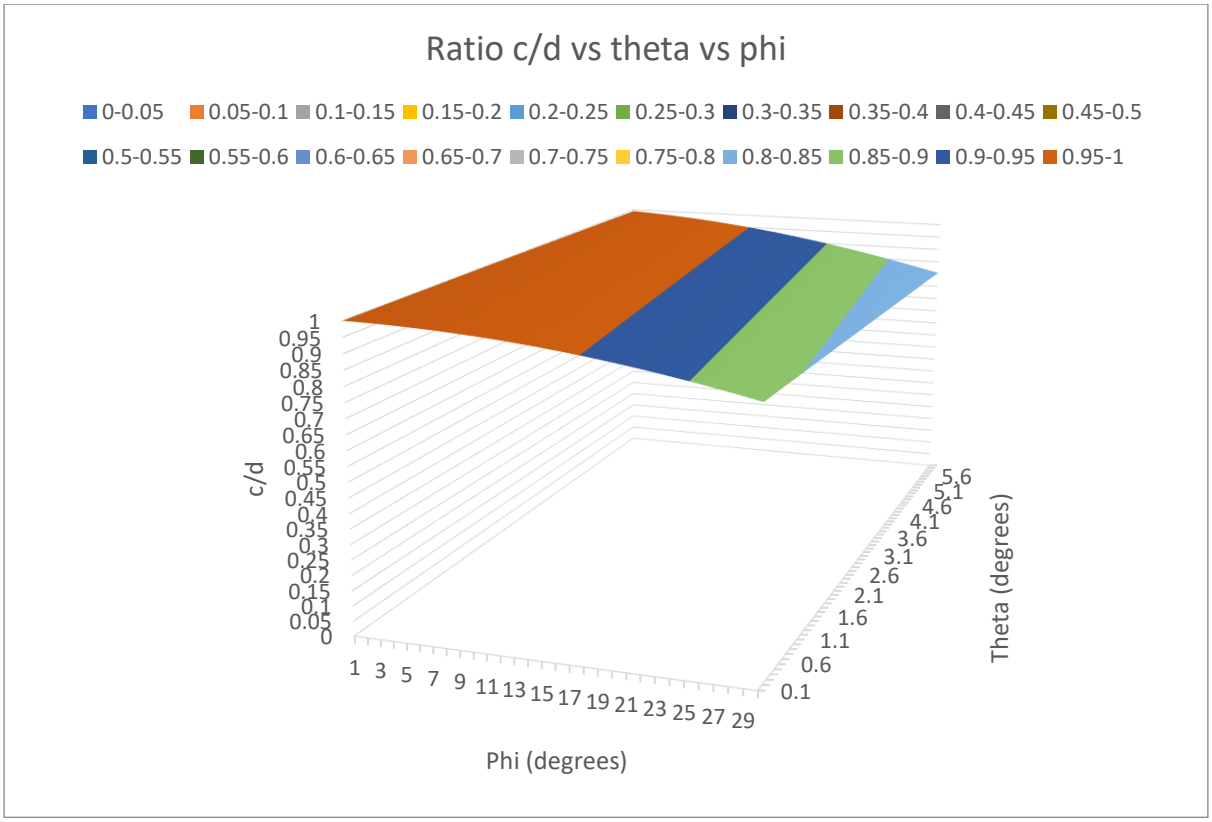


Figure 108. Accuracy c/d of estimating stone motion vs angle travelled by the stone (theta) and angle deviated away from the camera (phi). A ratio of c/d of 1 corresponds to perfect accuracy in estimating actual distance moved.

If the angle ϕ that the stone deviates away from the camera is ≤ 19 degrees, then the ratio *d/a* is > 0.9 at all times i.e. the error is < 10%. If the angle ϕ is ≤ 12 degrees, then the error is < 5%.

Finally the case where the stone deviates towards the camera is considered. A schematic of this situation is shown below in Figure 109.

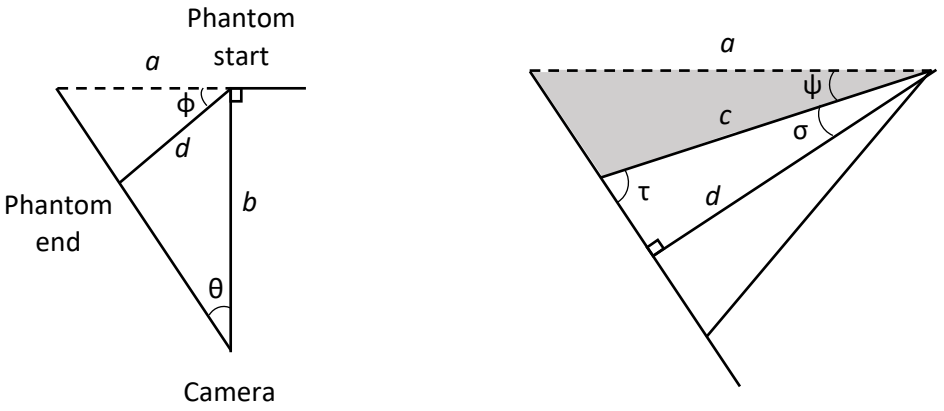


Figure 109. Schematic of geometric layout when phantom trajectory deviates towards the camera. The intended trajectory is shown as a dotted line. An expanded view is shown on the right.

Since the distance c is the estimated distance travelled by the stone based on the 2D camera images, it is clear that when the stone trajectory falls within the shaded region, the effect will be to bring the actual distance moved *a* closer to the estimated distance moved *c*. In other words, the error from the lateral motion will cancel out part of the parallax error, and reduce overall error.

The complementary angle to ψ can be calculated as it forms part of the isosceles triangle with base *c* and sides *b*. It is therefore equal to τ.

$$\tau = 90 - \psi = \frac{180 - \theta}{2}$$

$$90 - \psi = 90 - \frac{\theta}{2}$$

$$\psi = \frac{\theta}{2}$$

Therefore, deviations towards the camera with an angle of up to half the angular motion of the stone can be completely ignored as these will only serve to reduce the parallax error.

Deviations greater than this will result in an estimated distance *c* that overestimates the actual distance *d*, until a maximum error is achieved when the line *d* forms a right angle with the line between the camera and phantom as shown in Figure 109. Beyond this the error will again decrease

until the trajectory *d* forms an isosceles triangle with the estimated distance *c*. At this point there will be no error as these distances are equal. It is therefore sufficient to calculate the point where the maximum error occurs and the magnitude of that error.

In the maximum error configuration shown:

$$\tau = 90 - \frac{\theta}{2}$$

$$\sigma = 180 - 90 - \tau$$

$$\sigma = \frac{\theta}{2}$$

$$d = c\cos\sigma = c\cos\frac{\theta}{2}$$

Therefore the ratio of the estimated motion *c* to the actual motion *d* is:

$$\frac{c}{d} = \frac{1}{\cos\frac{\theta}{2}}$$

Then *c/d* can then be plotted as shown in Figure 110. This ratio is greater than 1 because in these scenarios, the estimated distance *c* overestimates the actual distance *d* whereas previous scenarios resulted in an underestimate.

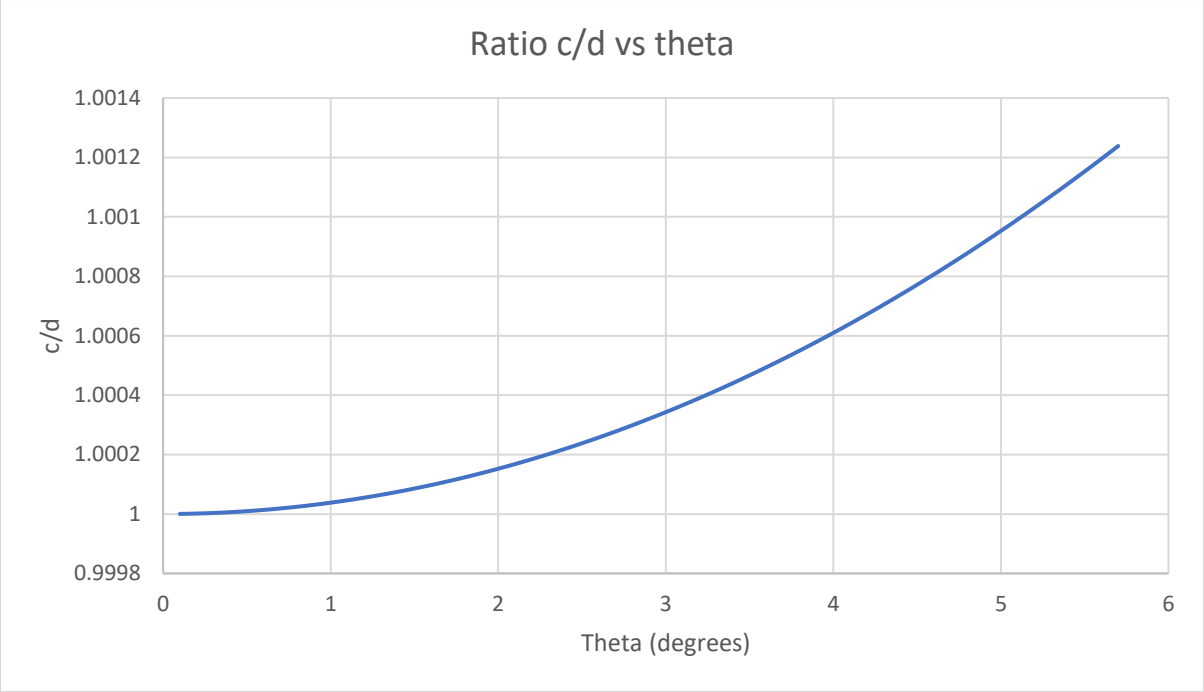


Figure 110. Accuracy c/d of estimating stone motion vs angle travelled by the stone (theta). A ratio of c/d of 1 corresponds to perfect accuracy in estimating actual distance moved.

All errors for expected values of θ (up to 5.7 degrees, as calculated previously) are less than 0.12% and can be considered negligible. As the deflection of the stone towards the camera increases beyond this maximum error, the error will decrease until the stone trajectory forms the other side of the isosceles triangle shown in Figure 109, i.e. when *d* = *c*. This occurs at an angle of:

$$\varphi = \psi + 2\sigma = \frac{3\theta}{2}$$

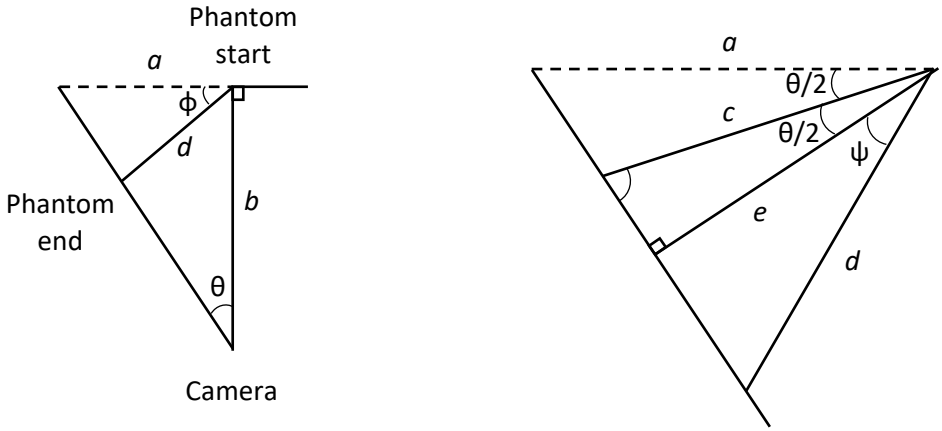


Figure 111. Schematic of geometric layout when phantom trajectory deviates towards the camera. The intended trajectory is shown as a dotted line. An expanded view is shown on the right.

When the stone trajectory deviates towards the camera at larger angles than 3θ/2, the geometry is shown in Figure 111. The line formed by the trajectory of the stone *d* is different, but the remaining geometry and angles remain identical to those calculated previously. The line that forms a right angle with the line between the camera and stone end point is now referred to as line *e*. Then *e* can be calculated from the two right-angled triangles of which it is a part:

$$e = c\ cos\frac{\theta}{2}$$

$$e = d\cos\psi$$

$$c\ cos\frac{\theta}{2} = d\cos\psi$$

But the total angle of deflection ϕ is the sum of the 3 angles shown:

$$\varphi = \psi + \frac{\theta}{2} + \frac{\theta}{2} = \psi + \theta$$

$$\psi = \varphi - \theta$$

Then the ratio of the estimated motion *c* to the actual motion *d* is:

$$\frac{c}{d} = \frac{\cos\psi}{cos\frac{\theta}{2}} = \frac{\cos(\varphi - \theta)}{cos\frac{\theta}{2}}$$

Note that when ϕ < θ, the geometry differs from that shown but the calculated ratio *c*/*d* (with a negative ψ) is still correct due to the symmetry of the cosine function about 0. This ratio can then be plotted as shown in Figure 112. This graph includes the overestimation errors calculated in the previous section, with identical values.

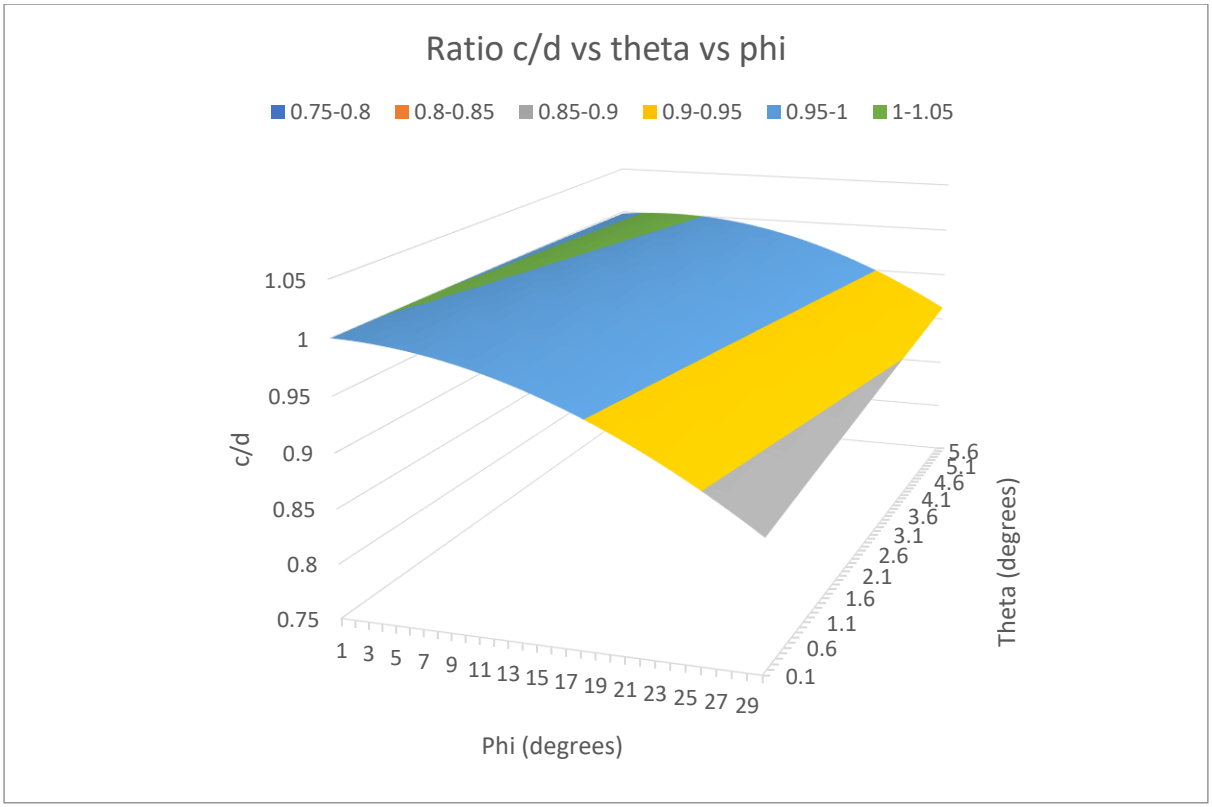


Figure 112. Accuracy c/d of estimating stone motion vs angle travelled by the stone (theta) and angle deviated towards the camera (phi). A ratio of c/d of 1 corresponds to perfect accuracy in estimating actual distance moved.

Therefore, the maximum overestimation error is 0.12%. If the angle ϕ that the stone deviates towards the camera is ≤ 25 degrees, then the ratio *d/a* is > 0.9 at all times i.e. the error is < 10%. If the angle ϕ is ≤ 18 degrees, then the error is < 5%.

Experimental constraints for linear retropulsion

As shown here, parallax and lateral stone motion both contribute to errors in estimating the true distance moved by the stone using a 2D image. This error can be limited by restricting the acceptable lateral deviation of the stone (towards or away from the camera).

An error of <10% can be maintained by keeping lateral motion <19 degrees away from the camera and <25 degrees towards the camera. An error of <5% can be maintained by keeping lateral motion <12 degrees away from the camera and <18 degrees towards the camera.

The experimental apparatus only included one camera, so precise measurement of every lateral deviation was not possible without a second overhead camera. Instead the lateral motion of the

initial pulse was limited by ensuring that the midpoint of the aiming beam remained visible on the phantom at the furthest part of its motion. Since the phantom is a cylinder with radius 3mm, the minimal retropulsion distance *l* to ensure a lateral angle of <12 degrees can be calculated as follows.

$$l = \frac{3}{\tan 12} = 14.1\ mm$$

The assessment of lateral phantom motion was therefore done as follows:

1. If the aiming beam was centred on the phantom at the end of motion, the amount of lateral motion was considered negligible.
2. If the aiming beam was not centred on the phantom at the end of motion but the centre of the aiming beam was still visible on the phantom, the amount of lateral motion was considered acceptable if the calculated retropulsion distance was at least 14.1 mm (corresponding to an error of <5%).

Despite these steps, some lateral motion beyond these limits was still inevitable when the retropulsion trajectory consisted of multiple phases from multiple pulses.

Pendulum stone trajectory

The pendulum experiment involved a stone phantom suspended in the water tank by strings of length 200mm. The strings were extremely thin cotton thread that was not expected to add any significant drag, with extremely small weights of approximate 10mg. It was therefore expected that, when propelled by a single laser pulse, the phantom's trajectory would follow the arc of a circle of radius 200mm. However, plotting the actual trajectories showed that this was not the case.

Figure 113 shows the horizontal and vertical trajectories of an example stone using the P120 from a single 1J pulse in standard short pulse mode. The motion appears to consist of 3 distinct phases. In the initial motion (in light grey), the motion describes the arc of a circle whose radius is smaller than the expected 200mm of string length. This appears to be a result of water resistance on the string

causing it to curve. The second phase involves the phantom descending vertically as the string catches up with the stone and re-straightens (dashed line). The final phase is where the stone returns to the starting position under gravity and describes the arc of a larger circle, whose radius appears to be approximately the 200mm of string length. This suggests that the final motion under gravity is slow enough that the string remains approximately straight.

The hysteresis seen here means that:

- The horizontal initial velocity can be used to approximate the initial velocity of the stone, where the trajectory remains essentially horizontal, but not the overall or any later velocity. Overall velocity should instead be used in those cases.
- The drag from the suspending strings is likely not inconsequential as it has a measurable effect on the phantom's trajectory. Quantifying this effect is likely to be complex.

Because of the complexity of the effect of the strings, only the initial phantom velocity was used for analysis for the pendulum experiment.

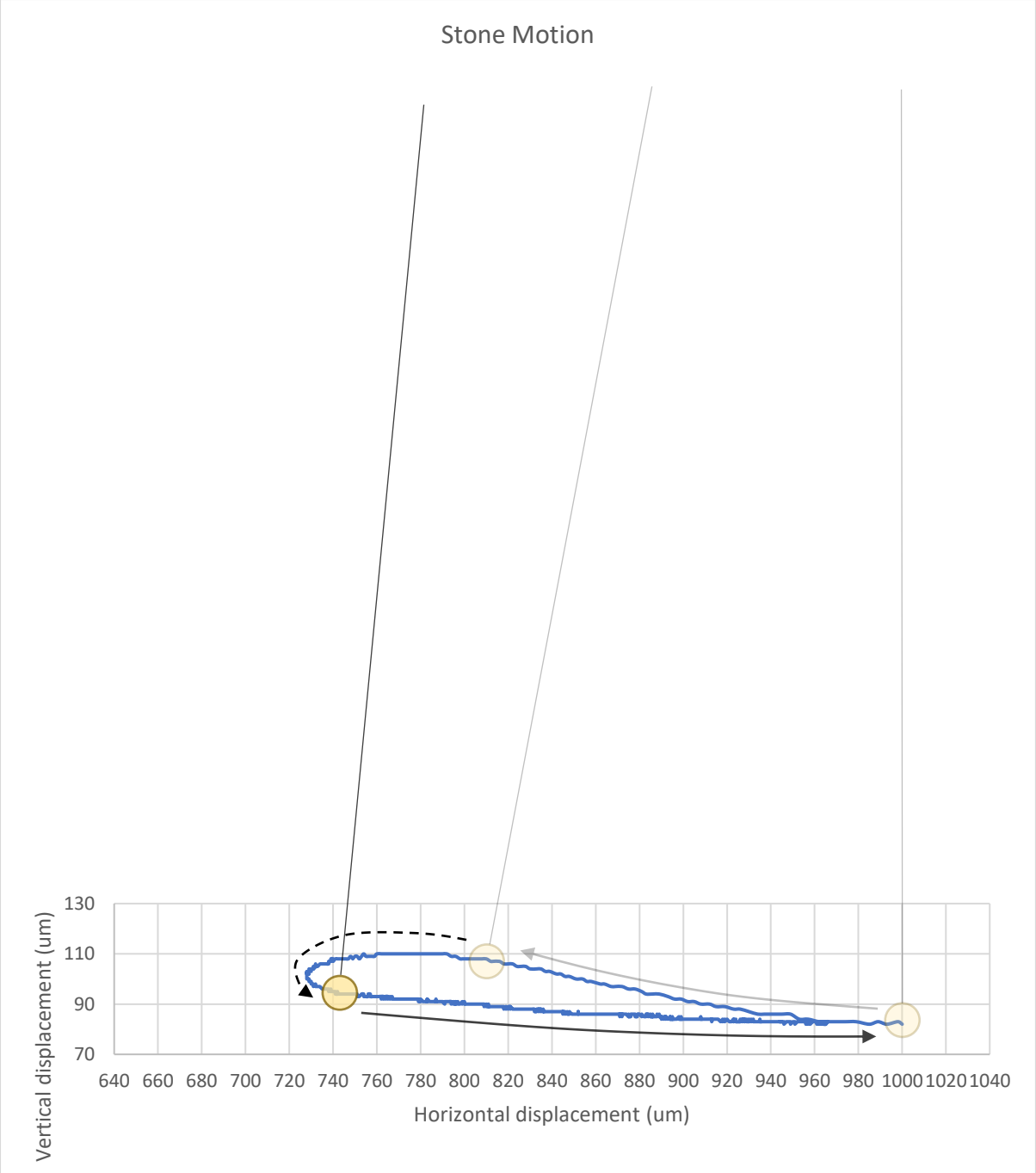


Figure 113. Annotated stone phantom trajectory from pendulum model. Initial motion is in the arc of a small circle (light grey), followed by an intermediate phase where the string re-straightens (dashed line) and the phantom returns in the arc of a larger circle (black).

Image tracking algorithm and limitations

Stone position measurements were captured from the high-speed video images using a Python script using the open-source computer vision library OpenCV2. This was written in conjunction with the team at Boston Scientific and based on the public domain OpenCV2 tutorial code at www.learnopencv.com.

Image tracking algorithms convert visual representations of objects (in the form of digital pixels) into numerical representations of the positions of those objects (in the form of coordinates). The tracking algorithms available in the OpenCV2 library all output a single pair of coordinate values – in other words, they attempt to identify a single point as the "centre" of the object and track the position of that point, and provide no information about the periphery. These are well suited for the desired purpose of calculating position and velocity values, but involve a degree of abstraction as the algorithms must estimate the centre point of a cylindrical stone phantom (which may be rotating, and without receiving any information about the shape of the object).

The available algorithms that were considered were: BOOSTING (based on AdaBoost), MIL, KCF and CSRT. The OpenCV2 library also supported TLD, MedianFlow, GOTURN and MOSSE but the OpenCV2 tutorial recommended against using these because of worse tracking accuracy, so they were not considered. Since image tracking was being performed on pre-recorded high-speed video footage, algorithm speed was unimportant as there was no requirement to run in real-time. Instead, the priorities were (in descending order):

1. Tracking accuracy (i.e. the tracking centre point identified by the algorithm should closely match that identified by a human observer).
2. Smooth tracking (i.e. a movement of the object should result in the same or similar movement in the tracking point).
3. Minimal tracking failure (i.e. where the algorithm is not able to identify the object at all in a given frame, requiring the algorithm to be re-run).

The 5 algorithms under consideration were tested on a selection of pendulum experiment videos at 0.5J, 1J and 2J pulse energies using the P120. Examples of tracking performance for a 1J pulse are shown in Figure 114. For each graph, the top lines show horizontal displacement and the bottom lines show vertical displacement. The blue lines are the actual displacements and the green lines are

“filtered” values (though in reality these appear to be averaged or smoothed values, which are not useful for analysis).

The BOOSTING algorithm provided high accuracy, but was not smooth. There was no drift, with the stone coming back to the laser fibre at the same pixel value as the first frame. It produced consistently noisy data with apparent oscillations of the tracking point from frame to frame. Tracking failures were minimal.

The MIL algorithm produced high accuracy, again with no drift. Tracking was generally extremely smooth as this was the only algorithm that outputted subpixel data such as 1.2 pixels, while all other algorithms rounded to a whole number of pixels. However, it produced occasional noise as can be seen in the spike in the graph, where the algorithm did not report tracking failure but instead would provide a single inaccurate frame. The frequency of these aberrant frames was high enough to be problematic.

The KCF algorithm produced satisfactory accuracy although it appear to require multiple consecutive frames of motion before reporting motion. This can be seen in the step-wise appearance of the tracking point as well as the long flat section where no motion was reported by this algorithm. In addition, no vertical movement was reported as the frame-to-frame motion was small, despite there being a significant overall change in vertical displacement throughout the video. There was a minimal amount of drift as seen by the second peak not quite matching up to the original position, but the stone remained within the tracking bounding box so this was considered to be minor.

The CSRT algorithm produced high accuracy with smooth tracking. There was a minimal amount of drift, similar to KCF, but again the stone remained within the tracking bounding box.

The MedianFlow algorithm produced satisfactory accuracy although with periods where the tracking motion misaligns with actual motion. This can be seen around frame 200 and frame 650 below. There was otherwise little noise. There was also occasional but significant drift, where the sides of

the bounding box can end up overlapping the edges of the stone. The vertical tracking accuracy was poor for unclear reasons, possibly related to the drifting.

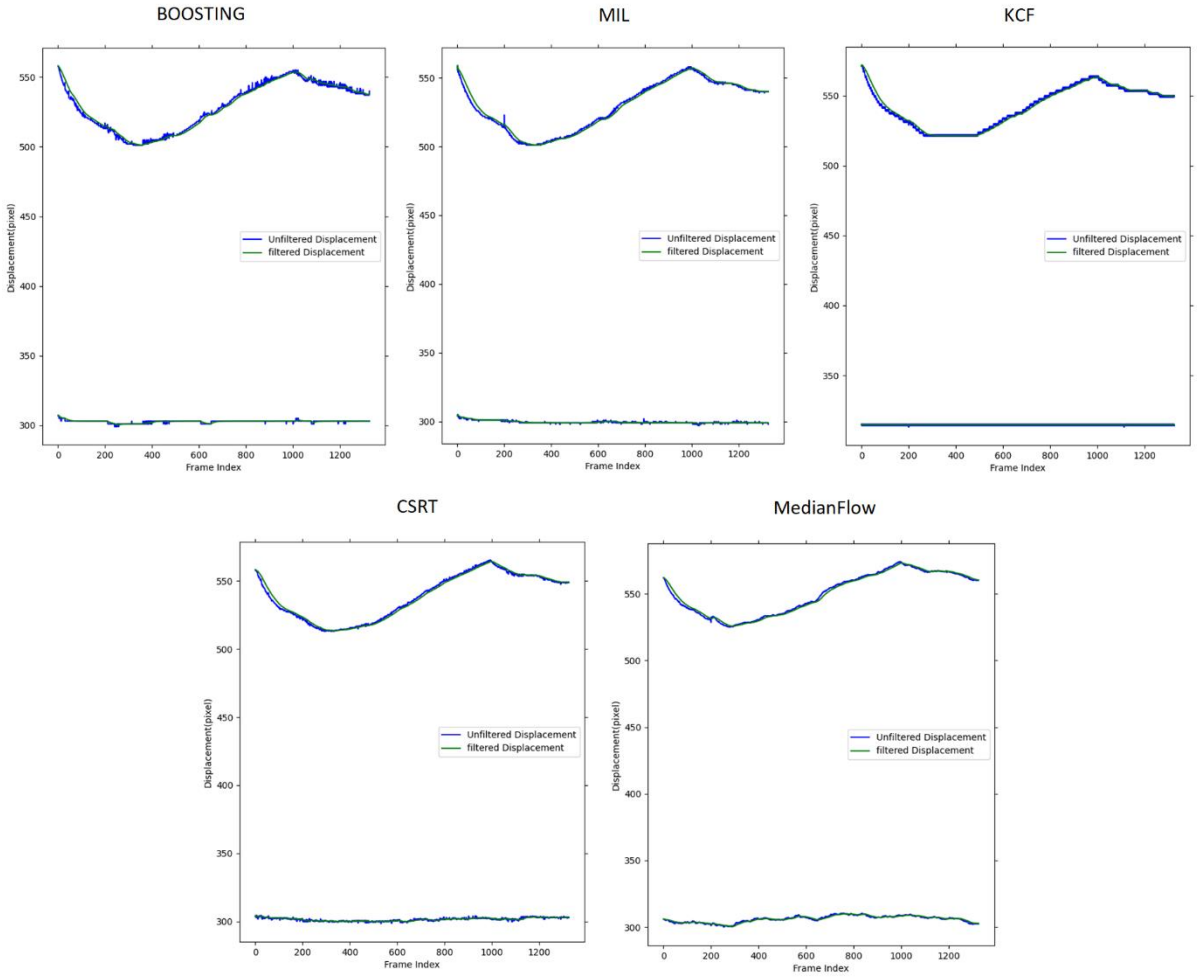


Figure 114. Image tracking performance for BOOSTING, MIL, KCF, CSRT and MedianFlow algorithms.

Based on this assessment, the CSRT algorithm was selected as the algorithm of choice for image tracking in both pendulum and linear retropulsion experiments.

Python image tracking script

```
from matplotlib.widgets import RadioButtons, Slider, TextBox, Button
import cv2
from matplotlib import pyplot as plt
import os, csv, ntpath, time
import numpy as np
from skimage import morphology
from tkinter import Tk
from tkinter.filedialog import askopenfiles

resultFilePath = os.getcwd()

#----------------
#initial window to get input directory
tk = Tk()
tk.withdraw()  # we don't want a full GUI, so keep the root window from appearing
```

```
rawFilePath = askopenfiles()  # show an "Open" dialog box and return the path to the selected
file
print(rawFilePath)
tk.destroy()

#------------------
#GUI related variables, don't change variables below
frame = None
previousFrame = None
tracker = None
bbox = (287, 23, 86, 320) # x, y, sizex, sizey
ypos = -1*np.ones((0,))
xpos = -1*np.ones((0,))
frameIndex = 0
totalFrameCount = 0
frameInterval = 100
pCov_realtime = 1.0
xs = np.arange(256)
fig = plt.figure(figsize=(18, 8))
plt.subplots_adjust(left=0.25)
ax1 = fig.add_subplot(121)
axcolor = 'lightgoldenrodyellow'

axbox_ymin = plt.axes([0.03, 0.65, 0.03, 0.03])
text_boxymin = TextBox(axbox_ymin, 'ymin:', initial="0")
axbox_ymax = plt.axes([0.10, 0.65, 0.03, 0.03])
text_boxymax = TextBox(axbox_ymax, 'ymax:', initial="392")
axbox_xmin = plt.axes([0.03, 0.55, 0.03, 0.03])
text_boxxmin = TextBox(axbox_xmin, 'xmin:', initial="0")
axbox_xmax = plt.axes([0.10, 0.55, 0.03, 0.03])
text_boxxmax = TextBox(axbox_xmax, 'xmax:', initial="394")
rax2 = plt.axes([0.04, 0.42, 0.08, 0.1], facecolor=axcolor)
radio_videoDirection = RadioButtons(rax2, ('Horizontal', 'Vertical'))
radio_videoDirection.set_active(0)
videoDirection = 'Horizontal'
rax_Interval = plt.axes([0.07, 0.35, 0.08, 0.02], facecolor=axcolor)
sInterval = Slider(rax_Interval, 'RefreshInterval', 1, 300, valinit=100, valstep=1)

ax_save = plt.axes([0.03, 0.25, 0.1, 0.075])
b_save = Button(ax_save, 'SaveResults')

ax2 = fig.add_subplot(122)
fig.show()
quitLoop = False
pauseLoop = True # initialized to be true, waiting for user to start the process
fileIndex = 0
goNextFrame = False

(major_ver, minor_ver, subminor_ver) = (cv2.__version__).split('.')
tracker_types = ['BOOSTING', 'MIL', 'KCF', 'TLD', 'MEDIANFLOW', 'GOTURN', 'MOSSE', 'CSRT']
tracker_type = tracker_types[7]
if int(minor_ver) < 3:
    tracker = cv2.Tracker_create(tracker_type)
else:
    if tracker_type == 'BOOSTING':
        tracker = cv2.TrackerBoosting_create()
    if tracker_type == 'MIL':
        tracker = cv2.TrackerMIL_create()
    if tracker_type == 'KCF':
        tracker = cv2.TrackerKCF_create()
    if tracker_type == 'TLD':
        tracker = cv2.TrackerTLD_create()
    if tracker_type == 'MEDIANFLOW':
        tracker = cv2.TrackerMedianFlow_create()
    if tracker_type == 'GOTURN':
        tracker = cv2.TrackerGOTURN_create()
    if tracker_type == 'MOSSE':
        tracker = cv2.TrackerMOSSE_create()
    if tracker_type == "CSRT":
        tracker = cv2.TrackerCSRT_create()


def press(event):
    global quitLoop, pauseLoop, fileIndex, goNextFrame
    if event.key == 'escape':
        print('pressed escape, Closed Figure!')
        quitLoop = True
```

```
    elif event.key == ' ':
        pauseLoop = not pauseLoop
    elif event.key == 'b':
        goNextFrame = True
        if fileIndex > 0:
            fileIndex = fileIndex - 1
    elif event.key == 'f':
        goNextFrame = True
        fileIndex = fileIndex + 1

def handle_close(evt):
    global quitLoop
    print('Closed Figure!')
    quitLoop = True

def changeVideoDirection(val):
    global videoDirection
    videoDirection = val
    processCurrentFrame()

def changeInterval(val):
    global frameInterval
    frameInterval = val
    processCurrentFrame()

def saveResults(event):
    global ypos, resultFilePath, xpos
    if os.path.exists(resultFilePath):
        os.remove(resultFilePath)
    data_rows = [["FrameIndex", "X Displacement(Pixel)", "X Filtered Displacement(Pixel)", "Y
Displacement(Pixel)", "Y Filtered Displacement(Pixel)"]]
    for frame, x, y in zip(xs, xpos, ypos):
        data_rows.append([frame,x[0], x[1], y[0], y[1]])
    with open(resultFilePath, 'w', newline='') as fout:
        writer = csv.writer(fout)
        writer.writerows(data_rows)

def processCurrentFrame():
    global frame, tracker, bbox, frameIndex, videoDirection, previousFrame, xpos, ypos,
frameInterval
    previousFrame = frame.copy()
    timer = cv2.getTickCount()
    trackFailed = False
    ok, bbox = tracker.update(frame)
    # Draw bounding box
    if ok:
        # Tracking success
        p1 = (int(bbox[0]), int(bbox[1]))
        p2 = (int(bbox[0] + bbox[2]), int(bbox[1] + bbox[3]))
        cv2.rectangle(frame, p1, p2, (255, 0, 0), 2, 1)
        xpos[frameIndex, 0] = bbox[0]
        xpos[frameIndex, 1] = kalmanFilteredPosesRealTime(bbox[0], xpos[:frameIndex, 1])
        ypos[frameIndex, 0] = bbox[1]
        ypos[frameIndex, 1] = kalmanFilteredPosesRealTime(bbox[1], ypos[:frameIndex, 1])
    else:
        # Tracking failure
        xpos[frameIndex, 0] = xpos[frameIndex-1, 0]
        xpos[frameIndex, 1] = kalmanFilteredPosesRealTime(xpos[frameIndex-1, 0],
xpos[:frameIndex, 1])
        ypos[frameIndex, 0] = ypos[frameIndex-1, 0]
        ypos[frameIndex, 1] = kalmanFilteredPosesRealTime(ypos[frameIndex-1, 0],
ypos[:frameIndex, 1])
        cv2.putText(frame, "Tracking failure detected", (100, 80), cv2.FONT_HERSHEY_SIMPLEX,
0.75, (0, 0, 255), 2)
    fps = cv2.getTickFrequency() / (cv2.getTickCount() - timer)

    if trackFailed:
        # Tracking failure
        cv2.putText(frame, "Tracking failure detected", (20, 10), cv2.FONT_HERSHEY_SIMPLEX,
0.25, (0, 0, 255), 1)
    # Display FPS on frame
    #cv2.putText(frame_roi, "FPS : " + str(int(fps)), (20, 30), cv2.FONT_HERSHEY_SIMPLEX,
0.25, (50, 170, 50), 1)
    if frameIndex%frameInterval==0:
        refreshUI(frame)

def kalmanFilteredPosesRealTime(pos, filteredDataAll, Q = 1e-5, R = 0.05**2):
```

```
    global pCov_realtime, frameIndex
    #Q = 1e-5  # process variance
    #R = 0.02 ** 2  # estimate of measurement variance, change to see effect
    # allocate space for arrays
    #hatminus = numpy.zeros(totalLen)  # a priori estimate
    #Intial guesses
    if frameIndex == 0: # first point not filtering
        return pos
    if pos > -1:
        totalLen = len(filteredDataAll) # current filtered data length
        # time update
        hatminus = filteredDataAll[frameIndex-1]
        Pminus = pCov_realtime + Q
         # measurement update
        K = Pminus / (Pminus + R)
        filteredPos = hatminus + K * (pos - hatminus)
        pCov_realtime = (1 - K) * Pminus
        return filteredPos
    else:
        return pos


def refreshUI(frame):
    global ypos, frameIndex, xpos
    ax1.cla()
    ax1.imshow(frame)
    ax2.cla()
    ypos[ypos == -1] = np.nan
    xpos[xpos == -1] = np.nan
    ax2.plot(xs, xpos[:, 0], color="b")
    ax2.plot(xs, xpos[:, 1], color="g")
    ax2.plot(xs, ypos[:, 0], color="b")
    ax2.plot(xs, ypos[:, 1], color="g")
    #ax2.plot(xs, ypos[:, 2], color="r")
    #ax2.plot(xs, ypos[:, 3], color="black")
    ax2.set_xlabel('Frame Index')
    ax2.set_ylabel('Displacement(pixel)')
    plt.legend(["Unfiltered Displacement", "filtered Displacement"])
    plt.draw()

def path_leaf(path):
    head, tail = ntpath.split(path)
    return tail or ntpath.basename(head)

def processAll():
    fig.canvas.mpl_connect('key_press_event', press)
    fig.canvas.mpl_connect('close_event', handle_close)
    sInterval.on_changed(changeInterval)
    radio_videoDirection.on_clicked(changeVideoDirection)
    b_save.on_clicked(saveResults)
    global frame, quitLoop, pauseLoop, fileIndex, goNextFrame, tracker, bbox, totalFrameCount,
xpos, ypos, xs, frameIndex, resultFilePath
    if rawFilePath is '':
        return
    cap = cv2.VideoCapture(rawFilePath[0].name)
    totalFrameCount = cap.get(cv2.CAP_PROP_FRAME_COUNT)
    ypos = -1*np.ones((np.int32(totalFrameCount),4))
    xpos = -1 * np.ones((np.int32(totalFrameCount), 4))
    xs = np.arange(totalFrameCount)
    cap.set(cv2.CAP_PROP_POS_AVI_RATIO, 0)
    ROISet=False
    resultFilePath = os.path.join(os.getcwd(), path_leaf(rawFilePath[0].name)[:-4] +'-'
+time.strftime("%Y%m%d-%H%M%S") +".csv")
    while (True and (not quitLoop)):
        # Capture frame-by-frame
        ret, frame = cap.read()
        if not ROISet:
            bbox = cv2.selectROI(frame, False)
            text_boxymin.set_val(bbox[1])
            text_boxxmin.set_val(bbox[0])
            text_boxymax.set_val(bbox[1]+bbox[3])
            text_boxxmax.set_val(bbox[0] + bbox[2])
            ok = tracker.init(frame, bbox)
            xpos[frameIndex, 0] = bbox[0]
            xpos[frameIndex, 1] = bbox[0]
            ypos[frameIndex, 0] = bbox[1]
            ypos[frameIndex, 1] = bbox[1]
```

```
            if ok:
                ROISet = True
        if (not quitLoop and ret):
            processCurrentFrame()
            while 1:
                # when user quit the application, race condition occurs. plt is closed while
pausing. plt.pause(0.02) hangs here. so close the plt in this thread using the quitLoop flag
                if quitLoop:
                    plt.close()
                    break
                plt.pause(0.002)
                if not pauseLoop:
                    break
            frameIndex = frameIndex + 1
        else:
            print("end of video")
            frame = previousFrame # retain the lastframe
            frameIndex = frameIndex -1 # revert the frame index to the lastframe
            while 1:
                if quitLoop:
                    plt.close()
                    break
                plt.pause(0.002)

def main():
    processAll()

if __name__ == '__main__':
    main()
```

References

1. Brown, J., *Diagnostic and treatment patterns for renal colic in US emergency departments.* Int Urol Nephrol, 2006. **38**(1): p. 87-92.
2. Antonelli, J.A., et al., *Use of the National Health and Nutrition Examination Survey to calculate the impact of obesity and diabetes on cost and prevalence of urolithiasis in 2030.* Eur Urol, 2014. **66**(4): p. 724-9.
3. Türk, C., et al., *EAU Guidelines on Diagnosis and Conservative Management of Urolithiasis.* European Urology, 2016. **69**(3): p. 468-474.
4. Türk, C., et al., *EAU Guidelines on Interventional Treatment for Urolithiasis.* European Urology, 2016. **69**(3): p. 475-482.
5. Jour, I., A. Lam, and B. Turney, *Urological stone disease: a 5-year update of stone management using Hospital Episode Statistics.* BJU International, 2022. **130**(3): p. 364-369.
6. BAUS. *Percutaneous nephrolithotomy (keyhole surgery for kidney stones)*. 08/03/2023]; Available from: http://www.baus.org.uk/_userfiles/pages/files/Patients/Leaflets/PCNL.pdf.
7. Einstein, A., *The collected papers of Albert Einstein*. 1987: Princeton, N.J. : Princeton University Press, c1987-.
8. Wikipedia. *Stimulated Emission*. 2008 [cited 2022 23/09/22]; Available from: https://en.wikipedia.org/wiki/File:Stimulated_Emission.svg.
9. Marshall, V.F., *Fiber Optics in Urology.* Journal of Urology, 1964. **91**(1): p. 110-114.
10. Goodman, T.M., *Ureteroscopy with pediatric cystoscope in adults.* Urology, 1977. **9**(4): p. 394.
11. Lyon, E.S., J.S. Kyker, and H.W. Schoenberg, *Transurethral Ureteroscopy in Women: A Ready Addition to the Urological Armamentarium.* The Journal of Urology, 1978. **119**(1): p. 35-36.
12. Pérez-Castro Ellendt, E. and J.A. Martinez-Piñero, *Ureteral and Renal Endoscopy.* European Urology, 1982. **8**: p. 117-120.
13. Berci, G. and L.A. Kont, *A new optical system in endoscopy with special reference to cystoscopy.* Br J Urol, 1969. **41**(5): p. 564-71.
14. Huffman, J.L., D.H. Bagley, and E.S. Lyon, *Treatment of distal ureteral calculi using rigid ureteroscope.* Urology, 1982. **20**(6): p. 574-577.
15. Watson, G. and J. Wickham, *The development of a laser and a miniaturised ureteroscope system for ureteric stone management.* World Journal of Urology, 1989. **7**(3): p. 147-150.
16. Bagley, D.H. and M.H. Rittenberg, *Percutaneous antegrade flexible ureteroscopy.* Urology, 1986. **27**(4): p. 331-334.
17. Grocela, J.A. and S.P. Dretler, *INTRACORPOREAL LITHOTRIPSY: Instrumentation and Development.* Urologic Clinics of North America, 1997. **24**(1): p. 13-23.
18. ZHONG, P., et al., *Transient oscillation of cavitation bubbles near stone surface during electrohydraulic lithotripsy.* Journal of endourology, 1997. **11**(1): p. 55-61.
19. Huffman, J.L., et al., *Transurethral removal of large ureteral and renal pelvic calculi using ureteroscopic ultrasonic lithotripsy.* J Urol, 1983. **130**(1): p. 31-4.
20. Green, D.F. and B. Lytton, *Early Experience with Direct Vision Electrohydraulic Lithotripsy of Ureteral Calculi.* The Journal of Urology, 1985. **133**(5): p. 767-770.
21. Farrell, J.R., *Transurethral Ureteroscopic Lithotripsy Procedures for the Treatment of Kidney Stones.* International Journal of Technology Assessment in Health Care, 1986. **2**(1): p. 161-167.
22. Denstedt, J.D., P.M. Eberwein, and R.R. Singh, *The Swiss Lithoclast: A New Device for Intracorporeal Lithotripsy.* The Journal of Urology, 1992. **148**(3, Part 2): p. 1088-1090.

23. Thomsen , S., *PATHOLOGIC ANALYSIS OF PHOTOTHERMAL AND PHOTOMECHANICAL EFFECTS OF LASER–TISSUE INTERACTIONS.* Photochemistry and Photobiology, 1991. **53**(6): p. 825-835.
24. Kuzyk, M.G. and N.J. Dawson, *Photomechanical materials and applications: a tutorial.* Advances in Optics and Photonics, 2020. **12**(4): p. 847-1011.
25. Welch, A. and M. van Gemert, *Optical-Thermal Response of Laser-Irradiated Tissue.* Optical-Thermal Response of Laser-Irradiated Tissue by Ashley J. Welch and Martin J.C. van Gemert. Berlin: Springer, 2011. ISBN: 978-9-048-18830-7, 2011.
26. Chan, K.F., et al., *Holmium:YAG laser lithotripsy: A dominant photothermal ablative mechanism with chemical decomposition of urinary calculi.* Lasers Surg Med, 1999. **25**(1): p. 22-37.
27. Niemz, M., *Laser-Tissue Interactions: Fundamentals and Applications*. 2019.
28. Maiman, T.H., *Stimulated Optical Radiation in Ruby.* Nature, 1960. **187**(4736): p. 493-494.
29. Mulvaney, W.P. and C.W. Beck, *The laser beam in urology.* J Urol, 1968. **99**(1): p. 112-5.
30. Anderholm, N.C., *LASER GENERATED STRESS WAVES.* Applied Physics Letters, 1970. **16**: p. 113-115.
31. Fair, H.D., Jr., *In vitro destruction of urinary calculi by laser-induced stress waves.* Med Instrum, 1978. **12**(2): p. 100-5.
32. Hofmann, R. and W. Schütz, *[Destruction of urinary calculi using laser beams. Experimental principles and in vitro studies].* Der Urologe. Ausg. A, 1984. **23**(3): p. 181-184.
33. Richou, B., et al., *Delivery of 10-MW Nd:YAG laser pulses by large-core optical fibers: dependence of the laser-intensity profile on beam propagation.* Applied Optics, 1997. **36**(7): p. 1610-1614.
34. Nath, G., W. Gorisch, and P. Kiefhaber, *First Laser Endoscopy via a Fiberoptic Transmission System.* Endoscopy, 1973. **5**: p. 208-213.
35. WATSON, G.M., et al., *Laser Fragmentation of Renal Calculi.* British Journal of Urology, 1983. **55**(6): p. 613-616.
36. Dretler, S.P., *Laser lithotripsy: A review of 20 years of research and clinical applications.* Lasers in Surgery and Medicine, 1988. **8**(4): p. 341-356.
37. Watson, G., et al., *The pulsed dye laser for fragmenting urinary calculi.* J Urol, 1987. **138**(1): p. 195-8.
38. Hofmann, R., et al. *Clinical Experience with Laser-Induced Shock-Wave Lithotripsy*. 1988. Berlin, Heidelberg: Springer Berlin Heidelberg.
39. Thomas, S., et al., *The pulsed dye laser versus the Q-switched Nd:YAG laser in laser-induced shock-wave lithotripsy.* Lasers in Surgery and Medicine, 1988. **8**(4): p. 363-370.
40. Dretler, S.P., et al., *Pulsed Dye Laser Fragmentation of Ureteral Calculi: Initial Clinical Experience.* The Journal of Urology, 1987. **137**(3): p. 386-389.
41. Bolton, D.M., J.S. Peters, and A.J. Costello, *Experience with the pulsed dye laser in management of ureteric calculi.* Aust N Z J Surg, 1992. **62**(10): p. 788-90.
42. Jiang, Z., C. Whitehurst, and T. King, *Fragmentation methods in laser lithotripsy*. Optics, Electro-Optics, and Laser Applications in Science and Engineering. Vol. 1421. 1991: SPIE.
43. Teng, P., et al., *Mechanisms Of Laser-Induced Stone Ablation*. Cambridge Symposium-Fiber/LASE '86. Vol. 0712. 1987: SPIE.
44. Uebelacker, W., *Laser lithotripsy with a Q-switched alexandrite laser system*. OE/LASE '92. Vol. 1643. 1992: SPIE.
45. Ell, C., et al., *Laser-induced shockwave lithotripsy of gallstones.* Endoscopy, 1986. **18**(3): p. 95-6.
46. Teng, P., et al., *Acoustic studies of the role of immersion in plasma-mediated laser ablation.* IEEE Journal of Quantum Electronics, 1987. **23**(10): p. 1845-1852.
47. Rink, K., G. Delacrétaz, and R.P. Salathé, *Fragmentation process of current laser lithotriptors.* Lasers in Surgery and Medicine, 1995. **16**(2): p. 134-146.

48. Zhong, P., *Transient Cavitation and Acoustic Emission Produced by Different Laser Lithotripters.* Journal of Endourology, 1998. **12**(4): p. 371-378.
49. Stern, D., et al., *Corneal Ablation by Nanosecond, Picosecond, and Femtosecond Lasers at 532 and 625 nm.* Archives of Ophthalmology, 1989. **107**(4): p. 587-592.
50. Weber, H., et al., *Alexandrite Laser Lithotripter in Experimental and First Clinical Application.* Journal of Endourology, 1991. **5**(1): p. 51-55.
51. Miller, K., et al., *Treatment of ureteral stone disease: the role of ESWL and endourology.* World Journal of Urology, 1985. **3**(1): p. 53-57.
52. Coptcoat, M., et al., *Lasertripsy for Ureteral Stones: 100 Clinical Cases.* Journal of Endourology, 1987. **1**(2): p. 119-122.
53. Brinkmann, R., et al., *Laser-induced shockwave lithotripsy by use of a 1-us Alexandrite laser*. OE/LASE '90. Vol. 1200. 1990: SPIE.
54. Maghraby, H., et al., *Laser lithotripsy: in-vitro comparison of different systems*. OE/LASE '90. Vol. 1200. 1990: SPIE.
55. Kwiatkowski, J., et al., *Resonantly pumped tunable Ho:YAG laser.* Laser Physics Letters, 2009. **6**(7): p. 531-534.
56. Traxer, O. and E. Keller, *Thulium fiber laser: the new player for kidney stone treatment? A comparison with Holmium:YAG laser.* World Journal of Urology, 2020. **38**.
57. Lilge, L., W. Radtke, and N.S. Nishioka, *Pulsed holmium laser ablation of cardiac valves.* Lasers in Surgery and Medicine, 1989. **9**(5): p. 458-464.
58. Stein, E., et al., *Acute and chronic effects of bone ablation with a pulsed holmium laser.* Lasers in Surgery and Medicine, 1990. **10**(4): p. 384-388.
59. Sayer, J., et al., *Ureteral Lithotripsy with the Holmium:YAG Laser.* Journal of Clinical Laser Medicine & Surgery, 1993. **11**(2): p. 61-65.
60. Denstedt, J.D., et al., *Preliminary experience with holmium: YAG laser lithotripsy.* J Endourol, 1995. **9**(3): p. 255-8.
61. Razvi, H.A., et al., *Intracorporeal Lithotripsy With the Holmium:YAG Laser.* The Journal of Urology, 1996. **156**(3): p. 912-914.
62. Webb, D.R., R. Kockelburgh, and W.F. Johnson, *The Verapulse holmium surgical laser in clinical urology: A pilot study.* Minimally Invasive Therapy, 1993. **2**(1): p. 23-26.
63. Jansen, E.D., et al., *Effect of pulse duration on bubble formation and laser-induced pressure waves during holmium laser ablation.* Lasers in Surgery and Medicine, 1996. **18**(3): p. 278-293.
64. Vassar, G.J., et al., *Holmium: YAG lithotripsy: photothermal mechanism.* J Endourol, 1999. **13**(3): p. 181-90.
65. Teichman, J.M., et al., *Holmium:YAG lithotripsy yields smaller fragments than lithoclast, pulsed dye laser or electrohydraulic lithotripsy.* J Urol, 1998. **159**(1): p. 17-23.
66. Zörcher, T., et al., *In vitro study concerning the efficiency of the frequency-doubled double-pulse Neodymium:YAG laser (FREDDY) for lithotripsy of calculi in the urinary tract.* Lasers Surg Med, 1999. **25**(1): p. 38-42.
67. Mueller, G., et al., *New alternative for laser lithotropsy-long pulse passively q-switched solid-state laser with fiber-based resonator.* 1994.
68. Yates, J., A. Zabbo, and G. Pareek, *A comparison of the FREDDY and holmium lasers during ureteroscopic lithotripsy.* Lasers in Surgery and Medicine, 2007. **39**(8): p. 637-640.
69. Dubosq, F., et al., *Endoscopic Lithotripsy and the FREDDY Laser: Initial Experience.* Journal of Endourology, 2006. **20**(5): p. 296-299.
70. Knipper, S., et al., *Is Prolonged Operation Time a Predictor for the Occurrence of Complications in Ureteroscopy?* Urologia Internationalis, 2015. **95**(1): p. 33-37.
71. Lane, J., et al., *Correlation of Operative Time with Outcomes of Ureteroscopy and Stone Treatment: a Systematic Review of Literature.* Current Urology Reports, 2020. **21**(4): p. 17.

72. Corrales, M., A. Sierra, and O. Traxer, *Moses and Moses 2.0 for Laser Lithotripsy: Expectations vs. Reality.* Journal of Clinical Medicine, 2022. **11**(16): p. 4828.
73. Sánchez-Puy, A., et al., *New Generation Pulse Modulation in Holmium:YAG Lasers: A Systematic Review of the Literature and Meta-Analysis.* J Clin Med, 2022. **11**(11).
74. Osman, M.M., et al., *5-year-follow-up of Patients with Clinically Insignificant Residual Fragments after Extracorporeal Shockwave Lithotripsy.* European Urology, 2005. **47**(6): p. 860-864.
75. Brain, E., et al., *Natural History of Post-Treatment Kidney Stone Fragments: A Systematic Review and Meta-Analysis.* Journal of Urology, 2021. **206**(3): p. 526-538.
76. Keller, E.X., et al., *What is the exact definition of stone dust? An in vitro evaluation.* World Journal of Urology, 2021. **39**(1): p. 187-194.
77. Hale, G.M. and M.R. Querry, *Optical Constants of Water in the 200-nm to 200-µm Wavelength Region.* Applied Optics, 1973. **12**(3): p. 555-563.
78. Mohammadzadeh, M., J.M. Mercado, and C.-D. Ohl, *Bubble Dynamics in Laser Lithotripsy.* Journal of Physics: Conference Series, 2015. **656**: p. 012004.
79. Isner, J., et al. *TRANSMISSION CHARACTERISTICS OF INDIVIDUAL WAVELENGTHS IN BLOOD DO NOT PREDICT ABILITY TO ACCOMPLISH LASER ABLATION IN A BLOOD FIELD-INFERENTIAL EVIDENCE FOR THE MOSES EFFECT*. in *Circulation*. 1986. AMER HEART ASSOC 7272 GREENVILLE AVENUE, DALLAS, TX 75231-4596.
80. Trost, D., *Laser pulse format for penetrating an absorbing fluid*. 1994, Google Patents.
81. Ibrahim, A., et al., *Double-Blinded Prospective Randomized Clinical Trial Comparing Regular and Moses Modes of Holmium Laser Lithotripsy.* J Endourol, 2020. **34**(5): p. 624-628.
82. Rodríguez Socarrás, M.E., et al., *Pulse Modulation for Holmium Laser: Vapor Tunnel–Virtual Basket–Bubble Blast.* Videourology, 2020. **34**(3).
83. Finley, D.S., et al., *Effect of Holmium:YAG Laser Pulse Width on Lithotripsy Retropulsion in Vitro.* Journal of Endourology, 2005. **19**(8): p. 1041-1044.
84. Alghamdi, A., et al., *Influence of the laser pulse shape in the treatment of stones in the upper urinary tract.* Investig Clin Urol, 2020. **61**(6): p. 594-599.
85. Olympus. *Olympus EMPOWER Holmium:YAG Laser Portfolio*. 2022 [cited 2022 23/09/2022]; Available from: https://www.olympus.co.uk/medical/en/Products-and-solutions/Products/Product/OLYMPUS-EMPOWER-H35-H65-and-H100.html.
86. Peter Rechmann, D.D.S., S.G. Dan, and H. Thomas. *Er:YAG lasers in dentistry: an overview*. in *Proc.SPIE*. 1998.
87. Teichman Joel, M.H., et al., *ERBIUM:YAG VERSUS HOLMIUM:YAG LITHOTRIPSY.* Journal of Urology, 2001. **165**(3): p. 876-879.
88. Teichman, J.M.H., et al., *Update On Erbium:YAG lithotripsy.* AIP Conference Proceedings, 2007. **900**(1): p. 216-227.
89. Petzold, R., A. Miernik, and R. Suarez-Ibarrola, *In Vitro Dusting Performance of a New Solid State Thulium Laser Compared to Holmium Laser Lithotripsy.* Journal of Endourology, 2020. **35**(2): p. 221-225.
90. Tünnermann, A., et al., *The renaissance and bright future of fibre lasers.* Journal of Physics B: Atomic, Molecular and Optical Physics, 2005. **38**(9): p. S681-S693.
91. Hardy, L.A., et al., *Analysis of thulium fiber laser induced bubble dynamics for ablation of kidney stones.* Journal of Biophotonics, 2017. **10**(10): p. 1240-1249.
92. Blackmon, R.L., P.B. Irby, and N.M. Fried, *Comparison of holmium:YAG and thulium fiber laser lithotripsy: ablation thresholds, ablation rates, and retropulsion effects.* Journal of biomedical optics, 2011. **16**(7): p. 071403-071403.
93. Huusmann, S., et al., *Tissue damage by laser radiation: an in vitro comparison between Tm:YAG and Ho:YAG laser on a porcine kidney model.* SpringerPlus, 2016. **5**(1): p. 266.
94. Luke, A.H., et al. *Fragmentation and dusting of large kidney stones using compact, air-cooled, high peak power, 1940-nm, Thulium fiber laser*. in *Proc.SPIE*. 2018.

95. Jansen, E.D., et al., *Temperature dependence of the absorption coefficient of water for midinfrared laser radiation.* Lasers in Surgery and Medicine, 1994. **14**(3): p. 258-268.
96. Andreeva, V., et al., *Preclinical comparison of superpulse thulium fiber laser and a holmium:YAG laser for lithotripsy.* World Journal of Urology, 2020. **38**(2): p. 497-503.
97. Enikeev, D., et al., *Superpulsed Thulium Fiber Laser for Stone Dusting: In Search of a Perfect Ablation Regimen-A Prospective Single-Center Study.* J Endourol, 2020. **34**(11): p. 1175-1179.
98. Corrales, M. and O. Traxer, *Initial clinical experience with the new thulium fiber laser: first 50 cases.* World J Urol, 2021. **39**(10): p. 3945-3950.
99. Carrera, R.V., et al., *Ureteroscopic Performance of High Power Super Pulse Thulium Fiber Laser for the Treatment of Urolithiasis: Results of the First Case Series in North America.* Urology, 2021. **153**: p. 87-92.
100. Geavlete, B., et al., *Romanian National premiere with the new Thulium SuperPulsed Laser in the endourological treatment of urolithiasis.* J Med Life, 2021. **14**(3): p. 316-322.
101. Taratkin, M., et al., *Prospective Single-Center Study of SuperPulsed Thulium Fiber Laser in Retrograde Intrarenal Surgery: Initial Clinical Data.* Urol Int, 2022. **106**(4): p. 404-410.
102. Belle, J.D., et al., *Does the Novel Thulium Fiber Laser Have a Higher Risk of Urothelial Thermal Injury than the Conventional Holmium Laser in an In Vitro Study?* Journal of Endourology, 2022. **36**(9): p. 1249-1254.
103. Sierra, A., et al., *Thermal Injury and Laser Efficiency with Holmium YAG and Thulium Fiber Laser—An In Vitro Study.* Journal of Endourology, 2022. **36**(12): p. 1599-1606.
104. Traxer, O. *BN89: Recommended rules for TmFibreLaser*. Twitter 2022 08/03/2023; Available from: https://twitter.com/OTRAXER/status/1527918351137259520?s=20.
105. Skolarikos, A., et al., *Training in ureteroscopy: a critical appraisal of the literature.* BJU International, 2011. **108**(6): p. 798-805.
106. Gridley, C.M. and B.E. Knudsen, *Digital ureteroscopes: technology update.* Res Rep Urol, 2017. **9**: p. 19-25.
107. Ding, J., et al., *Comparing the Efficacy of a Multimodular Flexible Ureteroscope With Its Conventional Counterpart in the Management of Renal Stones.* Urology, 2015. **86**(2): p. 224-9.
108. Dale, J., et al., *Evaluation of a Novel Single-Use Flexible Ureteroscope.* Journal of Endourology, 2016. **35**(6): p. 903-907.
109. Mager, R., et al., *Clinical outcomes and costs of reusable and single-use flexible ureterorenoscopes: a prospective cohort study.* Urolithiasis, 2018. **46**(6): p. 587-593.
110. Usawachintachit, M., et al., *A Prospective Case-Control Study Comparing LithoVue, a Single-Use, Flexible Disposable Ureteroscope, with Flexible, Reusable Fiber-Optic Ureteroscopes.* J Endourol, 2017. **31**(5): p. 468-475.
111. Dragos, L.B., et al., *Characteristics of current digital single-use flexible ureteroscopes versus their reusable counterparts: an in-vitro comparative analysis.* Transl Androl Urol, 2019. **8**(Suppl 4): p. S359-s370.
112. Williams, J.G., et al., *The Fluid Mechanics of Ureteroscope Irrigation.* Journal of Endourology, 2018. **33**(1): p. 28-34.
113. *Lumenis Pulse 120H Holmium Laser System with MOSES 2.0 Technology*. 2022 [cited 2024 12/02/24]; Available from: https://www.bostonscientific.com/content/dam/bostonscientific/uro-wh/portfolio-group/Lumenis/pdf/Lumenis-Pulse-120H-Brochure-EN.pdf.
114. Hardy, L.A., V. Vinnichenko, and N.M. Fried, *High power holmium:YAG versus thulium fiber laser treatment of kidney stones in dusting mode: ablation rate and fragment size studies.* Lasers Surg Med, 2019. **51**(6): p. 522-530.
115. Hardy, L.A., et al., *Thulium fiber laser lithotripsy in an in vitro ureter model.* J Biomed Opt, 2014. **19**(12): p. 128001.

116. Esch, E., et al., *A simple method for fabricating artificial kidney stones of different physical properties.* Urol Res, 2010. **38**(4): p. 315-9.
117. Prien, E.L. and E.L. Prien, *Composition and structure of urinary stone.* The American Journal of Medicine, 1968. **45**(5): p. 654-672.
118. Grant, C., et al., *Variation in Kidney Stone Composition Within the United States.* Journal of Endourology, 2018. **32**(10): p. 973-977.
119. Terry, R.S., et al., *Comparison of Different Pulse Modulation Modes for Holmium:Yttrium–Aluminum–Garnet Laser Lithotripsy Ablation in a Benchtop Model.* Journal of Endourology, 2021. **36**(1): p. 29-37.
120. Ventimiglia, E., et al., *Effect of temporal pulse shape on urinary stone phantom retropulsion rate and ablation efficiency using holmium:YAG and super-pulse thulium fibre lasers.* BJU International, 2020. **126**(1): p. 159-167.
121. Taratkin, M., et al., *How Lasers Ablate Stones: In Vitro Study of Laser Lithotripsy (Ho:YAG and Tm-Fiber Lasers) in Different Environments.* J Endourol, 2021. **35**(6): p. 931-936.
122. Winship, B., et al., *Dusting Efficiency of the Moses Holmium Laser: An Automated In Vitro Assessment.* Journal of Endourology, 2018. **32**(12): p. 1131-1135.
123. Panthier, F., et al., *Lasers and Stones: Towards an Approach that Depends on the Stone Type? A Point of View from PEARLS Members.* European Urology, 2024. **85**(3): p. e92-e93.
124. Aldoukhi, A.H., et al., *Strike Rate: Analysis of Laser Fiber to Stone Distance During Different Modes of Laser Lithotripsy.* J Endourol, 2021. **35**(3): p. 355-359.
125. MARGUET, C.G., et al., *IN VITRO COMPARISON OF STONE RETROPULSION AND FRAGMENTATION OF THE FREQUENCY DOUBLED, DOUBLE PULSE ND:YAG LASER AND THE HOLMIUM:YAG LASER.* Journal of Urology, 2005. **173**(5): p. 1797-1800.
126. Elhilali, M.M., et al., *Use of the Moses Technology to Improve Holmium Laser Lithotripsy Outcomes: A Preclinical Study.* Journal of Endourology, 2017. **31**(6): p. 598-604.
127. Kang, H.W., et al., *Investigation of stone retropulsion as a function of Ho:YAG laser pulse duration*. SPIE BiOS. Vol. 6078. 2006: SPIE.
128. White, M.D., et al., *Evaluation of retropulsion caused by holmium:YAG laser with various power settings and fibers.* J Endourol, 1998. **12**(2): p. 183-6.
129. Martov, A.G., et al., *Clinical Comparison of Super Pulse Thulium Fiber Laser and High-Power Holmium Laser for Ureteral Stone Management.* Journal of Endourology, 2020. **35**(6): p. 795-800.
130. Corrales, M. and O. Traxer, *Retrograde intrarenal surgery: laser showdown (Ho:YAG vs thulium fiber laser).* Curr Opin Urol, 2022. **32**(2): p. 179-184.
131. Kronenberg, P. and O. Traxer, *The laser of the future: reality and expectations about the new thulium fiber laser-a systematic review.* Translational andrology and urology, 2019. **8**(Suppl 4): p. S398-S417.
132. Blackmon, R.L., et al., *Fiber-optic manipulation of urinary stone phantoms using holmium:YAG and thulium fiber lasers.* J Biomed Opt, 2013. **18**(2): p. 28001.
133. Lovegrove, C.E., et al., *Natural history of small asymptomatic kidney and residual stones over a long-term follow-up: systematic review over 25 years.* BJU Int, 2022. **129**(4): p. 442-456.
134. Sea, J., et al., *Optimal Power Settings for Holmium:YAG Lithotripsy.* The Journal of Urology, 2012. **187**(3): p. 914-919.
135. Bader, M.J., et al., *Impact of pulse duration on Ho:YAG laser lithotripsy: fragmentation and dusting performance.* World Journal of Urology, 2015. **33**(4): p. 471-477.
136. Black, K.M., et al., *Pulse modulation with Moses technology improves popcorn laser lithotripsy.* World J Urol, 2021. **39**(6): p. 1699-1705.
137. Spore, S.S., et al., *Holmium: YAG lithotripsy: optimal power settings.* J Endourol, 1999. **13**(8): p. 559-66.
138. Pal, D., et al., *Continuous-wave and quasi-continuous wave thulium-doped all-fiber laser: implementation on kidney stone fragmentations.* Applied Optics, 2016. **55**(23): p. 6151-6155.

139. Rassweiler, J., M.-C. Rassweiler, and J. Klein, *New technology in ureteroscopy and percutaneous nephrolithotomy.* Current Opinion in Urology, 2016. **26**(1): p. 95-106.
140. Haynes, W.M.E., *CRC Handbook of Chemistry and Physics (95th ed.)*. 95 ed. 2014: CRC Press.
141. Bhuiyan, M.I.H., D.S. Mavinic, and R.D. Beckie, *A SOLUBILITY AND THERMODYNAMIC STUDY OF STRUVITE.* Environmental Technology, 2007. **28**(9): p. 1015-1026.
142. Walton, R.C., J.P. Kavanagh, and B.R. Heywood, *The density and protein content of calcium oxalate crystals precipitated from human urine: a tool to investigate ultrastructure and the fractional volume occupied by organic matrix.* J Struct Biol, 2003. **143**(1): p. 14-23.
143. Ngatiman, M., et al., *Investigation of struvite crystals formed in palm oil mill effluent anaerobic digester.* Heliyon, 2021. **7**(1).
144. Information, N.C.f.B., *PubChem Compound Summary for CID 24456, Calcium Phosphate.*
145. Lier, J.A.V., P.L.D. Bruyn, and J.T.G. Overbeek, *THE SOLUBILITY OF QUARTZ.* The Journal of Physical Chemistry, 1960. **64**(11): p. 1675-1682.
146. Khalil, I., et al., *Brushite: Synthesis, Properties, and Biomedical Applications*, in *Crystallization and Applications*, S. Youssef Ben and M. Riadh, Editors. 2022, IntechOpen: Rijeka. p. Ch. 7.
147. Schamel, M., *Novel dual setting approaches for mechanically reinforced mineral biocements*. 2017.
148. Abdelshehid, C., et al., *COMPARISON OF FLEXIBLE URETEROSCOPES: DEFLECTION, IRRIGANT FLOW AND OPTICAL CHARACTERISTICS.* The Journal of Urology, 2005. **173**(6): p. 2017-2021.
149. Ng, Y.H., et al., *Irrigant Flow and Intrarenal Pressure During Flexible Ureteroscopy: The Effect of Different Access Sheaths, Working Channel Instruments, and Hydrostatic Pressure.* Journal of Endourology, 2010. **24**(12): p. 1915-1920.
150. Haas, C.R., et al., *Pulse-modulated Holmium:YAG Laser vs the Thulium Fiber Laser for Renal and Ureteral Stones: A Single-center Prospective Randomized Clinical Trial.* J Urol, 2023. **209**(2): p. 374-383.
151. Ulvik, Ø., J.-R. Harneshaug, and P. Gjengstø, *What Do We Mean by "Stone Free," and How Accurate Are Urologists in Predicting Stone-Free Status Following Ureteroscopy?* Journal of Endourology, 2020. **35**(7): p. 961-966.
152. Grasso, M. and D.H. Bagley, *Flexible Ureteroscopic Lithotripsy Using Pulsed-Dye Laser.* Journal of Endourology, 1990. **4**(2): p. 155-160.
153. Dretler, S.P., *Laser Photofragmentation of Ureteral Calculi: Analysis of 75 Cases.* Journal of Endourology, 1987. **1**(1): p. 9-14.
154. Smith, D., et al., *Ureteroscopic treatment of urolithiasis: How do we measure and optimise outcomes?* Journal of Clinical Urology, 2024: p. 20514158241237278.
155. Brain, E., et al., *Natural History of Post-Treatment Kidney Stone Fragments: A Systematic Review and Meta-Analysis.* J Urol, 2021. **206**(3): p. 526-538.
156. Kakinuma, R., et al., *Ultra-High-Resolution Computed Tomography of the Lung: Image Quality of a Prototype Scanner.* PLoS One, 2015. **10**(9): p. e0137165.
157. Albeshan, S., et al., *Assessment of effective dose and radiation-induced cancer risk in CT-KUB.* Journal of Radiation Research and Applied Sciences, 2023. **16**(3): p. 100629.
158. Kluner, C., et al., *Does Ultra-Low-Dose CT With a Radiation Dose Equivalent to That of KUB Suffice to Detect Renal and Ureteral Calculi?* Journal of Computer Assisted Tomography, 2006. **30**(1).
159. Van Appledorn, S., et al., *Limitations of Noncontrast CT for Measuring Ureteral Stones.* Journal of Endourology, 2003. **17**(10): p. 851-854.